# Core-shell nanoparticles active in non-linear optics for the imagery and phototherapy of cancer

Rachael Taitt

N°d'ordre NNT : 2021LYSEC11

**THESE de DOCTORAT DE L'UNIVERSITE DE LYON**
**opérée au sein de l'Ecole centrale de Lyon**

**Ecole Doctorale** N° 160
**Electronique, Electrotechnique et Automatique**

**Spécialité de doctorat** : Ingénierie pour le vivant

Soutenue publiquement/à huis clos le 22/03/2021, par :
**Rachael Marie Taitt**

---

# Nanoparticules cœur-coquille actives en optique non linéaire pour l'imagerie et la photothérapie du cancer

---

Devant le jury composé de :

| | | | | |
|---|---|---|---|---|
| Pr. LE DANTEC, | Ronan | PR | Université Savoie-Mont Blanc | **Président du jury** |
| Dr. CHARNAY, | Clarence | MCF, HDR | Université de Montpellier | Rapporteur |
| Pr. GRANGE, | Rachel | PR | ETH Zurich | Rapporteure |
| Dr. TESTARD | Fabienne | Chercheure | CEA-Saclay | Examinatrice |
| Dr. MONNIER | Virginie | MCF, HDR | Ecole Centrale de Lyon | Directrice de thèse |
| Dr. CHEVOLOT | Yann | Directeur de recherche | Ecole Centrale de Lyon | Co-directeur de thèse |

# Contents

# List of Figures

# List of Tables

# Glossary

- AuNPs: gold nanoparticles
- BPEI: branched polyethylenimine
- CW: continuous wave
- DC: direct current
- DLS: dynamic light scattering
- EDX/S: energy dispersive X-ray spectrscopy
- EM: electromagnetic
- FWHM: full width at half maximum
- HNPs: harmonic nanoparticles
- HRS: Hyper Rayleigh Scattering
- ICP-AES: inductive coupled plasma atomic emission spectroscopy
- LN: $LiNbO_3$ nanoparticles
- LN@Au: gold shell $LiNbO_3$ nanoparticles
- LN@BPEI: BPEI coated $LiNbO_3$ nanoparticles
- LN@BPEI@AuSeeds: BPEI coated $LiNbO_3$ nanoparticles with AuSeeds attached
- NADH: nicotinamide adenine dinucleotide reduced form
- NCs: manocages
- $NH_2OH.HCl$: hydroxylamine hydrochloride
- NLO: non-linear optics

- NPs: nanoparticles
- NRs: nanorods
- NSs: nanoshells
- PDT: photodynamic therapy
- PPTT: plasmonic photothermal therapy
- RSF: relative sensitivity factor
- SPR: surface plasmon resonance
- TEM: transmission electron microscopy
- TOF-SIMS: time-of-flight secondary ion mass spectroscopy
- XPS: X-ray photelectron spectroscopy

# Acknowledgments

Completing this PhD thesis was indeed an exciting feat but a mammoth undertaking. Fortunately, it was a task with which I received a great amount of support from colleagues, friends and family alike, and it would be remiss of me to not publicly thank those to whom my gratitude is owed.

Firstly, I would like to thank Mr. Frank Debouck, president of the Ecole Centrale de Lyon, and Dr. Catherine Bru-Chevallier and Dr. Christian Seassal, directors of the Institute of Nanotechnologies Lyon, for the opportunity to conduct the thesis at their first-class institutions. I would also like to thank Dr. Gérard Scorletti and Dr. Phillipe Delachartre, past and present presidents of the EEA ecole doctorale during my tenure as a PhD candidate.

Thank you to all the members of my jury for accepting to read and evaluate the quality of my research. To the two rapporteurs, Dr. Clarence Charnay and Prof. Rachel Grange, who were tasked to also respond in writing to my maunscript, I say a grand thank you. Your comments and remarks were read with the most careful eye and aided in the enhancement of the quality of both my written and oral presentation. Thank you to Prof. Ronan LeDantec who not only served as the president of the jury, but who had also been readily available throughout the course of the PhD to give his expert opinion on all matters related to the non-linear optical response of materials. Your contributions have significantly enhanced my understanding of the subject matter. I also sincerely thank Dr. Fabienne Testard whose questions and comments made for an invigorating scientific discussion.

To my thesis director and co-director, Dr. Virginie Monnier and Dr. Yann Chevolot, I will be forever grateful for all the guidance, time and support you both have given me throughout my tenure as your PhD student. Thank you for pushing the boundaries of my critical thinking while still leaving me room for autonomous growth. You have witnessed my joys and my tears during this process, saw all the very rough, crudely written drafts of my manuscript, and reminded me that it was all a part of the process when I personally felt as though I was failing. Your careful leadership will undoubtedly serve as a model for me in my future career. I particularly thank you for your care

and empathy displayed to me during the unprecedented time of the Covid-19 pandemic. I cannot say it enough: thank you, thank you, thank you!

A special thank you to the researchers and support staff employees alike, who helped make the technical aspects of my research possible: Dr. Thomas Gehin who helped design the laser experimental set-up, Mrs. Isabel Nabeth who was always ready to tell me where my chemicals were or order more when they were running low, Dr. Nicolas Blanchard who taught me how to operate a TEM microscope autonomously, Dr. Giacomo Ceccone who conducted TOF-SIMS and XPS analysis for me, and countless other research collaborators who gave advice and lent their expertise to the topic. I owe the quality of the data I gathered to your efforts, and I thank you. To all my colleagues at INL, Ecole Centrale and the wider PhD community I found in Lyon, both past and present: it is true what they say, there is comfort in numbers. Your companionship and solidarity was invaluable. You made Lyon not just feel like my city of work, but truly like home. I thank you for all the laughs and for the support, the dance parties, the dinners, the karaoke sessions, and the spontaneous road-trips. It will all be fondly remembered and I wish you all the best for your future endeavors.

Finally, to my family. Family for me, is not defined solely by my blood-relations, but it is an extended network of people whom I have chosen as my family. You, my family, are scattered all around the globe. To my family in Trinidad and Tobago, Jamaica, United States of America, the UK and France, I love and thank you all for believing so fiercely in my potential.

To Mrs. Margaret Bonas-Taitt and Mr. Rupert Taitt, mom and dad, this work is truly for you. Thank you for allowing me to believe for all of my life, that we are never limited by our geography. The world is ours for the taking. I hope I have made you proud.

# General Introduction

Over the last 50 years, there has been a growing interest in materials with size dimensions in the nanometer region, as scientists have observed the novel properties that come with the decreased size. Some of the changes observable in nanomaterials are mechanical, optical, magnetic, electrical and chemical, and as such, the field of nanotechnologies crosses every scientific discipline, and has created new branches of science. One such branch is nanomedicine: the use of nanomaterials and nanotechnologies in medical practices. During the last two decades, researchers have been particularly interested in nanomaterials for cancer applications.[1–4] Cancer continues to be a major global health challenge, ranking as the 1st or 2nd leading cause of death in over 97 countries.[5] As synthesis of nanomaterials, specifically nanoparticles, have become simpler and more robust, they have been used as contrast agents and bio-probes to improve the detection limits and signal-to-background ratios of existing cancer diagnostic techniques. Additionally, the enhanced permeability and retention (EPR) effect which is believed to be (though now heavily debated[6]) the preferential uptake of nanoparticles in tumors as a result of the tumors' poor, leaky vascular system,[7] results in greater accumulation of these particles at tumor sites. This in theory gives nanoparticles specific utility as vehicles for cancer therapies.

Many of these nanoparticles that have already been integrated into medicinal applications are prepared via wet-chemistry methods. Though there are ongoing studies on the importance of each synthesis parameter on the final nanoparticles formed, there are still many ambiguities in the process which leads to various inhomogeneities (size, shape, morphology) and lower than desired reproducibility rates. This, in addition to nanoparticle aggregation tendencies, the formation of protein coronas around the particles *in-vivo*, as well as the lack of data on long-term toxicity effects, are some of the barriers in moving from the lab to the clinic. Despite these challenges, nanoparticles are still viewed as viable tools in cancer therapies as they have been demonstrated at both the laboratory and clinical levels to provide multi-functional cancer therapies and diagnostics at the nanoscale, and when active targeting is incorporated, they can provide a more disease-localized treatment solution, minimizing the dangerous side-effects of traditional therapies.[8]

The categories of nanoparticles most commonly used in nanomedicine can be classed by their composing materials. They are polymeric nanoparticles, liposomes and inorganic nanoparticles which can be further broken down to semiconductor, noble metal and metal oxide nanoparticles. Focusing on the inorganic nanoparticles, their synthesis can be readily achieved via wet-chemistry procedures such as sol-gel synthesis, solvothermal synthesis, co-precipitation, micro-emulsion, self-assembly and seed-mediated synthesis. Importantly, these wet chemistry procedures have been shown to provide control on the shapes, sizes, and surface properties of these nanoparticles. It is widely accepted and shown in the literature that the reaction conditions (pH, concentration of reacting species, temperature etc) determines the final nanoparticle form and changing one such parameter can produce an entirely different nanoparticle. Therefore, synthesis procedures of nanoparticles must be clearly defined and the nanoparticles produced must be well characterized.

Nanoparticles that can provide diagnostic and therapeutic functionalities simultaneously, termed theranostics nanoparticles, are the next phase in nanomedicine cancer therapies, however few have been developed and to date even fewer have made it to clinical trials. The combining of at least two materials, keeping their independently different properties at the nanoscale is one approach to designing theranostic nanoparticles. The term nanohybrids is used to describe such designs, and they are usually made up of a metal or metal-oxide core, with another metal, metal oxide or polymer covering the core particle. In choosing the materials to combine, one must firstly consider what type of diagnostic and therapeutic approach intended. In medical diagnostics, nanoparticles have been investigated for magnetic resonance imaging (MRI), ultrasound and photoacoustic imaging, computed X-ray tomography (CT), and optical based imaging. Nanoparticles have also been investigated for their applications in cancer therapeutic approaches, serving as drug delivery platforms, radiation sensitization, photodynamic therapy (PDT) and photothermal therapy (PTT) agents.

In this thesis, we are interested in the fundamental studies on the synthesis of core-shell nanohybrids with the potential to be used as cancer theranostic nanoparticles. The bio-imaging functionality envisioned for these nanohybrids is non-linear optic from the nanohybrid core, comprised of $LiNbO_3$. For the therapeutic functionality, we aim for plasmonic photothermal therapy to be achieved by depositing a gold shell on the $LiNbO_3$ core.

In chapter one, we firstly will present an introduction into the utility of nano-materials, discussing how and why they exhibit a change in their properties when compared to their bulk counterparts. The chapter then continues with a review of the literature pertaining to the use of nanoparticles for cancer imaging techniques and cancer therapeutic techniques. The chapter continues to focus on hybrid nanoparticles and their development for cancer theranostics, focusing on core-shell hybrid nanoparticles. Finally, the definitive objectives of the thesis are outlined.

In chapter two, the main characterization methods for nanoparticles and nanoparticle dispersions used throughout this work are presented. The characterization techniques outlined are transmission electron microscopy (TEM), X-ray photoelectron spectroscopy (XPS), energy dispersive X-ray spectroscopy (EDS), dynamic light scattering (DLS), laser doppler velocimetry, UV-visible absorption spectroscopy, inductive coupled plasma atomic emission spectroscopy (ICP-AES) and time-of-flight secondary ion mass spectroscopy (TOF-SIMS). The chapter presents a balanced discussion on the advantages and limitations of these listed techniques, along with specific examples pertaining to this work. This includes a discussion, comparing and contrasting the complementary techniques. Finally, the calculations pertaining to the evaluation of nanoparticle concentration used in this work are detailed.

In chapter three, the results of our work on the attachment of small spherical gold nanoparticles called AuSeeds, to the core $LiNbO_3$ nanoparticles is presented. Therein we detail the synthesis protocols, and present the results of their characterizations at different protocol steps. The physical and chemical properties of the nanoparticles were determined by XRD, XPS, TEM, EDS, DLS and laser doppler velocimetry. Finally, the nanoparticles formed were evaluated for their non-linear properties by performing Hyper Rayleigh Scattering experiments.

In chapter four, the work on the growth of the gold shell via seeded-growth methods, is presented. Along with the synthesis protocols, the characterizations of the nanoparticles produced at various steps of the synthesis is presented. As we were interested in the influence of experimental parameters such as pH, initial seed density, and concentration of the gold salt to be reduced, we present our results investigating these parameters which are then discussed in detail. Finally, we present our general conclusions based on this work, along with our perspectives.

# Chapter 1

# State of the Art

## 1.1 Moving from bulk to nano

Decreasing the size of matter from the bulk regime (>1 µm) to the nanoscale regime (1 to 100 nm in at least one dimension), has led to significant scientific progress over the last 50 years. In fact, nanotechnologies have been applied to almost every industry and impacted every aspect of our daily lives as illustrated in fig. 1.1. In the electronics industry it has led to the design of smaller, lighter electronics with higher data storage capacities. In the textiles industry it has advanced the development of materials with flame retardant, anti-bacterial, UV-protecting, self-cleaning properties and more. In the food industry it has allowed for prolonged food storage, addition of artificial flavoring and the encapsulation of nutrients in food. In the chemical industries, its applications vary from the development of novel chemical sensors and catalysts for detection and removal of pollutants in air and water, to nano-engineering novel properties for paints. In the medical industry, it has allowed for the development of optical tweezers for surgery, bio-sensors, bio-imaging probes, drug delivery platforms and other therapeutic advancements. Focusing on the use of nanomaterials and nanotechnology to medicine, we can plot its rise in importance over the last 4 decades by looking at the trend in number of research publications devoted to the topic. A search on the scopus journal database for the keywords "nanoparticles for cancer" reveals an exponential rise in publications from 1980 to 2019 (fig. 1.2), and we still have not reached the saturation point regarding its benefits and applicability across industries. To understand why this field has garnered so much attention and grown so rapidly, the changes upon moving from bulk to nano will be discussed, with focus placed on nanomaterials such as nanoparticles (NPs).

The physicochemical properties of nanomaterials, like nanoparticles, tend to differ from that of their bulk form. Although the property changes observable upon moving from bulk to nano vary for different materials, the factors that contribute to these changes are i) size, ii) shape, iii) surface chemistry/charge and iv) interactions with its environment (eg. particle-particle interactions,

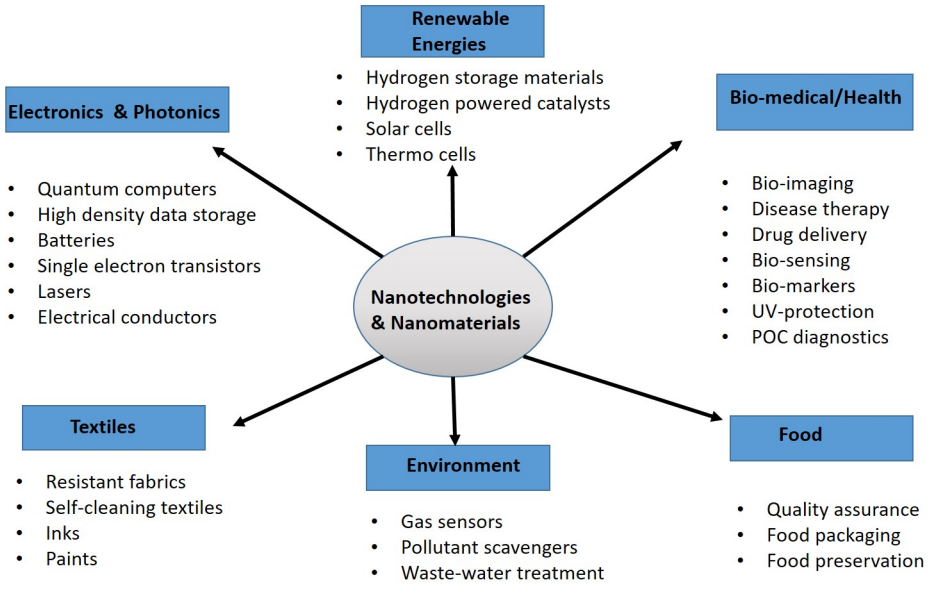


Figure 1.1: A categorization of some of the applications of nanomaterials and nanotechnologies to various essential industries. (POC= point of care)

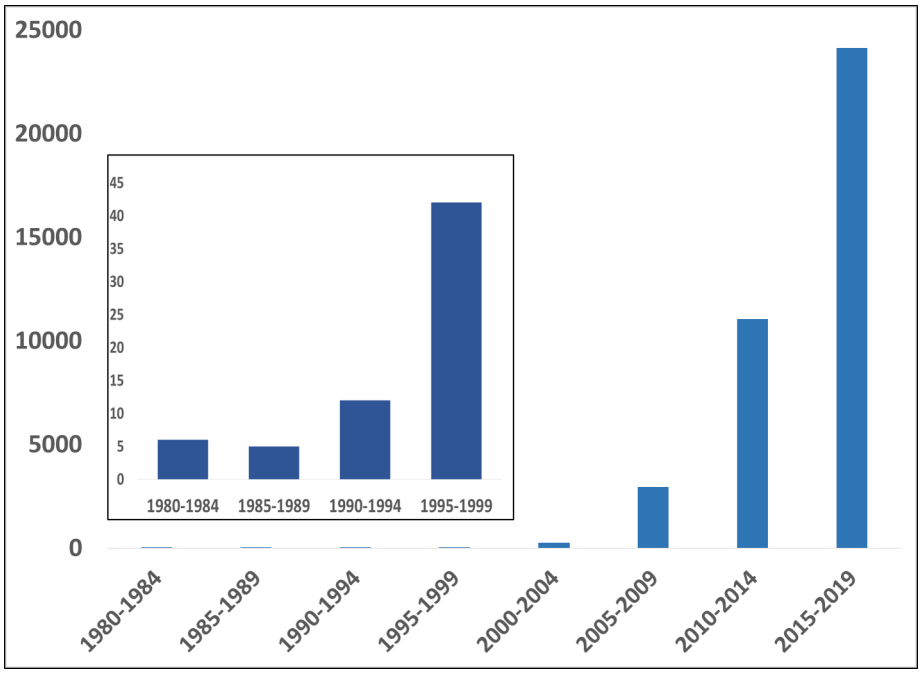


Figure 1.2: Grouped histogram showing the number of journal articles published on nanoparticles for cancer from 1980-2019. Insert showing a zoom of the graph for the data set 1980-1999. Data extracted from Scopus search database.

particle-solvent interactions). The technique chosen to obtain the nanomaterials is important as it influences these factors. The fabrication of nanomaterials is grouped into two categories: top-down techniques such as lithography, and bottom-up approaches such as self-assembly (fig. 1.3). For the context of this work, we will focus the discussion on the literature concerning nanoparticles that have been synthesized by bottom-up methods. Now let us first examine the impact of changing size and why this leads to a change in physical/chemical properties.

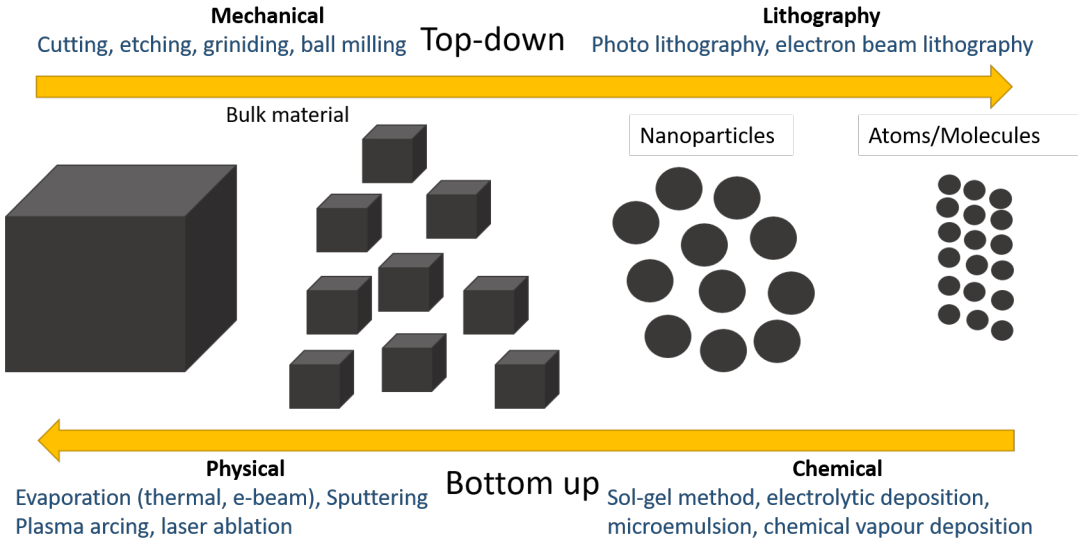


Figure 1.3: Illustration of the change in size and specific surface area of materials upon moving from bulk to nano and vice versa, detailing the common bottom up and top down techniques used.

In bulk matter, the atoms at the material's core are in a different physical and chemical environment than the atoms located at the material's surface. The atomic network in the material (whether metallic, ionic or covalent) will determine physical properties such as melting and boiling points, elasticity, and also optical properties. The surface atoms, located at the interface of the material and its surrounding matter (air/liquid/solid), are distinguishable from the bulk atoms; they experience a break in the symmetry and spatial geometry with respect to the bulk atoms. Consequently, we can make a distinction between the properties of the surface atoms and the bulk atoms. In the bulk regime, only a small proportion of the material's atoms are located at the surface, and so the material's properties are defined by the properties of the bulk atoms. However, as we start decreasing the size of the material to nanometer dimensions, the ratio of surface atoms to bulk/core atoms increases as is illustrated by fig. 1.4, and the material can no longer be defined by bulk properties.[9] For example, there is consensus in the literature, that decreasing the size to the nano regime, generally improves catalytic performance. A notable example of this is seen with the

gold element. In its bulk form, it is chemically inert, however, when it is in the form of nanoparticles and, in most examples, supported on oxide surfaces, gold becomes a highly active catalyst.[10,11]

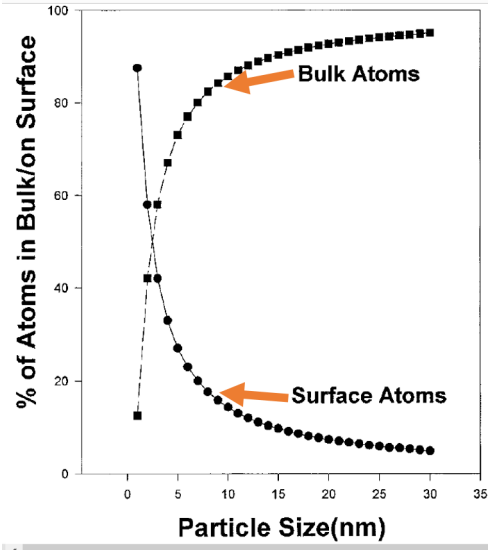


Figure 1.4: Percentage of bulk and surface atoms upon increasing particle size.[12]

Along with the absolute size, the absolute shape of nanoparticles also impacts their physicochemical properties. This is best illustrated by examples. If we examine the optical properties of nanoscale gold, we observe the impact of changing shape: spherical gold nanoparticles (AuNPs), gold nanorods (AuNRs), and gold nanostars all have characteristic extinction bands, which are then further tuneable by varying their sizes.[13–16] In fig. 1.5, the relationship between the aspect ratio of AuNRs and their corresponding extinction spectra, as well as that for core-shell $SiO_2$@Au NPs is presented.[13,14] Another example in the literature is on the cellular uptake of chitosan-capped AuNPs, AuNRs and gold nanostars. The authors Lee *et. al*[17] concluded that changing the core nanoparticles' shape impacted their cytotoxicity and cellular uptake.

Although it was mentioned earlier when discussing the size effect, the surface properties of nanoparticles deserve a closer examination on how it impacts its properties. All particles and surfaces have a natural surface charge. This charge is acquired by the adsorption of surrounding molecules or ions to their surface, and/or as a result of a "loose" bond as the surface atoms will not be bonded to the same number of the same kind of atoms as the bulk atoms. The surface state of the nanoparticles will affect its stability and its aggregation.[9] The environment of the NPs will also play a role in these surface effects. For example, by changing the ionic concentration of the medium the nanoparticles are dispersed in, it can shield the intra-particle surface charge repulsions and cause rapid aggregation, as shown in several studies of the effect of salt concentration on AuNPs.[18] So

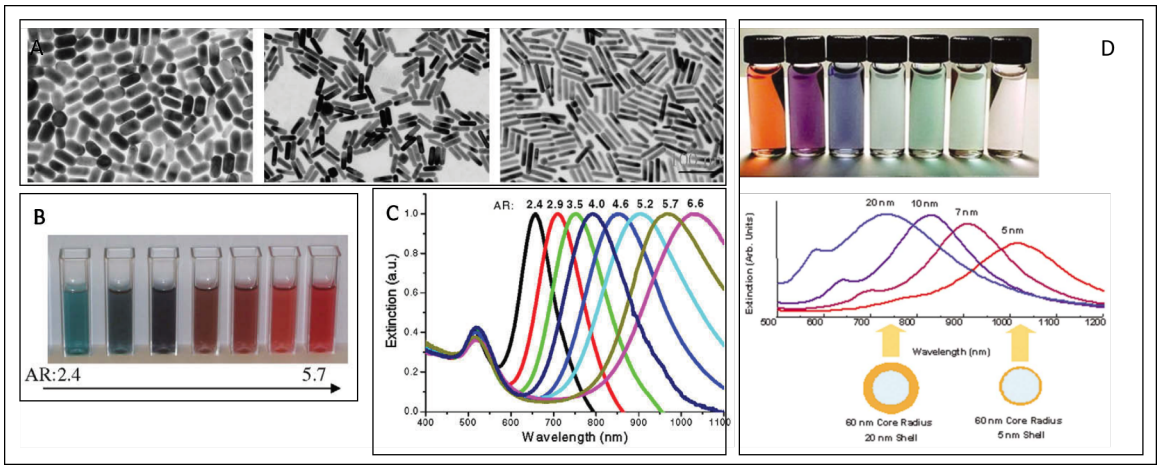


Figure 1.5: Illustration of the colour changes along with their corresponding extinction spectra of Au-nanorods and Au-nanoshells. (A) TEM image of Au-nanorods of different aspect ratios. (B) The colour changes observed upon changing aspect ratio of Au-nanorods and (C) the extinction spectra showing the SPR wavelengths of Au-nanorods of different aspect ratios.[13] (D) The change in colour and the extinction spectra corresponding to the variation of the core diameter/shell thickness ratio of Au nanoshells.[14]

in designing and characterizing nanoparticles, it is necessary for the researcher to detail clearly the composition, the shape, the size and the surface properties where possible and to understand the role the dispersing media will also have on its physical and chemical properties.

With all the advantages and novelty that nanoparticles bring, it is easy to understand why they have been employed to biological applications. Cellular uptake of molecules is a strictly regulated process that occurs primarily by diffusion or active transportation through the cellular membrane which is a lipid bi-layer. The nature of the bi-layer therefore limits the type and size of molecules permitted to cross the membrane. This has direct implications on drug development. Cellular uptake for nanoparticles however is charge, shape and size dependent and can be done through endocytic pathways, where the particles can be encapsulated in lysosomes and endosomes.[19] This has provided drug developers with a new pathway for introducing drug molecules into the cell, that would have been forbidden entry on its own. Nanoparticles have also been shown to collect in the tumor microenvironment. This preferential uptake has been termed the enhanced permeability and retention (EPR) effect. Additionally, by grafting and attaching biomolecules to their surface, nanoparticles can be made bio-compatible, can avoid detection by the body's immune response and therefore have longer circulation times (particularly useful for *in-vivo* imaging probes), can become a platform for active disease targeting, and can be used for controlled drug release.[20]

In the following sections, the literature concerning the application of nanoparticles for cancer di-

agnostics and treatment will be reviewed, with particular focus on plasmonic and non linear optic active nanoparticles and the synthesis of hybrid and core-shell nanoparticles.

## 1.2 Nanoparticles for cancer imaging

Cancer therapies are most effective when initiated at an early stage of the cancer's development. Therefore, the diagnostic tools used must be able to quickly and accurately identify the cancers. There are two complementary approaches for diagnosis: *ex-vivo* analysis (such as biopsies analysis and blood analysis), and *in-vivo* medical imaging. *In-vivo* medical imaging is an invaluable tool in the diagnosing and the post-treatment monitoring of cancers. There are imaging techniques that use ionizing radiation, radio frequency pulses, fluorescence signals, and ultrasound frequencies. Each technique however, has its inherent limitations that may prevent sufficient contrast between different organs and tissues, inhibit tissue depth penetration or impinge the spatial resolution. In the table 1.1, the spatial resolution, which informs the size objects that can be observed, and the depth penetration of the most common clinical imaging techniques are given. As we see from the data, magnetic resonance imaging (MRI) and computer tomography (CT) imaging, give the best resolution among these clinical techniques (resolving objects as small as 0.25 mm), which is ideal for observing tissue lesions and tumor masses of the mm dimensions. However, we know that cancerous events commence at the cellular level and as such, imaging techniques such as confocal microscopy imaging and optical coherence tomography, which are capable of spatial resolutions of the order of 0.1 µm are employed (fig. 1.6). The reality is no singular technique is complete with all the required capabilities, and they are often used in a complementary fashion to each other, the goal being to detect the earliest signs of abnormalities.

Besides the technological advancements of the imaging equipment itself, one strategy to improve upon the images obtainable and the information extractable from these techniques has been the use of nanoparticles as bio-imaging probes and contrast agents. In this way, an enhancement of the modalities such as sensitivity, resolution and depth penetration are achieved. In this section we will review the literature pertaining to the use of nanoparticles in the main cancer imaging techniques. There are many examples of nanoparticles that have been studied for their imaging functionalities and it is not the goal of this work to list them all, but focus is given to special classes and specific nanoparticles that will give us a full appreciation for what has been done. Some key scientific reviews and articles that discuss the nanoparticles in more details have been referenced in table 1.1.

| Imaging Technique | Excitation Radiation Source | Nanoparticle | Resolution | Penetration Depth | Reference |
|---|---|---|---|---|---|
| MRI | Radio frequency waves | SPION<br>$Gd_2O_3$<br>$MnFe_2O_4$<br>$Au@Fe_3O_4$<br>Gd chelate Au | 0.25-1 mm | limited by magnetic bore | Gupta, 2005[21]<br>Blasiak, 2013[22]<br>Alric, 2008[23] |
| Optical Imaging | Visible and NIR light | quantum dots<br>gold nanorods<br>$Au@Fe_3O_4$ | 2-3 mm | <1 cm | Han, 2019[24]<br>Na 2009[25] |
| US | Ultrasound frequency waves | microbubbles<br>PFC-NP<br>rattle-type MSN<br>PFOB NPs | 1-2 mm | a few cm | Int J<br>Li, 2018[26]<br>Jin, 2017[27] |
| PET | $\gamma$-rays | $^{18}$F-labelled MSN<br>[$^{64}$Cu]CuS<br>AuNPs | 1-2 mm | unlimited | Lee, 2013[28]<br>Bulte, 2017[29] |
| SPECT | $\gamma$-rays | $^{125}$I AgNP<br>[$^{59}$Fe]-SPIONs | 8-10 mm | unlimited | Zhao, 2016[30] |
| CT | X-rays | AuNPs<br>tantalum oxide<br>liposomal iodine | 0.5-1 mm | unlimited | Bulte, 2017[31] |

Table 1.1: A list of nanoparticles in the literature that have been used for different medical-imaging techniques. PFOB NPs= Perfluorooctylbromide nanoparticles, SPION= superparamagnetic iron oxide NPs, MSN= mesoporous silica nanoparticle, SPECT= single-photon emission computed tomography. The data on resolution and depth penetration was obtained from Sim and Parker, *Chem. Soc. Rev*, 2015.[32]

### 1.2.1 Magnetic Resonance Imaging (MRI)

Magnetic Resonance Imaging (MRI) is a routinely used clinical imaging technique, based upon the absorption and emission of radio frequency (RF) waves when subjected to an external magnetic field. Protons under the influence of this external magnetic field will precess at a specific frequency called the Larmor Frequency. In MRI, the static magnetic field is set so that the Larmor frequency of the protons are in the RF region. Then an RF pulse is supplied, which, if matched to the Larmor frequency of the protons, will cause excitation and phase matching. The magnetic field is sectioned into different magnetic strengths by a field gradient coil which means that the protons in the different regions of examination will be precessing at different Larmor frequencies. One way imaging contrast is achieved, is by the difference in the $T_1$ and $T_2$ relaxation times. The $T_1$ relaxation time refers to the time it takes to recuperate the net longitudinal magnetization of the protons which is a result of having more protons occupying the lower energy state when not excited. The $T_2$ relaxation time refers to the decay of the phase coherence achieved with the matching RF excitation pulse.

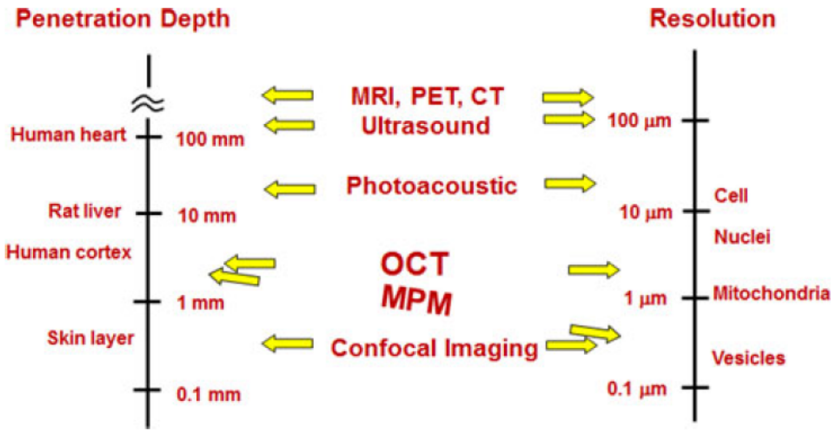


Figure 1.6: The depth penetration and spatial resolution of common imaging techniques. MRI= magnetic resonance imaging, PET= positron emission tomography, CT= computed X-ray tomography, OCT= optical coherence tomography, MPM= multiphoton microscopies. Image taken from reference.[33]

The strengths of the MRI technique is its ability to provide high contrast between soft tissues and lesions and its 3D imaging functionality. Additionally, as the imaging is based on magnetic fields and not on ionizing radiation like some other techniques, it is a low risk, non-invasive diagnostic tool. Though when compared to other clinical imaging techniques like PET, it has a greater spatial resolution, it is still within the range of millimeters. This is a disadvantage particularly for cancer diagnosis as a millimeter sized tumor already consists of billions of cancer cells. In addition to this, the results of some studies have revealed the low specificity of MRI for breast cancer diagnosis, reporting false-positive rates of 10% and as high as 40% in some cases.[34,35] The use of superparamagnetic iron oxide NPs (SPIONs) have improved the sensitivity of MRI as they "disturb" the magnetic field, causing the relaxation of the protons of water to occur faster, working as T2 weighted contrast agents, and have found particular application in the imaging of cancers of the liver, many of which are commercially available like Feridex, Endorem and Resovist.[22] Gadolinium oxide nanoparticles have also been used but the toxicity of the free Gd ions is non-negligible.

To further improve the specificity of MRI imaging for cancer, modifications of the NPs to have specific biomolecules attached to their surface has been done to give an active targeting. Some groups of biomolecules already successfully attached to the NPs surface are anti-bodies, proteins, peptides and aptamers.[25]

### 1.2.2 Ultrasound (US) & Photoacoustic Imaging

Ultrasound (US) imaging, is another common medical diagnostic tool which employs high-frequency sound waves (frequencies higher than 20,000 Hz) to produce an image.[36,37] The ultrasound waves are generated by a transducer and directed to the area of the subject to be imaged. The transducer also detects the US waves reflected back. The US reflection occurs when the sound wave contacts tissues, bones, and bodily fluids. The time for each US wave reflection to contact the transducer is based on the frequency of US signal used and the acoustic resistances of what it contacts. Then, it is possible to determine the distance between the transducer and the tissues/bones/bodily fluids that caused the reflection and a 2D image can be generated.

Photoacoustic (PA) imaging is also imaging based upon sound waves, but these sound waves are generated by the subject or material absorbing light. By using a pulsed laser, the subject is irradiated. This irradiation is absorbed and causes an increase in temperature of the absorber which then quickly dissipates this heat to its environment. Its environment then experiences thermal expansion followed by contraction to return to its original state. It is with this contraction that an acoustic wave is generated, which is then detected by a transducer, and finally generates an image much like the US imaging described above.

Though US imaging does not require contrast agents to work (as opposed to PET & SPECT), nanoparticles have been included to provide active targeting (attaching specific biomolecules to the surface) and/or to improve the contrast achievable. Microbubbles allow for higher contrast US imaging and so, nanoparticles with air cavities are the design prototypes for this technique. One study showed the improved imaging contrast observed when using gas-filled polymer nanobubbles in mice. Not only was the contrast improved but the contrast imaging duration was longer when compared to the clinically approved microbubbles.[37]

Photoacoustic imaging contrast is very dependent on the degree of optical absorbance, and this has been used to its advantage. For example, one of the major proteins found in blood, haemoglobin, is a strong optical absorber and as such, PA is useful for studying the blood. With respect to cancer diagnosis, it has been used for the imaging of tumor neoangiogenesis and monitoring antiangiogenic therapy.[38] Though PA imaging is possible without the need of exogenous markers and contrast agents, nanoparticles have been employed as their size make them ideal for observing biological scale events (cellular processes), and there are groups of nanoparticles like noble metal nanoparticles that can be tailored to have enhanced optical absorption.

### 1.2.3 Positron Emission Tomography (PET)

Positron emission tomography falls under the category of nuclear medical imaging. Nuclear imaging employs radionuclides, which are atoms possessing excess nuclear energy making them unstable. These radionuclides, also called radio tracers or PET tracers when applied to PET imaging, are administered in small concentrations to the subject (usually on the scale of nM or pM). To become stable atoms, they undergo a decay process. In the case of PET, the PET tracers emit positron particles in their decay process which quickly combine with a nearby electron, resulting in the annihilation of the two particles and the formation of two $\gamma$-photons that then proceed to travel in opposite directions. The PET cameras then detect, collect and measure these photons to create a 3D image. Traditionally, the radiotracers such as $^{18}$F, $^{11}$C, $^{13}$N and $^{15}$O are attached to a biomolecule to be safely administered to the patient. The biomolecule chosen would depend upon the purpose of the imagery. For example, since a high uptake of glucose is often associated with cancer tumors, a sugar biomolecule may be chosen as the carrier for the radionuclide. This tailoring of the carrier molecule is what makes PET imaging unique, but due to the radiotracers used for PET, it is a time consuming procedure. It is time consuming because of the short half-lives of the PET radiotracers, which means that they are prepared on site and linked to its carrier molecule approximately two hours before being administered to the patient. In addition to this, there is a required waiting time to allow the compounds to arrive at the target location in the body. Nevertheless, PET is routinely performed as there is no limit to the depth from which the signal will originate and therefore in principle, any part of the body can be imaged.

There are advantages to using nanoparticles as platforms for delivering radionuclides for PET imaging. Radio-labeled nanoparticles can enhance the contrast and sensitivity of the imaging modality as they can act as signal amplifiers.[39] The high specific surface of nanoparticles make it possible to graft a multitude of biomolecules for multiple targeting. This is particularly useful for cancer screenings when the doctor is unsure as to which cell receptors are over-expressed. Nanoparticles are a platform that can allow for multimodal imaging, for example MRI/PET scans. Radio-labeled nanoparticles can also be designed to include a therapeutic functionality.

Nanoparticles that have already been used to encapsulate or attach radionuclides for PET analysis are mesoporous silica nanoparticles, gold nanoparticles, and a particularly interesting group of nanoparticles called ultrasmall nanoparticles (less than 10 nm) have been used to study metabolic pathways and have sparked interest for more targeted therapies.[29]

### 1.2.4 Single-Photon Emission Computed Tomography (SPECT)

This is also a nuclear medical imaging technique quite similar to PET. It differs from PET as the signal is not due to a radionuclide decay by positron annihilation, but rather by single photon emitters, emitting single $\gamma$-rays. Due to this difference, SPECT is a less sensitive technique because geometrical constraints are placed on the location of the collimators for the emitted photons and therefore not all the photons emitted will be detected. However, the life-time of these single photon emitting radionuclides are longer than those used for PET and as such allows for longer observational times.

The advantages for using SPECT radiolabeled nanoparticles is identical to the reasons listed in the PET subsection. The common SPECT radionuclides include $^{99m}$Tc, $^{125}$I, $^{131}$I, $^{111}$In, $^{59}$Fe and $^{177}$Lu. Tang *et al* speak about the benefits of multimodal MRI/SPECT imaging as it provides both anatomical and molecular imaging modalities.[40] Iron oxide nanoparticles chelated with the radionuclides are the most common examples of this multimodal imaging platform.

### 1.2.5 Computed X-ray Tomography (CT)

This is an imaging modality that uses X-rays to anatomical image the body. CT differs from classical X-ray imaging in one aspect; the X-ray emitter and the detector are not in a fixed position but rotate about the subject to provide a 3D image. CT is limited in its ability to distinguish between soft tissues of similar densities. As such, CT contrast agents are used to improve vascular contrast between these different tissues. CT contrasts agents are mostly made up with iodine containing molecules as iodine is a sufficient absorber of X-rays. However, due to the high atomic number of Au and the ability to introduce Au in the form of AuNPs into the body, it has become an attractive CT contrast agent.[31] Other high atomic weight (high-Z) based nanoparticles have also been used as CT agents such as bismuth nanoparticles. Although X-rays are ionizing radiation, meaning they can possess the energy required to destroy matter (such as DNA), the X-ray energies used for CT are considered to be in a safe range for human contact. Still, the subject is exposed to these rays and absorbs them. Nanoparticles however have a higher interaction cross-section for higher energy X-rays than the soft tissue, and one advantage to using NP contrast agents is the possibility of filtering out the lower energy X-rays (as opposed to exposing the subject to all of the X-rays generated) thereby potentially reducing the effective radiation dose absorbed by the subject.

### 1.2.6 Conventional Linear Optical Imaging

The techniques discussed above, while capable of detecting lesions and abnormalities among healthy tissues and organs, have spatial resolutions that remain on the macroscopic level. Optical imaging techniques based on the single photon absorbance, fluorescence and scattering, are considered unique as they provide microscopic spatial resolution which can reveal finer details on dynamic cell processes such as cell signalling, intracellular transport and cell migration.[41] In this manner, the study of diseases at the cellular level can be achieved. This is advantageous for cancer diagnosis as it allows for earlier detection and monitoring of cancerous cells and tumors. Fluorescence based optical imaging is widely applied for biomedical analysis as it has a high sensitivity and uses relatively inexpensive equipment.[42] These techniques are however limited by the short tissue depth penetration distances of light (illustrated in fig. 1.7), and as such, they have been adapted to *ex-vivo* analysis such as biopsies, and blood tests which can include cell tracking, protein analysis and gene detection among other exams.[24] Having 3-dimensional images of the tumor or cells can provide the doctor with further information for cancer diagnosis. The nature of these single photon optical techniques results in a large excitation volume (i.e there is excitation of the sample beyond the mere focal point of the light source), and as such, it makes optical sectioning for 3-dimensional image construction difficult. Confocal microscopes have been developed to address this problem as it filters the excitation beam to a pinhole, allowing a small volume to reach the sample, and by scanning the sample, 3-dimensional image reconstruction can be done. Other tomographic techniques such as optical coherence tomography (OCT) have also been developed to aid in this image reconstruction but has been mainly applied to the field of ophthalmology.[43] Focus will be given to single photon optical fluorescence imaging for the rest of this section.

To provide image contrast, dye molecules such as indocyanine green (ICG) and methylene blue (MB)[45] have served as organic fluorescent markers, however, these molecules are subject to undesirable effects such as photo-bleaching, quenching and blinking. Simultaneously, the autofluorescence of tissues, impedes the contrast and reduces the signal obtainable from these markers. These are the main challenges that have hindered the application of optical imaging as a full-body diagnostic tool. Recent advances in reducing photon scattering, light absorption and autofluorescence, have made *in-vivo*, human optical imaging a reality. The 2017 review by Hong *et. al* shows the research done specifically on NIR *in-vivo* optical imaging. In the works reviewed, it was demonstrated that by applying technological advances in imaging instrumentation, using the NIR-I (700-900 nm) and NIR-II (1000-1700 nm) biological windows, and fluorophores adapted for *in-vivo* use, are key components to obtaining these images.[45] Clinical use of *in-vivo* optical imaging for real-time image guided surgery[46–48] and imaging of the two legs of a patient[49] have also been reported. While these are noteworthy progressions in this technique, *in-vivo* optical imaging is yet to be widely applied.

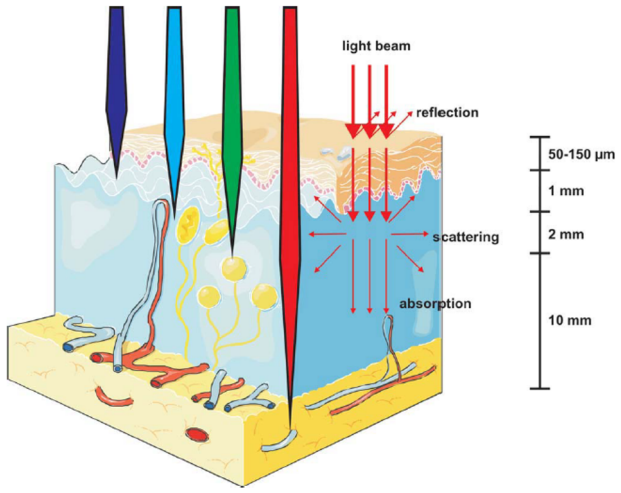


Figure 1.7: The propagation of light through tissues with respect to the wavelength of light: blue light ( 450-495 nm), green light ( 520-560 nm) and red light ( 635-700 nm)[44]

Nanoparticles have aided in overcoming many of these challenges to optical imaging. For example, using a core-shell design, organic fluorescent molecules can be encapsulated in a wide range of materials (eg. $SiO_2$), resulting in higher fluorescent molecule loading and consequently a higher signal from these probes, enhancing the image contrast.[50] This can also protect the fluorescent molecules from rapid photobleaching. Again, the ability of nanoparticles to provide both passive (through the EPR effect) and active (through surface-functionalization of nanoparticles) cancer targeting is used. Quantum dots, due to their inorganic nature, have greater photo-stability than their organic counterparts. They also exhibit higher fluorescence quantum yields (the parameter used to describe how much of the absorbed light is re-emitted as fluorescence), thereby providing a higher fluorescent signal.[51] Fluorescent nanoparticles have been applied in pre-clinical and clinical studies for detecting early stage breast cancer, monitoring therapeutic drug delivery, and cellular uptake of nanoparticles and detecting lymph nodes.

### 1.2.7 Conclusions

The goal of cancer imaging is to provide early detection and accurate diagnosis of cancers, and to be used as effective tools for disease monitoring. The prominent imaging techniques clinically used have been discussed. They all have their strengths and weaknesses and as such are usually used in a complementary manner. Ultimately, the most desirable techniques are those that are minimally invasive, with low side effects, high sensitivity and high accuracy. We have seen how the incorporation of nanoparticles have improved cancer diagnosis because of their EPR effect pro-

viding a passive targeting. In many of these techniques, nanoparticles have also allowed for active cancer targeting, increasing the imaging contrast. In other techniques such as CT, nanoparticles have helped to lower the risks of the harmful effects of ionizing radiation. The materials used for these nanoparticles have ranged from organic (polymers, micelles), to inorganic ($SiO_2$, quantum dots) to metals (noble metals such as Au). Surface functionalizations of these nanoparticles with polymers and biomolecules have helped to improve their bio-compatibility and increase their blood circulation times. While all the techniques discussed have their utility to cancer diagnosis, optical imaging techniques remain very promising as they have the potential for cancer diagnosis at the cellular level, though challenged by the scattering and autofluorescence of tissues.

## 1.3 Non linear optical (NLO) imaging for cancer diagnosis

In the previous section (section 1.2.6), optical imaging techniques based on fluorescence were discussed. These techniques are useful because they can image biological tissues at a cellular level, which can lead to earlier cancer diagnosis. The challenges regarding these techniques however, are the susceptibility of organic fluorescent dyes to photo-bleaching and blinking effects, as well as the short penetration depths of light through the human body, limiting their application to *ex-vivo* analysis. Even though nanoparticles have helped to improve the image contrast and the sensitivity of these fluorescence imaging techniques, there is still the competition from the auto-fluorescence of biological tissues. In light of these challenges, microscopy based on non-linear optical processes have risen to prominence as an alternative. In this section, the principles of non-linear optical (NLO) processes will be presented, as well as the imaging techniques based on NLO processes, with a deeper look at the role of nanoparticles in improving these techniques and their applications to cancer diagnosis.

### 1.3.1 Principles of NLO

Before we can discuss non-linear imaging, let us better understand the physics behind non-linear optical responses of light interacting with a medium. When describing this interaction, there are four main macroscopic properties to be considered: the polarization of the medium ($P$), the electric field ($E$), the electric susceptibility ($\chi$) and the vacuum permittivity ($\epsilon_0$). We can write the equation for a linear response to light as shown in eq. 1.1 where the polarization of the material is directly proportional to the applied electric field.

$$P = \epsilon_0 \chi^{(1)} E \tag{1.1}$$

When there is a non-linear response to the EM wave, we include on the right side of the equation additional tensor terms as seen in eq. 1.2, where the $\chi^{(2,3)}$ terms represent the second and third order non-linear susceptibilities. In fig.1.8 a graphical representation of the change in the polarization response of matter to the electric field, moving from a linear response to a second and third order non-linear response is depicted.

$$P = \epsilon_0(\chi^{(1)}E + \chi^{(2)}E^2 + \chi^{(3)}E^3...) \tag{1.2}$$

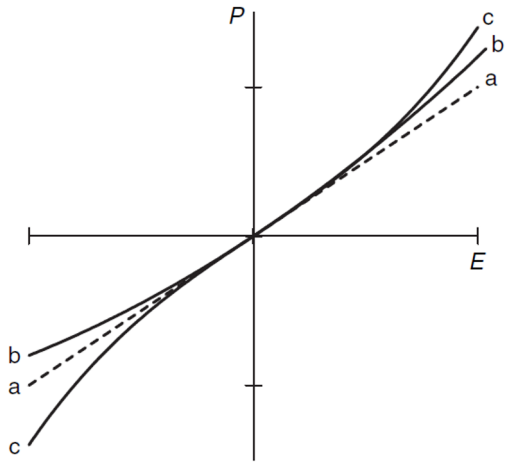


Figure 1.8: Graphical representation of the linear and non-linear responses of the polarization in a medium to the electric field. (a) The linear response is represented by the dotted line , (b) the second order quadratic response is represented by a solid line and (c) the third order cubic response is represented by a solid line.[52]

It is simple to understand the mathematics of a linear and non-linear response, but what is the physics responsible for the deviation from linearity in materials? The first non-linear responses, discovered in the late 1800's, were the Kerr and Pockels effects, that showed changes in the refractive index ($n = \sqrt{1 + \chi^{(1)}}$) of materials, upon application of a strong DC electric field. Then years later, with the birth of the laser providing a source of intense, coherent radiation, more non-linear effects were observed. The understanding is that non-linear responses are a result of strong electric fields interacting with the medium causing perturbations to the inherent electric fields inside the atoms and molecules. Typically, an optical medium with an electric field inferior to $10^4$ V/m imposed on it, will exhibit linear optical responses. At electric fields of magnitude $10^8$ V/m, dielectric breakdown sets in.[53] So, most non-linear effects can be safely observed with electric fields greater than $10^4$ V/m and up to magnitudes of $10^8$ V/m.

In addition to the strong electric field, the symmetry in the spatial arrangement of the optical

medium will also govern the non-linear processes. The electric susceptibilities ($\chi^{(1)}, \chi^{(2)}$ etc) are macroscopic tensors comprised of several elements that consider the spatial symmetry of the optical material. They relate all of the different fields' directions and frequencies to the direction and amplitude of the induced polarization.[54] The tensor elements provide information on the optical medium. For example, $\chi^{(1)}$ is comprised of 2 to 9 elements, whereas $\chi^{(2)}$ is comprised of 3 to 27 elements, therefore being potentially richer in information and $\chi^{(3)}$ comprising of a maximum of 81 elements, even richer in information.

There is a symmetry constraint for observing SHG and all even-numbered non-linear electric susceptibility events. SHG is observed in non-centrosymmetric materials and environments. This can be easily understood by inspection of the relationship between polarization and the second electric susceptibility, both of which are vector quantities. Since the SHG wave is also a vector quantity, its induced polarization in all directions in a centrosymmetric material, which is accounted for by the electric non-linear susceptibility, will be equal but opposite, summing to zero. However in non-centrosymmetric materials or at phase boundaries where centrosymmetry is broken (e.g membrane surfaces), this is not the case. Therefore, as a rule, only non-centrosymmetric materials allow second order ($\chi^{(2)}$) and to go further, even electric susceptibility tensor processes ($\chi^{(n)}, n = 2, 4...$). Non-centrosymmetric materials however, are not a requirement for odd $\chi^{(n)}$ tensors but there are other requirements for such materials that will be discussed further in the text.

There are numerous non-linear effects resulting from the second order and third order susceptibilities. From the second order non-linear susceptibility, we get Second Harmonic Generation (SHG), Parametric Mixing and Amplification (PMA) and Pockels Effect to name a few. From the third order non-linear susceptibility, there are effects such as Third Harmonic Generation (THG), Two Photon Excited Fluorescence (TPEF), Coherent Anti-Stokes Raman Scattering (CARS), Stimulated Raman Scattering (SRS) and more. It is not the goal of this work to detail each of these NLO effects, but focus will be placed on those that have been incorporated into biomedical microscopies, directly applicable to this work: SHG and TPEF.

SHG is a result of the second order non-linear susceptibility, and therefore is exhibited in non-centrosymmetric materials. At the risk of oversimplification, SHG is a two photon process, where two photons of equal energy, simultaneously interact with a medium, and undergo a frequency summation inside the material, to produce a single photon, double in energy/frequency (fig. 1.9,b). Note that the photons do not sum up to a real energy-level of the material, i.e the frequency summation does not require that the new photon be equivalent in energy to any of the energy orbitals of the material. SHG effects can therefore be observed over a range of incident photon energies.

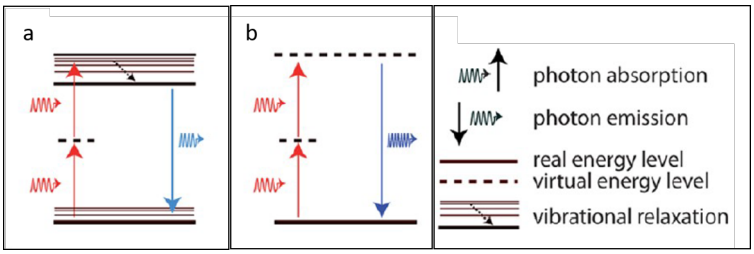


Figure 1.9: Illustration of the absorption and emission processes in (a) two photon excited fluorescence (TPEF) and (b) second harmonic generation (SHG) non-linear processes.[55]

TPEF is a result of the third order non-linear susceptibility. It is also a two photon process, but unlike SHG, the two photons simultaneously absorbed, sum up to a real energy level of the material, allowing for the molecule to transition to an excited state followed by emission in the form of fluorescence (fig. 1.9,a). While in principle there are no symmetry conditions for third-order non-linear susceptibility processes, there are certain classes of molecules that exhibit higher two photon absorption (TPA) and consequently higher TPEF efficiencies than others, namely $\pi$ conjugated donor-acceptor molecules which will be discussed later in this text.

### 1.3.2 NLO Characterization

NLO materials have utility for opto-electronics, lasers and more pertinent to this work, spectroscopies, microscopies and imaging. It is therefore important to be able to characterize the NLO properties and efficiency of the materials. In characterizing the non-linearity of optical media, we move from the macroscopic property, electric susceptibility, to the microscopic equivalent, the optical hyperpolarizability ($\beta$). This is achieved by averaging the response over a volume with a length much smaller than the wavelength of incident light. The first established method for NLO characterization was electric-field induced second harmonic generation (EFISH). This method was generally used on liquids and gases and uses a strong static electric field to direct the orientation of the molecules being examined, disrupting the isotropic arrangement of the molecules and resulting in a strongly coherent frequency conversion, allowing the collection of a strong SHG signal. However this method did not allow for an independent determination of $\beta$. Additionally, there were restrictions to the type of molecules that could be investigated; they required a strong dipole moment and could not be ionic to prevent electrolysis events.

As laser technology advanced to include pulsed lasers, a more direct method for obtaining the $\beta$ of a material became possible. Hyper Rayleigh Scattering (HRS) experiments rose to prominence as they allow for an independent determination of the $\beta$, unlike the EFISH method. HRS is the non-

linear scattering of light by particles that are smaller in size than the incident wavelength probing the particle, confining it to the Rayleigh regime. The general set-up for these HRS experiments is to collect the HRS signal at a 90° angle to the incident beam.

The HRS method can give additional information on the symmetry of the material being studied by varying the light polarization, given by the depolarization coefficient ratio. The depolarization ratio is derived by performing the HRS measurements with vertically and then horizontally polarized light, and the ratio in the HRS intensities gives us the depolarization ratios. From these experiments, it is possible to determine the independent coefficients of the hyperpolarizability tensors.

### 1.3.3 SHG and TPEF imaging

With a stronger understanding of NLO processes from the previous sections, imaging modalities based on SHG and TPEF will now be discussed. Microscopies based on both SHG and TPEF are very attractive for biological applications because they allow for the use of near infrared (NIR) wavelengths of light as opposed to single photon fluorescence microscopy which utilizes UV and visible wavelengths. The obvious advantage to this is that the samples are exposed to lower energy photons, resulting in a reduced photo-degradation. In addition to this, the absorption coefficients and light scattering of biological tissues are lower for these longer NIR wavelengths in comparison to UV-visible wavelengths. The absorption and scattering curves for some biological molecules is shown in fig. 1.10. This means greater depth penetration and a reduced attenuation by scattering and absorption effects from the surrounding tissues.

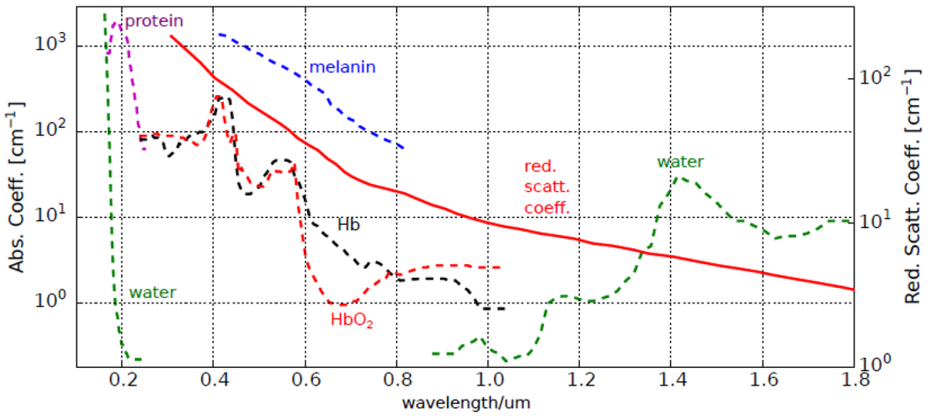


Figure 1.10: The absorption and scattering coefficients of various biomolecules as a function of wavelength.[56]

Another important advantage of these multi-photon microscopies is the limitation of the two photon signal (being SHG or TPEF) to a single pinpoint volume giving us a higher spatial resolution compared to single photon microscopies as illustrated in fig.1.11. This is because the signal is proportional to the square of the excitation intensity.[55] As a result, the event occurs at the focal point where the photon flux is highest, constraining the signal to a region smaller than the diffraction limited spot and allowing for 3D sectioning like that achieved with confocal microscopy, but intrinsically.


Figure 1.11: Image of the laser excitation volume from a (left) single photon excitation and a (right) two photon excitation.[57]

An important feature in all imaging modalities is the signal-to-noise ratio, that is, how well is the technique in distinguishing the signal from the background. In single photon fluorescence experiments, the wavelengths of excitation and the wavelengths of emission are spectrally close to each other, and to prevent the excitation light from also being detected, the bandpass filters often cut out a part of the emission. However, in the multi-photon microscopies, there is greater discrimination between the excitation and emission wavelengths. Additionally, because of the greater excitation volume in single photon microscopy, the autofluorescence signal of the tissues will be detected, reducing the image contrast as both the area of the specimen being observed and the surrounding tissue can produce an almost identical signal. The pinpoint excitation volume and consequently pinpoint signal from multi-photon microscopies eliminates this problem.

For these reasons stated, multi-photon microscopies are advantageous for bio-medical imaging. This would not be a balanced discussion without recognizing the potential drawbacks to multi-photon microscopies. In table 1.2 a comparision between single photon and multi-photon microscopy is presented. As NLO effects are observed when we have strong electric fields, and in the case of TPEF and SHG, two photon events occurring simultaneously, it requires the use of ultrafast lasers with pulse durations lower than 100 fs which is traditionally a more expensive set-up with higher maintenance cost than single photon fluorescence microscopy set ups, including confocal microscopy.

Advances in laser technology has seen a reduction in these laser costs over the last decade. Another challenge is the variety of NLO active materials suitable as bio-imaging probes. This will be discussed further in the next section.

| Single Photon Microscopy | Multi-Photon Microscopies | |
|---|---|---|
| Fluorescence | TPEF | SHG |
| Single photon equivalent to a real energy transition | Two photons summing to the equivalent of a real energy transition | Two photons summing to a virtual energy level, no energy restrictions |
| No symmetry restrictions of fluorescence probe | No symmetry restrictions of fluorescence probe | Non-centrosymmetric probe required |
| Volume of sample excited= volume of the beam | Femtoliter spot sized focal point | Femtoliter spot sized focal point |
| No inherent 3D imaging | Inherent 3D imaging | Inherent 3D imaging |
| Sample and probe photodegradation | Reduced sample and probe photogredation | Reduced sample photodegradation, no probe photodegradation |
| Lower S/N ratio due to large excitation volume, and close excitation and emission wavelengths | Higher S/N ratio | Higher S/N ratio |
| Simple experimental set-up with CW laser | Expensive experimental set-up with pulsed laser | Expensive experimental set-up with pulsed laser |
| Large emission band | Large emission band | Single peak, specificity |

Table 1.2: Table showing the main properties of single photon fluorescence based microscopy imaging and multi-photon TPEF and SHG microscopy imaging techniques.

### 1.3.4 Probes for SHG and TPEF microscopies

Microscopy based on multi-photon processes can be used directly for cellular imaging as there are endogenous non linear active biological structures such as collagen[58] and NADH, however not all tissues and organs will have high enough levels of these structures and molecules present, and so, relying on the naturally ocurring NLO properties of the body will not be sufficient, particularly when used for specific disease discovery such as cancer. Consequently, exogenous organic and inorganic probes have been developed specifically for these biological multi-photon microscopies. The SHG and TPEF efficiencies, biocompatibilities and cytotoxicities are necessary parameters to be known for incorporating these probes into regular clinical use. In this section, some of the organic and inorganic exogenous probes applied to these microscopies will be reviewed.

#### 1.3.4.1 NLO Organic probes

There has been extensive research on two photon absorption materials that exhibit high TPEF efficiencies.[59–61] Organic, $\pi$ conjugated molecules that have intramolecular charge transfer capabilities

have exhibited a strong correlation to two-photon absorption (and consequently TPEF) efficiency. That is to say, molecules consisting of a strong $\pi$-electron donor, a polarizable $\pi$-bridge and a $\pi$-electron acceptor tend to demonstrate high TPEF efficiencies. Some examples of common TPEF molecules used are shown in fig. 1.12.

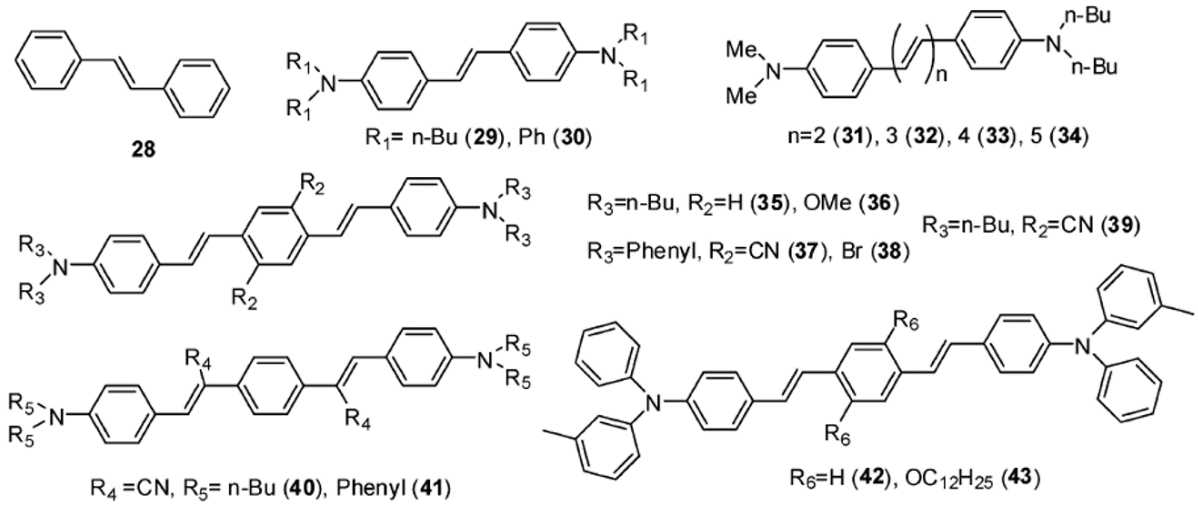


Figure 1.12: Examples of TPEF active organic molecules.[60]

In the work of Campagnola *et. al*,[62] they tested several naphthylstyryl (ANEP) dyes for their SHG bio-imaging efficiency. In addition to these organic molecules, organic liquid crystals like alkyl-cyanobiphenyls and Schiff bases, dendrimers (organometallic and all organic), fullerenes, metal-ligand organometallics and porphyrines are among the classes of organic materials that have also demonstrated multiphoton functionality.

#### 1.3.4.2 NLO Inorganic probes

A special class of inorganic probes termed harmonic nanoparticles (HNPs) have been developed specifically to address the flaws with traditional fluorescent probes. These nanoparticles are used for their SHG properties. They are non-centrosymmetric, non-fluorescent, crystal materials. As opposed to fluorescent probes, HNPs are photostable (no blinking or photobleaching). An additional advantage of HNPs is the additional information that can be extracted from their signal based on the polarization of the incident light and the orientation of the HNP.[55] The inorganic crystals proposed as SHG bio-imaging probes to date are $KNbO_3$,[63] $LiNbO_3$,[64] $BaTiO_3$,[65–67] KTP[68,69] and ZnO[70,71] based on their non-centrosymmetry and SHG efficiencies, given by their hyperpolarisability values. It must be noted however, that SHG signal is volume scaled, and as such, unlike their

fluorescent probe counterparts, the ultimate size of the HNP will impact its signal. In the table 1.3, the normalized hyperpolarizability values of these HNPs, determined by HRS experiments performed by Staedler *et. al*,[72] and their corresponding mean dynamic light scattering determined size (by number) is given. As is evident, by the values, they are all within the same range, and as such there is no advantage in terms of SHG signal in choosing one material over another.

| | Inorganic Harmonic Nanoparticles | | | | |
|---|---|---|---|---|---|
| | $KNbO_3$ | $LiNbO_3$ | $BaTiO_3$ | KTP | ZnO |
| Normalized $\beta$ (pm/V) | 3.4±1.1 | 4.8±1.6 | 4.6±0.7 | 1.4±0.3 | 1.9±0.6 |
| Size (nm)* | 123 | 113 | 119 | 119 | 133 |

Table 1.3: Table showing the normalized hyperpolarizability values for harmonic nanoparticles (HNPs) and the hydrodynamic size determined by dynamic light scattering (DLS).[72] *DLS size values reported by number.

### 1.3.5 Applications to cancer diagnosis

While the efficiency of generating a SHG signal is an important factor in choosing a material as a bio-imaging probe, an equally important factor is its biocompatibility. The published work of Staedler *et. al*[72] provides data on parameters such as HNPs stability, cytotoxicity and hemolytic analysis (analysis of its ability to break-down blood cells). To analyze the stability of the nanoparticles, they followed the same protocol of dispersing the nanoparticles in deionized water, adjusting the pH so as to have high absolute zeta potential values based on the relationship they determined, between pH and zeta potential as shown in fig. 1.13. The link between zeta potential and nanoparticle stability is explained in more details in section 2.1.5 of this manuscript, but in summary, an absolute zeta potential of 30mV and higher is considered to be a stable dispersion. All the nanoparticle dispersions were maintained at pH 7 except for $BaTiO_3$ which was maintained at pH 3. Being stable dispersions in the range of physiological pH is desirable for their biological applications. In leaving the dispersions to sediment over a period of 7 days, they observed that $LiNbO_3$ and $KNbO_3$ exhibited greater nanoparticle stability than the other HNPs. They attributed this to a higher polydispersity along with the formation of aggregates in the other HNPs. This argument was corroborated upon examining the images obtained from transmission electron microscopy (TEM).

Polyethylene glycol (PEG) is routinely used to coat particles to improve the biocompatibility, giving particles a "stealth" feature which can promote longer blood circulation times, and improve the efficiency of nanoparticle delivery to target cells and tissues.[73] Staedler *et. al*[72] were able to coat the NPs with PEG and observed that for all the HNPs studied, it improved their stability. The cytotox-

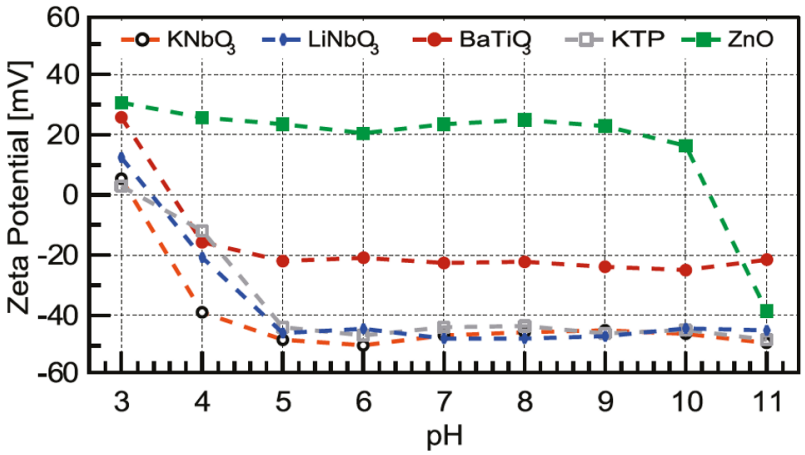


Figure 1.13: Zeta potential values for $KNbO_3$, $LiNbO_3$, $BaTiO_3$, KTP and ZnO nanoparticles dispersed in deionized water and varying pH.[72]

icity of these NPs were determined by measuring cell viability after an incubation period with the NPs. This was achieved by performing MTT (3-(4,5-dimethyl-2-thiazoyl)-2,5-diphenyltetrazolium bromide) tests. They demonstrated that the MTT tests were an appropriate method of analysis for HNPs cytotxicity, as they saw no interference from either the bare or PEG coated nanoparticles.

They observed the cell viability of three human lung cancer cell lines, A549, HTB-178 and HTB-182 as well as a non-cancer cell line BEAS-2B. The results they obtained when a concentration of 50 µg/mL of HNPs was used, showed that $BaTiO_3$ was the least cytotoxic, with $LiNbO_3$ and $KNbO_3$ exhibiting a very weak cytotoxicity. Indeed after 24 hours of incubation, a sufficiently high percentage of cells survived across each cell line for these 3 HNPs. KTP had a high cytotoxicity and ZnO caused a high percentage of cell death after as little as 5 hours incubation time. Therefore, $BaTiO_3$, $LiNbO_3$ and $KNbO_3$ were considered most viable for further biological analysis. The results of the hemolytic analysis concluded that these HNPs hemolyzed blood within a range of 4-7%, which is comparable to that of mesoporous silica nanoparticles (MSN), but the PEGylated HNPs exhibited a higher hemolytic function that PEGylated MSN. The takeaway from this point was that it may be possible to decrease the hemolytic ability of these nanoparticles if an appropriate polymer coating is given. In their article they also demonstrated the SHG cell imaging ability of the HNPs.

Silicon carbide (SiC) is another NLO active material that has been proposed for biological applications.[74–76] In the work of Boksebeld *et. al*,[77] they demonstrated the ability of SiC nanoparticles, 150 nm in diameter, with a PEG-folate coating, for SHG imaging of a cancer cell line (HuH7) and a healthy cell line (3T3-L1). The normalized hyperpolarizability values for these nanoparticles were not reported, however, by comparing the second order non-linear optical coefficients found in the

literature, SiC has a higher SHG efficiency than $LiNbO_3$. Though this means a higher SHG signal is obtainable, the processes of functionalizing SiC performed in this work, involved a lengthy silanization process with APTES. Additionally, the NP sizes were larger than what has been recommended as ideal sizes in literature. Nevertheless, the cell labeling ability of these PEG-folate functionalized SiC NPs was demonstrated, exhibiting a preferential labelling of the cancer cells as opposed to the healthy cells. This is in accordance with the literature concerning folate as an appropriate molecule for targeting cancer cells. The SiC NPs also exhibited low cytotoxicity.

To the best of my knowledge, the published research on HNPs for bio-imaging applications, specifically centered on cancer applications is not vast, but there are core groups around the world working in this area apart from the already discussed works. In 2008, a research group at the University of Buffalo, USA showed that biocompatible ZnO nanocrystals could be used as NLO probes for bio-imaging.[70] In 2010, the research group of Rachel Grange in Switzerland published their results on conjugating IgG antibody to the surface of $BaTiO_3$ NPs, and using the NPs as efficient biomarkers for SHG imaging.[78] There have been further studies by research groups in China showing the use of HNPs such as ZnO[79] and $BaTiO_3$,[80] not only for imaging, but for activating molecules that use absorbed light to perform reactions that produce reactive oxygen species that then can attack the cell and cell environment, and is a form of cancer therapy called Photodynamic Therapy which will be discussed in section 1.4.3. Most recently, in the work of Vasyl Kilin *et. al*,[81] HNPs (bismuth ferrite), were incorporated into an all optical set-up, and shown to be capable of cell imaging and therapy by heat generation upon laser irradiation.

### 1.3.6 Conclusion

Multi-photon microscopies based on non-linear processes were discussed as an improved alternative to single photon microscopies. Though they require more expensive instrumentation, they have higher spatial resolution and improved optical sectioning ability, facilitating easily 3-dimensional image reconstruction, and a greater discrimination between the excitation wavelengths and the emission wavelengths. Additionally, NIR wavelengths can be used, which allows for greater tissue penetration, as well as a lower risk of photodegradation due to the lower energy photons. The literature pertaining to organic and inorganic nanoparticles proposed as suitable NLO bio-imaging tools was discussed, and we were introduced to the special class of inorganic nanoparticles called harmonic nanoparticles. These nanoparticles were studied for the SHG properties and noteworthy biological results were discussed. SiC, $KNbO_3$, $LiNbO_3$ and $BaTiO_3$ were the most promising materials for SHG microscopy.

### General conclusion on nanoparticles for cancer imaging

After this systematic review of the existing medical imaging techniques used for cancer diagnosis, it is evident that there is no one imaging modality suited for every type analysis. Ultimately, the choice of imaging used will depend in part on what is the suspected nature of, and where the suspected cancer is located in the body. However, incorporating nanoparticles into these imaging techniques have increased the sensitivity, whether by designing the nanoparticles to actively target specific cell receptors, or by the passive EPR effect, or by the inherent composition of the nanoparticle to enhance the technique.

With early detection being a main goal in cancer diagnostics, though they are not adapted to in-patient examination, optical imaging techniques are advantageous as the resolutions attainable, allow for a greater occurrence to detect cellular abnormalities before large tumor growth. More specifically, NLO imaging techniques like SHG, allows for tuneability to longer wavelengths, and therefore greater depth penetration as well as reduced risk of photodamage. With the development of harmonic nanoparticles and an evaluation of their cytotoxicity, they can be considered as highly efficient exogenous imaging probes, that should be considered for future clinical applications.

## 1.4 Nanoparticles for cancer therapy

Traditionally, cancer therapy has been a three-pronged approach: surgery, chemotherapy and radiation therapy. Though they are still the most widely applied, tumor resection by surgery is invasive with long recovery times, chemotherapy drugs attack both the cancer cells and healthy cells, weakening the immune system and also causing a wide range of side effects, and radiation therapy exposes the patient to ionizing radiation which can lead to radiation burns and other long-term negative effects. With the objective of minimizing, and where possible, eliminating the adverse effects of cancer therapy, attention has been devoted to nanotechnology based solutions. The field of nanomedicine has allowed for the development of more precise, targeted therapeutic options, as well as improving the aforementioned techniques.[3,4] Some of the treatment options more routinely available thanks to nanotechnology are image-guided surgery, targeted drug delivery, radiation sensitization, immunotherapy, hormone therapy, photodynamic therapy and photothermal therapy. In this section, we will look at how nanotechnologies, and more specifically, nanoparticles, have been incorporated into these techniques. The table 1.4 provides a summary of the types of nanoparticles studied for cancer therapy found throughout the literature.

| Treatment Technique | Nanoparticle | Reference |
|---|---|---|
| Radiation Sensitization | AuNPs | Chithrani, 2010[82] |
| Drug Delivery | Liposomes | Murthy, 2007[83] |
| | Polymeric micelles | |
| Immunotherapy | Graphene oxide | Wang, 2019[84] |
| | Upconversion NPs | |
| Hormone Therapy | AuNPs | |
| PDT | SWCNTs | |
| | Quantum dots | Hong, 2016[85] |
| | Graphene oxide | Kim, 2016[86] |
| | AuNCs | ACS Nano, 2014[87] |
| Photothermal Therapy | AuNRs | Small, 2017[88] |
| | AuNSs | Loo, 2004[14] |
| | SWCNTs | |
| | Graphene oxide | Wang, 2013[89] |

Table 1.4: A list of nanoparticles used for cancer therapy. AuNPs= gold nanoparticles, SWCNTs=single walled carbon nanotubes, AuNCs= gold nanocages, AuNRs=gold nanorods .

### 1.4.1 Radiation Sensitization

Radiotherapy uses ionizing radiation to destroy the cancer cells. The challenge with radiotherapy is that it is as dangerous for the healthy cells as well as the cancer cells. Exposure to ionizing radiation destroys the cells by generating breaks in DNA, and while this is desirable in the cancerous cells, in healthy cells this can possibly lead to the generation of further genetic abnormalities that can become cancerous. Nevertheless, it is a powerful and effective tool in cancer therapy. Strategies to reduce the harm to the healthy cells, and to limit the exposure to ionizing radiation are being researched. One outcome of this research has been the use of nanomaterials as radiation sensitization tools. Gold nanoparticles have been the most widely studied for this application due to their high Z-value as well as their known biocompatibility, and the NPs investigated range in size from 2 nm in diameter to 50 nm in diameter.[82] The effectiveness of this technique is dependent on the concentration (number) of AuNPs taken up in the cell. The EPR effect lends to this increased preferential uptake, but also it has been shown to be dependent on the size of the NP.

### 1.4.2 Drug Delivery, Immunotherapy & Hormone Therapy

Using nanoparticles as carrier vectors for drug delivery, immunotherapy and hormone therapy allows for greater discrimination between healthy cells and cancer cells, for a more targeted therapy. This is due to the many advantages of nanoparticles already discussed in this work (the increased specific surface area, the EPR effect, the surface modifications for improved biocompatibility and biodistribution, the ability to embedded high concentration of molecules into the particles etc). Attaching to the surface of NPs, biomolecules such as anti-bodies, has been useful in developing

hormone therapy of cancers. Many cancer cells have an over-expression of hormones. A prominent example is the family of Epidermal growth factor (EGF) hormones, that are proteins that when bound to their receptor, signal instructions for cell growth and differentiation. The strategy is to therefore target the EGF receptors. In a similar fashion to drug delivery, nanoparticle platforms are used to deliver adjuvant molecules, i.e molecules that increases immunogenicity, which is sometimes lacking in tumor antigens.

### 1.4.3 Photodynamic Therapy

Photodynamic therapy (PDT) for cancer, is a minimally invasive technique that uses the activation of photo-sensitizing agents (PSA) by visible light in the presence of molecular oxygen, to initiate a chemical reaction generating reactive oxygen species (ROS), reactive nitrogen species (RNS) and other cytotoxic species in its local environment. These cytotoxic species then attack the cancer cells resulting in cell damage and ultimately cell death by apoptotic or necrotic pathways.[90–92] Though we have historical proof of phototherapy as far back as the ancient Egyptian civilizations,[93] modern phototherapy, specifically PDT as a cancer treatment, gained prominence in the early 1900's when it was observed by first Policard in 1924 and then Kordler, the preferential uptake of porphyrin molecules in the tumor upon UV light irradiation, by using the fluorescence signal of the molecules.[94] This was further corroborated by the experiments of Auler and Banzer in 1942, where they injected hematoporphyrin into tumor-bearing rats, and found the preferential accumulation in the metastic tumors and lymph nodes. In actuality, the true cancer fighting strength of PDT is due to three inter-related mechanisms: the direct cytotoxicity to the cancer cells, the damage inflicted on the tumor vasculature and lastly the inflammatory response which evokes a systemic immune system response to the cancer site.[44]

The effectiveness of PDT is determined by the quantity and location of the phototoxic species generated. According to the American Cancer Society, PDT is a less expensive treatment, with precise, localized targeting and no long-term side effects.[95] However, as visible light cannot penetrate deep into the body (it is completely attenuated within short distances due to the high extinction coefficients of biomolecules such as haemoglobin, melanin and protein as shown in fig. 1.10, section 1.3.3), PDT has been mostly limited to treating skin cancers. Unfortunately, one of the advantages of PDT, the localized precision, is also a disadvantage as it is not an efficient treatment for metastic cancers, which are the most frequent cause of death for cancer patients. In addition to this, the photosensitizing effect leaves the subject vulnerable to sunlight for some time. PDT is more commonly applied as a complementary therapy along with the three traditional treatments. The classical PSAs used are based on a tetrapyrrole structure very similar to the porphyrin structure.

Nanoparticles have been incorporated in PDT as they can serve as PSA carriers, or as the PSA themselves or as energy transducers to catalyse the reactions to form the cytotoxic species. Noble metal nanoparticles like AuNPs, AuNRs and AuNCs have found utility in PDT therapy as their high absorption cross-section at their plasmon wavelengths allows for energy transfer reactions to occur to form the ROS species.[96–98] The plasmon extinction wavelengths of these noble metal NPs can also be tuned to the NIR region. In this way, tumors located deeper than skin level can be treated, while also allowing for plasmonic photothermal therapy (discussed in greater detail in a later section, 1.5). In addition to these metal nanoparticles, single-walled carbon nanotubes (SWNTs), graphene oxide (GO) and upconversion nanoparticles (UCNPs) have all proven to have function for PDT.[86]

### 1.4.4 Photothermal Therapy (PTT)

The idea to apply thermal remedies for disease treatment can be traced back thousands of years. In fact, there is a famous quote by Hippocrates which translates to "those who cannot be cured by medicine, can be cured by surgery. Those who surgery cannot cure, can be cured by heat. Those who cannot be cured by heat are truly incurable".[99] In the 1927 dissertation of Nils Westermark, he suggested based on his experimental work on tumors in rats that tumor cells were more sensitive to heat than healthy cells.[100] Advances in thermal cancer therapy was placed on hold with the advent of ionizing radiation, however there has been a return to thermal therapy as it has been definitively proven that healthy cells can withstand temperatures up to 45°C whereas cancer cells cannot, therefore allowing a more selective cancer therapy as opposed to ionizing radiation which is harmful to both cancer cells and healthy cells (fig. 1.14).

Photothermal therapy (PTT) employs photothermal conversion agents (PTAs) to absorb light, and through their relaxation processes, deposit thermal energy to its local environment. Ideal PTAs should have a larger absorption cross section in any of the two biological windows mentioned in section 1.3.3, depicted in fig. 1.10. They should also have a high photothermal conversion efficiency (percentage of absorbed light converted to heat), good photothermal stability, be non-toxic and allow for easy surface modifications.[102] The NIR light source for PTAs activation can be with a pulsed laser as seen in the works of Zharov *et al.*[103–105] or a continuous wave (CW) laser as seen in works of Elsayed and other research groups.[106–110] The examples of PTAs found in the literature can be classified as noble metal based nanoparticles, semiconductor nanocrystals, carbon based nanoparticles and organic semiconducting polymeric nanoparticles. In table 1.5, a list of PTAs, along with their photothermal conversion efficiency values is provided.

The carbon based PTAs have demonstrated excellent light-to-heat conversion efficiency. As a result

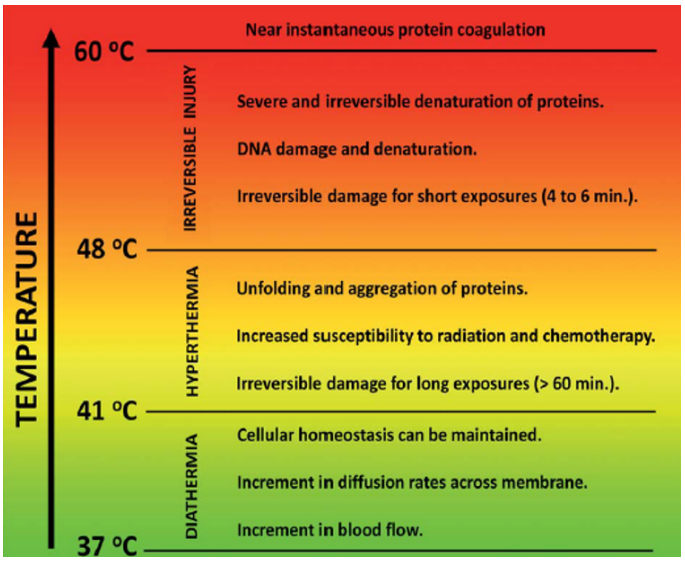


Figure 1.14: Stages of cell destruction by thermal effects in cancer tumors.[101]

| **Photothermal Agent** | **Laser $\lambda$ (nm)** | **Photothermal Conversion Efficiency** | **Reference** |
|---|---|---|---|
| Noble metal NPs | | | |
| AuNRs | 808 | | Qiu, 2017[88] |
| Au-nanostars | 980 | 78.8% | Bi, 2018[111] |
| AuNCs | | | |
| Pt NPs | 809, 980 | | Zhu, 2016[112] |
| SCNPs | | | |
| Cu–Ag2S/PVP | 808 | 58.2% | Dong, 2018[113] |
| CuS | | | |
| Carbon-based NPs | | | |
| Graphene oxide | 808 | N/A | Wang, 2013[89] |
| CNTs | | | |
| SCPNPs | 635 | 62.3% | Zhang, 2017[114] |

Table 1.5: Photothermal nanoparticle agents and their reported light-to-heat conversion efficiency. SCNPs= semi-conducting nanoparticles, CNTs= carbon nanotubes, SCPNPs= semi conducting polymer nanoparticles

of the various geometric configurations that can be seen (mainly in the carbon nanotubes (CNTs), single-walled carbon nanotubes (SWCNTs) or multi-walled carbon nanotubes (MWCNTs)), they can exhibit different optical, electrical and mechanical properties. Their light-to-heat conversion pathways is in competition with their luminescence de-excitation pathways. This luminescence (fluorescence) de-excitation can be quenched by the interaction between carbon layers, and as a consequence, especially in MWCNTs, it can be assumed that all the absorbed energy is transferred into heat.[101] The absorption efficiencies of these carbon based PTAs however have been shown to be solvent dependent, exhibiting 100% efficiencies in toluene, but then dropping by 50% in other

solvents such as water.

The noble metal PTAs, particularly the Au based nanostructures are very attractive as Au has been extensively studied for its biocompatibility. Additionally, they have excitation wavelength tunability depending on their shape and morphology. The Au nanostructures that are interesting for PTT are the AuNRs, AuNSs and Au-nanostars. Of these, the AuNS is particularly interesting as it is inherently a hybrid nanoparticle and can be combined with other materials to provide multifunctional applications (for example a gold shell encapsulating a material used for imaging). These noble metal PTAs have a special mechanism controlling their light-to-heat conversion. This is discussed in greater detail in the following section, 1.5.

## 1.5 Plasmonic photothermal therapy (PPTT)

Plasmonic photothermal therapy (PPTT), a subsect of PTT, refers to the photothermal nanoagents, that owe their high absorption cross-section to the presence of a localized surface plasmon resonance. Then, through their relaxation process, they release to their local environment a large deposit of thermal energy. Studies on PPTT look at the effectiveness of these plasmonic nanomaterials based on their size, shape, concentration and composition. Before we review the pertinent literature pertaining to PPTT, let us firstly have an understanding of the principle and theory of plasmons and nanoplasmonics.

### 1.5.1 Principles of nanoplasmonics

Noble metal nanoparticles such as Cu, Ag and Au in particular have unique optical responses to light when compared to their bulk components, called a localized surface plasmon resonance (LSPR). To understand fully the LSPR observed in noble metal nanoparticles, we will first have a cursory review of electromagnetic (EM) wave propagation and surface plasmons in bulk metals.

Considering the free electron gas model of metals, we can imagine that there is a natural electron density flux present throughout the metal. At the metal's surface boundary (between itself and air or another dielectric medium), this natural flux takes the form of waves which can be classically derived from Maxwell's equations of electromagnetism:

$$\nabla \cdot D = \rho_{ext} \tag{1.3}$$

$$\nabla \cdot B = 0 \tag{1.4}$$

$$\nabla \times E = \frac{\partial B}{\partial t} \tag{1.5}$$

$$\nabla \times H = J_{ext} + \frac{\partial D}{\partial t} \tag{1.6}$$

where $D$ is the dielectric displacement, $B$ is the magnetic flux density, $E$ is the electric field, $H$ is the magnetic field and $\rho_{ext}$ and $J_{ext}$ are the external charge and current densities.

It is not in the scope of this thesis to show the derivations of all the equations pertaining to the interaction of light at a metal-dielectric surface, however, some key equations derived will be discussed. Firstly, the equations for the wave vectors formed from an incoming EM wave at the interface of two surfaces, surface 1 and surface 2 (shown in eq. 1.7) are of importance as they reveal how the dielectric constants of the two materials impact the wave propagation.

$$k_x = \frac{\omega}{c}\sqrt{\frac{\epsilon_1\epsilon_2}{\epsilon_1+\epsilon_2}} \quad and \quad k_{yi} = \frac{\omega}{c}\sqrt{\frac{\epsilon_i}{\epsilon_1+\epsilon_2}} \tag{1.7}$$

where $\omega$ is the angular frequency of the EM wave, $c$ is the speed of light, $\epsilon_1$ & $\epsilon_2$ are the dielectric constants of the two materials and $i$ equals 1 or 2.

Now consider surface 2 to be a metal, where there is an infinite number of electrons. There is a natural frequency for the movement of these electrons called the plasma frequency, $\omega_p$ which is determined by eq. 1.8.

$$\omega_p = \sqrt{4\pi n_e e^2/m_e} \tag{1.8}$$

where $n_e$ is the free electron density, and $e$ and $m_e$ are the charge and mass of the electron respectively.

As a result of this plasma frequency, when $\omega < \omega_p$, the dielectric constant of the metal ($\epsilon_2$) given by eq.1.9, is negative, meaning that these frequencies of EM waves cannot propagate through the metal.

$$\epsilon_2(\omega) = 1 - \frac{\omega_p^2}{\omega^2} \tag{1.9}$$

Of greater interest to our purposes, if $\epsilon_2 > -\epsilon_1$ , the $k_{yi}$ interface becomes imaginary whereas the $k_x$ interface remains real (eq. 1.7), resulting in a EM wave propagating along that $x$ interface, called

the surface plasmon, depicted in fig. 1.15.[115]

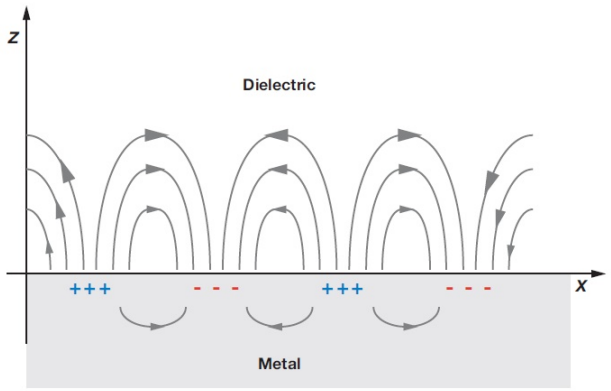


Figure 1.15: Illustration of the surface plasmon waves propagating along the x interface of a metal and a dielectric surface.[116]

As we reduce the size of the metal to that of nanoparticles, the length of the incident EM wave becomes considerably larger than the particle itself. The electric field of the EM wave polarizes the particles, pushing the conduction band electrons towards one side of the particle (depicted in figure 1.15). These electrons continue to oscillate at their natural plasma frequency, bound by the particle's surface. When the frequency of the incident EM wave matches this oscillation, it causes optical excitation or amplification of the frequency. This is observable by the absorption of the incident EM wave, and this specific frequency/wavelength is called the localized surface plasmon resonance (LSPR) wavelength which is dependent on the particle's size and geometry along with its inherent composition.

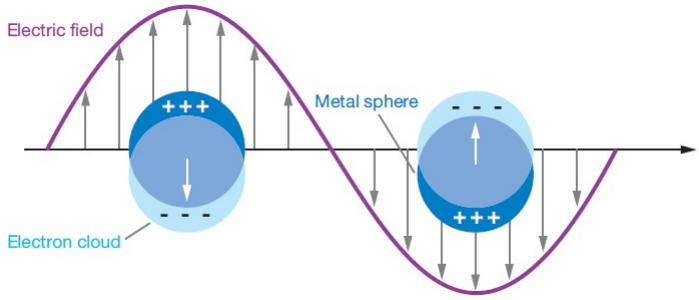


Figure 1.16: Illustration of the amplification of the oscillation of the electrons on the surface of a nanoparticle when interacting with incident light of resonance frequency.[116]

Now that we have detailed the dielectric function of metals and how the dielectric functions at the metal-dielectric interface affect the surface plasmon, it is necessary to mention more specifically

the noble metals. For the noble metals such as Au and Ag, their inter-band transitions occur at relatively low energies (within the IR, visible and UV region) which effectively impacts the real and imaginary parts of the dielectric functions, causing them to deviate from the *Drude* model as seen in fig. 1.17. The impact this has on the LSPR is a dampening effect if the energy of the LSPR EM wave and the interband transition energies coincide.

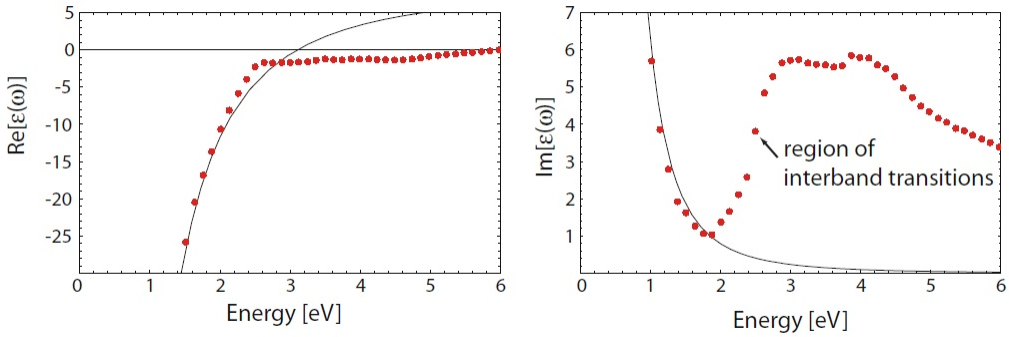


Figure 1.17: Graphical representation of the real and imaginary parts of the dielectric function of Au. The dots correspond to data from the literature of the dielectric function and the solid line corresponds to the dielectric function of the free electron gas Drude model.[117]

### 1.5.2 Mechanism of light-to-heat conversion

The last thing for us to understand is how these plasmonic nanostructures are able to convert the absorbed light to heat. When radiative energy is absorbed by any material, it is in an unstable, excited state. As such, the de-excitation can follow radiative and non-radiative decay pathways. In plasmonic structures, when the light absorbed is at the maximum of its plasmon resonance, the non-radiative decay pathways, which result in the conversion and transfer of heat to the environment of the plasmonic nanostructure, are quite rapid (fig. 1.18). With more details, after the light absorption, there is a rapid non equilibrium heating, followed by non-radiative relaxation by electron-electron collisions, which increases the temperature at the surface of the material. It then returns to equilibrium temperature via energy exchanges between electron-phonon and phonon-phonon interactions, which dissipates the thermal energy in its local environment. It must be noted that radiative decay processes can also occur simultaneously and as such, the photothermal efficiency values will depend also on the luminescence quantum yield of the material. The discussion has been focused on the light absorbed by these plasmonic nanostructures but we must not neglect that they can also be efficient light scatterers. Their absorbance cross-section ($\sigma_{abs}$) and scattering cross-section ($\sigma_{scat}$) combine to give us their extinction spectra ($\sigma_{ext}$). The relative efficiency of either process in plasmonic nanostructures is dependent on morphology.[118] An interesting and use-

ful physical response that can occur during this light-to-heat conversion process is the formation of microbubbles. The work of Baffou *et. al*[119] revealed that irradiating plasmonic gold nanostructures with a continuous wave laser (CW) produced microbubbles that consisted of air with lifetimes up to several minutes. The formation and then dissolution of these microbubbles have been flagged as a means for cell destruction as they can impose a mechanical force on the cell membranes, causing rupture.[120]

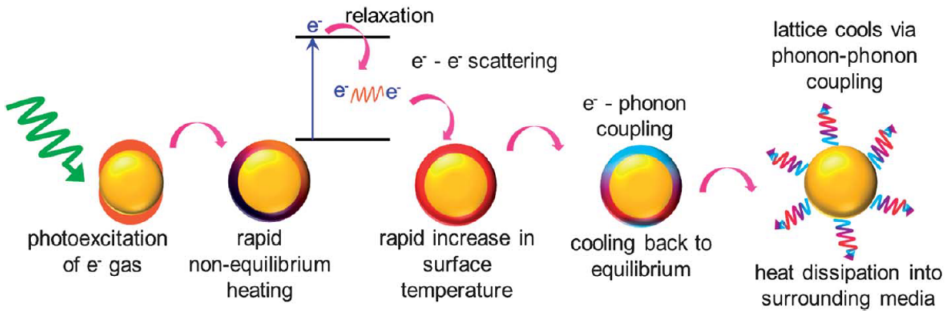


Figure 1.18: Figure describing the principle of photothermal conversion process in plasmonic nanostructures.[1]

### 1.5.3 PPTT nanoparticles for cancer therapy

Photothermal, and more specifically, PPTT cancer therapy has had recent noteworthy human clinical trial success. The AuNSs, which were developed by the Halas group and were the first hybrid nanoparticles used to demonstrate photothermal therapy of cancer, have passed to phase two of a clinically trial for prostate cancer therapy.[121] The AuNSs are delivered intravenously and rely on the EPR effect to accumulate at the site of the prostate tumor. The various methods of synthesis of AuNSs will be discussed further in section 1.7.2. Photothermal therapy will remain an important research area in cancer therapy as it utilizes non-ionizing radiation, can deposit the heat in the local tumor environment, and can be achieved with materials with a proven biocompatibility and easy surface modification like gold. Gold as PTAs is desirable as its light-heat conversion efficiency can be tailored by changing its size and shape, and structures like the aforementioned AuNS, does not only allow for PTT, but can also be used to encapsulate other materials to deliver a complementary therapeutic function or even an imaging modality.

## 1.6 General conclusion on nanoparticles for cancer therapy

Nanoparticle-mediated cancer therapy has been included in all the main therapeutic techniques. They have been used as sensitizers for radiotherapies, as platforms for drug and hormone delivery as well as performing the roles as agents for photodynamic and photothermal therapy. They have, in most cases, improved the targeting efficiency of these therapies as they can be modified on their surface to target specific cell-receptors. Nanoparticle assisted photothermal therapies are particularly attractive as they can convert light wavelengths that are themselves, not dangerous to the body, into heat which can locally increase the temperature of its environment. It is however limited by the penetration depth of the light sources. Though the effective use of nanoparticles as cancer therapy agents requires detailed studies on the bio-compatibility, toxicity and clearance of nanoparticles, they are more and more passing clinical trials and becoming incorporated into the treatment options offered worldwide.

## 1.7 Nanohybrids with gold shell for cancer theranostics

Theranostics, the combination of diagnostics and therapeutic modalities in a single platform using nanotechnology, is a growing area of research. Theranostic nanoparticles not only allow one to condense the number of steps between diagnosis and therapy, but has the potential to provide real-time multi-modal monitoring of disease treatment. Theranostics nanoparticles are most often hybrid nanoparticles or nanohybrids. They combine at minimum two materials that keep their individual functionality when coupled together (although we have in the literature examples of AuNPs used for both optical imaging via light scattering as well as PPTT,[13] and iron oxide NPs used for magnetic hyperthermia and MRI contrast agent[122]).

| **Nanoparticle** | **Therapeutic function** | **Diagnostic function** | **Reference** |
|---|---|---|---|
| Liposome loaded drug | drug therapy | pH sensitive polymer | Devalapally, 2007[123] |
| Iron Oxide conjugated NPs | MRI | hormone therapy | Hadjipanayis, 2010[124] |
| AuNRs | PTT | CT | Maltzahn, 2009[125] |
| Silica-gold | optical imaging | PTT | Singh, 2018[126] |

Table 1.6: A list of some theranostic nanoparticles with their therapeutic function and diagnostic function.

The design of theranostic nanoparticles can be placed into two categories: i) encapsulation (imaging agent inside therapeutic agent and vice-versa) or ii) attaching therapeutic agent to the surface of imaging agent or vice-versa. There are many imaging and therapeutic combinations imaginable,

the main restriction being that they must be compatible and not interfere with their individual functioning. A list of some of the cancer theranostic nanoparticles found in the literature at the stage of clinical trials, is given in table 1.6, but we will focus the rest of this section on nanohybrids where one component is a gold shell. Firstly, we will have a general look at the synthesis methods for spherical gold nanoparticles and some of the anisotropic shapes. Then we will look specifically at the classic gold nanoshells (AuNSs) on dielectric $SiO_2$ core, and then how varying the core has impacted the synthesis procedures. Finally we will discuss combining NLO materials with gold as a potential theranostic probe, which will lay the foundation for the objectives of this thesis.

### 1.7.1 Synthesis of gold nanostructures

As was mentioned in section 1.1, this work is focused on bottom up synthesis methods, where precursor atoms/molecules assemble via physical interactions and/or chemical reactions to form the nanoparticle. We aim to control the synthesis conditions so as to have monodisperse nanoparticles, i.e nanoparticle distribution that is homogenous in both size and shape. A school of thought on what controls the degree of homogeneity obtained is the Lamer theory.[127] First proposed in the 1950's by Lamer and his colleagues, it outlines that the homogeneity of the nanoparticles formed, is a result of the kinetics of the assembling of the atoms, controlled by the atom concentration. When the atom concentration is increased rapidly, past its saturation concentration, to what is called the minimum nucleation concentration, we observe burst nucleation- the formation of tiny nuclei comprised of the atoms. They will continue to form until the concentration of the atoms drops below this minimum nucleation concentration. At this point, the concentration of the atoms is still above saturation concentration. This is the growth point, where the additional atoms attach to already formed nuclei. The Lamer model of nanoparticle growth is depicted in fig. 1.19. Various research groups have devoted their work to studying the formation of nuclei and the subsequent balance between the concentration of the atoms being added to the nuclei present, with the hope of elucidating how to control the homogeneity of the nanoparticles. What *in-situ* techniques have revealed is that the nucleation process is more complicated than originally outlined by Lamer's classical approach.[128] Lamer's model still remains a useful guide, highlighting the role the kinetics of nanoparticle formation (driven by changing concentration) plays in the homogeneity of the nanoparticles formed.

The 2004 review by authors Daniel and Astruc,[10] though almost two decades old, provides a solid background on the established spherical gold nanoparticle synthesis techniques. The methods covered in their review article include the citrate (Turkevich) reduction of gold chloride,[130] the Brust-Schiffrin method[131] (a two phase synthesis and thiol stabilizing method), variations on this method using other stabilizing ligands, as well as the seeded-growth method. The review also covers physical

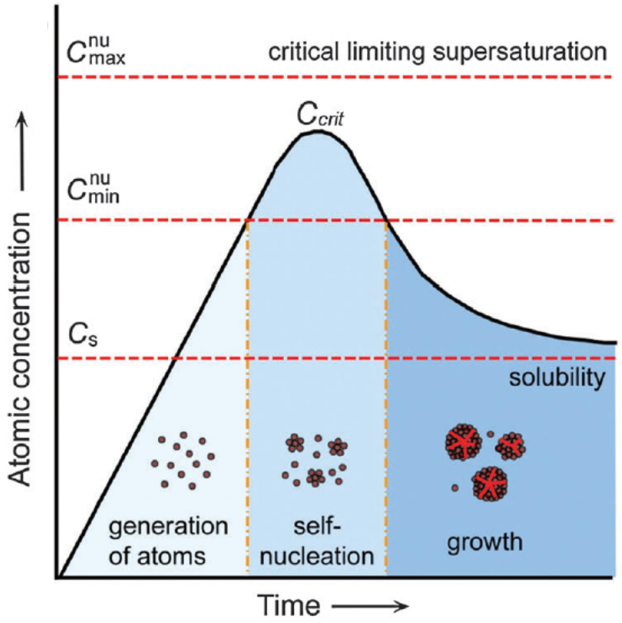


Figure 1.19: Lamer diagram depicting the kinetics of the formation of nanoparticles upon changing atomic/monomer concentration[129] $C_s$= atom saturation concentration, $C_{min}{}^{nu}$= minimum atom concentration for nucleation, $C_{max}{}^{nu}$= atom concentration at which supersaturation occurs and $C_{crit}$= atom critical concentration, maximum nucleation.

chemistry methods of AuNP synthesis such as performing the gold salt reduction under UV irradiation. Since that 2004 review, a large volume of methods have been published for the synthesis of gold nanoparticles varying parameters such as i) the reducer,[132–135] ii) the reaction media,[136,137] iii) the pH[136,138] iv) the stabilizers[139] v) the concentration[136,140] vi) the reaction temperature,[141,142] to control the size[140,143,144] and shape[145–151] of the resulting nanoparticles.

As was stated in the 2008 review by Liz-Marzan *et. al*[152] on the synthesis of anisotropic gold nanostructures, when focused on spherical nanoparticle formation, a one pot, rapid burst nucleation and growth (as described by the Lamer model) will suffice, however, when trying to favour the growth of specific facets to produce anisotropic geometries, a two step process is necessary. The first step is the formation of the gold nuclei. The second step is where the myriad of variations are reported, but can be summarized as the step of gold reduction in the presence of the nuclei. The conditions under which this reduction is done is varied. For example, one reaction parameter that is often changed is the reducer. $NaBH_4$, sodium citrate, formaldehyde and hydroxylamine hydrochloride are a few of the reducing agents used.

The main technique applied to enlarge the diameter of spherical gold nanoparticles is to use a seeded-growth method. In the work of Rodriguez-Fernandez,[144] they demonstrated the ability to

control the shape morphology of pure gold nanoparticles by performing the gold reduction reaction at a higher temperature (35°C), but also by performing a purification step to remove non isotropic geometries after the first gold reduction. They also attributed greater control of nanoparticle size to other experimental parameters such as the concentration of the capping ligand (in their work it was CTAB) and the reducer.

Undoubtedly, all the literature on gold nanoparticle synthesis cannot be covered in the scope of this thesis manuscript. However, knowledge of the experimental factors (already stated) that have been manipulated in gold nanoparticle synthesis and their reported impact on the formation of stable nanoparticles, is important know-how for branching off into the synthesis of hybrid gold nanostructures.

### 1.7.2 Synthesis of gold nanoshells on dielectric $SiO_2$ core

AuNSs were first synthesized on a $SiO_2$ dielectric core by the team of Halas in 1997.[153] The optical properties of AuNSs make them ideal candidates for bio-medical applications.[154] AuNSs, like their spherical and rod-shaped pure gold counterparts, have localized surface plasmon resonances (LSPR). Similar to AuNRs, the plasmon resonance of AuNSs is tuneable. For AuNSs, this tuneability is a result of the ratio of the inner core radius with respect to the radius of the entire core shell particle. For a given inner core radius, $r_i$, (as depicted in fig. 1.20) if the entire core-shell radius is decreased, i.e the gold shell thickness decreases, then the plasmon resonance is red-shifted.[155] AuNSs plasmon resonance can be red-shifted well into the NIR region (728 nm was the reported value by the team of Halas[156]), which has already been discussed for its biological advantages.

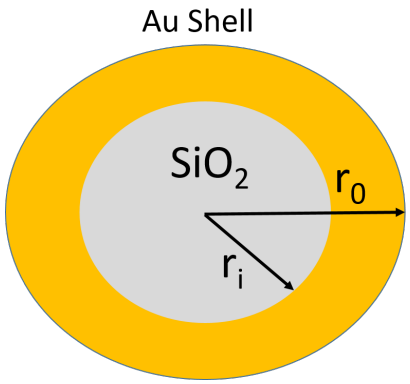


Figure 1.20: Depiction of a silica-gold core-shell nanoparticle of inner radius $r_i$ and outer radius of $r_0$.

To synthesize the AuNSs, firstly silica nanoparticles are usually produced by the Stöber method, where tetraethyl orthosilicate (TEOS) is hydrolyzed and condensed under alkaline conditions (usually involving the use of ammonium and performed in ethanol solvent) to form monodisperse nanoparticles, usually around 100 nm in diameter.[157,158] Variations on the sequence of reactant addition[159,160] have been reported but in most variations, the reaction time remains a lengthy process, most requiring overnight reactions.[161,162] The resulting nanoparticles have a negative surface charge, usually having a zeta potential value ranging between -70 mv and -80 mV.[163] The silica nanoparticles are modified to have amine groups present on their surface to facilitate the adsorption of small gold nanoparticles. This surface modification usually involves a process of overnight silanization, the most common silane used being APTES (3-aminopropyl-triethoxysilane). This process can also inculde a reflux step to ensure the condensation of the organosilane molecules onto the silica surface which promotes better gold adsorption in the latter steps.[155]

The preparation of the silica nanoparticles is one step, but as the gold shell synthesis is a seeded-growth method, the preparation of the "seeds" and subsequent gold plating solutions is required. The established Duff protocol[164] using THPC (tetrakis(hydroxymethyl)phosphonium chloride), NaOH and $HAuCl_4$ solution, for the preparation of negatively charged gold nanoparticles, approximately 2-3 nm in diameter, is commonly used for seed preparation. There is at minimum, a one day aging process, in the dark to allow the speciation of the gold. The adsorption of the "seeds" to the amine-functionalized silica surface is facilitated by electrostatic interactions as well as coordination bonding between the nitrogen atoms of the amine group and the gold.[165] In trying to probe the influence of the gold "seeds" on the gold shell growth, some researchers have performed the synthesis of the gold shell using differently aged gold seed dispersions. The findings were that freshly prepared "seeds" and aged "seeds" (up to 3 weeks aging) can attach to the amine-functionalized silica surface. However, the aged seeds facilitate gold coalescence upon the further reduction of gold species in the presence of the nanoparticles wheras the fresh seeds seemed to promote the dettachment of the gold from the silica nanoparticle. This is believed to be a result of the oxidation of the residual THP-Au(I) promoting a rearrangement that has a stronger affinity to the amine groups.[166] Due to the amine groups, the gold adsorption was preferred in lower pH (less than 8) as this ensures the positive charge of the amine group.[163]

The process of the gold shell growth requires putting the gold-seeded silica nanoparticles in contact with an aqueous solution of chloroauric acid containing potassium carbonate, which is called a K-gold solution. As reported in the thesis of Oldenburg,[166] the K-gold solution in contact with the silica nanoparticles needed to be aged in the dark for a minimum of 12 hours, to allow a thorough distribution of the gold species around the surface of the silica nanoparticles. With gold "seeds" acting as nucleation sites, reduction with $NaBH_4$ produces Au atoms which then attach and cause

the coalescing of the gold "seeds". In later variations of this synthesis, the reducer was changed to formaldehyde[156] and also to carbon monoxide.[167] In practice, an excess of the reducer quantity necessary to cause the complete reduction of the gold species was used, to ensure a faster and complete reduction. The gold ion concentrations have been varied, keeping the reducer quantity the same to observe the effect on the gold shell and it was found that low concentrations did not promote the complete shell coverage (31% surface covered) whereas high concentrations promoted complete shell coverage and then further shell thickening (99% surface covered).[168]

While these early synthesis protocols allowed the formation of a continuous smooth gold shell, the synthesis is time consuming. Variations to reduce the time to produce AuNSs on silica have been published. They involve skipping the step of gold seeding by providing another surface on the silica such as tin, to promote the nucleation of gold.[169] Others proposed depositing $Au(OH)_3$ over the either bare, or aminated silica nanoparticles which will serve as the nucleation sites instead of the gold "seeds".[170,171] The results of these variations have remained similar to that of the original procedure, producing silica nanoparticles with continuous gold shell coatings.

### 1.7.3 Synthesis of gold nanoshells changing the core material

While the synthesis of AuNSs on silica nanoparticles is well-developed, there are some challenges when using them for biological applications. Firstly, the final size of these nanoparticles are usually within the range of 100-150 nm, which may not be optimal size for efficient cellular uptake. However, in trying to make these nanoparticles smaller, it can affect the ratio between core radius and core-shell radius which impacts the optical properties. As the tuneability of the plasmonic gold shell has a proven therapeutic benefit, there is also an interest in changing the core material to provide additional functionality to the nanoparticle (multi-therapeutic pathways or theranostic functioning). The question to be answered therefore is, is the synthesis procedure of AuNSs on silica core transferable to the synthesis of AuNSs on other core materials? We must first consider the geometry of the silica core. Perfectly spherical nanoparticles are used, that are also monodisperse in size. If one aims to reproduce the synthesis on other cores, this may be a crucial starting point. Another factor to consider is the silanization process to give the silica nanoparticle a positive surface charge which is a process highly sensitive to the presence of water. Therefore, the nanoparticles need to be suited to stable dispersion in a non-aqueous environment. In the literature, there are examples of gold shells on different cores such as $BaTiO_3$,[80] $KNbO_3$,[172] iron oxide[173,174] and other magnetic core,[175,176] silver nanoparticles,[177] polystyrene,[178] semiconductor[179] and more. We will now look more specifically at some examples in the literature.

In the work of Wang *et. al*,[80] they synthesised a gold shell on spherical barium titanate ($BaTiO_3$)

nanoparticles, approximately 63 nm in diameter. They were able to start with core particles of sub-100 nm diameter (50 nm to be exact). By treating the nanoparticles to $H_2O_2$, they hydroxylated the surface, and then converted the OH groups to amine groups with APTES. They proceeded to use the seed-mediated growth method for the gold shell. They also used the same gold seed dispersion as described by Duff *et. al*,[164] but they consistently chose 2 weeks aged seed dispersions. They performed the same process of seed attachment to the aminated silica nanoparticles, and also reduced $HAuCl_4$ solution with formaldehyde in the presence of these nanoparticles to form the gold shell. They were finally stabilized by polyethylene glycol (PEG). Their result was a homogenous core-shell structure, confirmed by Transmission Electron Microscopy (TEM) analysis, with a gold shell thickness of approximately 10nm, and a maximum plasmon absorbance at 800 nm. The photothermal capability of the nanoshells was observed by measuring the temperature change of the nanoparticle dispersion upon a 10 minutes irradiation with a 808 nm, 1 W/cm$^2$ CW laser in comparison to the same irradiation of equal volume of water. In this work, they also examined the *in-vitro* cellular uptake of these core-shell nanoparticles by human glioblastoma U87 cells and since $BaTiO_3$ is a NLO active material, SHG imaging was performed as well as photothermal experiments. The particles exhibited both functionalities. The *in-vivo* PPTT of these particles were tested in a mouse 4T1 breast adenocarcinoma cell tumor model. They injected 50 µl of 12 mg/mL nanoparticle dispersion and then irradiated with an 808 nm, 1.2 W/cm$^2$ CW laser for 3 minutes, and then measured the temperature using an IR camera 6 hours later. The tumor temperature was elevated from 26.4°C to 58.4°C.

The synthesis of gold shells on iron oxide nanoparticles has been explored for biological applications because of the potential imaging and therapeutic applications. The gold shell is furthermore attractive as it promotes the stabilization of the iron oxide core in biological media.[174] In an effort to have great control on the gold shell formation, a layer-by-layer shell growth protocol was designed by Lee *et. al*.[173] In their synthesis, negatively charged iron oxide particles, approximately 100 nm in diameter, were coated with a positive polymer branched polyethylenimine (BPEI), causing a complete surface charge reversal evidenced by the changing of the zeta potential from negative to positive values. The polymer with its abundant amine groups facilitated the adsorption of separately synthesized gold "seeds" to the surface. The negative gold seeds caused the surface charge to reverse once more to a negative zeta potential. Then another BPEI polymer coating was performed. At this step, they performed the reduction of $HAuCl_4$ solution in the presence of the polymer coated nanoparticles with the reducer hydroxylamine hydrochloride which they termed the ion-reducible step. They would then wash the particles, coat with BPEI polymer and repeat the ion-reducible step until a gold shell was attained. They reported that after repeating this process 6 times, they were able to attain a gold shell, 14.1 nm thick, of a rough topography. Indeed, using an amine based polymer instead of an aminosilane is attractive as it reduces the time for surface functionalization.

Attempts to synthesis a gold shell on $LiNbO_3$ nanoparticles were performed during the internship of Eloise Millet in our laboratory (Institute of Nanotechnologies). The silanization functionalization was tested and compared to BPEI functionalization. It was found that the BPEI functionalization resulted in a low polydispersity of the nanoparticles, and was a simpler synthesis process as compared to the silanization. The seeded growth method was tested, and gold "seeds" were attached to the polymer functionalized $LiNbO_3$ nanoparticles. Further tests on the efficacy of different reducers for the gold shell growth step was done and the results from that work concluded that hydroxylamine hydrochloride promoted the reduction of the $HAuCl_4$ solution, and allowed for the coalescing of the gold nucleation spots on the nanoparticle. However, a complete gold shell was not attainable in one step.

### 1.7.4 Combining NLO and plasmonic nanomaterials for cancer theranostics

Researchers Boksebeld *et al* demonstrated the proof of concept for combining NLO nanoparticles (in their case SiC) and plasmonic gold (AuNRs).[180] In their work, AuNRs, (aspect ratio 3:9, 47.6 $\pm$ 3.9 nm in length and 12.3 $\pm$ 1.2 nm in width) were attached to SiC NPs approximately 150 nm in diameter to have a cancer theranostic hybrid nanoparticle. The important result from this work was that the hybrid nanoparticles were capable of both SHG and TPEF imaging when incubated with 3T3-L1 healthy cells. Using an IR camera, the photothermal effect of the hybrid nanoparticles was observed by noting the temperature increase upon irradiation with 808 nm CW laser, 40 $mW/cm^2$, from 17°C to 45°C. No temperature increase was observed with bare SiC nanoparticles, but a temperature increase was observed for the pure AuNRs dispersion. Therefore the photothermal activity could be attributed to presence of the gold nanorods. When the cell toxicity analysis was done on these hybrid nanoparticles, it was seen that they were non-toxic, however the gold nanorods themselves, which are stabilized by the surfactant CTAB, has non-negligible cell toxicity. The toxicity of the nanorods is attributed to the presence of the CTAB ligands. In using these SiC-AuNR nanohybrids, it will be essential to ensure that the AuNRs are securely attached. Though, the nanohybrids exhibited the ability to perform cellular SHG and TPEF imaging, as well as demonstrate its photothermal activity, combining the NLO material with gold in a more secure manner will avoid the possible toxicity challenges that can arise from detached AuNRs.

We have discussed the advantages of NLO microscopy techniques, such as SHG, for cancer diagnostic applications and discussed the exogenous nanoparticles already tested for this purpose. However, the strength of the SHG signal is scaled to volume. As such, small nanoparticles sizes result in weak SHG signals. However, it has been consistently demonstrated in the literature that sub-100 nm nanoparticles, ideally between 10-60 nm diameter, have an enhanced cellular uptake.[24] Though a SHG active nanoparticle of this size may be ideal for cellular uptake, it means sacrificing the

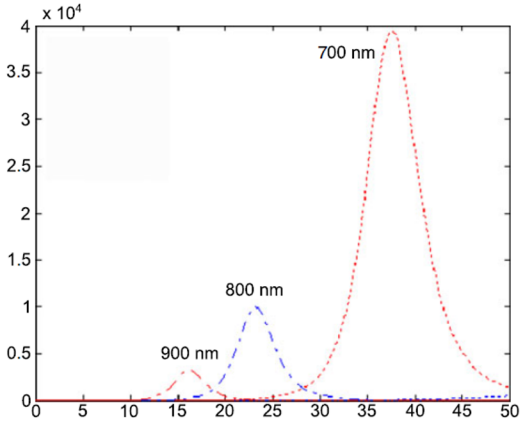


Figure 1.21: Simulation results of the SHG enhancement of $KNbO_3$ nanowires with a gold shell coating at different excitation wavelengths (700, 800 and 900 nm) as a function of gold shell thickness. The x-axis is the gold shell thickness in nanometers and the y-axis is the SHG enhancement intensity.[172]

strength of the SHG signal from a single particle. To combat this volume scaling effect, researchers Richter *et al*, demonstrated the SHG signal enhancement of $KNbO_3$ nanowires by coating with a gold shell.[172] The nanowire coating with Au was achieved via a seeded growth method. The nanowires underwent a silanization process with an aminosilane, to give it a positive surface charge to facilitate the attachment of the separately synthesized negative gold "seeds". Then, once the gold "seeds" were attached, $Au(OH)_3$ was added and the reduction to $Au^0$ performed with hydroxylamine. With simulations based on the electrostatic approximation, they demonstrated the SHG signal enhancement possible with varying thickness of gold shell, with a maximum enhancement factor of $4 \times 10^4$ (fig. 1.21) using the formula in equation 1.10.

$$\Gamma_{SHG} = |\frac{E_{shell}}{E_{bare}}|^4 \tag{1.10}$$

From the results of that work, we can plausibly hypothesis the enhancement of the SHG signal of a harmonic nanoparticle by coating it with a gold shell for a more sensitive SHG microscopy. In addition to this possible SHG enhancement, such a nanoparticle will also exhibit PPTT giving it a therapeutic modality. The biological potential of these NLO and plasmonic nanomaterials have yet to be further explored. There is no literature on combining $LiNbO_3$ and gold nanostructures for biological applications to date.

### 1.7.5 Conclusion

Gold nanoparticle synthesis is on the surface a simple procedure, but it indeed requires a balancing of many experimental parameters such as pH, temperature, concentration of reactants, choice of reducers and possible stabilizing agents. There are many reported protocols for moving from the spherical nanoparticle to anisotropic shapes. The hybrid gold shell structure is interesting as it can allow for the encapsulation of various materials, protecting it with the bio-compatible gold shell surface, which is also easily modified (for example PEG addition), and allows one to take advantage of its unique optical properties for therapeutic functions.

## 1.8 Objectives of thesis

In light of the literature discussed, we can draw the following conclusions.

1. Optical bioimaging techniques are desirable as they permit microscopic spatial resolutions which can lead to early cancer diagnosis.
2. NLO based bioimaging further improves the spatial resolution of traditional optical imaging techniques and can perform imaging at NIR wavelengths of light.
3. NIR wavelengths are ideal as they have greater tissue depth penetration than visible light, and also has lower photon energies, minimizing the risk of photodegradation.
4. Photothermal therapies are attractive as there is a window of thermal resistivity exhibited by healthy cells that does not exist for cancer cells, thereby allowing for a selective heat destruction of cancer cells.
5. Plasmonic photothermal therapies are attractive options as they rely on the enhanced light absorbance of plasmonic nanostructures which can be tuned to the NIR region by size and shape.
6. Synthesis of gold shells on various core materials is possible.
7. Literature points towards the possibility of SHG signal enhancement by coupling the material with plasmonic materials.
8. Coupling NLO active SiC with plasmonic AuNRs allowed for simultaneous SHG cell imaging as well as photothermal activity.

As such, the goal of this work is to synthesize nanohybrids of a core-shell structure, combining the NLO active material $LiNbO_3$ as the core, with a gold shell. The gold shell will be synthesized by a

seeded-growth method and the parameters that can possibly influence the shell growth process such as gold seed attachment, the pH, the reducing agent, and the concentration of the $HAuCl_4$ solution to be reduced with respect to the concentration of the core nanoparticles will be investigated. The gold shell morphology, the plasmon resonance, the NLO efficiency and the photothermal property of these nanoparticles will be examined.

In this work, many nanoparticle characterization techniques will be used in both a complementary and comparative nature. The characterization of nanoparticles in literature can vary significantly, making comparisons between different studies a challenge at times. As such, this work also aims to provide a guide to understanding what information is obtained from the various techniques and how to better compare the various results presented in literature.

# Chapter 2

# Characterization Methods

Nanomaterials present characteristics that are often an enhancement of, or even novel to, the intrinsic properties of their bulk counterparts.[181] Their optical,[182] magnetic,[183] mechanical[184] and chemical[10] properties can vary significantly by changing their size, shape and composition. As such, nanomaterials have found applications in material development, electronics, catalysis, optics/photonics, and biology and nanomedicine. In the fields of biology and nanomedicine in particular, over the last two decades, nanoparticles have been demonstrated as vectors for drug delivery,[185,186] as *in-vivo* bio-imaging probes,[187] as probes in bio-sensors[188,189] and as vectors for other mechanisms of disease therapy.[190] The interactions that occur between the nanoparticles and the biological medium are primarily dependent on their surface chemistry and their size, so it is vital to have these nanoparticles well characterized.

To date, there is no one analytical technique that can provide a comprehensive characterization of nanoparticles. As such, multiple techniques that probe different properties of the nanoparticles are used to obtain a complete characterization. The characteristics that are considered to be important will depend on the intended application of the nanoparticles, but the features that are always characterized are their size and shape. Further characteristics such as surface, optical and magnetic properties as well as stability in a given dispersing media can also be of interest. In working with more complex hybrid nanoparticles in this thesis work, which are also referred to as nanohybrids, it became evident that a clear understanding of the characterization techniques was needed to interpret the sometimes differing results obtained via complementary techniques. This allowed for a working knowledge on what information could be obtained, what are the limitations of each technique, and what, if any, assumptions must be made when analysing the results. The conclusions derived from this work is hinged on the interpretation of these data sets, and therefore, it is necessary to dedicate a chapter of this thesis to the characterization techniques used in this work. This chapter will firstly give a general overview of the routine techniques used, and then we will look at the specific application of these techniques to the nanohybrids of this work, comparing tech-

niques when applicable, and discussing all the limitations, assumptions and approximations applied.

## 2.1 General theory of main analytical techniques

### 2.1.1 Transmission Electron Microscopy (TEM)

The principle of transmission electron microscopy (TEM) is based upon the wave-particle duality of electrons. Instead of a light source, as used in conventional optical microscopy, an accelerated beam of electrons is used to produce an image. As the *De Broglie* wavelength of an electron (1.22 nm for a 1 eV electron), which is calculated by the equation shown in eq. 2.1, is much smaller than the wavelengths of visible light, an electron source can visualize objects with nanometer precision and higher spatial resolution. The two common electron sources for TEM microscopes are thermionic (such as tungsten filament or a $LaB_6$ filament), and field emission gun (FEG), and with improvements to these electron sources, TEMs are nowadays able to achieve a resolution of better than 4 Å in both hard and soft materials.[191] The electrons are accelerated at high voltages (typically 100 kV and higher),[192] and the beam is then focused and aligned onto the sample by a series of electromagnetic lenses. Finally, the sample image is magnified usually onto a fluorescent screen, and the image capturing is performed by a digital camera system incorporated into the microscope.

$$\lambda = \frac{1.22}{E^{1/2}},\ \textit{where } \lambda \textit{ is in nm and } E \textit{ is in eV} \tag{2.1}$$

TEM imaging is a staple tool in the characterization of 1-dimensional, 2-dimensional and 3-dimensional nanostructures. One must, however, be mindful of the challenges in interpreting these electron images. TEM imaging provides us with a 2-dimensional image of 3-dimensional objects viewed in transmission mode, and while our brains and eyes can easily "translate" a 2-dimensional image of our everyday surroundings into the 3-dimensional reality, we are ill-equipped to do this with TEM images of nano-objects.[191] This becomes more evident when trying to decipher the top and bottom of objects in the image, particularly when the objects are stacked as seen in fig. 2.1.

As TEM images are obtained by averaging the electron volume densities that are transmitted through the entire depth of the objects, it is not possible to retrieve depth information from the final image, i.e TEM has no real depth sensitivity.[192] Electron tomography is a technique developed to combat this challenge, which compiles images of the object taken at different angles and in small slices, into a single 3-dimensional image.[191] In some TEM microscopes, the sample holders can be tilted, allowing one to view the sample from a different angle. The TEM samples in this work however were always loaded onto a single-tilt sample holder, with no tilt angle used.

Another challenge lies with the potential of electron beam damage to the samples, more commonly observed with polymers and organic materials. One must therefore consider which operating voltage of the microscope is best suited for a given sample. However, even when working at an appropriate voltage, sample beam damage can occur. In fig. 2.2, an example is given of damage done to a holey carbon grid by the electron beam.

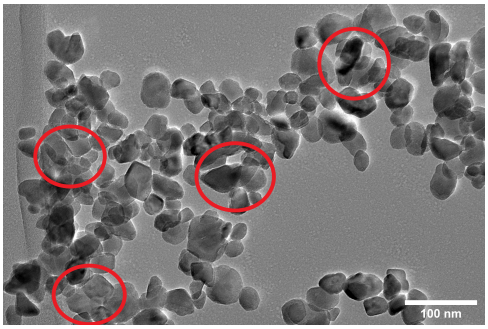


Figure 2.1: TEM image of LN nanoparticles. Red circles on image highlights sections where it is challenging to distinguishing the top and bottom of these 3-D particles in the 2-D representation as well as the challenge in delineating the boundaries of each particle.

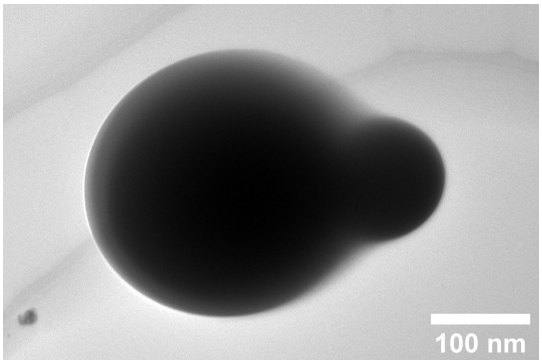


Figure 2.2: TEM image of a section of a TEM grid, damaged from the electron beam.

TEM imaging requires that the objects to be imaged are transparent to electrons, such that a sufficient intensity of electrons can contact the photographic plate/CCD camera to project the image. The objects must therefore be sufficiently thin, which in practice means objects of the order of hundreds of nanometers and less are considered suitable (although depending on the material and operating voltage of the microscope, objects of a thickness of 1 µm can be used). As a result of this, the stacking of objects to be imaged by TEM will impact the image quality as shown in fig. 2.3. In addition to the thickness of the sample, the surface of the TEM grid must also be suited for the even deposition of the sample. In this work, as the nanohybrids were dispersed in water,

we observed drying-artifacts[193] in the image. The most common challenge was the nanohybrids being concentrated on the edges of the TEM grid, and aggregated together. Treating the TEM grid surface with a UV-ozone etching, created a more hydrophilic surface, increasing the wetting of the grid by aqueous nanoparticle dispersions, which in turn gave a better distribution of the nanohybrids on the grid.

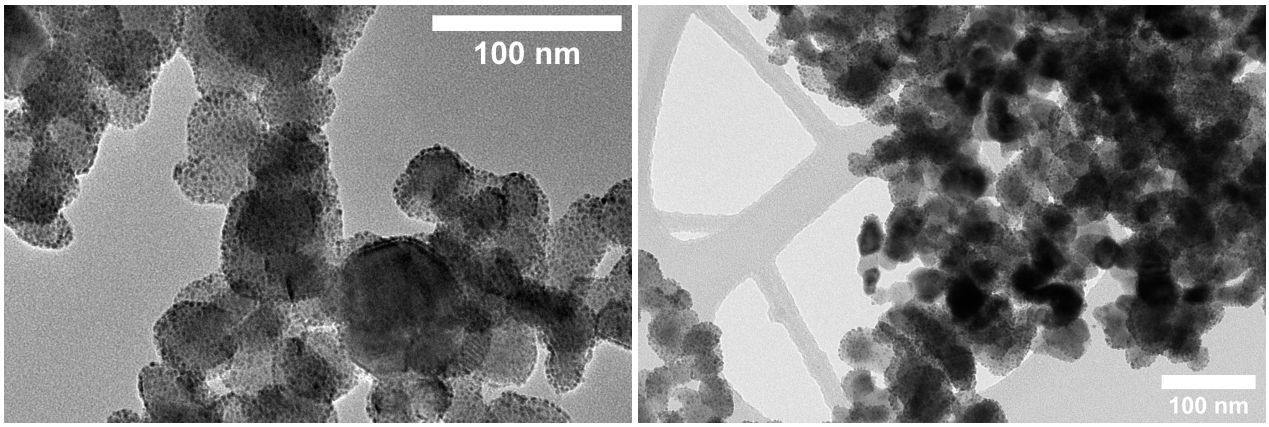


(a) (b)

Figure 2.3: TEM image of lithium niobate NPs with AuNP decorated surface. In the images, the darker spots are due to the greater thickness of the sample as a result of the stacking of NPs on top of each other. (a) NPs deposited on a UV-ozone etched carbon holey grid and (b) on an untreated carbon holey grid.

The TEM imaging for this work was performed with a JEOL-2100HT microscope, with a $LaB_6$ electron source, at a 200 keV operating voltage. The microscope was also equipped with a bottom mount Orius SC1000 CCD camera (Gatan). To prepare the nanoparticle samples for imaging, a carbon-coated 400 mesh copper alloy grid from TED PELLA INC, underwent UV-ozone etching at 25°C for 30 minutes. Then 2 $\mu$L of nanoparticle dispersion, ranging in concentration between 0.03 and 0.06 mg/mL for LN and hybrid LN nanoparticles, and 0.035 mg/mL for the pure AuSeeds dispersions, was dropped onto the grid and allowed to first air dry and then placed in an oven at 50°C for 10 minutes. All of the TEM images were analyzed with the ImageJ software.

### 2.1.2 X-Ray Photoelectron Spectroscopy (XPS)

X-Ray photoelectron spectroscopy (XPS) is an analytical technique used to quantify and characterize the elements (except hydrogen and helium) at the surface of a sample. Although the X-rays beam used interacts with the surface as well as can penetrate deeper into a sample, XPS is surface sensitive because the photoelectrons generated have a fixed travel distance within a solid before

losing their kinetic energy. This is called the inelastic mean free path (IMFP). As a result, there is a definite "escape depth" for the photoelectrons generated during XPS analysis. This escape depth is calculated as shown in equation 2.2, where $\lambda_e$ is the IMFP, and $\theta$ is the angle of photoelectron detection from normal to the surface.

$$escape\ depth = 3\lambda_e cos\theta \tag{2.2}$$

The IMFP ranges between 4 and 30 Å depending on the material and the kinetic energy of the electrons. It not only gives the elemental composition of the sample's surface, but also provides information concerning the chemical environment (eg. chemical bonds, oxidation state etc). It is an effective surface technique compatible with a wide range of organic and inorganic materials, however the samples must be compatible with an ultra high vacuum environment.

In this work, XPS measurements were performed at two locations. The first instrumentation used a VSW spectrometer at INL, equipped with a monochromatic X-ray source (Al K$\alpha$ 1486.6 eV) in which the angle between the incident beam and the detector was the magic angle. The angular resolution was 3° and the take-off angle was 90° relative to the substrate surface. The energetic resolution was 0.2 eV. The data analysis was performed with CasaXPS software. C1s binding energy was set at 285 eV. A Shirley background was subtracted on Si2p and O1s spectra when coming from bulk elements while a linear background was subtracted on C1s and N1s spectra as surface elements. Peaks were fitted by a Gauss-Lorentz curve and the Scofield cross sections were used for quantification.

The second instrumentation was performed at the JRC Nanobiotechnology laboratory, Italy, using a Axis Ultra-DLD from Kratos. The X-ray source was Al K$\alpha$ 1486.6 eV, operating at a power of 225 W. Wide scan spectra were recorded from 0 to 1200 eV binding energy in hybrid mode, "slot" (400 x 700 $\mu m^2$ analysis area) and FoV2 (100 $\mu$m spot) at 80 eV and 160 eV pass energy, whereas core level spectra were recorded in "hybrid" mode using pass energy of 40 eV. The take-off angle respect to the sample normal was 0° for survey and high-resolution (HR) spectra and operating pressure was $1.5 \times 10^{-8}$ mbar. Surface charging was compensated using low energy (3.8 eV) electrons and adjusted using the charge balance plate on the instrument. All the spectra were processed with CasaXPS. Spectra were calibrated setting hydrocarbon C1s at 284.6 eV and Au $4f_{5/2}$ at 84.00 eV. The surface composition was evaluated from the survey spectra, after background subtraction, using Relative Sensitivity Factors (RSF) based on Scofield cross sections and corrected for magic angle emission, electron mean free path and spectrometer's transmission functions. Peak fitting was performed with no preliminary smoothing. Lorentzian finite functions, LF(a,b,w,n), were used to approximate the line shapes of the fitting components after a background substraction.

### 2.1.3 Energy Dispersive X-Ray Spectroscopy (EDX/EDS)

Energy dispersive X-ray spectroscopy (EDX/EDS), uses the characteristic X-rays emitted from a sample upon bombardment by electrons or X-ray beam, to have an elemental characterization. When electrons or X-ray beam are focused onto a sample, the inner shell electrons of the atoms can be excited and subsequently ejected (fig. 2.4). This ejection leaves an electron hole, which can be filled by another electron located in a higher energy shell. During this process, an X-ray can be emitted, which will be equivalent to the energy difference between the two shells. The energies of the X-rays emitted will be characteristic of the elements present.

EDS uses electron beam bombardment to cause the expulsion of core electrons. This allows EDS to probe the entire depth of the sample and not be limited to surface analysis as was seen for XPS . However, for the determination of the relative abundances of the elements present, it is necessary to probe a thin area of the sample (on the order of a few hundred nanometers) so that the characteristic X-rays produced throughout the entire depth of the sample can escape to the detector and not be absorbed. The accuracy of the relative element abundances in the sample is therefore dependent on i) the composition of the sample, as there are some elements with overlapping X-ray energies, and ii) the thickness of the sample, which can prevent produced X-rays from exiting the sample for detection. In addition to this, EDS technique is not useful for low atomic number elements. EDS detectors are generally combined in electron microscopes, and so by scanning the sample, elemental mapping images, indicative of the spatial variations of a given element, can be produced along with the corresponding electron image. Though the detection limit for EDS spectroscopy is dependent on the sample surface conditions (roughness of sample etc), generally, EDS can detect elements once they are between 1-10 % wt and is not suited for trace element analysis.[194]

In this work, the electron beam was focused on different spots on the sample, and the characteristic X-rays emitted, were detected and used to give an element spectrum, an example of which is shown in fig. 2.5. The risks in focusing the electron beam on a singular spot was the electron damage to the sample itself. It was therefore necessary to collect all TEM images first, and then proceed to do the EDS analysis. The electron beam would then be focused on multiple spots on the grid in an attempt to minimize sample beam damage. The EDS analysis in this work was used for qualitative analysis to confirm which elements were present, which we used to prove the attachment of gold seeds to LN (discussed further in chapter 3) and the presence of gold shells (discussed further in chapter 4).

The EDS analysis for this work was performed with the JEOL-2100HT microscope equipped with

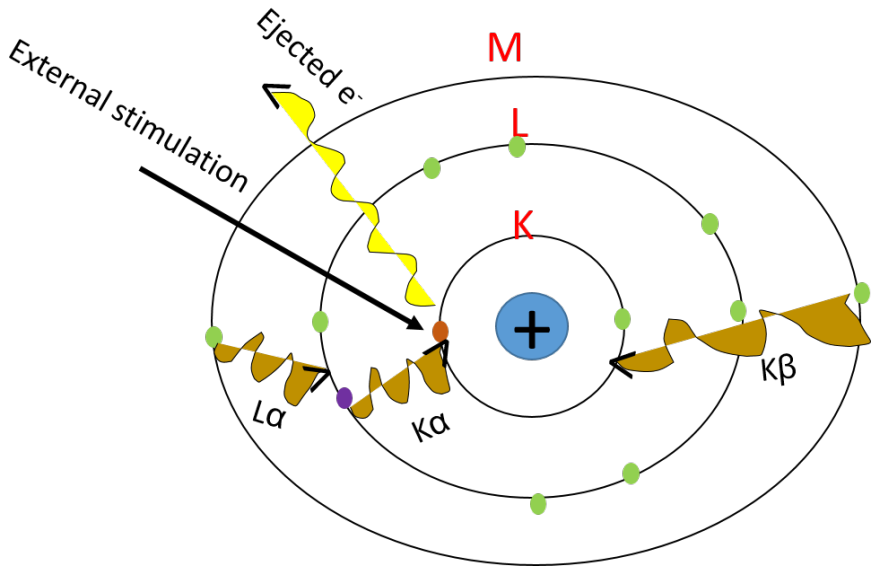


Figure 2.4: Representation of the electron transitions in an atom upon an external X-ray stimulation. The electron ejection leaves an electron hole which is filled by an electron in another energy orbital. An X-ray is emitted as the electron fills the electron hole, corresponding to the difference of the energy orbitals. (K$\alpha$, K$\beta$ etc.). The characteristic X-rays emitted from the electron transitions are labeled using the Siegbahn notation.

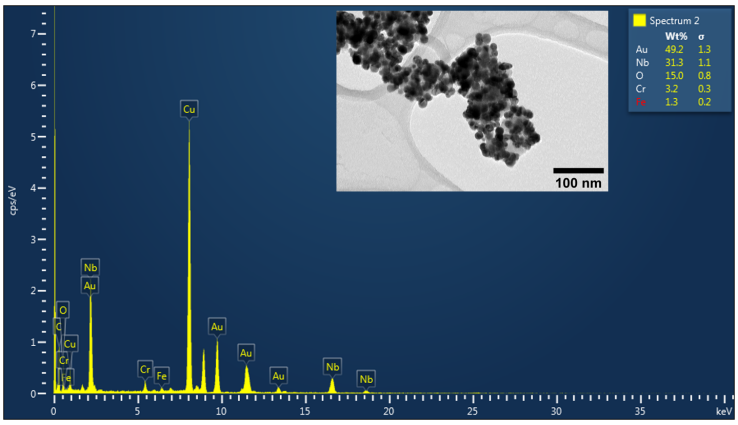


Figure 2.5: EDS spectrum of the elements identified by the characteristic X-rays emitted (using the Siegbahn notation) upon a focused spot electron beam on the sample shown in the TEM image included. Spectrum shows the peaks for Nb at 16.6 and 18.6 keV, Au at 9.7 and 11.4 keV. The spectrum also shows peaks for O, Cu, Cr and Fe, which are from the TEM grid.

a EDX XMAX 80 mm$^2$ silicon drift detector. The microscope's operating voltage was set at 200 keV. The EDS spectra were obtained using spot sizes of 35, 25 and 7 nm. EDS chemical maps were also collected using a TITAN ETEM FEI microscope. The sample preparation was the same as detailed for TEM imaging in section 2.1.1. The EDS data was analyzed by Aztec software (OXFORD

INSTRUMENTS).

### 2.1.4 Dynamic Light Scattering (DLS)

The random motion of particles in a dispersing medium (gas or liquid) is called Brownian motion. The combined work of Einstein on Brownian particles, and Stokes on the mobility of spherical particles in a fluid, produced an equation that shows the relationship between the diffusion coefficient of particles to their radius. The dynamic light scattering (DLS) technique uses the fluctuations in the intensity of scattered light detected upon irradiating particles dispersed in a liquid medium, to determine the particles diffusion coefficient and subsequently their hydrodynamic radius. The DLS software of devices such as the Malvern nanoseries, generates an intensity auto-correlation function of the light scattering, $G(\tau)$, within a short decay time as shown in equation 2.3, where $b$ is a constant dependent on the instrument and optic settings, $D_t$ is the translational diffusion coefficient and $q$ is the scattering vector.[195]

$$G(\tau) = 1 + b.e^{-2D_t q(\tau)} \tag{2.3}$$

Once $D_t$ is known, using the *Stokes-Einstein* equation (equation 2.4), the hydrodynamic radius ($R_H$), can be calculated.

$$D_t = \frac{k_B T}{6\pi\eta R_H} \tag{2.4}$$

where $k_B$ is the Boltzman constant ($1.38 \times\ 10^{-23}\ JK_{-1}$), $T$ is temperature, and $\eta$ is the absolute visocosity.

The results of a DLS measurement are based on the intensity correlation, an example of which is shown in fig 2.6. The terms used to describe the results of a DLS measurement is explained below. The Z-avg, also known as the cumulants mean is the primary result and considered as the most reliable obtained from the measurements. According to the National Institute of Standards and Technology (NIST), at minimum the average Z-avg and average PDI of at least three measurements, with their standard deviations, should be reported.[196] The Z-avg is the harmonic intensity averaged particle diameter, and is used to describe the average hydrodynamic radius of the nanoparticle sample. It is possible to convert the intensity distributions to volume and number distributions based on Mie theory, but it assumes that the particles are spherical, homogenous and all optical properties are well known (absorption value of the sample at the wavelength of light used is known). The next term is the polydispersity index (PDI) which is a dimensionless number, derived from a 2 parameter fitting of the correlation data, used to indicate the dispersion of the particles' diameters distribution in the sample. It is scaled so that values above 0.7 indicate a broad

size d of the sample and values below 0.05 are rarely observed. In this work, a PDI value of 0.2 and lower is indicative of an acceptable size distribution of the nanoparticles.

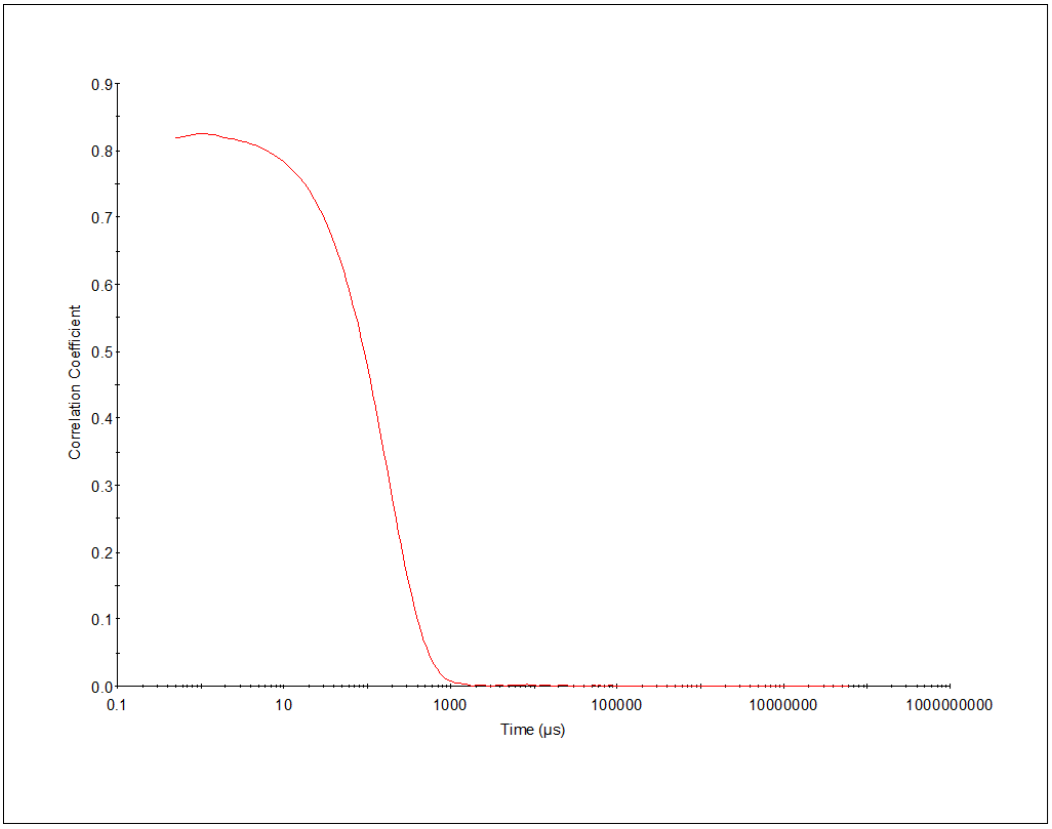


Figure 2.6: Example of a correllogram created during a DLS measurement.

In this work, the Malvern nanoseries zetasizer ZS was used to obtain the hydrodynamic radii of the various nanoparticle dispersions. The nanoparticles were dispersed in water and concentrations were kept between 0.03 and 0.06 mg/mL for LN and hybrid LN nanoparticles, and 0.035 mg/mL for the pure AuSeeds dispersions. All measurements were done at 173° back-scattering angle with DTS1070 disposable folded capillary cells. The Z-avg values reported were the average of triplicate measurements.

### 2.1.5 Laser Doppler Velocimetry & Electrophoresis

Particles dispersed in liquid media develop a net charge at their surface due to either the presence of ionizable compounds and/or the adsorption of charged species from the liquid onto the particles' surface or the self-dissociation of surface molecules. This surface charge impacts the distribution of the particles in the media, and results in a high concentration of tightly bound, oppositely charged species in a sphere around the particles, forming an electrical double layer. There are two main

liquid regions around the particle; the *Stern layer*, which is the region comprising of the tightly held oppositely charged species, and the *Diffuse layer* where the charged species are more loosely bound to the particle. The zeta potential is the electrical potential at the hypothetical plane within the diffuse layer, which separates the mobile liquid region from the liquid region that remains fixed to the particle, called *the slipping plane*.[195,197] The electrical double layer is illustrated in fig.2.7.

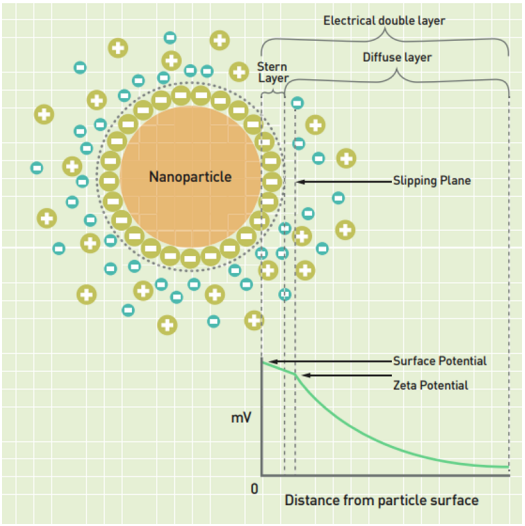


Figure 2.7: Graphical representation of the electrical double layer around a particle, showing the Stern layer, diffuse layer and the slipping plane, with an illustration included depicting at which boundary zeta potential is measured. Taken from Malvern Panalytical Zetasizer ZS brochure.

Laser Doppler Velocimetry (LDV) is a technique that is used to determine the velocity of moving particles in a fluid flow. To extract the zeta potential of the particle from this technique, it is combined with electrophoresis: applying an electric field which causes the migration of charged particles towards the oppositely charged electrode. By performing LDV during the electrophoresis, one can determine the electrophoretic mobility of the particles from equation 2.5.

$$\mu_e = \frac{V}{E} \tag{2.5}$$

where V is velocity ($\mu m\, s^{-1}$) and E is electric field strength ($V\, cm^{-1}$). Once the $\mu_e$ is known, the $\zeta$ can be determined from the equation 2.6

$$\mu_e = \frac{2\epsilon_r \epsilon_0 \zeta}{3\eta} \tag{2.6}$$

where $\epsilon_r$ is the relative permittivity/dielectric constant, $\epsilon_0$ is permittivity of vacuum, $\eta$ is viscosity at experimental temperature and $\zeta$ is the zeta potential.

In this work, the Malvern nanoseries zetasizer ZS was used to obtain the zeta potential of the various nanoparticle dispersions. The dispersing media was water and the sample temperature was set at 25°C. The sample concentrations were kept between 0.03 and 0.06 mg/mL for LN and hybrid LN nanoparticles, and 0.035 mg/mL for the pure AuSeeds dispersions. The data were fitted by the *Smoluchowski* model. All measurements were done with DTS1070 disposable folded capillary cells fitted with gold electrodes for applying an electric field. The zeta potential values reported were the average of triplicate measurements.

### 2.1.6 UV-visible Absorption Spectroscopy

UV-visible absorption spectroscopy is an optical characterization technique used in chemistry, physics and biology, based on the absorption of UV-visible light of molecules. As the molecular orbitals of a compound are of discrete energies, only a specific wavelength of light will permit the temporary electronic transition of an electron from its current orbital to the next available orbital. When a photon of given energy, that corresponds to the energy difference between the highest occupied molecular orbital (HOMO) and the lowest unoccupied molecular orbital (LUMO) interacts with the compound, an absorption phenomenon occurs, temporarily promoting the electron(s) of the HOMO to the LUMO. Compounds whose HOMO to LUMO energy difference is within the UV-visible region of the electromagnetic spectrum, can be examined with UV-visible spectroscopy.

Spectroscopists use UV-visible absorption spectra to elucidate the structure of a compound, the kinetics of a reaction, the concentration of a compound in a solution, the impact on changing surrounding environment of a compound (examining shifts in known peaks) and other information. The absorbance values of a compound in solution (or a gas) at any wavelength of light is the logarithm of the monochromatic intensity of light entering the compound ($I_0$) as a ratio of the intensity of light transmitted through the compound (I) (eq. 2.7).

$$A \;=\; log\frac{I_0}{I} \;=\; log\frac{1}{T} \;=\; -logT \tag{2.7}$$

where A is absorbance and T is transmission.
The relationship between the absorbance of a compound to its concentration is described by the Beer-Lambert law, given in eq. 2.8, where A = absorbance, $\epsilon$ = extinction coefficient for the wavelength of light, $l$ = the path length of the light through the sample and c = concentration.

$$A = \epsilon \times l \times c \tag{2.8}$$

While the classical use of UV-visible spectroscopy probes the electronic transitions of compounds, it has been used to characterize the plasmon resonances of gold (and other) nanoparticles. As explained in section 1.5.1, if the incident light contacting the plasmonic nanoparticles is at the plasmon frequency of the nanoparticles, this light will be absorbed. Nanoparticles are also light scattering objects, and as such the attenuation of light observed is due to both absorption and scattering events. The propensity of a nanoparticle to absorb or scatter a specific wavelength of light is given by its absorbance and scattering cross-sections. These cross-sections can be deduced mathematically for spherical geometries but become more complex for anisotropic nanoparticle shapes. As such, when the absorbance and scattering cross-sections are unknown, the raw data obtained from performing the UV-visible spectroscopy, is no longer called absorbance, but extinction. The growth of gold nanoshells can be followed by UV-visible spectroscopy as its optical properties (wavelength at which the plasmon resonance occurs), vary with respect to the completeness of the gold shell and then when a complete shell is obtained, it varies with respect to the ratio of the thickness of the shell to the radius of the core particle.

The UV-visible absorption spectroscopy for this work was performed with a SAFAS-UV mc2, double beam spectrometer. The spectra acquisition was done by scanning the wavelengths from 400 to 1000 nm, using a bandwidth of 2 nm and a wavelength step of 1 nm. The samples were placed in a quartz cell with 1.0 cm path length.

### 2.1.7 Inductive Coupled Plasma Atomic Emission Spectroscopy (ICP-AES)

Inductive coupled plasma atomic emission spectroscopy (ICP-AES), also known as inductive coupled plasma optical emission spectroscopy (ICP-OES), is an elemental quantification technique. The sample is firstly digested in an acidic medium. A plasma is produced through the inductive coupling method, and the digested sample is introduced into the plasma. The atoms immediately collide with the charged particles of the plasma leading to a process of electron loss and recombination which produces radiation of wavelengths characteristic of the elements present. The intensity of this radiation is compared to that produced from known concentrations of the element and therefore the exact concentrations of the element in the sample is determined. ICP-AES is suited for the analysis of almost 70 elements, and can determine concentration values in the range of µg/L. ICP-AES is not suited for the halogens as there is no wavelength of analysis that can bring sufficient sensitivity. Due to the mineralization of sulphur, its analysis tends to be complex and so ICP-AES is not generally used for its concentration determination. As our samples consist mainly of Li, Nb, O, Au, ICP-AES was able to give the quantification of these elements present in our samples easily.

ICP-AES analysis was performed by CREALINS laboratory Lyon, who is equipped with an ICP-

AES ICAP 6300 and an ICP-AES ICAP 6500 analyser by Thermofisher Scientific. The samples were digested in a solution comprised of 4% $H_2SO_4$, 4% $HNO_3$ and 4% HCl. The HCl was used for our samples containing gold.

### 2.1.8 Time-Of-Flight Secondary Ion Mass Spectrometry (TOF-SIMS)

Time-of-flight secondary ion mass spectrometry (TOF-SIMS) is a surface-sensitive analytical technique which provides detailed elemental and molecular information on the topmost layer of a solid surface (1-3 nm). In this technique, the solid is bombarded by a pulsed primary ion beam, with a few keV in energy. Upon collision, the ion penetrates into the solid, all the while losing its kinetic energy. The penetrating ion collides with the nuclei of the atoms of the solid, which in turn causes collision cascades that imparts energy and momentum sufficient enough for the surface atoms to escape as molecular ions and their fragments, referred to as secondary ions. These secondary ions are what are detected. The different secondary ions produced are distinguished by their mass-to-charge ratio, but in order to do this, the ions are accelerated by a fixed voltage so that their kinetic energy is also fixed. Their velocity will then be solely dependent on their masses, lighter mass ions will arrive at the detector first, and the heavier mass ions later, resulting in a mass spectrum.[198] As it is necessary for the ions produced to be detected without interference by other bombarding molecules, the analysis is done under ultra high vacuum. A simplified schematic representation of TOF-SIMS is shown in fig. 2.8.

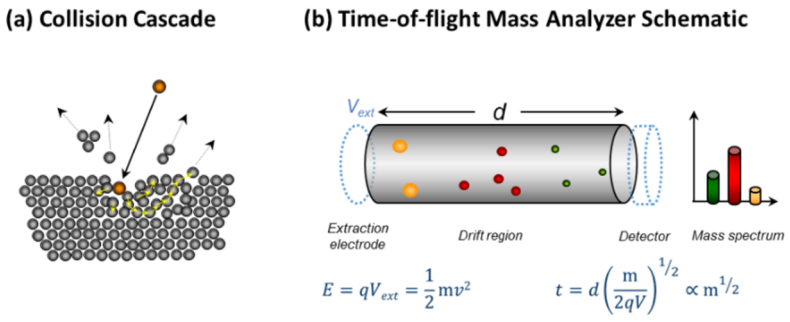


Figure 2.8: A Simplified diagram of a general TOF-SIMS experimental set-up.[199]

In this work, the TOF-SIMS was performed at the JRC Nanobiotechnology laboratory, Italy, using a TOFSIMS IV from IONTOF GmbH (Munster, Germany), equipped with a bismuth nanoprobe ($Bi_3^{++}$) 25 keV ion beam as primary ion gun in high-current bunched mode. The sample was deposited on a silica substrate. The raster area was set to 200 x 200 $\mu$m in random mode to minimise sample charging. The primary ion dose was kept under the static limit ($10^{13}$ ions/cm$^2$). A low-energy electron flood gun was used for charge compensation during analysis. Eight spectra were

acquired for each sample in positive and negative polarity. TOF-SIMS data were pre-processed using the SurfaceLab V6 software (IONTOF GmbH). Mass spectra were calibrated using unique mass calibration peak lists containing $C^+$, $CH_2^+$, $CH_3^+$, $C_3H_5^+$, $C_6H_3^+$, $C_6H_7^+$, $C_8H_9^+$ for positive polarity, and $C^-$, $CH^-$, $CH_2^-$, $C_2H_-$, $C_3H^-$, $CHO_2^-$, $C_4H_3^-$ for the negative polarity spectra. After a preliminary inspection of the data, and considering the high yield of certain fragments in the positive spectra coming from irrelevant chemistry (or contaminants), further analysis was carried out only with the negative polarity spectra. A list containing a combination of peak areas of characteristic peaks from each type of sample was created and exported as a text file excluding saturated peaks. The text file was uploaded into the simsMVA software (http://mvatools.com) for Principle Component Analysis. Data was normalized by total ion intensity, Poisson scaled and mean centered before performing PCA.

## 2.2 Discussion of analytical techniques for nanohybrid characterization

The techniques described in the previous sections allow one to characterize the properties of nanoparticles. A summary of the extractable characteristics of nanoparticle dispersions from each technique is given in table 2.1. In the following sections, we will discuss and compare the data obtained from the techniques specific to the nanoparticles studied in this work.

| | Characteristic of the nanoparticles | | | | |
|---|---|---|---|---|---|
| Technique | Size | Elemental Composition | Concentration | Colloidal Stability | Surface Properties |
| DLS | ✓ | X | X | ✓ | X |
| EDS | X | ✓ | X | X | X |
| ICP-AES | X | ✓ | ✓ | X | X |
| LDV/Electrophoresis | X | X | X | ✓ | ✓ |
| TEM | ✓ | X | X | X | ✓ |
| TOF-SIMS | X | ✓ | X | X | ✓ |
| UV-Vis | X | X | ✓ | X | ✓ |
| XPS | X | ✓ | X | X | ✓ |

Table 2.1: The extractable characterization data from the various analytical techniques, specific to the nanoparticle dispersions of this thesis work.

### 2.2.1 Comparison of techniques used to determine nanoparticle size

The nanoparticles used in this work are lithium niobate nanoparticles (LN), nanohybrids that are gold decorated LN (LN@BPEI@AuSeeds), and core-shell gold coated LN nanohybrids (LN@Au). To characterize the nanoparticles' sizes, TEM and DLS method were frequently used. It should be stated that for LN, the nanoparticle size was also determined by X-ray diffraction (XRD) analysis, however as this was only performed on LN and not all the nanoparticle categories listed above, the XRD analysis will be discussed specifically in chapter 3, section 3.2.1, page 90.

TEM provides us with images of the nanoparticles, and as such, the size determination represents the size using the grain boundaries of the nanoparticles. We can consider it as the real particle size, although, as discussed in the section 2.1.1, we must be careful in identifying the boundaries of each particle, particularly in cases where there is nanoparticle stacking. This was the major challenge with the TEM imaging of the nanoparticles in this work, as there were many regions of interest in the images where the stacking of nanoparticles made it difficult to perform accurate size analysis. To combat this, a two-fold complementary approach was employed. Firstly, a hydrophilic TEM grid surface was prepared by exposing it to a UV/ozone treatment for 30 minutes at 25°C. This promoted an even wetting of the grid by the nanoparticle dispersions. The difference was noticeable by the eye. On the non-treated grid, a droplet of the nanoparticle dispersion would not wet the surface, whereas on the treated grid, the droplet would immediately spread. A comparison was also made between a slower and faster drying process by allowing the sample to dry at room temperature, or directly placing the grid with the sample in the oven at 50°C. There was no marked difference between the images obtained from the two drying methods. As such, it was decided to allow the grid to dry at room temperature until the liquid was no longer visible by the eye, all the while covered by a clean glass lid to protect from dust contamination, and then to complete the drying in an oven for 10 minutes at 50°C.

The second approach was to increase the number of images taken to have the highest count of nanoparticles possible for the analysis. Typically, 15-20 images per sample were taken. This however meant longer exposure time of the sample to the electron beam and also long sessions with the microscope for image acquisition. TEM suffers from statistically low sample sizing and depending on the magnification at which the imaging was performed, the number of nanoparticles that could be visualized in a single image was at most a few tens of particles. This therefore required many images to be taken to have a large enough sample size for determining the geometric mean diameter. The magnification used for the TEM images of this work varied between 10 kX and 80 kX.

The LN NPs used in this work was determined to be of a quasi-spherical geometry (further discussed

in chapter 3, section 3.2.1, page 90), and as such had two diameters (an example is shown in fig. 2.9). For simplification of the calculations however, the particles were considered to be of spherical geometry. As such, the mean diameter determined from TEM was the geometric mean of the longer diameter of the particles. It was acknowledged that as there was no control over the orientation at which the particles were deposited on the grid, we cannot say whether the longer diameter always corresponded to the same crystallographic direction. The number of particles counted for the mean diameter determination was 100 particles.

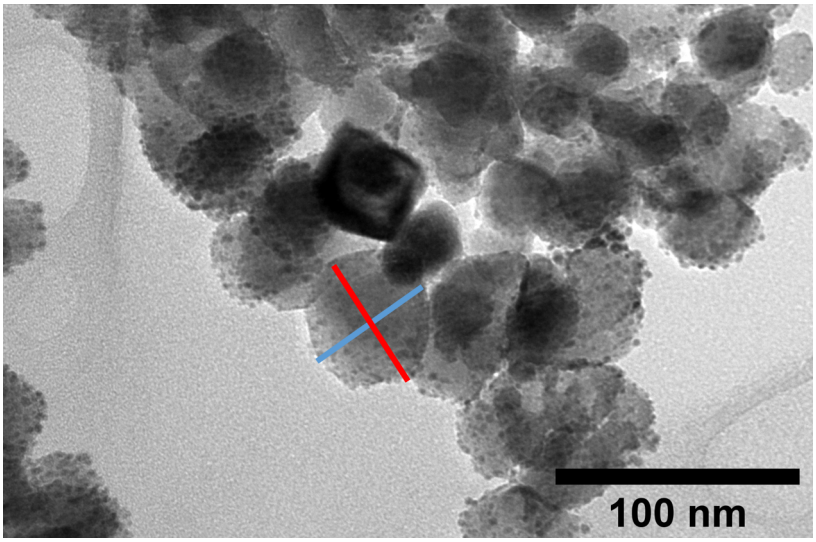


Figure 2.9: TEM image of LN@AuSeeds NPs used in this work. The quasi spherical shape of the LN is evidenced by the varied lengths of the particle. The red line is equal to 54.8 nm whereas the blue line is equal to 50.2 nm.

The DLS determination of the nanoparticle size relies on the Brownian motion of the nanoparticles in the aqueous media (already detailed in section 2.1.4). The size results obtained from light scattering techniques are the hydrodynamic sizes of the particles, which corresponds to the particle, plus the Stern layer and a portion of the diffuse layer that moves with the particle (see figure 2.7). As it was stated, the equations used to calculate the particle size assumes perfect spherical geometry of the nanoparticles. Though the LN in this work was determined to be of a quasi-spherical geometry, we made no adjustments to the calculation to reflect this, working with the assumption that the deviation in size due to the particle shape was negligible (the degree of sphericity was determined to be 0.8, detailed in chapter 3, section 3.2.1). We acknowledge that there should be some modifications to account for the true geometry of the particles. However, as the sizing data received from the DLS analysis was used to qualitatively identify particle growth from one step of the synthesis to the next and as an indication of aggregation in the nanoparticle dispersions, the absolute number value of the diameter was of lesser importance, and we were more interested in

the difference in the number value moving from one step in the synthesis to the other.

### 2.2.2 Comparison of techniques used to determine surface properties of nanoparticles

The chemical and physical properties of the surface was important to characterize for the nanoparticles in this work. As was shown in table 2.1, there were 5 techniques used to obtain data on the surface of these nanoparticles. We will first discuss the techniques that provided information on the physical nature of the nanoparticles.

As we moved from LN to LN@BPEI@AuSeeds to LN@Au nanoparticles, due to the plasmonic properties of nanoscale gold, it was expected that the optical properties of the nanoparticles in the UV-visible region would evolve. Indeed, monitoring the UV-visible spectra of these different nanoparticle categories, allowed us to infer whether the LN nanoparticles were coated in gold. When the amount of gold on the LN surface increased, this was also reflected by the UV-visible spectra. In fig. 2.10, an example of the UV-visible spectra for different nanoparticle dispersions is given. TEM imaging provided the complementary physical characterization of the morphology of the nanoparticles. An example of this is shown in fig. 2.11 where LN@Au nanoparticles where the Au coating can be described as a raspberry shell, a smooth shell and a mix between the raspberry and smooth. In chapter 4 we will go into more details about what can be infered about the nanoparticle structure from the the UV-Visible spectrum shape.

The surface chemical properties of the nanoparticles is firstly qualitatively assessed by the zeta potential analysis. The positive or negative value of the zeta potential was used as an indicator of the surface charge. For example, the bare LN, which is an oxide nanoparticle, had a negative zeta potential when dispersed in water. When the nanoparticles were coated with a cationic polymer, branched polyethylenimine (BPEI), the zeta potential reflected this by becoming positively charged. This however was not able to tell us which chemical species on the surface were responsible for the positive or negative zeta potential values. To obtain this information, XPS and TOF-SIMS analysis was used. Indeed, the XPS and TOF-SIMS analysis provide similar information on the surface nature of the nanoparticles and were used in a corroborative manner in this work. XPS also allowed for semi-quantitative determination of the amount of given species on the surface of the nanoparticles, and was used to determine the amount of polymer molecules coated onto each nanoparticle (detailed in chapter 3). The combined results of these analytical techniques provided a full comprehension of the surface properties of these nanoparticles, useful for predicting their future applications.

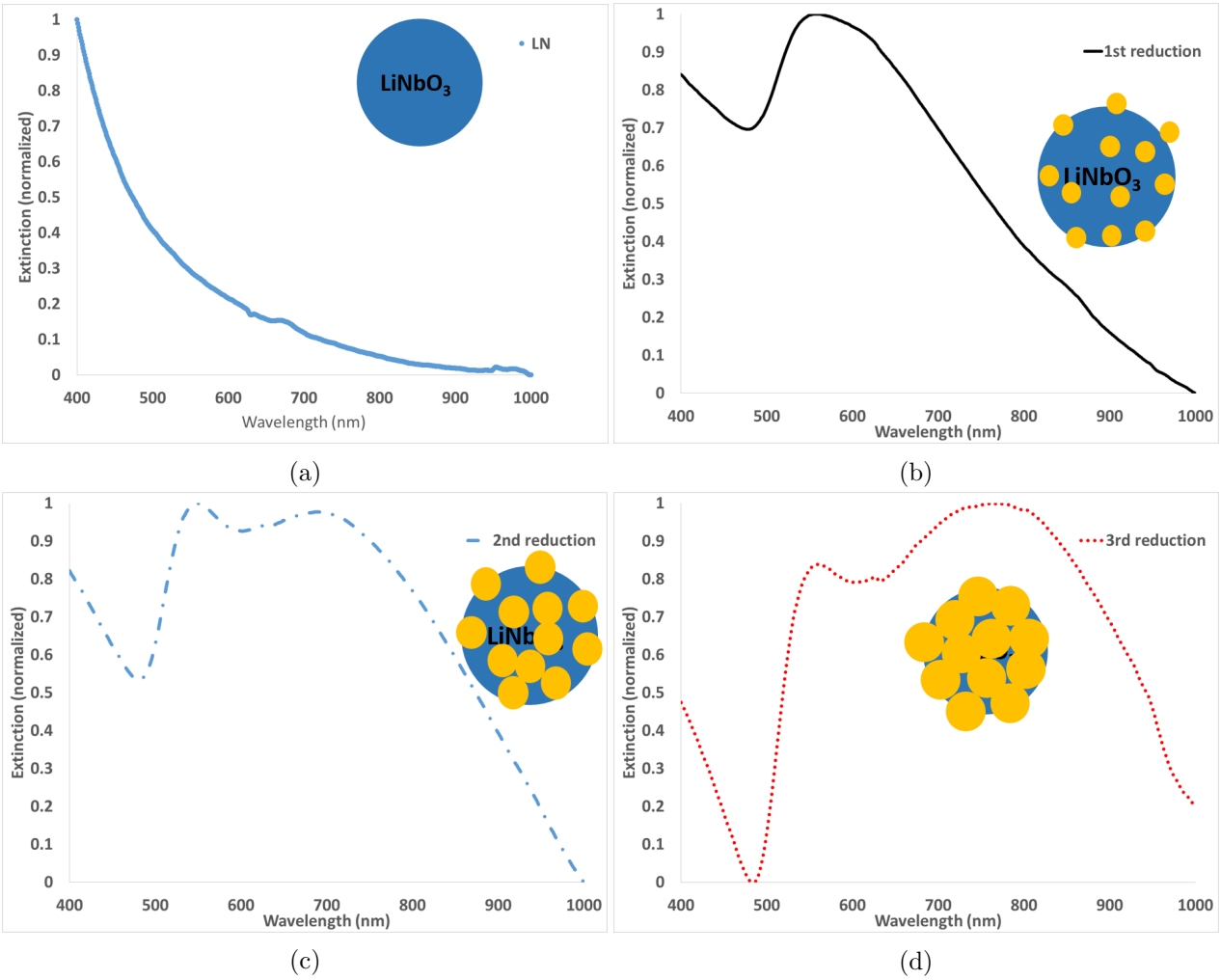


Figure 2.10: UV-visible spectra of LN and LN@Au dispersions. Inset images are a representation of the nanoparticles present in the dispersions corresponding to the UV-visible spectra. (a) LN, (b) LN@Au formed after one reduction of $HAuCl_4$, (c) LN@Au formed after two reductions of $HAuCl_4$ and (d) LN@Au formed after three reductions of $HAuCl_4$.

### 2.2.3 Comparison of techniques used to determine LN and nanohybrid concentrations

Upon the synthesis of the LN nanoparticles, the powder is weighed and then dispersed in water. In this manner, we obtain the mass concentration of the nanoparticle dispersion. UV-visible analysis was then used at this point to have a concentration calibration curve for LN, by performing a series of dilutions and recording the spectra which are shown in fig. 2.12. Using the LN diameter as determined from XRD analysis, we could easily convert the mass concentration to a nanoparticle per mL concentration (calculation detailed in section 2.2.4). When the LN were transformed to hybrid nanoparticles containing gold, this changed the optical response and as such, the calibration curve was no longer used for determining the concentration of the nanoparticle dispersion. Additionally, we

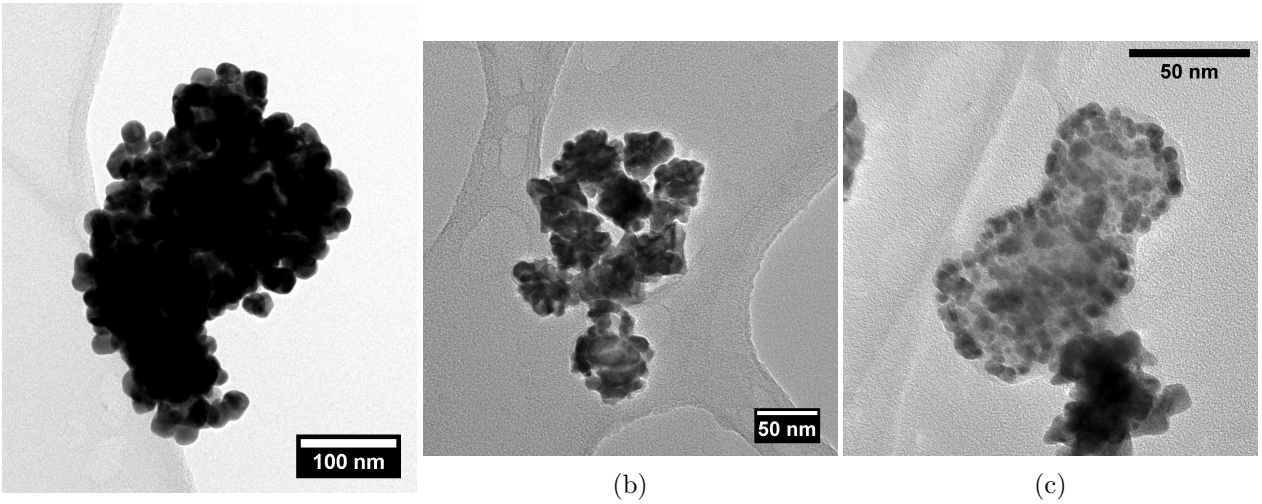


(a) (b) (c)

Figure 2.11: TEM images showing the varied gold shell morphology on LN NPs. (a) Raspberry gold shell, (b) continuous smooth shell and (c) mixed shell.

wanted to know the concentration of gold per nanoparticle in the LN@BPEI@AuSeeds dispersions, so to do this, we used two techniques, TEM imaging and ICP-AES analysis, which we will now discuss.

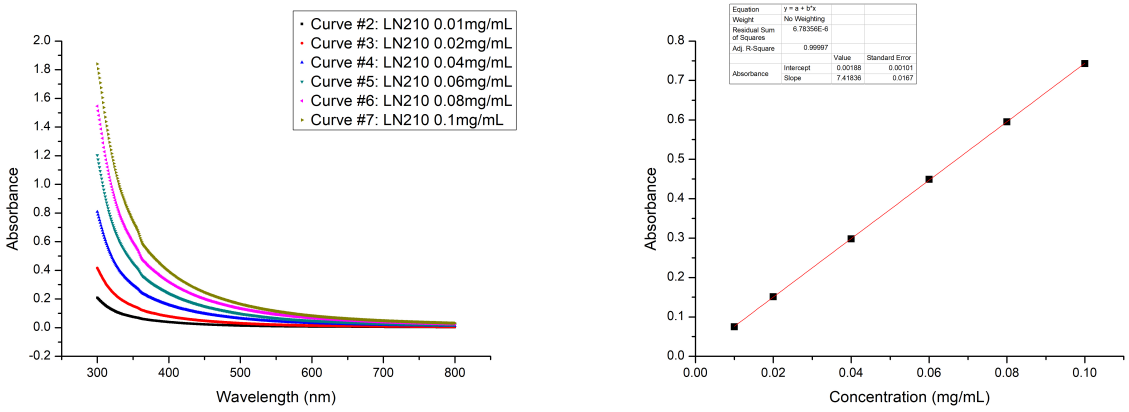


(a) (b)

Figure 2.12: (a) UV-visible spectra and (b) corresponding concentration calibration curve for LN. The extinction value at 350 nm was used to plot the concentration calibration curve.

The first method was to use the TEM images of these LN@BPEI@AuSeeds nanoparticles and, using the ImageJ software, physically count the number of AuSeeds seen attached. There are a number of assumptions that were made. First assumption was that the face of the nanoparticles visualized in the TEM image is a complete hemisphere of the nanoparticles. Based on this assumption, if we count all the AuSeeds we see on a single nanoparticle and multiply it by two, we obtain the number

of AuSeeds attached to the entire nanoparticle. This required the additional assumption that the distribution of AuSeeds on each hemisphere of the nanoparticle is equivalent. We again encountered the same statistical limitations previously discussed with respect to the use of TEM images to perform size analysis. Another challenge unique to the TEM imaging of the LN@BPEI@AuSeeds nanohybrids, is the blurring of the seeds at the boundaries of the nanoparticles. From the mean number of AuSeeds per LN, we could then determine the percentage of the LN surface covered by the AuSeeds. Using this method, we are more prone to underestimating the true mean of AuSeeds on the LN (which was observed in the results that will be discussed in chapter 3). However, the advantage of this technique was to have directly a number of AuSeeds per nanoparticle.

The second approach to determine the concentration of AuSeeds on the LN was by ICP-AES analysis. ICP-AES provided the absolute concentrations of each element (Au and Nb) in the sample in parts per million. We then converted the concentrations to mol/L and, using the stoichiometric ratio of the molecular formula of $LiNbO_3$, we could calculate the mass of $LiNbO_3$ which is present in the sample. Then using the average diameter of LN as determined by XRD analysis, assuming spherical geometry, and with the density and molar mass of $LiNbO_3$, we could calculate the concentration of LN nanoparticles in NPs/mL (calculations precised in section 2.2.4). In also having the same data for gold (the diameter of the AuSeeds, the density of Au and molar mass), we could also calculate the number of AuSeeds in the sample. Assuming a homogenous distribution of the AuSeeds to the LN, we could determine the number of AuSeeds per LN, and similarly as with the TEM approach, the percentage of the LN surface covered by the AuSeeds.

### 2.2.4 Calculations for the determination of particle concentrations and the percentages of LN surface covered by AuSeeds

Here we present the step-by-step calculations for converting from mass concentrations to concentration in NPs/mL as well as the calculations to determine the number of AuSeeds attached per LN using ICP-AES analysis and the calculation to determine the percentage of the LN surface covered by the AuSeeds. This provides the necessary context for the conclusions that will be drawn in the subsequent chapters 3 and 4 of this work.

In table 2.2 the density, molar mass, and diameters of the $LiNbO_3$ and AuSeeds nanoparticles are provided.

Assuming spherical geometry of the nanoparticles the following equations are applied:

$$Volume\ of\ a\ sphere = \frac{4}{3}\pi r^3 \tag{2.9}$$

| | Density ($g\,cm^{-3}$) | Molar mass (g/mol) | NP Diameter (nm) |
|---|---|---|---|
| $LiNbO_3$ | 4.65 | 147.86 | 45 |
| Au | 19.3 | 196.97 | 2.5 |

Table 2.2: Density and molar mass of $LiNbO_3$ and Au and the nanoparticle diameters of LN and AuSeeds.

$$Mass\ of\ 1\ NP = Density\ \times\ Volume \tag{2.10}$$

$$Number\ of\ NPs = \frac{Total\ mass\ of\ NPs}{Mass\ of\ 1\ NP} \tag{2.11}$$

With the above data, it is possible to convert any mass concentration of LN and AuSeeds to a concentration in nanoparticles per mL.

Then, once the concentrations are converted to NPs/mL, the percentage of the $LiNbO_3$ NPs surface covered by the AuSeeds was calculated using the equations below.

$$Surface\ area\ of\ a\ sphere = 4\pi r^2 \tag{2.12}$$

$$Area\ of\ a\ circle = \pi r^2 \tag{2.13}$$

$$\%\ LiNbO_3\ NPs\ surface\ covered = \frac{\#AuSeeds \times\ area\ of\ 2.5nm\ circle}{Surface\ area\ of\ a\ 45nm\ sphere} \times 100 \tag{2.14}$$

## 2.3 Conclusion

The complete characterization of nanoparticles requires one to be able to use and interpret multiple techniques. Use of the techniques discussed in this chapter allows one to obtain both a physical and chemical characterization of the nanoparticles. We have demonstrated a clear acknowledgment of the drawbacks and challenges associated to the various techniques and shown how we use the techniques in either a complementary or corroboratory manner to draw conclusions on the nanoparticle dispersions.

# Chapter 3

# Gold Seed Attachment to $LiNbO_3$ Nanoparticles

The aim of this chapter is to present the work on gold seeds (AuSeeds) attachment to the $LiNbO_3$ core nanoparticle. After the review of the literature, it was concluded that a seeded-growth method was the best suited synthesis route for core-shell gold nanohybrids as it relies on providing fixed nucleation sites for gold atoms to coalesce and grow on the surface of the core particles (discussed in section 1.7). In this chapter, we will detail the synthesis procedure for attaching small spherical gold nanoparticles (AuSeeds) onto the $LiNbO_3$ core, to serve as the template for gold shell growth which will be discussed in chapter 4. Two methods of AuSeeds attachment will be presented (the general scheme of both methods is depicted in fig. 3.1). Aside from the AuSeeds attachment, we will also discuss the attempts to control the density of gold seeds on the $LiNbO_3$ surface detailing the characterization of the nanoparticles at each step of the synthesis protocol as well as the non-linear optical properties, determined by Hyper Rayleigh Scattering spectroscopy.

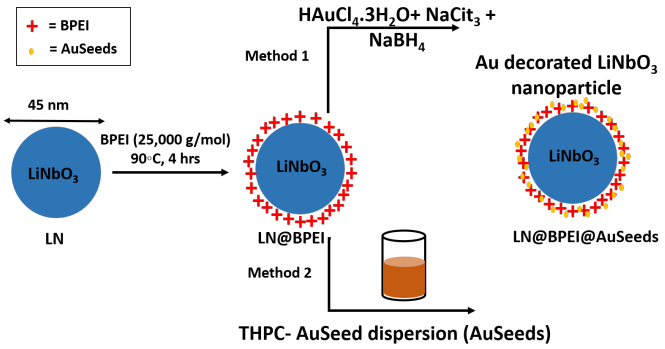


Figure 3.1: Scheme of protocol for preparation of Au-decorated $LiNbO_3$ nanoparticles (LN@BPEI@AuSeeds).

## 3.1 Materials and methods of synthesis

The following materials were used for the synthesis procedures detailed below. Lithium niobium ethoxide ($LiNb(OEt)_6$), (99+% metal basis, 5% w/v in ethanol) was obtained from Alfa Aesar, Teflon cup model number 4749 was obtained from Parr Instrument, and Nalgene centrifugation tubes were obtained from ThermoFisher. Butane-1,4-diol (99%), ethanol, sodium hydroxide (NaOH) pellets, tetrakis(hydroxymethyl)phosphonium chloride (THPC) solution (80% w/v in water), polyethylenimine branched (BPEI), ~25,000 g/mol, gold (III) chloride trihydrate ($HAuCl_4.3H_2O$, ≥99.9%, trace metal basis), sodium citrate ($Na_3Cit$), fluorescamine and sodium borohydride ($NaBH_4$) were all obtained from Sigma Aldrich. A 0.05 M sodium borate buffer solution at pH 9 was prepared. The $HAuCl_4$ was dissolved in deionized water to give a concentration of 313 mM, stored in a dark bottle and kept in the dark until needed. Unless otherwise stated, any water used was deionized water (18.2 MΩ.cm).

### 3.1.1 Synthesis of $LiNbO_3$ NPs

The $LiNbO_3$ NPs (LN) were synthesized by a solvothermal process at the SYMME laboratory in Annecy. Inside an autoclave equipped with a 23 mL Teflon cup, 2.25 mL lithium niobium ethoxide, 1.25 mL butane-1,4-diol and 25 $\mu$L distilled water were added. The mixture was then heated in an oven (Memmert) increasing the temperature by 5°C intervals every ten minutes until the temperature of 235°C was attained, and this temperature was maintained for three days. After cooling to room temperature, the precipitate was transferred to Nalgene centrifuge tubes. Three centrifugation rounds at 13500 rpm for three minutes were carried out to collect the powder which was washed with ethanol and ultrasonicated for ten minutes. The final $LiNbO_3$ NPs were dried at 75°C. The $LiNbO_3$ NPs were dispersed in deionized water to give a concentration of 1 mg/mL. The protocol for TEM imaging outlined in section 2.1.1 on page 66 was used to image the resulting nanoparticles. The zeta potential and hydrodynamic diameter were determined using a zetasizer by Malvern Instruments, protocol detailed in sections 2.1.4 and 2.1.5.

### 3.1.2 BPEI adsorption on $LiNbO_3$ NPs (LN@BPEI)

BPEI polymer was used to coat the $LiNbO_3$ NPs. Firstly, approximately 5 mg of BPEI was weighed into a glass reactor vessel and dissolved in 5 mL of deionized water while heating at 90°C. The temperature was maintained at 90°C with continuous stirring and 0.5 mL of the 1 mg/mL $LiNbO_3$ NPs dispersion was added to the reactor and left for 4 hours. The mixture was allowed to cool to room temperature and then the resulting BPEI coated $LiNbO_3$ NPs (LN@BPEI) were separated from any BPEI excess by performing six, 10 minutes centrifugation washing steps at 10°C and 9103g.

The NPs were re-dispersed in deionized water to give a final concentration of ∼0.35 mg/mL, and the zeta potential value and hydrodynamic diameter were determined using a zetasizer by Malvern Instruments, protocol detailed in sections 2.1.4 and 2.1.5.

### 3.1.3 Preparation of Au-decorated LN nanoparticles (LN@BPEI@AuSeeds)

#### 3.1.3.1 Direct reduction of $HAuCl_4$ onto LN@BPEI

Two methods for preparing LN@BPEI@AuSeeds were attempted. The first method is an *in-situ* preparation of AuNPs in the presence of LN@BPEI and the subsequent attachment of the AuNPs to the LN@BPEI surface. The protocol is as follows. A 20 mL solution of 30 mM $HAuCl_4$ was prepared and kept in a falcon tube and out of direct light. A 5 mL solution of 0.17 M $Na_3Cit$ was also separately prepared. Then 1 mL of the 0.35 mg/mL LN@BPEI NPs was added to 19.7 mL of the $HAuCl_4$ solution. The mixture was placed in an ice-bath and the temperature was controlled at 4°C. While stirring and still in the ice bath, 0.12 mL of the $Na_3Cit$ solution was added, followed by 1.18 mL of a freshly prepared $NaBH_4$ and the reagents were allowed to react for 6 minutes. Finally, the mixture was subjected to centrifugation for 10 minutes at 20°C and 9103g. The supernatant was removed and the Au-decorated LN nanoparticles, LN@BPEI@AuSeeds, formed were re-dispersed in 1 mL of water. The protocol for TEM imaging outlined in section 2.1.1 on page 66 was used to image the resulting NPs, and the zeta potential value and hydrodynamic diameter were determined using a zetasizer by Malvern Instruments, protocol detailed in sections 2.1.4 and 2.1.5.

#### 3.1.3.2 Attachment of preformed AuSeeds onto LN@BPEI

The second method for preparing LN@BPEI@AuSeeds was a two-step process. Firstly, gold seeds (AuSeeds) were synthesized using the protocol reported by Duff *et al.*[164] In brief, 540 $\mu$L of 0.1 M NaOH was added to 45.5 $\mu$L of deionized water followed by 2.14 $\mu$L of a 4.2 mM solution of THPC. While stirring, 360 $\mu$L of 25 mM $HAuCl_4$ solution was added to the mixture and the stirring was continued for ten minutes, with the mixture undergoing a colour change from colourless to brown-red in under 30 seconds. The protocol for TEM imaging outlined in section 2.1.1 on page 66 was used to image the resulting AuSeeds. The AuSeeds dispersion was stored at 4°C and used for further procedures up to two months post synthesis. The AuSeeds dispersion's concentration was calculated based on the concentration of gold determined by ICP-AES analysis (refer to sections 2.1.7 and 2.2.4) and the AuSeed volume as determined by TEM evaluation of their diameter.

To attach the AuSeeds to LN@BPEI, we tested the following theoretical ratios of AuSeeds to LN nanoparticles, 100:1, 300:1, 700:1, 1000:1, 2000:1 and 3000:1. To do so, a series of dilutions

of the AuSeeds dispersion with water was completed (given in table 3.1), with a final volume of 10.588 mL in each case, and placed in a 50 mL falcon tube. Then, while under stirring, 1 mL of LN@BPEI (∼0.35 mg/mL or $1.58 \times 10^{12}$ NPs/mL) NPs were added to the AuSeeds dispersions and allowed to mix for 30 minutes. The nanoparticle dispersion was then kept for 24 hours at 4°C, after which, two 10 minutes rounds of centrifugation at 10°C and 9103 g were done to remove the unattached AuSeeds. The resulting nanoparticles, LN@BPEI@AuSeeds, were redispersed in 1 mL of deionized water to obtain again a final concentration of ∼0.35 mg/mL. The protocol for TEM imaging outlined in section 2.1.1 on page 66 was used to image the resulting LN@BPEI@AuSeeds NPs. The zeta potential value and hydrodynamic diameter were determined using a zetasizer by Malvern Instruments, protocol detailed in sections 2.1.4 and 2.1.5.

| Sample Name | Volume of AuSeeds (mL) | Volume of $H_2O$ (ml) | Final AuSeeds Concentration (NPs/ml) | Theoretical ratio (AuSeeds:LN) |
|---|---|---|---|---|
| LN@BPEI@AuSeeds100 | 0.349 | 10.239 | $6.98 \times 10^{12}$ | 100 |
| LN@BPEI@AuSeeds300 | 1.046 | 9.542 | $2.09 \times 10^{13}$ | 300 |
| LN@BPEI@AuSeeds700 | 2.441 | 8.147 | $4.88 \times 10^{13}$ | 700 |
| LN@BPEI@AuSeeds1000 | 3.486 | 7.102 | $6.97 \times 10^{13}$ | 1000 |
| LN@BPEI@AuSeeds2000 | 6.973 | 3.615 | $1.39 \times 10^{14}$ | 2000 |
| LN@BPEI@AuSeeds3000 | 10.459 | 0.129 | $2.09 \times 10^{14}$ | 3000 |

Table 3.1: Table showing the volumes and final concentrations of the AuSeeds dispersions used for varying the density of AuSeeds attached to the LN@BPEI surface. The stock AuSeeds dispersion had a concentration of $2.32 \times 10^{14}$ NPs/mL. For each sample, 1 mL of $1.58 \times 10^{12}$ NPs/mL of LN@BPEI was used.

### 3.1.4 Fluorescence spectroscopy for BPEI concentration determination

Standard BPEI solutions of concentration 0.1, 0.5, 0.25, 0.1 and 0.05 mg/mL were prepared in water. For each BPEI solution separately, 100 $\mu$L of the BPEI solution was added to 2.9 mL of 0.05 M sodium borate buffer solution at pH 9. 1 mL of 0.3 mg/mL fluorescamine in acetone solution was added to the buffered BPEI solution and the mixture was allowed to react for 12 hours in the dark. Finally, fluorescence measurements of the solutions were realized using a FLS920 Edinburgh Photonics spectrofluorometer. The fluorescence intensities at the emission maximum of 472 nm (excitation at 388 nm) were extracted from the data and used to plot a concentration calibration curve for BPEI. Then 100 $\mu$L of the supernatant after each of the 6 washing steps of the BPEI polymer adsorption procedure (detailed in section 3.1.2) was added to 2.9 mL of 0.05 M sodium borate buffer solution at pH 9. Finally, 1 mL of 0.3 mg/mL fluorescamine in acetone solution was added and the mixture was allowed to react for 12 hours in the dark and fluorescence measurements

were performed to determine the concentration of BPEI using the calibration curve.

### 3.1.5 Hyper Rayleigh Scattering measurements of nanoparticle dispersions

The SHG properties of $LiNbO_3$ NPs as well as LN@BPEI@AuSeed NPs were evaluated at laboratory Institute Lumiere Matiere (ILM), Lyon, using a Hyper Rayleigh scattering (HRS) experimental set-up as shown in fig. 3.2. A femtosecond pulsed laser, wavelength 800 nm, with a repetition rate of 80 MHz pulses for 140 femtoseconds was used. The laser beam was polarized using a half-wave plate and focused onto the sample with the use of a 10X microscope objective lens. In a $0.5 \times 0.5$ $cm^2$ quartz cell, 1 mL of the sample was placed and the harmonic light produced was collected at a 90° angle, passing through the analyzer. A photomultiplier tube working in the photon counting regime was used to record the photons of light and was placed after a spectrometer for wavelength selection.

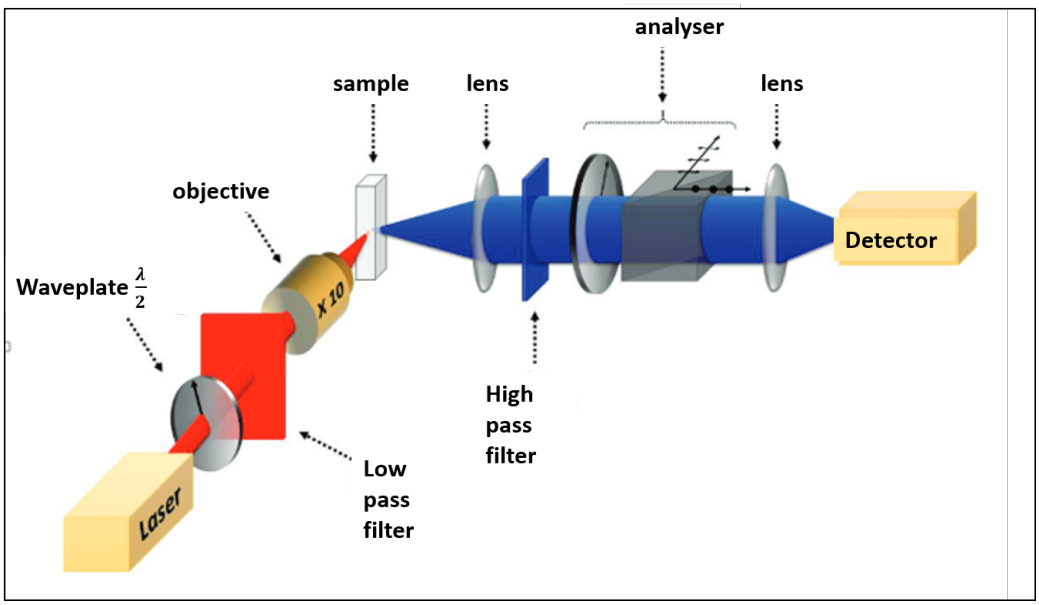


Figure 3.2: Illustration of a general set-up of a Hyper Rayleigh Scattering experiment for obtaining the first hyperpolarizability.

## 3.2 Results & Discussions

### 3.2.1 Synthesis and characterization of $LiNbO_3$ nanoparticles

The LN used in this work were defined by five characteristics: their crystalline phase, average diameter, size distribution, morphology and extent of aggregation. The synthesis as well as the

X-ray diffraction (XRD) characterization were completed by the research group in the SYMME laboratory, Annecy France. In the thesis manuscript of Mathias Urbain, 2020, it was shown that in the synthesis of LN, varying the ratios of the precursor, lithium niobium ethoxide, to the co-solvent, butane-1,4-diol, as well as changing the co-solvent, resulted in marked variations in the five aforementioned properties of the final nanoparticles. Under the given synthesis conditions reported in this work (section 3.1.1), the LN formed were of monocrystalline trigonal structure, determined by their XRD analysis (fig. 3.3). We recall that the width of the XRD peaks of a crystalline material is characteristic of its crystalline size. As these are monocrystalline particles, the average LN diameter was calculated by the Scherrer formula (eq. 3.1) which uses the full width at half maximum (FWHM) of the associated XRD peaks.

$$t_{hkl} = \frac{K \times \lambda}{l \times cos\ \theta} \tag{3.1}$$

where $t$ is the mean size of the ordered crystal domain, $h,k,l$ are the Miller indices that define each family of crystal planes, $K$ is a dimensionless constant called the Scherrer constant, and is equal to 0.9, $\lambda$ is the wavelength of the incident X-rays, $l$ is the FWHM of the diffraction peak, and $\theta$ is the Bragg angle also known as the half-angle of diffraction. LN NP diameter of 45 nm was determined using the value of Scherrer diameter along [110] crystallographic direction, which corresponds to the direction along which the maximum Scherrer diameter value is obtained.

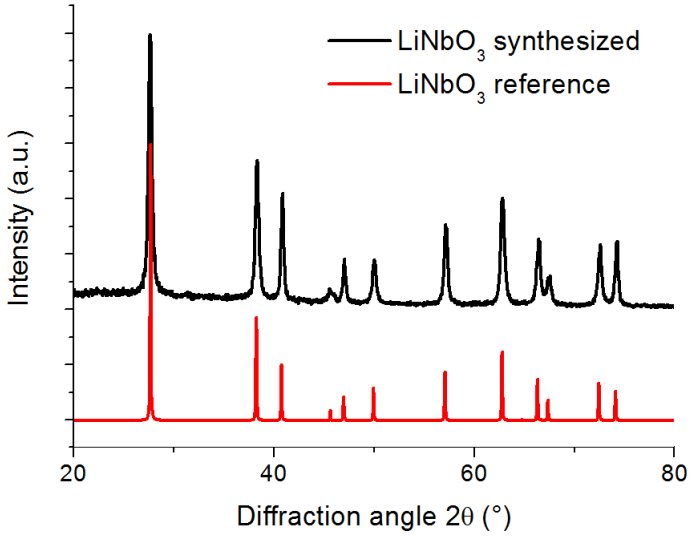


Figure 3.3: X-ray diffractogram of $LiNbO_3$ (LN) obtained under the given synthesis protocol detailed in section 3.1.1. Diffractogram retrieved from thesis of Mathias Urbain, 2020. $LiNbO_3$ reference diffractogram taken from ICSD pattern #80628 for $LiNbO_3$ bulk crystal of stoichiometric composition.[200]

Along with the XRD analysis, TEM analysis was also used to determine the average diameter of the

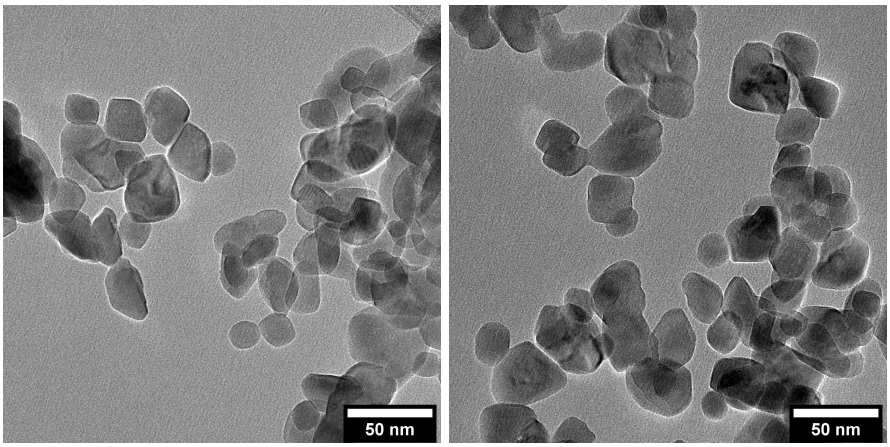


Figure 3.4: TEM images of LN used in this work, synthesis protocol detailed in 3.1.1, showing the pseudo-spherical morphology of LN.

particles. Using a sample size of 300 nanoparticles, the ImageJ software was used and the average diameter of LN was determined to be 34 ± 12 nm. It was noted from the TEM images in fig. 3.4, the presence of larger and smaller LN nanoparticles. The TEM images allowed us to define the morphology of the nanoparticles. In all the nanoparticles sampled by TEM, we observed a major and minor diameter, which was measured using the ImageJ software. By measuring these two diameters, we were able to determine the degree of sphericity, $r$, by calculating the ratio between the major and minor diameters $minor\ diameter/major\ diameter$ for each particle. The average $r$ value for LN is 0.8, and as such we have described these particles as having a pseudo-spherical morphology. As the nanoparticles are deposited in random orientations on the TEM grid, and the nanoparticles are pseudo-spherical, when measuring the diameters from the TEM images, we do not control along which crystallographic direction the measurement is taken. However, using the XRD data, we chose to use the diameter corresponding to the [110] direction, which gave the largest diameters. As such, the diameter reported by XRD is larger than that obtained from TEM analysis. Additionally, the TEM size determination is limited by the relatively small sample size where as the XRD determination takes into account all of the particles used for the analysis. It was therefore decided that throughout this work, the LN diameter determined by XRD analysis would be used.

The hydrodynamic diameter of LN nanoparticles, as determined by the Malvern Zetasizer (ZS) was 135 ± 15.7 nm. This reported value is the average of the three measurements consisting of 30 runs. The hydrodynamic diameter is significantly greater than both the average diameters determined by XRD and TEM analysis as it considers the entire solvation sphere consisting of the ions in the Stern layer and diffuse layer around the nanoparticles as opposed to XRD and TEM that only consider the boundaries of the crystal nanoparticles. The hydrodynamic diameter however is important as it has been used in a qualitative manner to indicate the aggregation dynamics of the nanoparti-

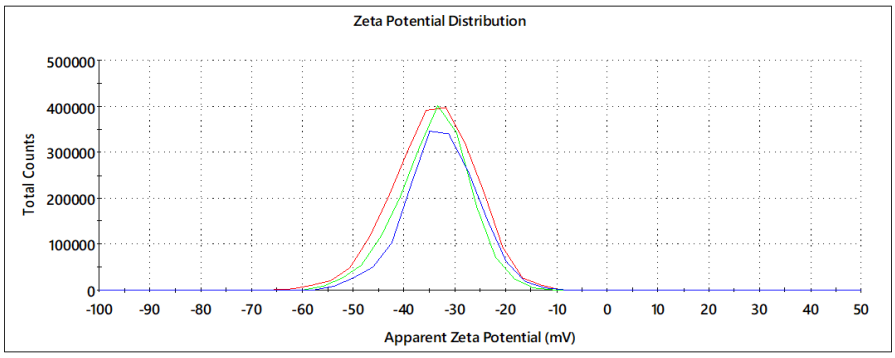


Figure 3.5: Zeta potential graph for LN, synthesis protocol detailed in section 3.1.1, dispersed in water. Three measurements were taken, each measurement consisting of 30 runs.

cle dispersions. Typically throughout this work, when the hydrodynamic diameter measured was greater than 300 nm, it was an indication of particle aggregation. The Malvern Zetasizer (ZS) also determined the zeta potential of the LN dispersions to be on average -43.2 ± 3.6 mV, leading to a high stability of the nanoparticles dispersed in aqueous media (fig. 3.5). The negative zeta potential is attributed to the Li-O surface groups.

### 3.2.2 BPEI polymer surface modification of $LiNbO_3$ NPs

In order to attach the AuSeeds to LN, LN had to undergo surface modifications. In the published works of authors Westcott *et. al*,[201] they investigated the influence of three coating materials on spherical silica nanoparticles and how it impacted the ability of gold nanoparticles to attach to the core nanoparticle. The three materials investigated were (3-Aminopropyl)trimethoxysilane (APTMS), 2-(diphenylphosphino)ethyltriethoxysilane (DPPETES), and 3-mercaptopropyl-trimethoxysilane (MPTMS), whose surface groups are amino, phosphine and thiol respectively. Their results showed that both the amino and thiol groups facilitated the gold nanoparticle attachment to the core particle. In addition to this study, different methods of surface modification of $LiNbO_3$ nanoparticles were tested in our laboratory during the master internship of Eloïse Millet (2017): two silanization methods using (3-Aminopropyl)triethoxysilane (APTES) in aqueous and organic media respectively, adsorption of polyelectrolytes poly-L-lysine (PLL) and BPEI (fig. 3.6), and lastly adsorption of $Sn^{2+}$ ions to favour the reduction of Au at the surface of LN nanoparticles. The effectiveness of each method to reverse the negative surface charge of the LN nanoparticles was determined by zeta potential measurements, and it was concluded from this work that the BPEI was best adapted to reversing the surface charge of the LN nanoparticles. In addition to this, PEI and its variants are already widely used in biology. The high cationic charge make them suitable for complexation with nucleic acids,[202] its pH buffering nature supports gene and drug delivery[203] and the high reactivity of the amino groups ensures a wide range of possible chemical modifications.[204]

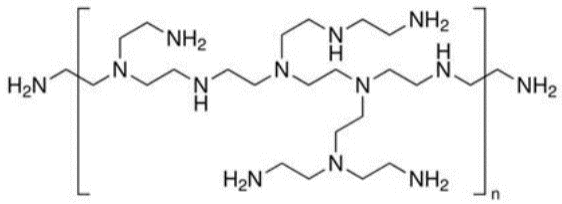

Figure 3.6: Molecular formula of branched polyethylenimine (BPEI). Image retrieved from Sigma Aldrich BPEI product information website.[206]

There have been many studies on the toxicity of PEI coated nanoparticles, which have determined that PEI is a non-toxic polymer. More specifically, the study by Xia *et. al*[205] used MTS assay to determine the *in-vitro* cytotoxicity of PEI coated silica nanoparticles and what they found was a low PEI molecular weight (<8 kDa) rendered the silica nanoparticles completely non-toxic at all PEI concentrations tested, but when the molecular weight was increased to 10 and 25 kDa, there were cytotoxic effects exhibited at polymer concentrations of 50 $\mu$g/mL. When they performed *in-vivo* toxicity analysis, all PEI molecular weights showed no signs of toxicity and as such we consider the BPEI polymer to be a safe polymer to coat our LN nanoparticles.

In addition to its already established biological uses, BPEI has been used to successfully coat metal oxide nanoparticles.[173,207] Additionally, it has been shown to facilitate the attaching of small, negatively charged, spherical gold nanoparticles to larger metal oxide nanoparticles (due to the presence of amino groups), and depending on the molecular weight (MW) of BPEI with respect to the size of the core particle, it can improve the colloidal stability of these coated NPs. In a study on the effect of the MW of BPEI polymer on the colloidal stability of 50 nm diameter, spherical, magnetite nanoparticles, it was shown that among BPEI of MW 25, 600 and 800 kDa, the 25 kDa BPEI allowed for the best colloidal dispersion, and prevention of particle aggregation.[208] As the core LN particles in this work is 45 nm in diameter, it was decided to also use the 25 kDa BPEI polymer to coat the particles.

Working with the hypothesis that the AuSeeds loading capacity of LN@BPEI would be primarily dependent on the number of protonated $NH_2$ groups present on the surface, which can be altered by changing pH of the solution, it was important to consider under which conditions the AuSeed attachment would be performed. The degree of protonation of the $NH_2$ moieties of BPEI polymer (2.5 kDa) is approximately 44% at neutral pH (pH 7.5)[209] and increases as the pH decreases. As the protonation of subsequent amine groups in the polymer chain is affected by the already protonated amine moieties, we can assume that this degree of protonation remains approximately the same for 25 kDa polymer. Balancing this with the desired further biological applications imagined for these

particles, the BPEI attachment was carried out in neutral pH conditions. The LN@BPEI NPs had an average zeta potential of +36.05 ± 2.9 mV. The average hydrodynamic diameter by intensity of LN@BPEI is 159.6 ± 34.1 nm.

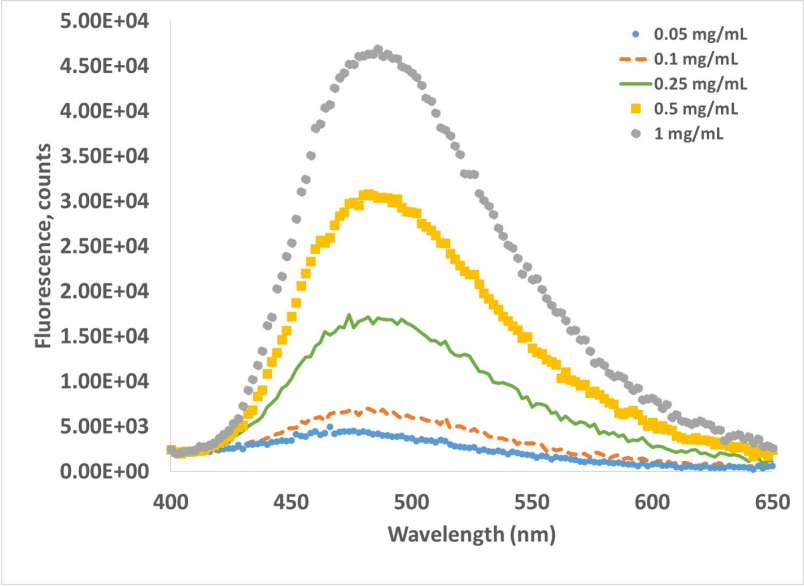


(a)

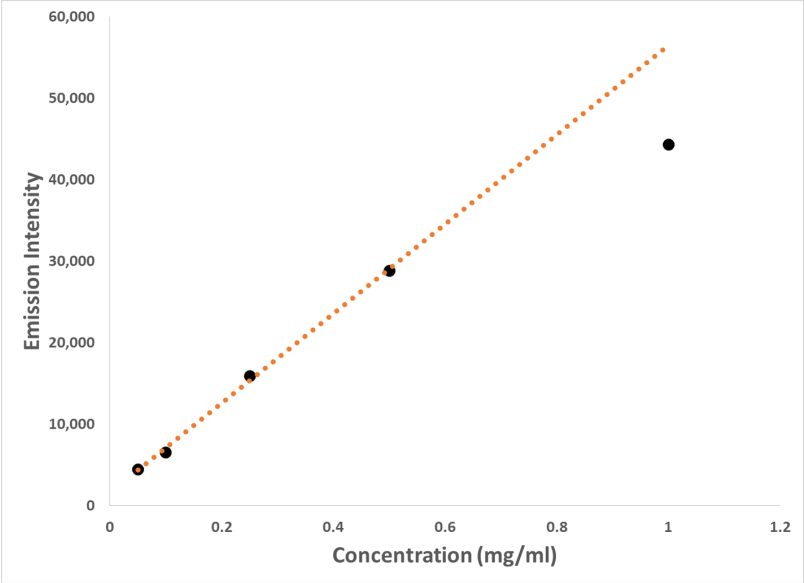


(b)

Figure 3.7: (a) Fluorescence spectra of fluorescamine bound to BPEI at different standard BPEI concentrations, excitation at 388 nm and (b) calibration plot of fluorescence intensity at 472 nm of the fluorescamine-BPEI standard solutions.

It was important to have no free BPEI in the nanoparticle dispersion so as to ensure all AuSeeds would be attached to LN and not form BPEI-AuSeed composite particles. To determine the num-

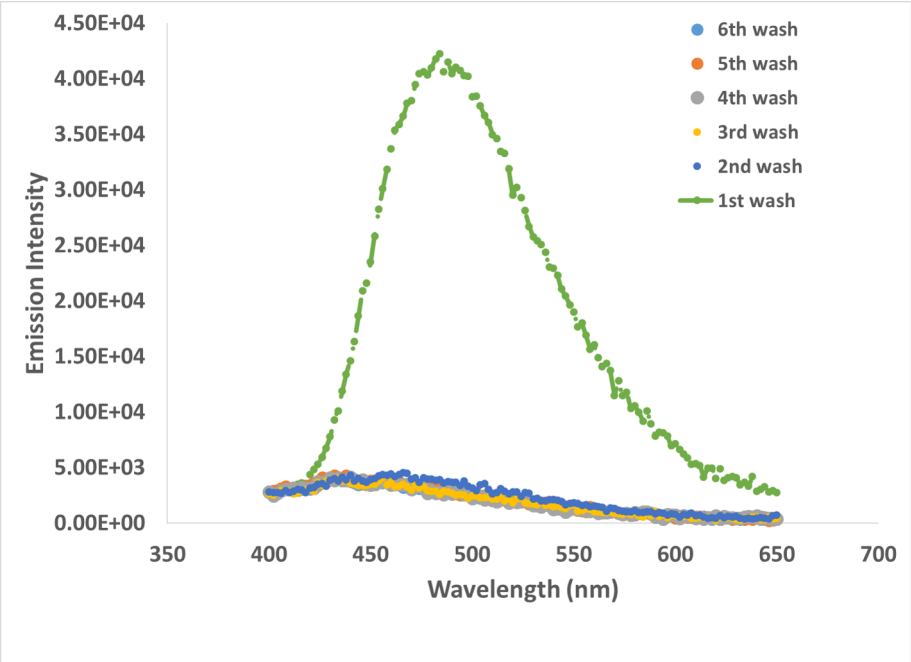


Figure 3.8: Fluorescence spectra of the BPEI present in the supernatants bound to fluorescamine collected from each washing step after the BPEI coating of LN. Excitation wavelength set at 388 nm.

ber of washing steps needed, an amine based fluorescence analysis was performed, protocol adapted from the work of Khan *et. al.*[210] Fluorescamine, a non-fluorescent compound that upon reaction with primary amines, becomes fluorescent, was reacted with standard solutions of BPEI. Both BPEI and fluorescamine on their own show no fluorescence signal. Conversely, the fluorescamine-BPEI compound has a fluorescence maximum at 472 nm upon excitation at 388 nm, and so by plotting the intensity values at 472 nm for fluorescamine bound to BPEI, the standard concentration curve was obtained (fig. 3.7). When the BPEI calibration measurements were performed, to obtain this standard concentration curve, a deviation from the linear relationship between BPEI concentration and fluorescence emission was observed for BPEI concentrations of 1 mg/mL and higher, seen in fig. 3.7, most likely due to self quenching between the fluorescamine-BPEI groups and as such this method would be inappropriate for quantifying BPEI concentrations greater than 1 mg/mL.

The fluorescence spectrum of the supernatant of each washing step after BPEI coating of LN showed a large decrease in fluorescence intensity immediately after the first wash, and by the third wash, a total suppression of the 472 nm band was observed (fig. 3.8). The supernatant from the first washing had the highest quantity of fluorescamine-BPEI and the concentration determined from its emission spectrum was 0.69 mg/mL, well below the upper limit of quantification. While this method of analysis is sensitive, as the concentration of fluorescamine-BPEI decreases, the emission spectra become noisy. By the third washing, the concentration of fluorescamine-BPEI in the su-

pernatant was found to be 0.03 mg/mL, and this value remained constant for all the subsequent washing. We must then consider that there is a lower limit of detection for the fluorescamine-BPEI concentration. However, what was evident from this analysis was that there is a significant amount of unbound BPEI present in the supernatant of the first washing step. We do not neglect to consider the possibility of LN@BPEI nanoparticles being present in the supernatant to then form LN@BPEI-fluorescamine nanoparticles, but we attempt to minimize this risk by our centrifugation protocol that causes the nanoparticles to form a pellet at the bottom of the centrifugation tube which is then redispersed by vigorous shaking and sonication. Using this fluorescence based analysis, the concentration and then mass of BPEI present in the supernatants was determined and consequently the mass of BPEI that remained was assumed to be coating the nanoparticles. From this method, we determined that approximately 1000-1600 BPEI polymer chains were attached to a single LN nanoparticle.

XPS analysis also provided a quantification of BPEI molecules on the surface of LN. The XPS spectra allowed for the determination of atomic percentages of each element present relative to all the elements identified. Furthermore, it is a surface specific technique that allows analysis of a depth of approximately 10 nm depending on the angle. Extracting the data from the spectra shown in fig. 3.9, the atomic ratio of Nb to N was obtained 5.26:3.09. Taking the XPS maximum analysis path to be 10 nm, and assuming spherical LN geometry with a diameter 45 nm, the surface area of a single NP is 6362 $nm^2$, and the volume of each $LiNbO_3$ NP analyzed by XPS was determined to be $6.36 \times 10^{-4}$ $nm^3$ using eq. 3.2.

$$volume\ of\ LN\ analyzed\ per\ particle = XPS\ analysis\ depth \times surface\ area\ of\ LN \tag{3.2}$$

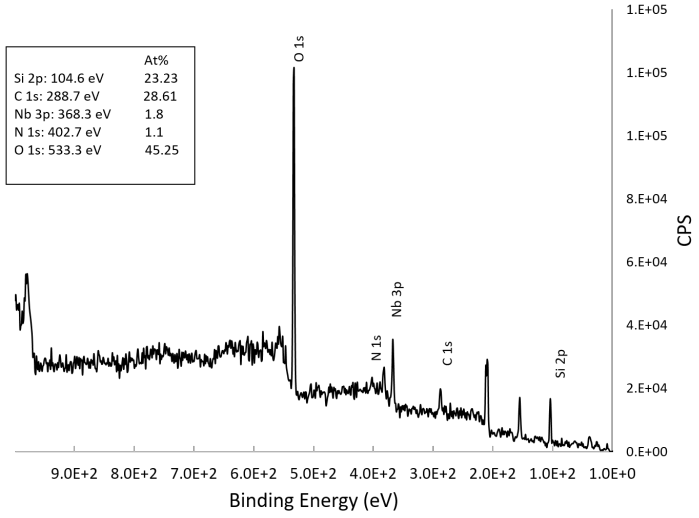


Figure 3.9: XPS spectra of the LN@BPEI NPs.

Then using the density of $LiNbO_3$ (4.65 g/cm$^3$), the mass of $LiNbO_3$ per particle that was analyzed by XPS was calculated to be $2.96 \times 10^{-16}$ g. The mass ratio of Li, Nb and O as percentages in $LiNbO_3$ compound is 5%, 63% and 32% respectively, and so using the mass of $LiNbO_3$, the mass of Nb atoms per LN particle seen by the XPS experiment was calculated to be $1.85 \times 10^{-16}$ g or 1,204,922 atoms.

The molecular structure of BPEI is shown in fig. 3.6. The molecular weight of a polymer is the summation of all the molar masses of the atoms present in one polymer chain. Therefore, starting from the MW of the BPEI, 25,000 g/mol, the number of monomer units that comprises of a single chain was calculated as shown in eq. 3.3.

$$\#\ monomer\ units = \frac{(25000 - ((2 \times molar\ mass\ NH_2) + (2 \times molar\ mass\ CH_2)}{molar\ mass\ of\ one\ repeat\ unit} = \frac{(25000 - 60)}{473} = 53 \tag{3.3}$$

From the number of monomer units per polymer chain, the number of N atoms per polymer chain could then be calculated as shown in eq. 3.4.

$$\#\ N\ atoms\ per\ polymer\ chain = (\#monomer\ units \times 11) + 2 = 585 \tag{3.4}$$

Returning to the stoichiometric ratio between Nb and N as determined by XPS, (5.26:3.09 ), and having calculated the number of Nb atoms per LN analyzed by XPS to be 1,204,922, the number of N atoms per LN was calculated to be $7.08 \times 10^5$. As the only source of N atoms is from BPEI, we can calculate the number of polymer chain molecules present on the surface of LN by dividing this value by the number of N atoms in one polymer chain. From this calculation we obtain 1210 polymer chains per LN particle, which corresponds to 23% wt of polymer to LN nanoparticle. In the work of Rosenholm *et. al*,[211] they report 18% wt of PEI polymer on their $SiO_2$ NPs, determined by thermogravimetry. The surface sensitivity of XPS analysis made it well adapted to quantifying the amount of BPEI adsorbed to the surface of the LN nanoparticles, and the results are reliable. Finally, the results from both methods of analysis, the fluorescamine based titration and XPS, are in good agreement, further validating the fluorescence determination which is a simpler, less expensive method of quantification.

### 3.2.3 Attaching AuSeeds to BPEI polymer modified $LiNbO_3$ NPs

The first method to prepare LN@BPEI@AuSeeds nanoparticles was adapted from the work of Wang *et. al*.[135] The protocol, detailed in section 3.1.3.1, page 88, uses $NaBH_4$ as the gold ions' reducing

agent as opposed to $NH_2OH.HCl$. They reported a rapid reduction of the $HAuCl_4$, with the AuNPs formed being approximately 4 nm in diameter and uniformly distributed on the surface of the aminated $SiO_2$ NPs as seen in the TEM image in fig. 3.10(a). When applied to the BPEI coated $LiNbO_3$, while there were indeed gold spheres attached to the LN@BPEI surface, it resulted in an unhomogenous decoration of AuNPs much larger than 4 nm in diameter (AuNPs ca. 18 nm in diameter) on the LN@BPEI surface as seen in fig. 3.10(b). In addition to this, the zeta potential measured for this sample was -15.5 ±0.6 mV, indicating that there may not be sufficient electrostatic repulsion to keep the particles dispersed in water. The hydrodynamic diameter determined from DLS measurements by Malvern Zetasizer was 159.6 ± 5.8 nm with a PDI value of 0.37. This value indicated to us a high degree of size inhomogeneity. As such, it was concluded that this *in-situ* gold-seeding method was not suited to the LN@BPEI nanoparticles.

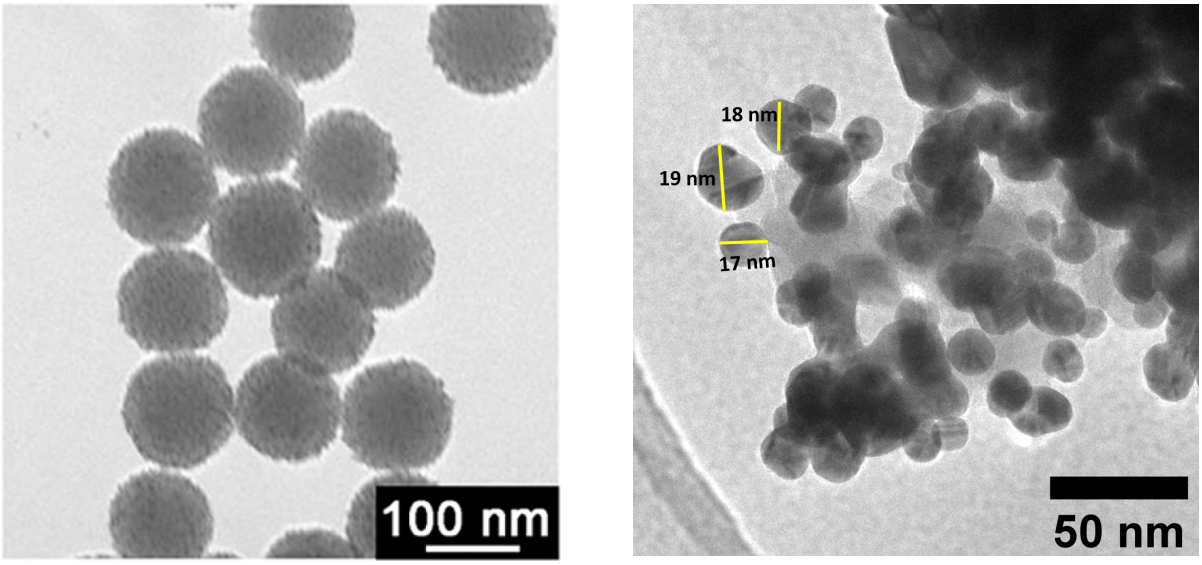


(a) (b)

Figure 3.10: TEM images of *in-situ* formation of (a) Au-decorated $SiO_2$ NPs taken from Wang *et. al*[135] and (b) Au-decorated $LiNbO_3$ NPs formed by reduction of $HAuCl_4$ by $NaBH_4$.

The second method (protocol in section 3.1.3.2, page 88) required a separate synthesis of AuSeeds and then adding them to the LN@BPEI NP dispersions to achieve the attachment. We will first discuss the AuSeeds synthesis. The method for the synthesis of the AuSeeds had been established since 1993 by Duff *et. al*[164] to produce homogenous, spherical nanoparticles, 2-3 nm in diameter. In this method, the reaction to produce the gold seeds is done at a pH of 11.1. It is accepted that the presence of the $OH^-$ ions is necessary for the neutralization reaction of the THPC to give THP, tris(hydroymethyl) phosphine and formaldehyde. The $HAuCl_4$, already dissolved in water hydrolyzes to give different $AuCl_xOH_{4-x}$ species.[212] The basic pH of the solvent causes the $Au(OH)_4^-$ to be the predominant gold ion species (fig. 3.12). When the Au salt solution is added

to the mixture of THP and formaldehyde, the THP is able to partially reduce the Au(III) to form THP-Au(I) complexes, and the formaldehyde, a known reducer, reduces these Au(I) species to form Au(0) nanoparticles. The possible reactions are shown in figure 3.11 below.[165] Due to the complexation that occurred between the THP and the gold, the phosphine groups are incorporated onto the gold nanoparticles, which we would expect to result in positively charged particles. However, our zeta potential measurements show a negative charge of -25.3 ± 8.0 mV, which is in agreement with the negative zeta potential values reported by Park *et al.*[163] This negative charge is therefore thought to be due to the continued presence of $AuCl_4^-$ ions, a hypothesis well supported by the literature.[213,214] Spherical gold nanoparticles with diameter of 2.5 nm do not have a characteristic UV-visible absorption band, and the typical spectrum for these particles was obtained (fig. 3.13 c).

Step 1: Neutralization of THPC to form THP and formaldehyde

$P(CH_2OH)_4^+ + OH^- \longrightarrow P(CH_2OH)_3 + H_2CO + H_2O$

Step 2 (a): Gold ion reduction

i) By formaldehyde

$4HAuCl_4 + 3H_2CO + 16OH^- \longrightarrow 4Au^0 + 3CO_2 + 16Cl^- + 13H_2O$

ii) By THP

$2HAuCl_4 + 3P(CH_2OH)_3 + 8OH^- \longrightarrow 2Au^0 + 3PO(CH_2OH)_3 + 8Cl^- + 5H_2O$

(b): Gold ion reduction and complexation

$HAuCl_4 + 5P(CH_2OH)_3 + 3OH^- \longrightarrow [Au(P(CH_2OH)_3)_4]^+ + PO(CH_2OH)_3 + 4Cl^- + 2H_2O$

Figure 3.11: Scheme of chemical reactions during the AuSeed formation. The first reaction is the neutralization of THPC to form THP and formaldehyde. Both compounds are further used for $Au^{3+}$ reduction to $Au^0$. The last reaction is the complexation reaction between THP and $Au^+$.

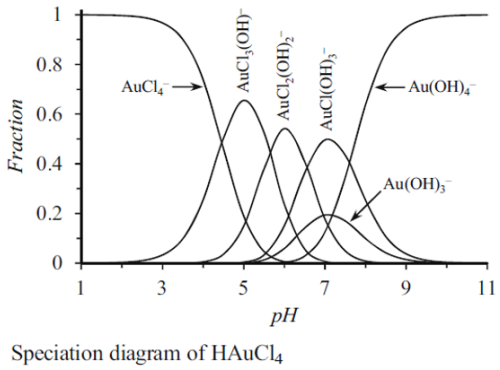


Figure 3.12: The speciation of $HAuCl_4$ with respect to pH of the aqueous medium.[165]

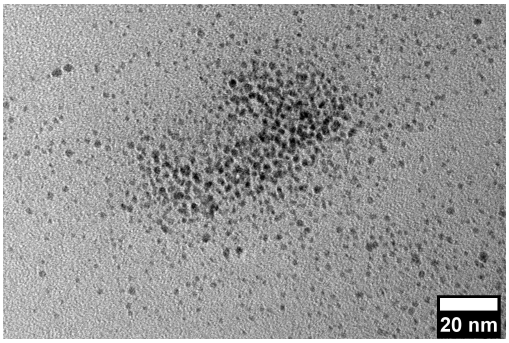


(a)

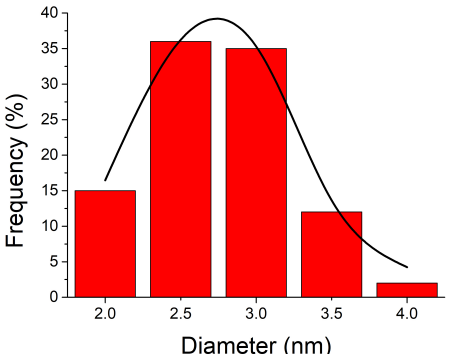


(b)

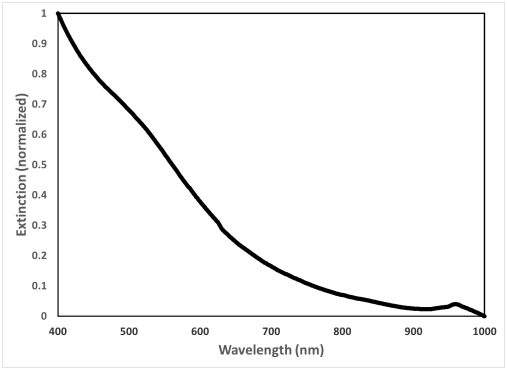


(c)

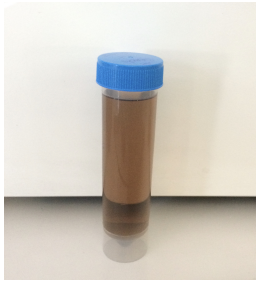

(d)

Figure 3.13: (a) TEM image of the synthesized AuSeeds representative of the sample's size and spherical shape. (b) histogram showing the distribution of the diameters of the AuSeeds. (c) The UV-visible spectrum of the AuSeeds. (d) Photo of AuSeeds dispersion.

Using the TEM images of the AuSeeds (fig. 3.13), and the ImageJ software, the geometric mean diameter of the spherical AuSeeds synthesized in this work was determined to be 2.5 ±0.5nm.With the mean diameter, and the spherical geometry, the volume of each seed was calculated to be 8.2 $nm^3$. The mass of Au in one AuSeed was also calculated using the density of Au (19.3 $g/cm^3$) to give a mass of $1.58 \times 10^{-19}$g. Assuming all the $Au^{3+}$ from the $HAuCl_4$, in the seed synthesis is reduced to $Au^0$ and consumed to form the AuSeeds, the total mass of $Au^0$ present was calculated to be $1.78 \times 10^{-3}$g. From this, the theoretically expected concentration of AuSeeds was determined to be 0.037 mg/mL or $2.32 \times 10^{14}$ NPs/mL, which is in agreement with the order of magnitude of particles reported in the literature for this synthesis. In the review article by García-Soto *et. al*,[165] the concentration in particles is reported to be between $10^{14}$ and $10^{15}$ particles per mililitre.

ICP-AES analysis determined the concentration of $Au^0$ present in the AuSeeds nanoparticle dispersion to be 0.028 mg/mL. By using the method outlined in section 2.2, using the diameter determined by TEM, the ICP-AES mass concentration was converted to concentration in NPs/mL which is $1.77 \times 10^{14}$ NPs/mL. The order of magnitude for the concentration of the AuSeeds dispersion

determined by the both methods are of the same magnitude, with the theoretical value obtained differing from the experimentally obtained value by ∼20%. ICP-AES analysis provides accurate, experimental atomic quantification. The difference between the theoretical and experimental values, can be inferred as proof that not all the $Au^{3+}$ ions in the reaction are reduced to $Au^0$. The theoretical calculation therefore provides an acceptable estimation of the true concentration of the AuSeeds.

The attachment of AuSeeds to the LN@BPEI NPs was then achieved by way of electrostatic and coordination interactions between the positive surface charge of the LN@BPEI (+36.05 ± 2.9 mV) and the negative surface charge of the AuSeeds (-25.3 ± 8.0 mV). The controlled attachment of the AuSeeds to the LN is facilitated by the primary amine groups of the BPEI, in addition to the electrostatic interactions between the protonated amines and the negative AuSeeds surface. It also allows for complexation reactions between the gold ion complexes (found at the surface of the AuSeeds).[215] Considering the fact that at neutral pH, BPEI is 44% charged, there are 213 $NH_2$ moieties per polymer chain, and XPS analysis gave an estimation of 1210 polymer chains per LN, theoretically a maximum of 257,620 $NH_2$ sites are available for AuSeed attachment on each LN. There are however, additional considerations for the availability of these attachment sites such as the conformation of the BPEI molecule on the LN surface, steric hindrances, and the electrostatic repulsion between two negatively charged gold seeds that will determine the minimum inter-particle distance allowed on the LN surface.

We aimed to determine the maximum surface coverage achievable with the AuSeeds on the LN@BPEI surface. Working with the hypothesis that fixing the number of LN@BPEI nanoparticles, and varying the number of AuSeeds present in the dispersion, we could observe whether the number of AuSeeds that attach to the LN@BPEI surface will also vary. To test this hypothesis, the following AuSeeds to LN@BPEI nanoparticles dispersions were prepared- 100:1, 300:1, 700:1, 1000:1, 2000:1 and 3000:1 (see table 3.1 in section 3.1.3.2). The samples corresponding to these ratios were labeled LN@BPEI@AuSeeds100, LN@BPEI@AuSeeds300, LN@BPEI@AuSeeds700, LN@BPEI@AuSeeds1000, LN@BPEI@AuSeeds2000 and LN@BPEI@AuSeeds3000 respectively.

TEM analysis showed a random distribution of the AuSeeds on the LN nanoparticle surface for all AuSeed concentrations, with only the AuSeeds densities changing (fig. 3.14). These results can be compared by those reported by De Silva Indrasekara *et. al*[216] where they showed that the architecture of AuNPs attached to a core $SiO_2$ nanoparticle was controllable by pH when the AuNPs diameter was greater than 5 nm. In their work, when the condition for attaching separately synthesized citrate-capped AuNPs of 5, 10 and 15 nm in diameter, to amine terminated $SiO_2$ 60 nm in diameter, was at neutral pH, they observed a random orientation of the AuNPs on the $SiO_2$ core. This random orientation was observed regardless of pH for the 5 nm AuNPs. As our AuNPs

(AuSeeds in our work) are 2.5 nm in diameter, we believe that the random distribution we observed is coherent with their observations.

TEM imaging and ICP-AES analysis techniques were both employed for the quantification of the number of AuSeeds attached to each LN@BPEI and consequently to determine the percentage of the LN@BPEI surface covered. For the quantification based on TEM imaging (fig. 3.14), the ImageJ software was used to count the number of AuSeeds per particle. The sample size for the statistical analysis was 50 LN, of which, the average number of AuSeeds per particle was calculated. The ICP-AES analysis however, determined the total concentration of the Nb and Au atoms in the samples, which allowed for the determination of the concentration of LN@BPEI NPs (in mg/mL and NPs/mL), and the concentration of AuSeeds (in mg/mL and NPs/mL). From the NPs/mL concentrations, it was then possible to calculate the number of LN@BPEI and AuSeeds particles present, and assuming that all the gold that was detected by the ICP-AES was from AuSeeds attached to the LN@BPEI, the average number of AuSeeds per LN particle was determined. Calculation is shown in equation 3.5 below.

$$\begin{aligned} Concentration\ of\ LN\ (mg/mL) &= \frac{Concentration\ of\ Nb\ (mg/mL)}{0.63} \\ \#\ of\ LN\ per\ mL &= \frac{Concentration\ of\ LN\ (mg/mL)}{mass\ of\ 1\ LN} \\ \#\ of\ AuSeeds\ per\ mL &= \frac{Concentration\ of\ Au\ (mg/mL)}{Mass\ of\ 1\ AuSeed} \\ \#\ AuSeeds\ per\ LN &= \frac{\#\ AuSeeds}{\#\ LN\ NPs} \end{aligned} \tag{3.5}$$

The concentrations of Nb and Au were obtained directly from the ICP-AES results, 0.63 is the mass contribution of Nb based on the empirical formula of $LiNbO_3$, and the *mass of 1 LN* as well as the *mass of 1 AuSeed* was calculated based on the volume and density of a single LN and AuSeed nanoparticle respectively.

The plot of percentage of LN@BPEI surface covered as a function of the concentration of AuSeeds as determined by TEM and ICP-AES is presented in fig. 3.15 below. From TEM analysis, the number of gold nanoparticles attached to each LN@BPEI core was determined to vary with a positive linearity with respect to the concentration of the AuSeeds dispersion. TEM determined the LN@BPEI@AuSeeds3000 sample to have a percentage surface coverage of 21%. The linear trend however indicated a potential to increase the percentage of the surface covered by increasing the concentration of AuSeeds. There must however be a maximum percent of the LN surface that

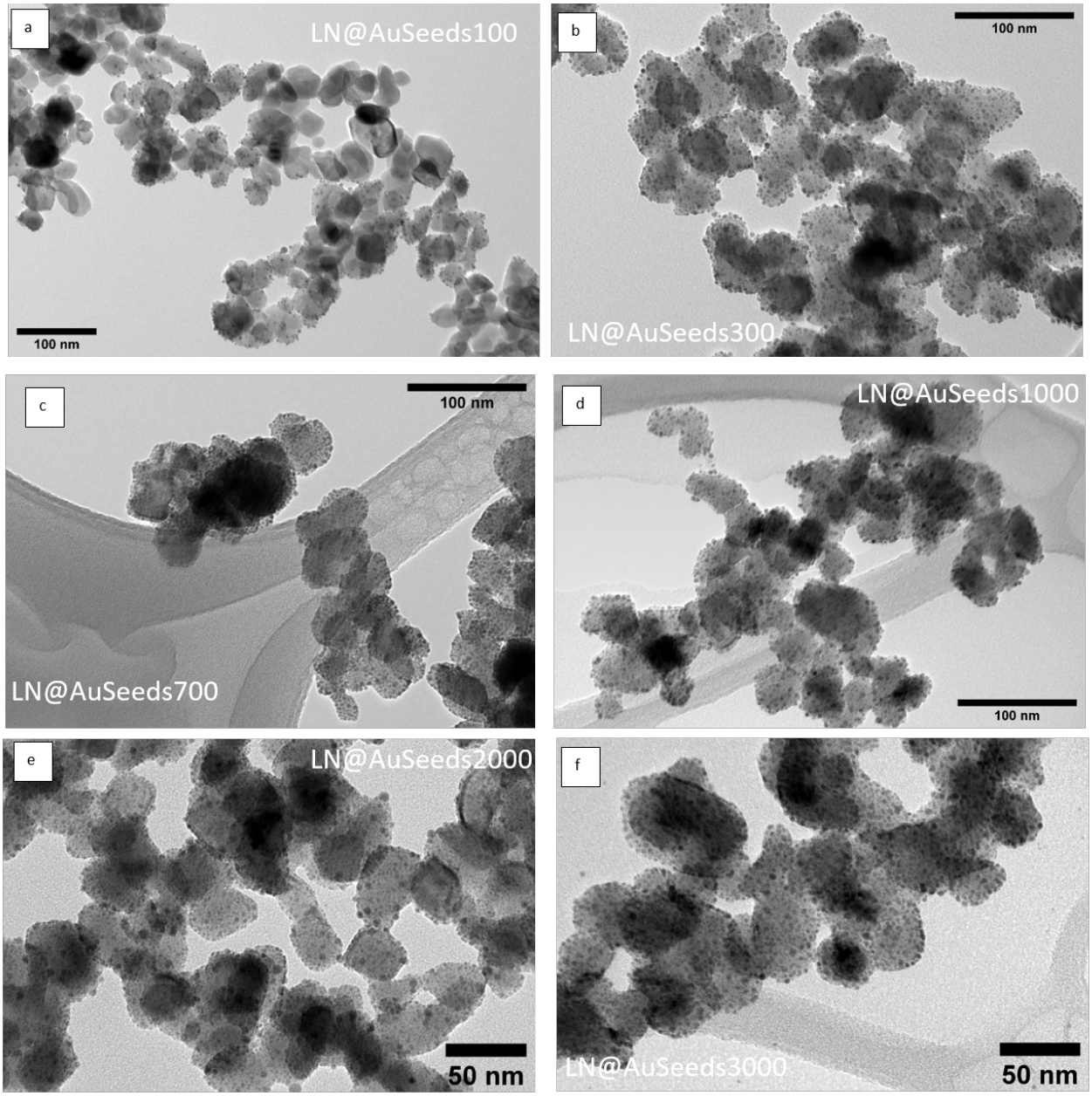


Figure 3.14: TEM images of gold seeds attached to $LiNbO_3$ nanoparticles, at different gold seed loading densities. (a) LN@BPEI@AuSeeds100, (b) LN@BPEI@AuSeeds300, (c) LN@BPEI@AuSeeds700, (d) LN@BPEI@AuSeeds1000, (e) LN@BPEI@AuSeeds2000 and (f) LN@BPEI@AuSeeds3000

can be covered by the AuSeeds. This limit is a result of the summation of effects acting upon the particles such as the electrostatic repulsion between particles, the VDW attractive forces between the particles, the hydrophobic forces and steric forces due to the polymer and solvation forces, as well as the conformation of the BPEI molecules on the LN core which impacts the positioning of $NH_2$ groups on the surface. These factors determine the optimal radial distance between two

neighbouring AuSeed particles and prevent control on the spatial arrangement of the seeds on the particles. It was expected that the estimation obtained from TEM would be undervalued because we are firstly limited statistically, i.e, we performed the imaging of the LN NPs at a higher magnification so as to better visualize the AuSeeds on the surface, which reduced the nanoparticle count per image and consequently the sample size for the statistical analysis. Additionally, we assume that there is homogeneity in the number of AuSeeds attached to the visualized hemisphere of LN and the un-visualized hemisphere. By multiplying the number of seeds we can count on the 2-D projection of the 3-D image by two, we presume to have accounted for the unseen hemisphere. This approach is however a simplification of the reality, as the AuSeeds located at the curved boundaries of LN appear blurred and does not permit a true count of the AuSeeds located in those regions.

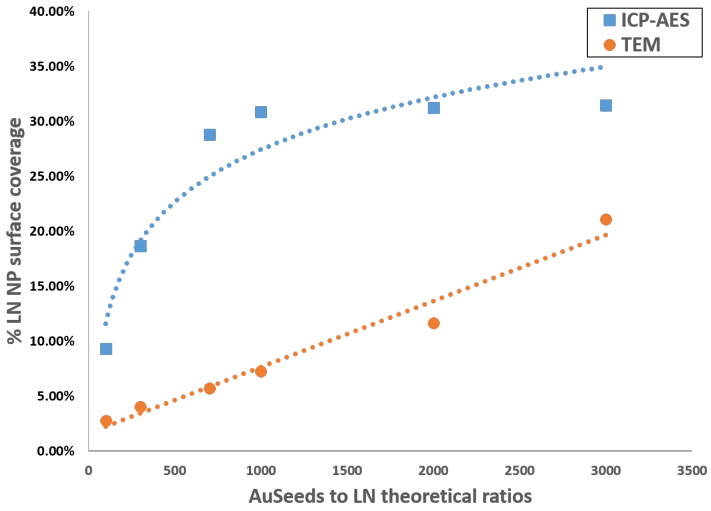


Figure 3.15: Theoretical ratio of AuSeeds to LN@BPEI as a function of the percentage of the LN@BPEI surface covered by the AuSeeds as determined by TEM analysis and ICP-AES analysis.

The plot based on the ICP-AES results revealed an asymptotic trend among the data points, with LN@BPEI@AuSeeds3000 achieving the highest surface coverage of 31.5%, corresponding to a 29% wt of Au. In the work of Goon *et. al*,[208] they reported 47.7 wt% of Au on their $Fe_3O_4$ 50 nm cubic nanoparticles, as determined by ICP-AES analysis. To better compare these results, we used their reported mass percentage to calculate the percent of $Fe_3O_4$ surface covered by the AuNPs, and determined this percentage to be 74%. An explanation for the difference in these achievable percentage surface coverages can be due to the shape of the nanoparticles. In the literature, $Fe_3O_4$ cubic shaped nanoparticles were used, which is firstly a greater surface area than the spherical nanoparticles, although the AuNPs being attached in both works are approximately the same diameter. In addition to this, the cubic shape may possibly contribute to a different (possibly less compact) BPEI polymer conformation than that on the spherical nanoparticles. This different con-

figuration could then lead to the availability of more $NH_2$ terminal groups to facilitate the AuSeeds attachment and therefore we have varied maximum percentage of surface covered. Indeed the data showed that by the LN@BPEI@AuSeeds1000 sample, it was already close to covering the maximum surface of LN and increasing the concentration no longer increased the coverage significantly. This was also noted during the experimental process, where in the samples LN@BPEI@AuSeeds100 to LN@BPEI@AuSeeds700, after centrifugation, the supernatant was colourless to the eyes, however from the samples LN@BPEI@AuSeeds1000 to LN@BPEI@AuSeeds3000, the supernatant had the colour of the AuSeeds dispersion (refer to fig 3.13). A possible limitation to the accuracy of percentage surface LN@BPEI covered for the ICP-AES method is linked to the size polydispersity of the samples. However, as is presented in fig. 3.16, the PDI measured by the Malvern zetasizer was below 0.3 for all the LN and LN@BPEI@AuSeeds samples except for LN@BPEI@AuSeeds100 which experienced significant, visible aggregation. For this work, these PDI values were considered to be acceptable.

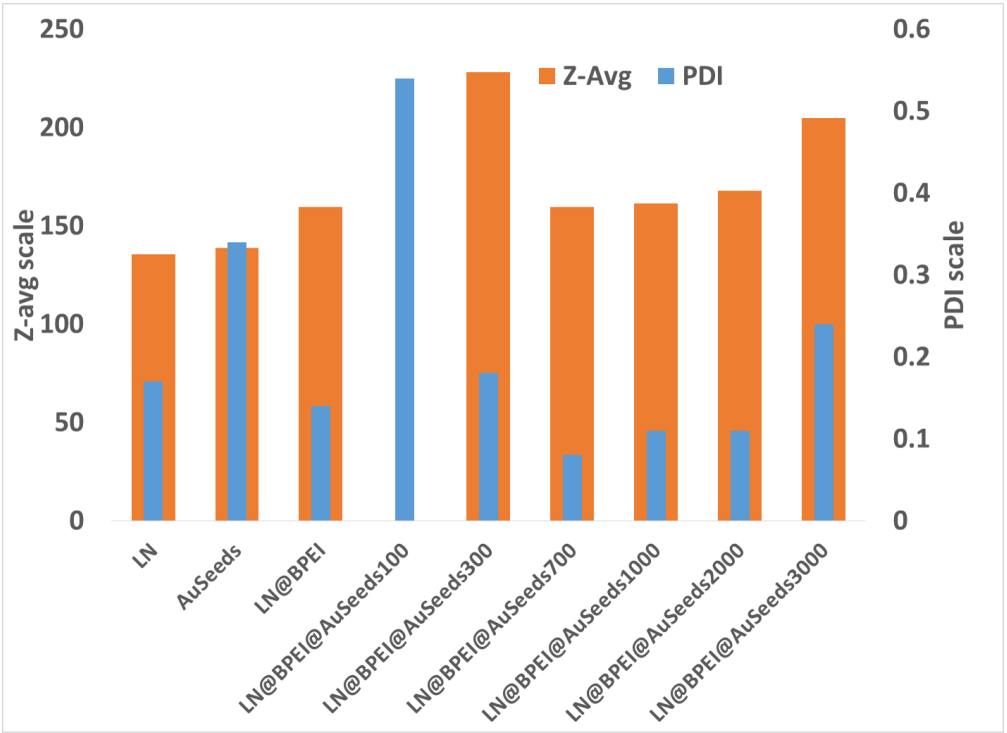


Figure 3.16: Z-avg and PDI values for LN, AuSeeds, LN@BPEI and LN@AuSeeds nanoparticles. The Z-avg value obtained for sample LN@AuSeeds100 was greater than 1000 nm due to aggregation and not representative of individual nanoparticle size and was therefore omitted from the graph.

The zeta potential values as well as the hydrodynamic diameters of LN, AuSeeds, LN@BPEI, and LN@BPEI@AuSeeds samples were measured by Malvern Zetasizer. The values reported by the Zetasizer are themselves an average of 30 measurements, and then an average of these averages

were taken for each sample and used to plot the graph shown in fig.3.17 below. The change in the surface of the LN particles is qualitatively assessed by regarding the change in sign of the zeta potential value. As is shown in figure 3.17, after each surface modification (with BPEI and then with AuSeeds), we reverse the surface charge of the nanoparticles. From the zeta potential data, we expected samples from LN@BPEI@AuSeeds100 to LN@BPEI@AuSeeds700 to be prone to aggregation. This was indeed observed during the experimental process as the nanoparticles in those dispersions would quickly sediment at the bottom of their storage container after a few minutes (roughly 10 to 15 minutes), whereas the LN@BPEI@AuSeeds1000 to LN@BPEI@AuSeeds3000 samples remain well dispersed as observed by the naked eye. This was important in determining what samples would be used for attempting to grow the gold shell (further discussed in chapter 4).

Now that we have demonstrated the ability to control the surface coverage of LN nanoparticles with AuSeeds, we will characterize the non-linear optical properties of these particles in the following section.

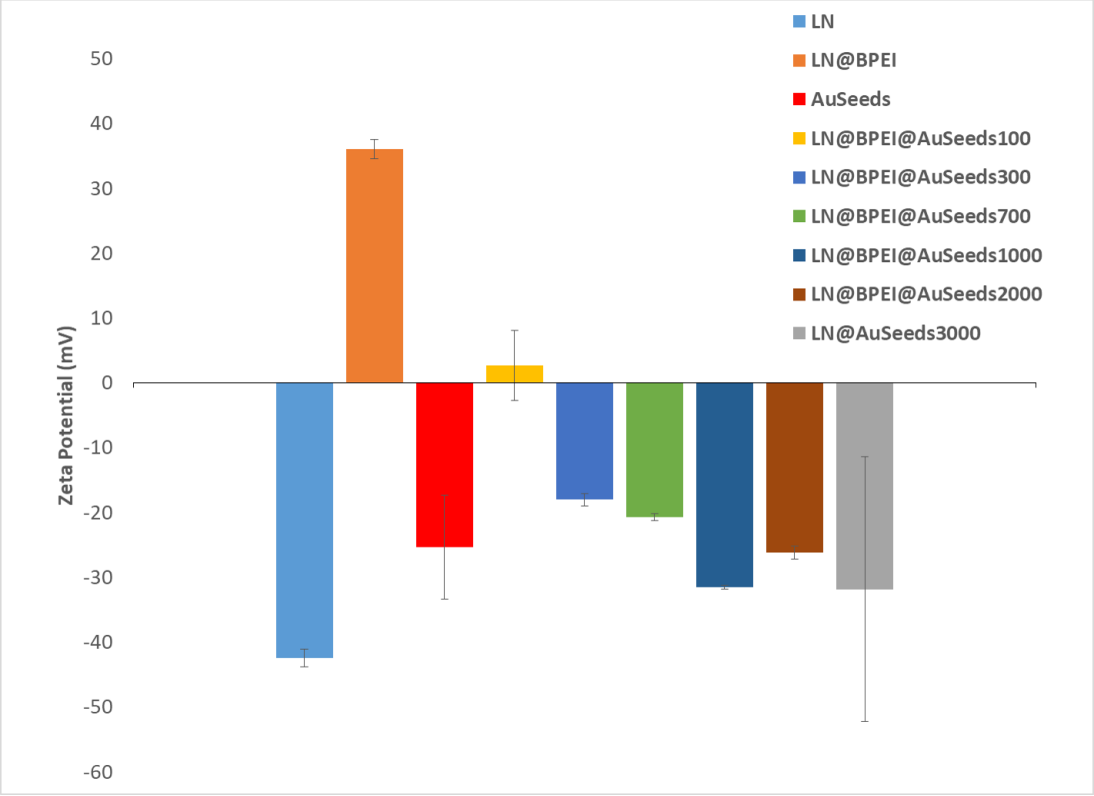


Figure 3.17: Zeta potential for LN, LN@BPEI and LN@BPEI@AuSeed nanoparticles. Graph shows the alternating negative and positive zeta potential upon changing the surface of the nanoparticles.

### 3.2.4 Hyper Rayleigh Scattering Results

As discussed in section 1.3.2, the microscopic entity used to quantify the SHG response of nanoparticles is $\beta$. The Hyper Rayleigh Scattering (HRS) intensities of a nanoparticle dispersion can be expressed as the following:

$$I_{HRS} = G(N_s < \beta_s^2 > + N_{np} < \beta_{np}^2 >) \tag{3.6}$$

where $I_{HRS}$ is HRS intensity, $G$ is an experimental proportionality constant, $N_s$ is the solvent concentration, $\beta_s$, is the solvent hyperpolarisability, $N_{np}$ is the concentration of the nanoparticles, and $\beta_{np}$ is the average hyperpolarisability of the nanoparticles and the brackets indicate orientational averaging. By varying the nanoparticle concentration and measuring the corresponding HRS intensity, using an external reference, the hyperpolarisability values of a nanoparticle dispersion can be deduced from the slope.

The set-up described in section 3.1.5 was used to collect the raw HRS intensities of $LiNbO_3$ NP dispersions, at different concentrations. After a correction for extinction (scattering and absorption) of the amplitude, which we supposed was due mainly to scattering, the corrected HRS intensities were obtained (corresponding plots are shown in fig. 3.18.(a)). At zero concentration, only the solvent HRS intensity is measured, and we used this intensity to re-normalize all the curves and a plot of the maximum HRS intensities as a function of concentration was made (fig. 3.18.(b)). The normalized HRS intensity is given by the equation 3.7.

$$I_{HRS} = 1 + \frac{< \beta_{LN}^2 >}{N_W < \beta_W^2 >} N_{LN} \tag{3.7}$$

The hyperpolarisability ($\beta$) could then be extracted from the slope using the internal reference method. The solvent's (in our case water) HRS intensity was known for $N_W$= 55.56 mol/L, with a $\sqrt{< \beta_W^2 >}$ value of $0.087 \times 10^{-30} esu$ and $N_{LN}$ is the concentration of the nanoparticles. The HRS intensity were also measured for the samples LN@BPEI@AuSeeds300, LN@BPEI@AuSeeds1000 and LN@BPEI@AuSeeds3000, as well as for AuSeeds dispersion, and their normalized HRS intensities as a function of nanoparticle concentration are shown in fig. 3.19. The $\beta$ values for the AuSeeds as well as LN@BPEI@AuSeeds nanoparticles are presented in table 3.2. As the determination of $\beta$ is dependent on one knowing precisely the nanoparticle concentration, it is necessary to state that the LN initial concentration was determined by weighing the dry powder and dispersing in it the necessary volume of water to give the desired mass concentration, whereas the LN@BPEI@AuSeeds initial concentration was determined by ICP-AES analysis (refer to calculation in section 3.2.3 equation 3.5). The dispersions were then further diluted to have the different concentrations.

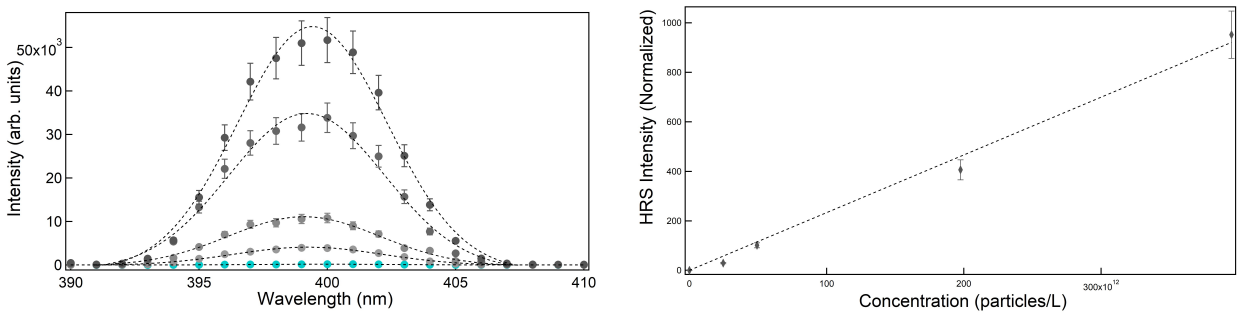


(a) (b)

Figure 3.18: (a) Graphical plot of the HRS intensities of $LiNbO_3$ NP dispersions upon using an incident laser wavelength of 800 nm, vertically polarized, and varying the concentration of the nanoparticle dispersions. (b) Graphical plot of the maximum HRS intensities corrected of $LiNbO_3$ NP as a function of nanoparticle concentration.

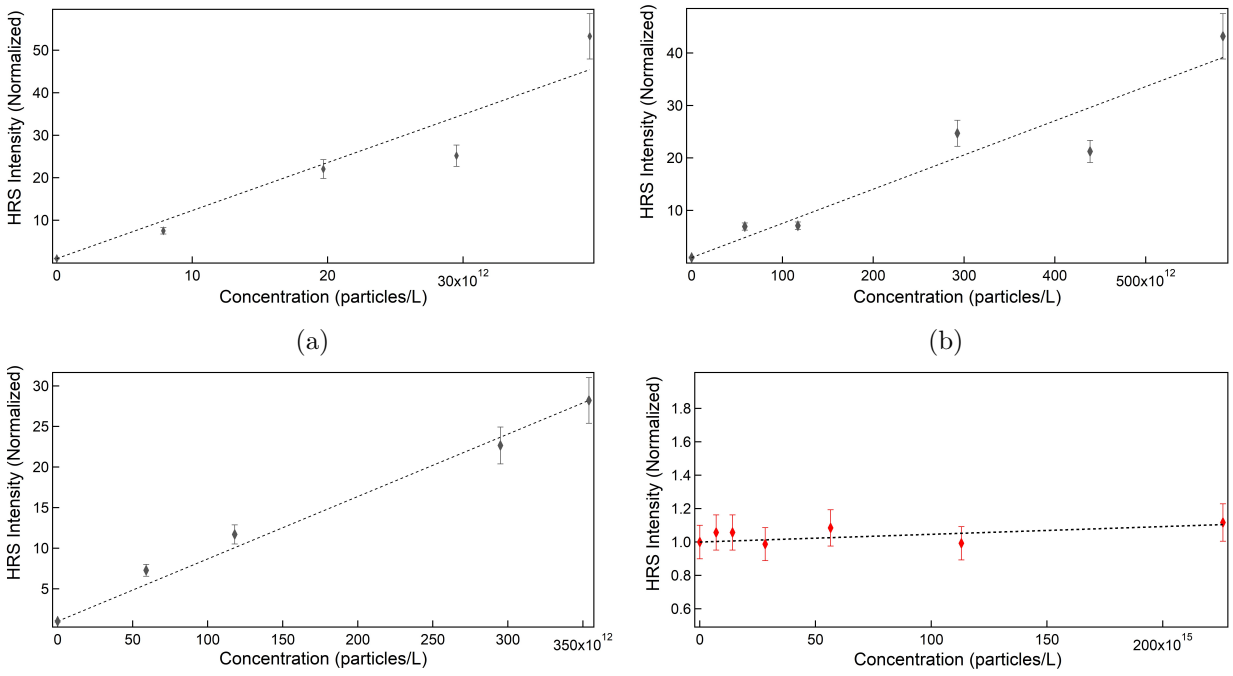


(a) (b)

(c) (d)

Figure 3.19: Graphical plot of the HRS intensities corrected as a function of the nanoparticle dispersion concentration. (a) LN@BPEI@AuSeeds300, (b) LN@BPEI@AuSeeds1000, (c) LN@BPEI@AuSeeds3000 whose concentration units are expressed in NPs/mL. (d) AuSeeds whose concentration values are expressed in mol/L.

In determining $\beta$, there are some assumptions that were made. Firstly, by taking the mean nanoparticle volume of LN, we assume particle size monodispersity, thereby discounting the influence of the size polydispersity on the $I_{HRS}$. In the same article by Joulaud *et. al*,[217] they demonstrated that by assuming monodispersity of the sample, there is indeed an overestimation of the NLO response. We also fail to account for possible aggregation effects. The aggregation effects would have been more

| Sample | $\sqrt{<\beta^2>}esu$ |
|---|---|
| AuSeeds | (3.42 ± 2.8) e-28 |
| LN@BPEI@AuSeeds300 | (0.535 ± 0.2) e-24 |
| LN@BPEI@AuSeeds1000 | (0.129 ± 0.04) e-24 |
| LN@BPEI@AuSeeds3000 | (0.140 ± 0.03) e-24 |
| LN | (0.768 ± 0.14) e-24 |
| Reference LN | 16.3 e-24 |

Table 3.2: Table showing the hyperpolarizability results determined from the slope of the plots of HRS intensities vs nanoparticle concentration (fig. 3.18 and 3.19) for AuSeeds, LN@BPEI@AuSeeds300, LN@BPEI@AuSeeds1000, LN@BPEI@AuSeeds3000, LN used in this work (45 nm diameter) and reference LN found in the literature (125 nm diameter).[217]

pronounced for the sample LN@BPEI@AuSeeds300, whose zeta mean potential value is -18.0 mV (fig. 3.17), which leads to a dispersion that is less stable, and more prone to aggregating. Although these assumptions are made, we have a high degree of confidence in our measurements.

The second observation was that the non-linear efficiency of LN decreases upon attaching AuSeeds to its surface. This was an unexpected yet interesting result as it probes the question, why do AuSeeds impact the SH response of LN. One hypothesis is that the surface contributions to the HRS intensity of LN is significant, and therefore changing the surface changes the response. To further probe this occurrence, we decided to take polarization resolved measurements of the samples, where the input polarization angle is rotated and the output intensity vertically polarized. Then using the intensities obtained for vertically and horizontally polarized fundamental light, $I^V_{HRS}$ and $I^H_{HRS}$ respectively, we can introduce the depolarization ratio, D, which is given in equation 3.8 below. Table 3.3 gives the depolarization values of the samples.

$$D = \frac{I^H_{HRS}}{I^V_{HRS}} \tag{3.8}$$

| Sample | D |
|---|---|
| LN | 0.16 ± 0.01 |
| LN@BPEI@AuSeeds100 | 0.2 ± 0.02 |
| LN@BPEI@AuSeeds300 | 0.17 ± 0.02 |
| LN@BPEI@AuSeeds1000 | 0.18 ± 0.03 |
| LN@BPEI@AuSeeds3000 | 0.18 ± 0.03 |
| AuSeeds | 0.43 ± 0.1 |

Table 3.3: Depolarization values for LN, AuSeeds and LN@BPEI@AuSeeds

Theoretically, the depolarization ratio for a purely 1D single tensor element molecule is 0.2. Conversely, planar symmetric molecules of point group $D_{3h}$ have depolarization ratio of 2/3.[218] Lithium

niobate, which belongs to the point group $C_{3v}$ has a strong non-linearity along a single axis. This results in there being a non-vanishing independent element that is largely dominant, and as such, one can expect a depolarization value close to that of a pure single tensor element (0.2). We do in fact observe this for the samples of LN and LN@BPEI@AuSeeds, as they all have a value close to 0.2. The AuSeeds however have a depolarization value closer to that of the $D_{3h}$ system. A reason for this could be the highly spherical geometry of the AuSeeds, which results in there being an almost equivalent HRS response for both vertically and horizontally polarized light at all incident light angles. The polar plots corresponding to LN and AuSeeds are given in figure 3.20. As is seen from the figure, for LN, the HRS intensity response to vertical polarization is stronger than that of the horizontally polarized light, whereas for the AuSeeds, the response is very similar for both polarizations. Interestingly enough, the addition of the AuSeeds to LN did not vary significantly the D values when compared to the bare LN sample. The strong HRS response of the LN from vertically polarized light dominated the overall HRS response of the hybrid LN@BPEI@AuSeeds nanoparticles. Therefore it is still yet to be understood why the addition of AuSeeds to the surface of LN decreased the $\beta$ values. Simulation and modelization have been proposed as a next step to study this optical change of the nanoparticles.

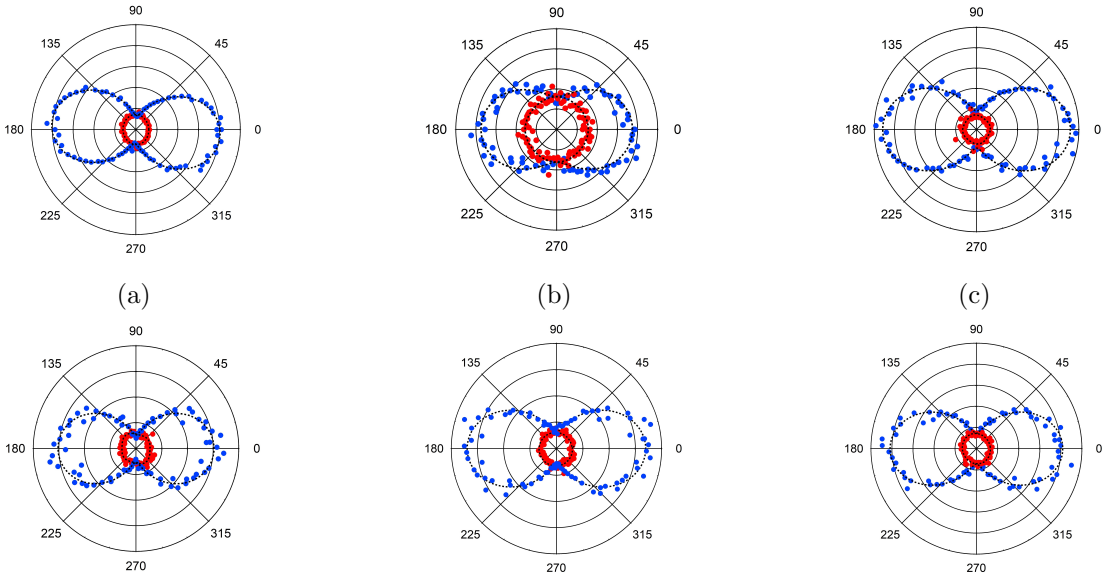


Figure 3.20: Polar plots of HRS intensities as a function of the polarization angles of the incident light for nanoparticle dispersions. The blue data points correspond to vertical polarization and the red data points correspond to horizontal polarization. (a) LN, (b) AuSeeds, (c) LN@BPEI@AuSeeds100, (d) LN@BPEI@AuSeeds300, (e) LN@BPEI@AuSeeds1000 and (f) LN@BPEI@AuSeeds3000.

## 3.3 Conclusion

The synthesis protocol to produce pseudo-spherical LN nanoparticles of 45 nm in diameter was outlined. The most suitable means of permanently reversing the surface charge was determined to be with BPEI 25,000 g/mol polymer, which is also a biocompatible polymer. Its abundance of $NH_2$ groups make it suitable for the attachment of AuSeeds by means of both covalent bonds and electrostatic attraction. It was further demonstrated that there is variability in the percentage of the LN@BPEI surface that can be covered by the AuSeeds, with a maximum surface coverage of 31%, determined by ICP-AES analysis. When the percent of the surface covered is inferior to 19%, the LN@BPEI@AuSeeds dispersions are not stable, marked by the observation of aggregation and sedimentation processes. Conversely, at the maximum surface coverage of 31%, the dispersions are stable. The non-linear characteristics of the nanoparticles were determined from Hyper Rayleigh Scattering experiments. The hyperpolarisability as well as the depolarization ratio values revealed that the non-linear response of the LN nanoparticles decreases upon the attachment of AuSeeds to its surface.

# Chapter 4

# Synthesis of Gold Shell on $LiNbO_3$ Nanoparticles (LN@Au)

In this final chapter of this manuscript, we detail the synthesis of a gold shell around lithium niobate core to give $LiNbO_3$/Au core-shell nanoparticles (LN@Au), commencing from LN@BPEI@AuSeeds nanoparticle dispersions. This chapter is the realization of the main objective of this thesis work, i.e, the synthesis of core-shell hybrid nanoparticles, with the potential to be used as cancer therapeutic and bio-imaging probes. In sections 1.3.2 and 1.3.4.2, pages 36 and 40, we discussed non-linear optical (NLO) properties of non-centrosymmetric materials such as $LiNbO_3$. We showed that these materials at the nanoscale can be used for NLO bio-imaging techniques, even though the NLO response is volume scaled. In section 1.7.2, page 57, we introduced gold nanoshells (AuNSs) focusing on their tuneable plasmonic properties and why this makes them excellent candidates for photothermal energy conversion. The goal therefore, was to prepare hybrid core-shell nanoparticles, whose plasmonic response from its gold shell would be centered on 800 nm, which is within the biological optical window, while retaining the NLO properties of the LN core. To achieve this, it was desired to have a protocol for gold shell synthesis that provided sufficient control on the thickness of the gold shell, with a shell morphology suited for the intended biological applications.

We present in this chapter, the protocols of LN@Au NPs synthesis that were tested, based on a seeded-growth approach. A scheme of the main synthesis protocols detailed in this chapter is shown in fig 4.1. The accompanying discussion is focused on the influence of experimental parameters such as the pH, initial gold seed density, and gold salt concentration. In addition to presenting the LN@Au NPs formed, we will provide the surface characterization data of these LN@Au NPs at different steps of the synthesis process, as well as our study on the impact of ageing on the properties of the nanoparticle dispersions. Finally, the non-linear optical characterization along with the photothermal properties of the final nanoparticle dispersions are presented.

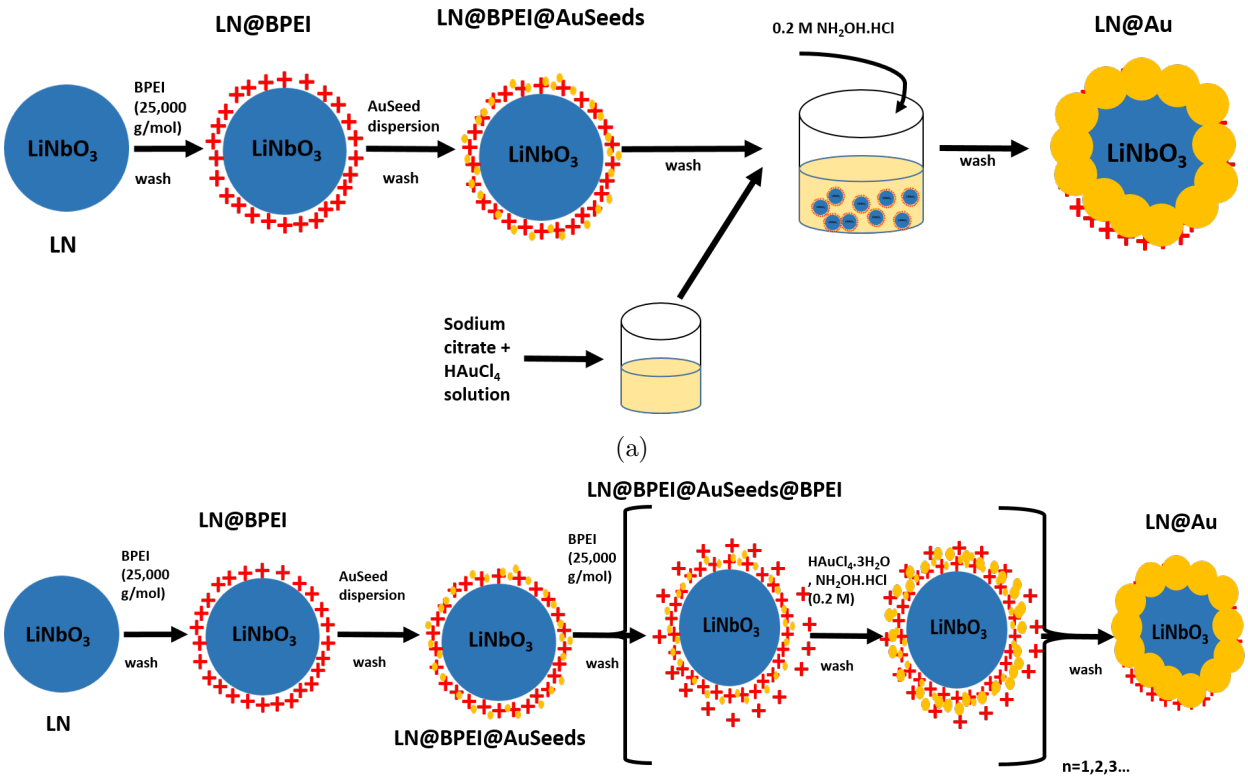


Figure 4.1: Schemes for the two protocols for LN@Au NPs synthesis. (a) LN@Au NPs synthesis using a sodium citrate to gold chloride ($HAuCl_4$) growth solution. (b) LN@Au NPs synthesis using a layer-by-layer (LbL) approach.

## 4.1 Materials and methods of synthesis

The following materials were used for the synthesis procedures detailed below. Lithium niobium ethoxide ($LiNb(OEt)_6$), (99+% metal basis, 5% w/v in ethanol) was obtained from Alfa Aesar, Teflon cup model number 4749 was obtained from Parr Instrument, and Nalgene centrifugation tubes were obtained from ThermoFisher. Butane-1,4-diol (99%), ethanol, sodium hydroxide (NaOH) pellets, tetrakis(hydroxymethyl)phosphonium chloride (THPC) solution (80% in water), polyethylenimine, branched (BPEI), ~25,000 g/mol, gold (III) chloride trihydrate ($HAuCl_4.3H_2O$)($\geq$99.9%, trace metal basis), $NH_2OH.HCl$ (hydroxylamine hydrochloride), and sodium citrate ($Na_3C_6H_5O_7$), were all obtained from Sigma Aldrich. Unless otherwise stated, any water used was deionized water (18.2 M$\Omega$.cm)

### 4.1.1 Synthesis of $LiNbO_3$ NPs

The protocol for the synthesis of $LiNbO_3$ NPs is detailed in section 3.1.1 page 87 and was performed at Symme laboratory, Annecy.

### 4.1.2 BPEI adsorption on $LiNbO_3$ NPs (LN@BPEI)

The protocol for the synthesis of LN@BPEI NPs is detailed in section 3.1.2 page 87.

### 4.1.3 Synthesis of Gold Seeds

The protocol for the synthesis of AuSeeds is detailed in section 3.1.3.2 page 88.

### 4.1.4 Attaching Gold Seeds to $LiNbO_3$ NPs (LN@BPEI@AuSeeds)

The protocol for the synthesis of LN@BPEI@AuSeeds is detailed in section 3.1.3.2 page 88.

### 4.1.5 Synthesis of LN@Au NPs using sodium citrate growth solution

Stock solutions of 0.15 mM, 1.2 mM and 6 mM sodium citrate ($Na_3Cit$) solutions were prepared. Gold growth solutions composed of $Na_3Cit$ solution and $HAuCl_4$ solution were then prepared, having $Na_3Cit$ to $HAuCl_4$ mole ratios of 1:1, 8:1 and 40:1. Each growth solution contained 37.5 $\mu$L of 40 mM $HAuCl_4$ solution, and 10 mL of $Na_3Cit$ solution of different concentration given in table 4.1 below. All gold growth solutions were prepared under continuous stirring. Then, to each growth solution, 1 mL of LN@BPEI@AuSeeds3000 NPs (approximately 0.35 mg/mL by the $LiNbO_3$ mass) was added and allowed to mix for one minute, followed by the addition of 10.7 $\mu$L of 0.2 M $NH_2OH.HCl$ which was left to mix for 10 minutes. The samples were then centrifuged for 10 minutes at 20°C and 9103g. The supernatant was removed and the particles redispersed in 1 mL of water. The protocol for TEM imaging outlined in section 2.1.1 on page 66 was used to image the resulting NPs, and the zeta potential value and hydrodynamic radius were determined using a zetasizer by Malvern Instruments.

| $Na_3Cit$: $HAuCl_4$ ratio | Concentration $Na_3Cit$ (mM) | Volume (mL) |
|---|---|---|
| 1:1 | 0.15 | 10 |
| 8:1 | 1.2 | 10 |
| 40:1 | 6 | 10 |

Table 4.1: Quantities of sodium citrate for each gold growth solution.

### 4.1.6 Layer-by-layer synthesis of LN@Au NPs

A layer-by-layer method was used to synthesize LN@Au NPs. The general protocol is detailed below and depicted in fig. 4.1 (b).

BPEI, 4 mg, was weighed in a reaction vessel and dissolved in 5 mL of water at 60°C. Upon complete BPEI dissolution, 1 mL of 0.35 mg/mL LN@BPEI@AuSeeds was added and left to mix for two hours while maintaining the 60°C temperature. The nanoparticle dispersion was cooled to room temperature, and transferred to a centrifuge tube, where two centrifugation rounds of 10 minutes at 10°C and 9103g were conducted, removing the supernatant and replacing it with water between each centrifugation. The nanoparticles were then re-dispersed in 1 mL of water. In a 50 mL Nalgene tube, 18 mL of water was added. Depending on the experiment, the pH of the water was kept as it is (approximately pH 7.7) or adjusted to pH 11.5 using 0.1 M NaOH. Then, while under stirring, the 1 mL NP dispersion was added to the 18 mL of water and allowed to homogenize for one minute, followed by 50 $\mu$L of $HAuCl_4$ solution and lastly 75 $\mu$L of 0.2 M $NH_2OH.HCl$. The contents of the Nalgene tube was left under stirring for 10 minutes after which two centrifugation rounds of 10 minutes at 10°C and 9103g were performed, removing the supernatant and replacing it roughly by 5 mL of water between each centrifugation. The final nanoparticles were again dispersed in 1 mL of water. This entire procedure was then repeated two more times. The protocol for TEM imaging outlined in section 2.1.1 on page 66 was used to image the NPs, and the zeta potential values and hydrodynamic diameters were determined using a zetasizer by Malvern Instruments. UV-visible spectra of all the nanoparticle dispersions were obtained using a SAFAS-UV mc2 spectrometer in a quartz cell with 1.0 cm path length.

The above protocol was modified to examine the influence of pH, initial gold seed coverage, and $HAuCl_4$ concentration on the final hybrid nanoparticles. The experimental parameters changed are detailed in table 4.2.

| Experimental Variable | Experimental Conditions |
|---|---|
| pH | 1) LN@BPEI@AuSeeds3000, **pH 11.5**, $HAuCl_4$= 30 mM<br>2) LN@BPEI@AuSeeds3000, **pH 7.7**, $HAuCl_4$= 30 mM |
| LN@BPEI@AuSeeds | 1) **LN@BPEI@AuSeeds3000**, pH 7.7, $HAuCl_4$= 30 mM<br>2) **LN@BPEI@AuSeeds1000**, pH 7.7, $HAuCl_4$= 30 mM |
| $HAuCl_4$ concentration | 1) LN@BPEI@AuSeeds1000, pH 7.7, **$HAuCl_4$= 3 mM**<br>2) LN@BPEI@AuSeeds1000, pH 7.7, **$HAuCl_4$= 10 mM**<br>3) LN@BPEI@AuSeeds1000, pH 7.7, **$HAuCl_4$= 30 mM**<br>4) LN@BPEI@AuSeeds1000, pH 7.7, **$HAuCl_4$= 100 mM** |

Table 4.2: Experimental conditions for layer-by-layer gold shell growth.

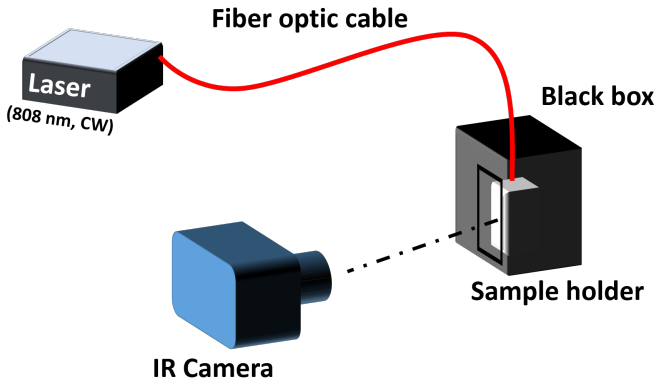


Figure 4.2: Experimental set-up for IR-thermographic measurement.

### 4.1.7 Photothermal measurements of nanoparticle dispersions

A home-made laboratory laser set-up (see fig. 4.2) was configured for conducting the photothermal evaluation of the nanoparticle dispersions. In brief, a sample holder was fixed inside a black box. A F110SMA-780 lens from Thorlabs was attached to an 808 nm continuous wave (CW) laser, with a beam spot size of 1.36 mm by way of a fiber optic cable. The measured output power was 47 $mW/cm^2$. The laser was then positioned at 0° with respect to the normal of the liquid surface. An IR-thermographic camera (THERMOPRO TPS8S), was positioned at 90° with respect to the laser beam, at a distance of 10 cm from the sample. For each experiment, 200 $\mu$L of the sample was placed in a 2 mL eppendorf tube. The IR-thermographic camera was used to capture images of the eppendorf tube in real time. An image was taken before switching on the laser to have the baseline temperature for the tube and its contents. Then the laser was switched on and the IR images with the temperature data embedded was taken at one minute intervals for 30 minutes. Upon extracting the temperature data from the images using the software Guide IRAnalyser V1.9, the temperature versus time profile for the samples were plotted.

## 4.2 Results & Discussion

### 4.2.1 Synthesis of LN@Au using sodium citrate

In an attempt to control the deposition of Au on the LN@BPEI NPs, a growth solution of sodium citrate ($Na_3Cit$) and aqueous $HAuCl_4$ was used (protocol outlined in section 4.1.5, page 115). This was directly inspired by the work of authors Wang *et. al.*[135] They obtained two distinct gold shell morphologies when their gold-seeded $SiO_2$ NPs (120 nm in diameter) were placed in the growth solution with the reducer $NH_2OH.HCl$ at ambient temperature. These two morphologies were correlated to the ratio of $Na_3Cit$ to $HAuCl_4$ as shown in the scheme in fig. 4.3.

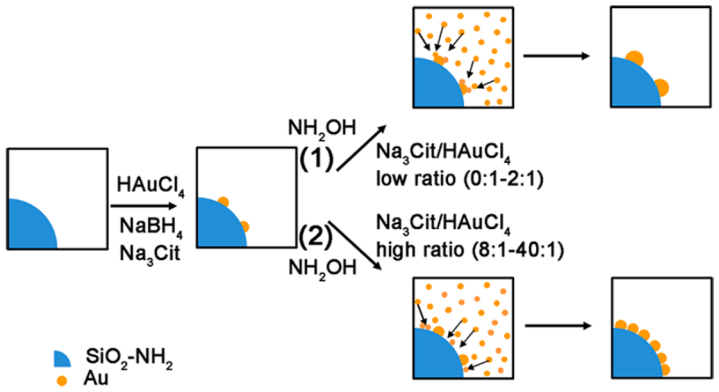


Figure 4.3: Scheme of preferential Au atom attachment to aminated $SiO_2$ nanoparticles based on $Na_3Cit$ to $HAuCl_4$ ratio, taken from Wang *et. al.*[135] The reduction of gold ions is facilitated by $NH_2OH.HCl$. (1) Preferential attachment of the newly formed Au atoms to the already present AuNPs on the surface of the aminated $SiO_2$ NPs. (2) Preferential attachment of the newly formed Au atoms to the Au-free surfaces of the aminated $SiO_2$ NPs.

It was already demonstrated in chapter 3, section 3.2.3, page 98, that adapting the *in-situ* gold-seeding method using $NaBH_4$ as reducer to our LN@BPEI NPs, resulted in an inhomogeneous deposition of gold spheres with an average diameter of 18 nm on the LN surface, and a polydispersity index (PDI) value of 0.37. Consequently, we concluded that this gold seeding method was not suited to our LN@BPEI NPs. Instead, we opted to use the successful gold seeding method which was also presented in chapter 3 section 3.2.3 page 98. The LN@BPEI@AuSeeds3000 nanoparticle dispersions were chosen as they were stably dispersed in water with a zeta potential of -31.8 $\pm$ 20.3 mV, and a PDI value of 0.2.

The LN@BPEI@AuSeeds3000 NPs were placed in gold growth solutions with $Na_3Cit$ to $HAuCl_4$ mole ratios 1:1, 8:1 and 40:1. The absolute molar quantity of $HAuCl_4$ was set at 1.5 $\times 10^{-6}$ moles in all the growth solutions. This number of moles was ultimately determined to be 8% less than

the molar quantity theoretically needed to completely cover the surface of 1 mL of 0.35 mg/mL LN NPs using 2.5 nm diameter gold seeds. The reducer was used in excess, to promote complete $Au^{3+}$ reduction. In both the 1:1 and 8:1 solutions, upon addition of the reducer, the solution visibly changed colour from the red-brown of the LN@BPEI@AuSeeds dispersion (same colour as the AuSeeds dispersion displayed in chapter 3, fig. 3.13, page 101) to a purple coloured dispersion. UV-visible spectroscopic analysis revealed that both dispersions had a single extinction band, with their maxima at 535 and 526 nm respectively. This is close to the characteristic absorption peak of 520 nm for a dispersion of spherical gold nanoparticles.[154] The z-avg and PDI values reported in table 4.3 however, allowed us to conclude that the nanoparticle dispersions consisted of one size population. With this data, we strongly hypothesized that the nanoparticles formed were indeed LN@Au hybrid nanoparticles, and that the Au attached to the LN core are gold islands, sufficiently distanced from each other so as to not have any plasmon coupling effects. As such, what we observed was the collective plasmonic response of isolated gold islands. This is in agreement with the mechanism of gold shell growth proposed by Wang *et. al*,[135] who reported that at low $Na_3Cit$ to $HAuCl_4$ ratios, the reduced Au atoms favoured the attachment directly at the AuSeeds to ripen/grow them. We therefore decided to test a higher $Na_3Cit$ to $HAuCl_4$ ratio to observe the impact on the hybrid nanoparticles formed.

| Growth Solution | Zeta Potential (mV) | Z-Avg (nm) | PDI |
|---|---|---|---|
| 1:1 | -24.0 ± 0.62 | 169.9 ± 1.00 | 0.198 |
| 8:1 | -40.9 ± 0.70 | 138.0 ± 0.60 | 0.187 |

Table 4.3: Zeta Potential, Z-Avg and PDI values for LN@Au nanoparticles synthesized after dispersing LN@BPEI@AuSeeds3000 in a 1:1, and 8:1 $Na_3Cit$ to $HAuCl_4$ solution followed by reduction with $NH_2OH.HCl$.

When LN@BPEI@AuSeeds3000 NPs were placed in the 40:1 $Na_3Cit$ to $HAuCl_4$ solution, the UV-visible spectrum of the resulting NP dispersion had a single band, with a maximum at 597 nm (see fig. 4.4 (a)). This corresponds to a red-shifting of the plasmon peak by approximately 60 nm as compared to the nanoparticles formed in the 1:1 and 8:1 growth solutions, however it is not as significant as the 200 nm shift observed by the team of Wang *et. al*.[135] TEM imaging was performed on these NPs (see fig. 4.4 (b)). What we observed was individual gold islands, much like what we hypothesized to be formed in the 1:1 and 8:1 ratios. Indeed, in comparing the TEM images of our nanoparticles to that reported by Wang *et. al*,[135] the morphology of the gold deposition on the core particle more closely resembled the morphology they obtained in their 1:1 growth solution (see fig. 4.4 (c)), as opposed to the morphology obtained in their 40:1 growth solution (see fig. 4.4 (d)). One hypothesis for the differing results between the work of Wang *et. al* and this work is the pKa values of $NH_2$ attached to $SiO_2$ (approximately 9),[219] and that of the $NH_2$ of BPEI (ap-

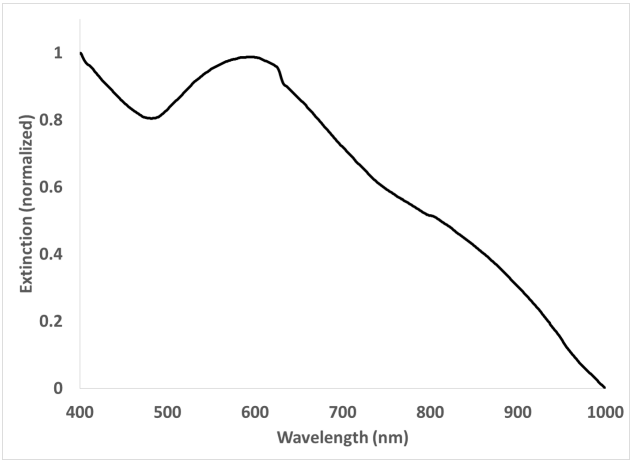


(a)

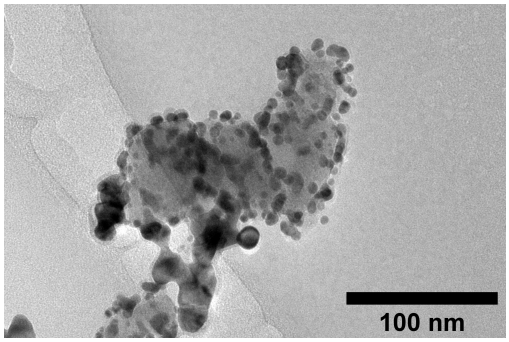


(b)

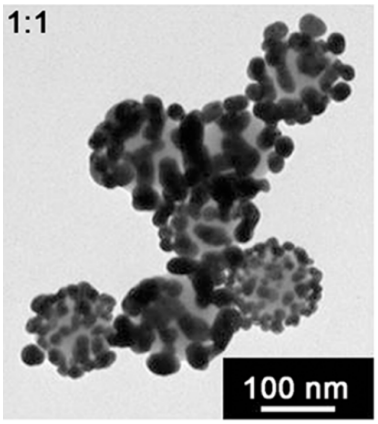


(c)

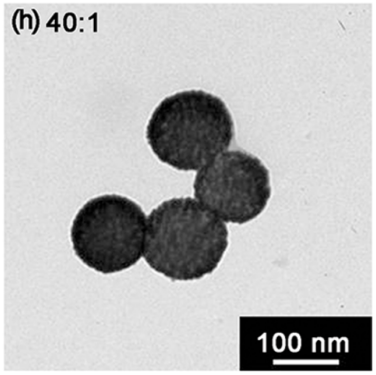


(d)

Figure 4.4: UV-visible spectra and TEM images for LN@Au NPs and and $SiO_2$@Au NPs synthesized using $Na_3Cit$ to $HAuCl_4$ growth solution. (a) The UV-visible spectrum of the LN@Au nanoparticle dispersion formed in a 40:1 $Na_3Cit$ to $HAuCl_4$ solution, with an extinction maximum at 597 nm. (b) TEM image of LN@Au NPs formed in a 40:1 $Na_3Cit$ to $HAuCl_4$ solution. (c) TEM image of $SiO_2$@Au NPs formed upon placing aminated $SiO_2$ NPs in a 1:1 $Na_3Cit$ to $HAuCl_4$ solution. (d) TEM image of $SiO_2$@Au NPs formed upon placing aminated $SiO_2$ NPs in a 40:1 $Na_3Cit$ to $HAuCl_4$ solution. Images (c) and (d) taken from article by Wang *et. al.*[135]

proximately 7).[209] The $Na_3Cit$ has a pH regulating function from its three carboxyl groups (see fig. 4.5). When we increase its molar quantity, we increase the basicity of the solution. This however lowers the degree of protonation of the $NH_2$ moieties of BPEI. As such, we favor the attachment of the AuNPs formed to the existing AuNPs on the LN core and not on the Au-free, amine surface. It was therefore concluded that this protocol was not suited for the formation of a gold shell on LN@BPEI@AuSeeds nanoparticles.

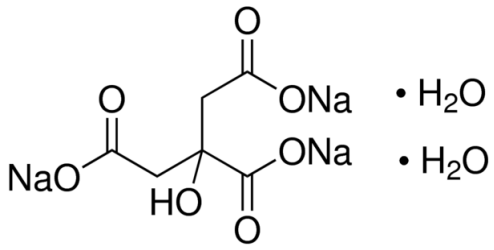


Figure 4.5: Structural formula of sodium citrate.

### 4.2.2 Layer-by-layer gold shell growth

A layer-by-layer (LbL) synthesis technique was investigated for its utility in controlling the gold shell growth on the LN core. Based on what is seen in the literature, the process of alternate charge reversal in a LbL manner, is a versatile nanoscale synthesis technique that is used to control the deposition of thin films.[220,221] While there are examples of seeded-growth, iterative reduction of Au ions to form core-shell nanoparticles as in the work of Goon *et. al*,[208] it often results in the uncontrolled and undesired encapsulation of multiple core particles in a single gold shell resulting in a heterogeneous size dispersity of the core-shell particles. A LbL protocol for gold shell growth on spherical iron oxide NPs built upon this iterative reduction method was proposed by Lee *et. al*.[173] In their protocol, between each gold reduction step, a layer of the cationic polymer BPEI was used to completely coat the NPs. Their protocol was loosely adapted to our work detailed in this chapter, but we went further in the optimization process to observe the role of pH, initial gold seed density on the core particles and $HAuCl_4$ concentration. In the following sections, we will discuss the effect of changing these parameters on the final nanoparticles formed.

#### 4.2.2.1 Investigating the role of pH during the gold shell synthesis

In the protocol outlined by Lee *et. al*,[173] they performed the $Au^{3+}$ reduction under basic conditions, bringing the pH of the reaction medium to 11.5 before adding their gold-seeded iron oxide nanoparticles to the aqueous solution. Although the pH at which the gold reduction is performed controls the particle growth of AuNPs[222] and by consequence the gold shell morphology obtained, this is balanced against the optimal pH for the functioning of the BPEI polymer. As was already discussed in section 3.2.2 page 93, BPEI is 44% charged in neutral conditions, with this percentage decreasing upon increasing pH. We therefore decided to test both basic and neutral pH conditions for the gold reduction reaction in the presence of our LN@BPEI@AuSeeds NPs, to observe its effect on the LN@Au NPs obtained.

At both pH conditions, we observed the progressive red-shifting of the UV-visible extinction pro-

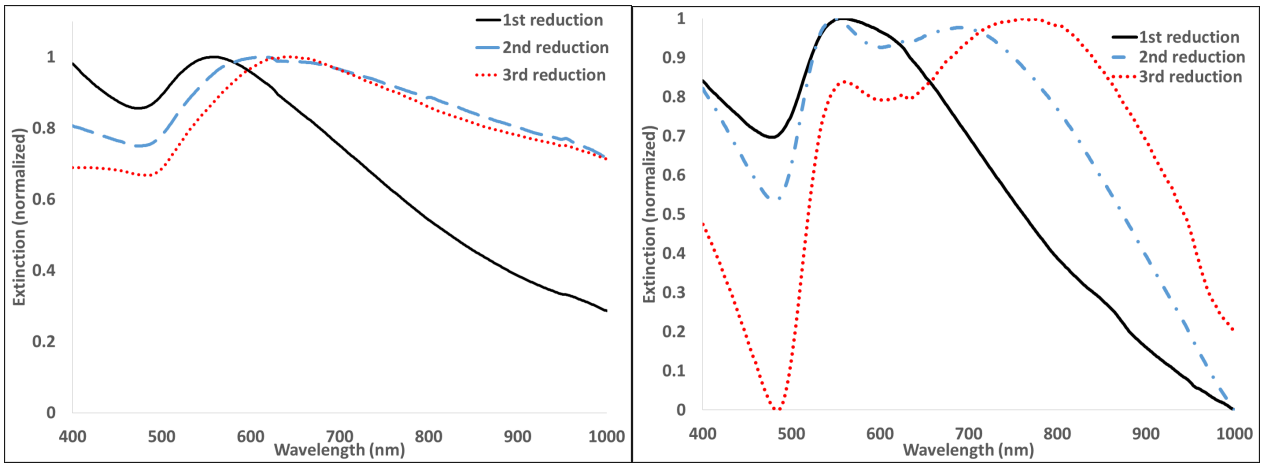


(a) (b)

Figure 4.6: (a) UV-Visible spectra of the nanoparticle dispersions after the 1st, 2nd and 3rd reduction steps at pH 11.5. (b) UV-visible spectra of the nanoparticle dispersions after the 1st, 2nd and 3rd reduction steps with no pH adjustment to the reaction medium.

files shown in fig. 4.6 (a) and (b). The progressive red-shifting of the plasmon band is thought to be due to the plasmon coupling interactions that occur between gold islands present on the LN surface. With each round of Au ion reduction, the interparticle distance between each gold island decreases until they coalesce. This red-shifts the longitudinal plasmonic response, until a complete shell is obtained. In the 2007 review by Ghosh *et. al*,[223] it is stated that for interparticle distances lower than 5 times the radius of the individual NPs, coupling effects become predominant, generally resulting in the red-shifting of the plasmon response.

At the basic conditions (fig. 4.6 (a)), the extinction profiles at the first, second and third reduction steps were broad single peak spectra. By the third reduction step, the extinction band spanned from 500-1000 nm with a maximum at 625 nm. Similarly reported by Lee *et. al*,[173] after six reduction steps the UV-visible profile of their final nanoparticles had a broad peak spanning from 500-1100 nm. The TEM image of the final LN@Au NPs shown in fig. 4.7 (a) revealed a more complete gold deposition on some of the LN@BPEI@AuSeeds NPs. Not all LN particles were completely coated with gold, as is evidenced by the EDS spectrum also shown in fig. 4.7 (a), which corresponds to the red circled region on the inserted TEM image. This may indeed be correlated to the lower degree of protonation of the amine groups of BPEI, which in turn could have disrupted the electrostatic attachment of the AuSeeds on the LN@BPEI surface. From the literature,[224] as well as from our own in-laboratory experiments, we know that the $Au^{3+}$ reduction by $NH_2OH.HCl$ is catalysed by the presence of the AuSeeds on the LN@BPEI surface, and the reduction reaction does not occur in the presence of LN, LN@BPEI NPs or AuSeeds. From the TEM images, the diameters of the LN@Au nanoparticles formed in basic pH conditions were measured to be greater than 200 nm. As

such, we concluded that there must have been multiple LN cores encapsulated by the Au coating.

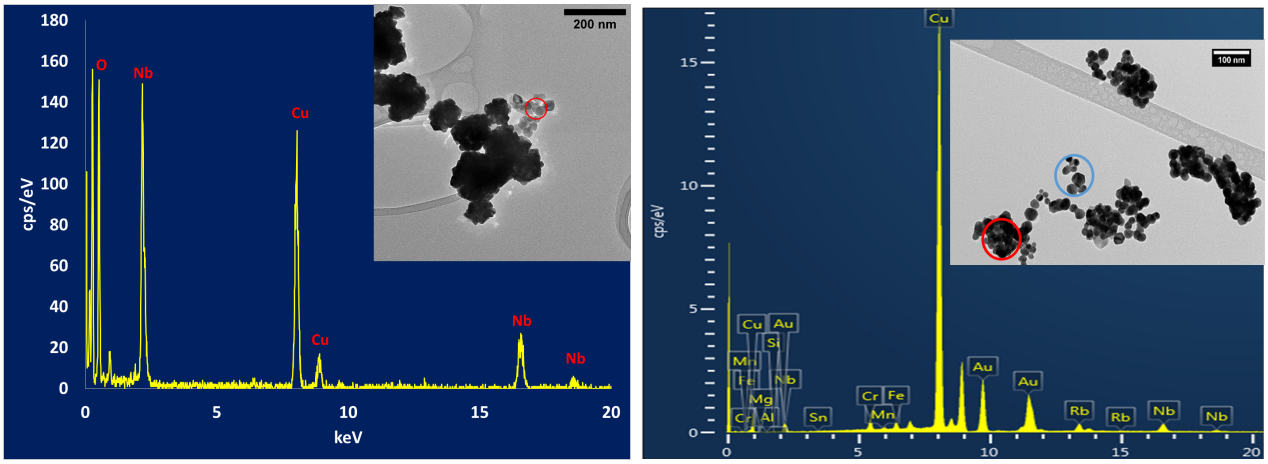


(a) (b)

Figure 4.7: EDS spectra and associated TEM images for LN@Au NPs synthesized under basic and neutral pH conditions. (a) EDS spectrum and corresponding TEM image of the nanoparticles formed after the 3$^{rd}$ reduction of $HAuCl_4$, 30 mM with $NH_2OH.HCl$ in the presence of LN@AuSeeds3000, with the reaction medium adjusted to pH 11.5 before each reduction. Red circle corresponds to the region at which the spectrum was obtained. (b) EDS spectrum (x-axis in keV) and corresponding TEM image of the nanoparticles formed after the 3$^{rd}$ reduction of $HAuCl_4$, 30 mM with $NH_2OH.HCl$ in the presence of LN@AuSeeds3000, with no pH adjustment to the reaction medium (pH approximately 7) before each reduction. Red circle corresponds to the region at which the spectrum was obtained. The blue circle corresponds to a region of pure AuNPs.

In examining the UV-visible spectra of the nanoparticles formed under the neutral pH conditions (see fig. 4.6 (b)), at the first reduction step, the extinction profile was a single peak spectrum, maximum at 557 nm. This peak is believed to be the plasmon response corresponding to individual, spherical gold nanoparticles on the LN surface. However, after the second and third reductions, it became a double peak spectra with the first peak centered on 550 nm, and the second peak progressively red-shifted into the NIR region. At the third reduction step, the UV-visible spectrum had a narrower peak width as compared to that of the basic conditions, spanning from 700-900 nm, with the maximum centered on 776 nm. As the targeted extinction maximum for these core-shell nanoparticles is centered on 800 nm, the nanoparticles synthesized under these neutral pH conditions were closer to this goal than the nanoparticles produced in the basic pH conditions.

TEM analysis of the LN@Au NPs at the third reduction step under neutral conditions revealed the smoother, spherical morphology of the AuNPs deposited on the LN surface (fig. 4.8 (b)), giving the LN@Au nanoparticle a raspberry-like morphology. The EDS analysis (see fig. 4.7 (b)) revealed that they were indeed individual Au spheres as it was possible to position the electron beam on a single

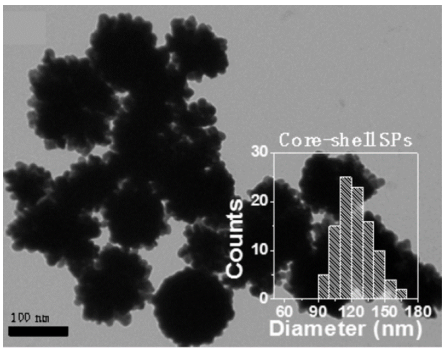


(a)

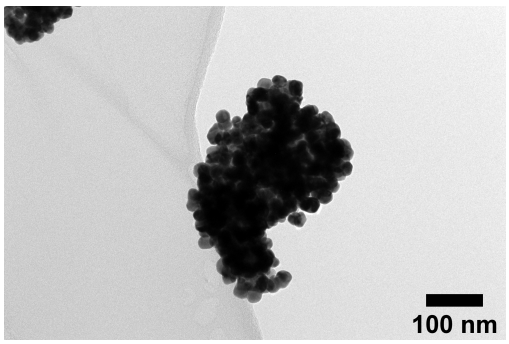


(b)

Figure 4.8: TEM images showing the morphology of the $Fe_3O_4$@Au NPs synthesized under basic pH conditions and LN@Au NPs synthesized under neutral pH conditions. (a) The spiky morphology of $Fe_3O_4$@Au NPs synthesized under basic pH conditions, after six reduction steps, taken from the article of Lee *et. al.*[173] (b) The raspberry morphology of LN@Au NPs synthesized under neutral pH conditions after three reduction steps.

AuNP on the surface, and obtain only a response for the Au element, and not Nb. This is already in direct contrast to the spiky, rough, surface morphology reported by Lee *et. al*[173] (see fig. 4.8 (a)) and what we observed in our basic synthesis conditions. Indeed, in seeded-growth methods, pH 7 is often the pH selected as it promotes an even deposition of the $AuCl(OH)^-_3$ nanocrystals (the gold species predominant at this pH depicted in fig. 3.12 on page 100) on the desired surface, which upon subsequent reduction to $Au^0$ produces a more homogenous Au coating.[165] The diameter of these LN@Au nanoparticles as determined by TEM were in two size categories: 80-120 nm and 200 nm and greater. As such, we believe that the gold coating may involve both single and multiple LN core encapsulation.

Further evaluation of the LN@Au nanoparticles formed under the neutral conditions by EDS analysis revealed a co-localization of the Nb, O and Au elements further confirming the core-shell structure. EDS chemical mapping showed the distribution of the elements Nb, O and Au in a single LN@Au nanoparticle, presented in fig. 4.9.

Though a gold deposition was achieved on the LN@BPEI@AuSeeds NPs at both basic and neutral pH conditions, the neutral conditions appeared to be more favourable for the following reasons: the narrower UV-visible band centered at 776 nm, the predominance of single LN core encapsulation by gold, and lastly conducting the synthesis under conditions closer to that of physiological pH which would allow us to collect data on the stability and behaviour of the nanoparticles in this environment. As such, the neutral pH conditions was selected as the optimal condition.

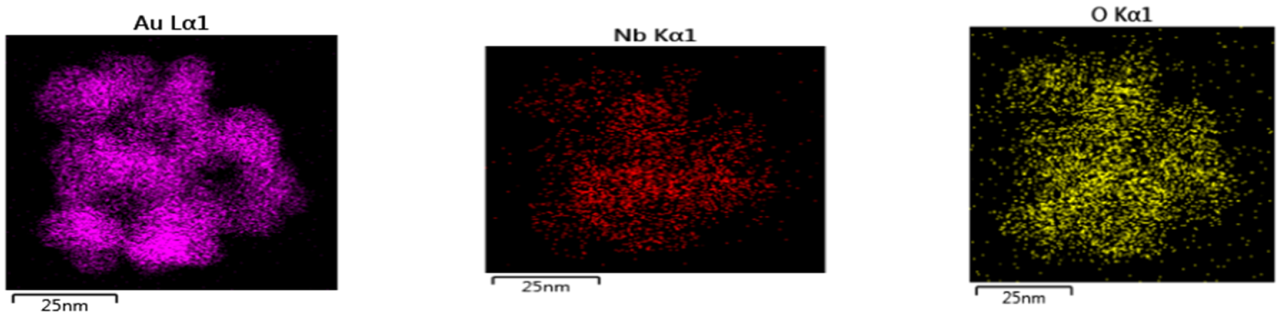


Figure 4.9: EDS chemical mapping of Au, Nb and O elements in LN@Au nanoparticle after 3 reduction steps. The synthesis conditions for the nanoparticle was LN@BPEI@Auseeds3000, neutral pH, $HAuCl_4$ 30 mM.

#### 4.2.2.2 Investigating the role of initial AuSeeds density on LN@BPEI NPs in the synthesis of LN@Au NPs

Having concluded that the neutral pH conditions were better suited for the gold shell synthesis, the influence of the initial AuSeed density on the LN surface was the next parameter investigated. The work of Bastús *et. al*[225] indicates that in a seeded growth mechanism, the ratio between gold seeds and the Au species precursor to be reduced is a factor to be optimized as it influences the type of AuNP growth observed (homogenous or inhomogeneous). From the results discussed in section 3.2.3 we see from the ICP-AES analysis (fig. 3.15 page 105), that from the LN@BPEI@AuSeeds1000 sample, we are already approaching the maximum LN surface coverable by the AuSeeds. Balancing this against the stability of the LN@BPEI@AuSeeds dispersion, as determined by the zeta potential values displayed in figure 3.17 on page 107, nanoparticle stability in water is achieved in the LN@BPEI@AuSeeds1000, LN@BPEI@AuSeeds2000, LN@BPEI@AuSeeds3000 samples. As the LN surface coverage was firstly evaluated by TEM analysis, the 13.8% difference between the AuSeeds density in the LN@BPEI@AuSeeds1000 and LN@BPEI@AuSeeds3000 led us to choose these two samples as varied seed densities. The other synthesis conditions (pH and $HAuCl_4$ concentration) were kept constant and have been precised in table 4.2 on page 117. The characterization data of the nanoparticles after each reduction step is given in table 4.4 and the UV-visible extinction profiles shown in fig. 4.10.

In comparing the two initial seeding conditions, it was observed that after three gold ion reduction steps, both the LN@BPEI@AuSeeds1000 and LN@BPEI@AuSeeds3000 samples produced nanoparticle dispersions with a double peak UV-visible extinction profile. For both samples, the first peaks were centered at 538 and 557 nm respectively after the first reduction step. These peaks are attributed to the plasmon response of the individual spherical AuNPs on the core nanoparticle, and is present in the double peak spectra of the nanoparticle dispersions after the second and third reduc-

| | 1st reduction | | 2nd reduction | | 3rd reduction | |
|---|---|---|---|---|---|---|
| LN@BPEI@AuSeeds | 1000 | 3000 | 1000 | 3000 | 1000 | 3000 |
| $\lambda$ extinction peak (nm) | 513 | 557 | 553, 698 | 549, 690 | 571, 803 | 560, 776 |
| Zeta potential (mV) | +14.2 | +7.27 | +25.7 | -2.51 | +30.2 | -11.6 |
| Z-avg (d.nm) | 155.6 | 230.6 | 218.1 | 238.6 | 163.3 | 202.0 |
| PDI | 0.140 | 0.291 | 0.289 | 0.384 | 0.118 | 0.349 |

Table 4.4: Characterization data for LN@Au nanoparticles after each $HAuCl_4$ reduction step. 50 $\mu$L of 30 mM $HAuCl_4$ is reduced by 75 $\mu$L of 0.2 M $NH_2OH.HCl$ in the presence of LN@BPEI@AuSeeds1000 or LN@BPEI@AuSeeds3000.

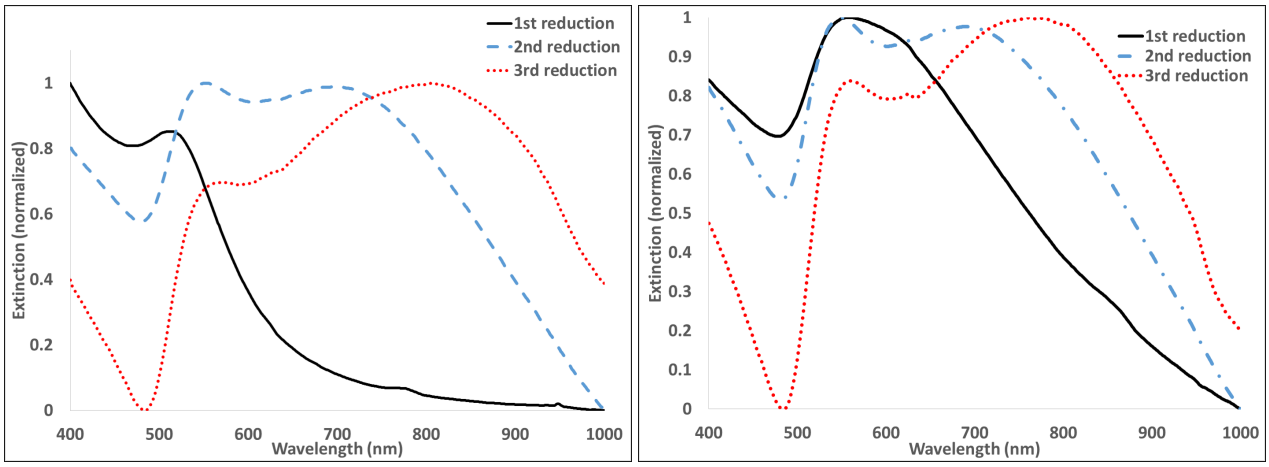


(a) (b)

Figure 4.10: UV-Visible spectra corresponding to LN@Au nanoparticles after each $HAuCl_4$ reduction step, where the initial LN@BPEI@AuSeeds samples were (a) LN@BPEI@AuSeeds1000 or (b) LN@BPEIAuSeeds3000.

tion steps. The extinction maximum of the second peaks at the second reduction step was 690 nm for both samples, and finally at the third reduction step, the second peaks were centered at 803 nm for LN@BPEI@AuSeeds1000 and 776 nm for LN@BPEI@AuSeeds3000 respectively. As there was a similar progressive red-shifting of the wavelength of extinction maximum in both samples, we can assume that the mechanism of gold shell growth is similar in both samples. The peak widths of both samples at the third reduction step spanned from 700 to 900 nm. This was a desirable wavelength span when considering the intended applications for these nanoparticles as *in-vivo* photothermal agents upon irradiation with a NIR laser. From the UV-visible analysis, one might assume that the two samples are nearly identical. Indeed, when taking into account the LN surface covered by the AuSeeds as determined by ICP-AES (refer to fig. 3.15, page 105), we see that the difference between the two LN@BPEI@AuSeeds samples is less than 1%.

Although based on the UV-visible analysis, we may be led to infer that both samples are very

similar, the zeta potential, Z-avg and PDI values tell a different story. As is seen from table 4.4, the LN@BPEI@AuSeeds3000 samples' zeta potentials had an absolute value of less than 20 mV at each step. This is usually an indication of lower colloidal, or in our case, nanoparticle dispersion stability, prone to aggregation. The LN@BPEI@AuSeeds1000 samples' zeta potentials however became progressively more positive after each reduction step, with the final LN@Au NPs having a zeta potential of +30.2 mV. Further to this point, the Z-avg and PDI values of LN@Au NPs corresponding to the LN@BPEI@AuSeeds3000 samples were higher than that of the LN@BPEI@AuSeeds1000 samples. By the final reduction step, the LN@Au dispersion from the LN@BPEI@AuSeeds3000 sample had a PDI of 0.349 (0.118 for the LN@BPEI@AuSeeds1000). This increasing PDI can be rationalized as a result of the increasing number of free AuNPs in the sample, which is evidenced by the TEM image in fig. 4.11 (c). This too can explain the zeta potential values as the free AuNPs will have also contributed to its quantification.

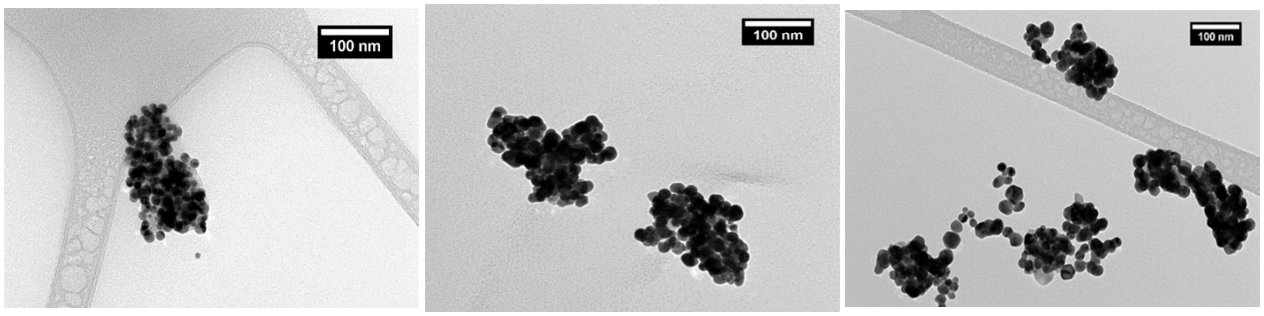


(a) (b) (c)

Figure 4.11: TEM images of LN@Au nanoparticles at (a) 1$^{st}$, (b) 2$^{nd}$ and (c) 3$^{rd}$ reduction steps starting from initial LN@BPEI@AuSeeds3000. Reduction performed at neutral pH, using 30 mM $HAuCl_4$ and 0.2 M $NH_2OH.HCl$.

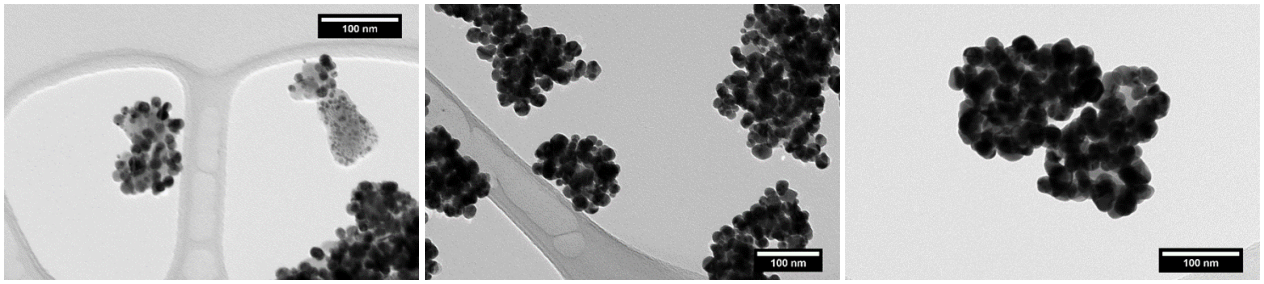


(a) (b) (c)

Figure 4.12: TEM images of LN@Au nanoparticles at (a) 1$^{st}$, (b) 2$^{nd}$ and (c) 3$^{rd}$ reduction steps starting from initial LN@BPEI@AuSeeds1000. Reduction performed at neutral pH, using 30 mM $HAuCl_4$ and 0.2 M $NH_2OH.HCl$.

The TEM imaging of LN@Au corresponding to each reduction step starting from LN@BPEI@AuSeeds-

3000 showed the same progression of gold shell growth as the LN@Au corresponding to LN@BPEI@AuSeeds1000 sample (see fig. 4.12). However, in the latter, we observed no free AuNPs on the TEM grids. This is corroborated by the low PDI value of 0.118 for the final LN@Au NPs. The question therefore is why does the LN@BPEI@AuSeeds3000 sample produce both LN@Au and free AuNPs whereas the LN@BPEI@AuSeeds1000 sample produces only LN@Au? If we look at the data in table 4.5, we see clear differences in the initial LN@BPEI@AuSeeds samples. Although the absolute number of seeds per LN as determined by ICP-AES analysis vary by less than 1%, the absolute number of AuSeeds used to prepare the LN@BPEI@AuSeeds3000 is three times the amount used for the LN@BPEI@AuSeeds1000 preparation. It is therefore probable that excess AuSeeds remain in the dispersion, held by the positive surface charge of the BPEI polymer, but not securely attached to the NP, having a place in the solvation sphere around the NPs. As the reducer is added, the gold seeds, in the presence of the LN oxide surface, catalyze the reduction of the $Au^{3+}$ to $Au^{0}$, but there is insufficient surface area for each individual AuSeed to grow, and the loosely held AuSeeds separate completely from the LN NPs, forming free AuNPs. For the LN@BPEI@AuSeeds1000 sample, the amount of AuSeeds added to prepare the sample seems to be sufficient such that all the AuSeeds present attach securely, without leaving much AuSeeds excess in the aqueous media.

| Sample | Zeta Potential (mV) | Z-Avg (nm) | PDI |
|---|---|---|---|
| LN@BPEI@AuSeeds3000 | -31.8 ± 20.8 | 204.9 | 0.24 |
| LN@BPEI@AuSeeds1000 | -31.5 ± 0.28 | 161.3 | 0.11 |

Table 4.5: Zeta potential, Z-Avg and PDI values for LN@BPEI@AuSeeds3000 and LN@BPEI@AuSeeds1000.

Further analysis of the TEM images revealed that both the LN@BPEI@AuSeeds1000 and LN@BPEI@AuSeeds3000 samples, produced the same raspberry-like shell morphology. Using the ImageJ software, the average diameter of these attached gold spheres on the LN core was measured at each reduction step. For both samples, at each gold reduction step, the AuNP diameter progressively increased. The average diameters measured were 12.5 ± 2.5, 19.0 ± 4.1 and 26.0 ± 5.6 nm after the $1^{st}$, $2^{nd}$ and $3^{rd}$ reduction steps respectively for LN@BPEI@AuSeeds1000. When the gold spheres were 26 nm in diameter, it was possible to position the electron beam in EDS to obtain a response from both the gold sphere and the LN core as in fig. 4.13 (a) or solely a response from the gold sphere as shown in fig. 4.13 (b).

In considering all of the data presented above, we concluded that starting with the LN@BPEI@AuSeeds1000 sample, allowed for more homogeneity, producing a single population of LN@Au NPs than the LN@BPEI@AuSeeds3000 sample that produced both LN@Au NPs and free AuNPs.

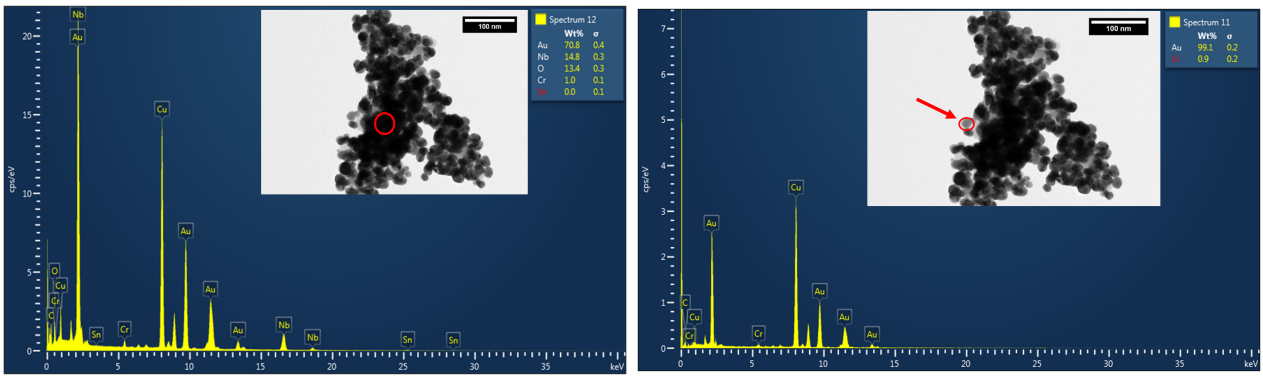


(a) (b)

Figure 4.13: EDS spectra and corresponding TEM images of LN@Au nanoparticles showing the element composition in different regions of the nanoparticles. (a) EDS spectrum corresponding to the red circle on the TEM image showing the presence of both Au and Nb elements. (b) EDS spectrum corresponding to the red circle on the TEM image showing the presence of only Au element.

#### 4.2.2.3 Investigating the role of $HAuCl_4$ concentration on the LN@Au NPs synthesis

We have at this point concluded that our LN@BPEI@AuSeeds1000 are the optimal gold-seeded LN NPs for our gold shell synthesis, and furthermore that performing the gold ion reduction in neutral pH conditions allows for more control on the deposition of the reduced gold atoms onto the desired core surface. The final parameter we opted to test was that of the gold salt concentration used at each reduction step. Varying the molar quantity of the $HAuCl_4$ to be reduced, is effectively experimenting with the kinetics of the gold reduction reaction. In the works of Zhao *et. al*,[226] they experimented with the reaction kinetics in their gold-seeded growth of AuNPs by changing the concentration of the reducer (which changes the [reducer]/[$HAuCl_4$] ratio) and found that upon increasing their reducer concentration, they were able to change the shell morphology from smooth spheres to what they called "nanoflowers". Their nanoflowers, have a likeness in appearance to our raspberry-like morphology already attained.

As the reducer $NH_2OH.HCl$ was always used in excess, making the $HAuCl_4$ the limiting reagent, we decided to play with the gold chloride concentration instead. The default gold ion concentration of 30 mM was based on the work of Goon *et. al*[208] and Lee *et. al*.[173] We therefore decided to test three more $HAuCl_4$ concentrations, 3 mM, 10 mM and 100 mM, keeping the other experimental parameters (pH and LN@BPEI@AuSeeds) fixed (detailed in table 4.2, page 117). Upon the first reduction using the 100 mM $HAuCl_4$ concentration, a rapid aggregation of the nanoparticles was observed, forming large aggregates that quickly settled to the bottom of the reaction vessel. As

such, for the rest of this section, we will be discussing the results from the 3 mM, 10 mM and 30 mM $HAuCl_4$ concentrations.

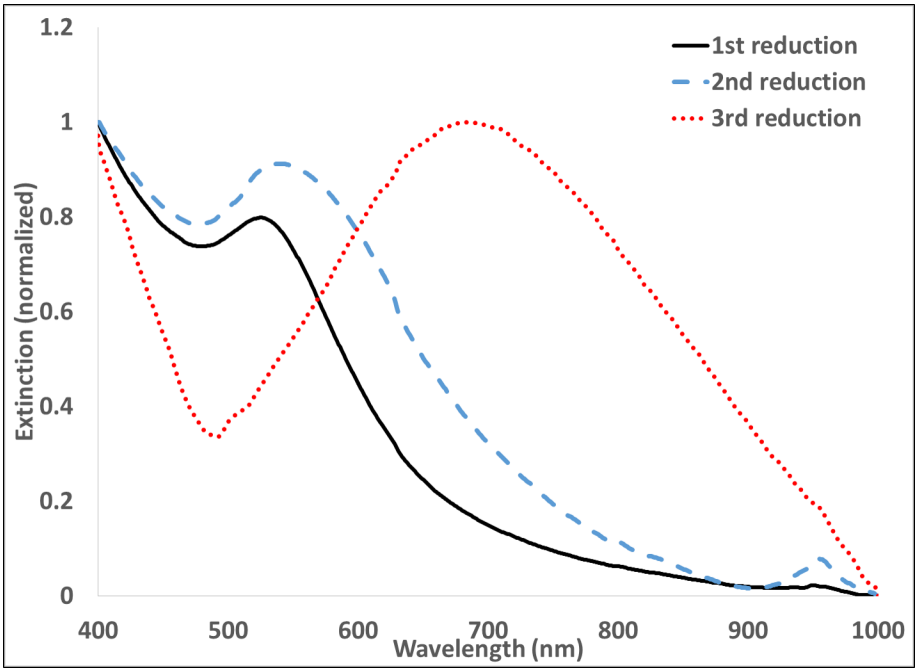


Figure 4.14: UV-visible spectra of LN@Au NPs formed after 1st, 2nd and 3rd reduction with 3 mM $HAuCl_4$ and 0.2 M $NH_2OH.HCl$ beginning with LN@BPEI@AuSeeds1000 NPs.

From the UV-visible spectra for the LN@Au NPs produced using the 3 mM $HAuCl_4$ concentration shown in fig. 4.14, we observed a red-shifting of the single peak extinction profile upon each reduction step. The single peak spectral profile already distinguishes the 3 mM synthesis from the double peak spectral profile of the 30 mM synthesis (already discussed in the previous section). Furthermore, after the third reduction the extinction peak for the 3 mM synthesis was at 693 nm, 110 nm blue-shifted as compared to the extinction peak at the equivalent number of reduction steps but using the 30 mM $HAuCl_4$.

In figure 4.15, we provide the TEM images of the LN@Au NPs after the third reduction using 3 mM $HAuCl_4$. What was observed from the images was an incomplete filling of the LN nanoparticle surface. We also marked an elongation of the gold deposition on the LN, as opposed to spherical Au deposits as was seen in our particles formed using 30 mM $HAuCl_4$. This difference in shell morphology helps us to better interpret the UV-visible spectra. Indeed, in our 30 mM $HAuCl_4$ synthesis, we observed distinct gold spheres, attached to the LN core. This then resulted in a double band spectral profile, the first peak located between 530-570 nm corresponding to the plasmon response of the gold spheres, and the progressively red-shifting, second band, due to the plasmon coupling in-

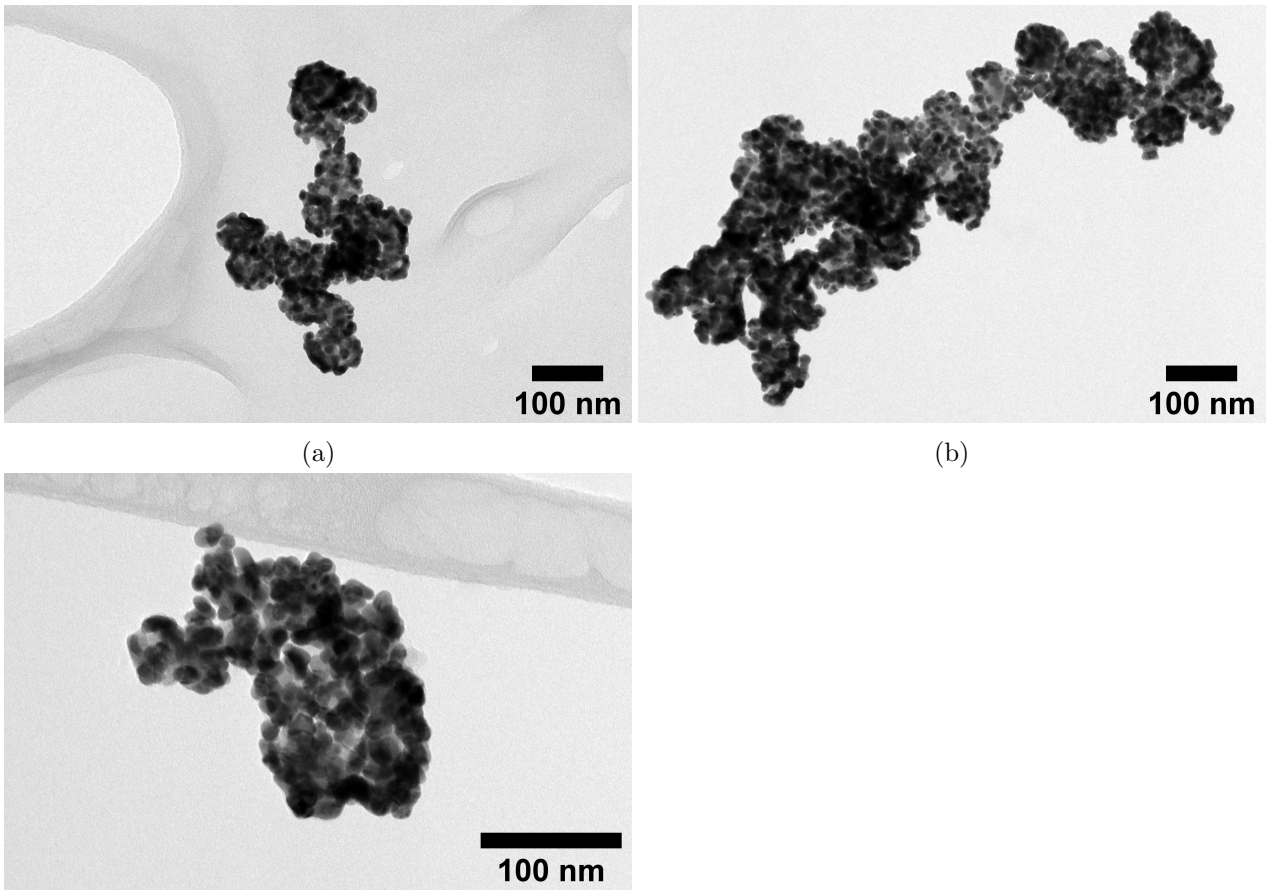


(a) (b)

(c)

Figure 4.15: TEM images of LN@Au NPs after 3rd reduction with 3 mM $HAuCl_4$, starting with LN@BPEI@AuSeeds1000, and reducing with 0.2 M $NH_2OH.HCl$

teractions between these gold spheres. However, in the case of the 3 mM $HAuCl_4$, the gold deposits are elongated and flattened along the surface of the LN, hence eliminating the plasmon response pertaining to gold spheres and resulting in a progressively shifting, single peak plasmon response. We therefore believe that the mechanism of the gold shell growth in the 3 mM case is different from that of the 30 mM case. Real-time analysis of the synthesis, by taking aliquots of the dispersion at different points of the synthesis, as was done by Zhao *et. al*[226] process could allow us to determine what species are present in the dispersion at different points. What we hypothesis is that in the 30 mM synthesis, we have the $AuCl(OH)^-_3$ on the surface of the LN as well as throughout the aqueous media, and upon addition of the reducer, there is a burst formation of $Au^0$ that quickly agglomerate to the most thermodynamically stable form, which is a sphere. In the 3 mM case, we suspect that due to the lower molar quantity of the $AuCl(OH)^-_3$, upon reduction, the $Au^0$ atoms arrange and re-arrange themselves on the LN surface. Real-time UV-visible analysis, similar to those performed by Natan *et. al*[134] and other groups, has also been discussed as future experiments to investigate this, but due to time restraints for the thesis, were not conducted.

| | Zeta Potential | Z-Avg(nm) | PDI |
|---|---|---|---|
| 1st reduction | +27.2 ± 0.29 | 166.6 | 0.141 |
| 2nd reduction | +19.9 ± 0.90 | 188.9 | 0.188 |
| 3rd reduction | +26.1 ± 0.49 | 198.1 | 0.260 |

Table 4.6: Zeta potential, Z-avg and PDI values of the LN@Au NPs after the 1st, 2nd and 3rd reduction steps using 3 mM $HAuCl_4$, 0.2 M $NH_2OH.HCl$ and starting from LN@BPEI@AuSeeds1000 NPs.

In table 4.6 the additional characterization data (zeta potential, Z-avg and PDI values) are provided to enhance our qualitative assessment of the nanoparticle dispersions. From the zeta potential values, we can infer that, generally, this synthesis results in nanoparticles that are stably dispersed in the aqueous media. The Z-avg values show that the particles measured in the solution are increasing in their hydrodynamic diameter upon each reduction step, though from the PDI, the size polydispersity is also increasing. We never neglect that there is a degree of size dispersity in the initial LN NPs, and this is possibly an influencing factor in the increasing PDI value upon growing the shell.

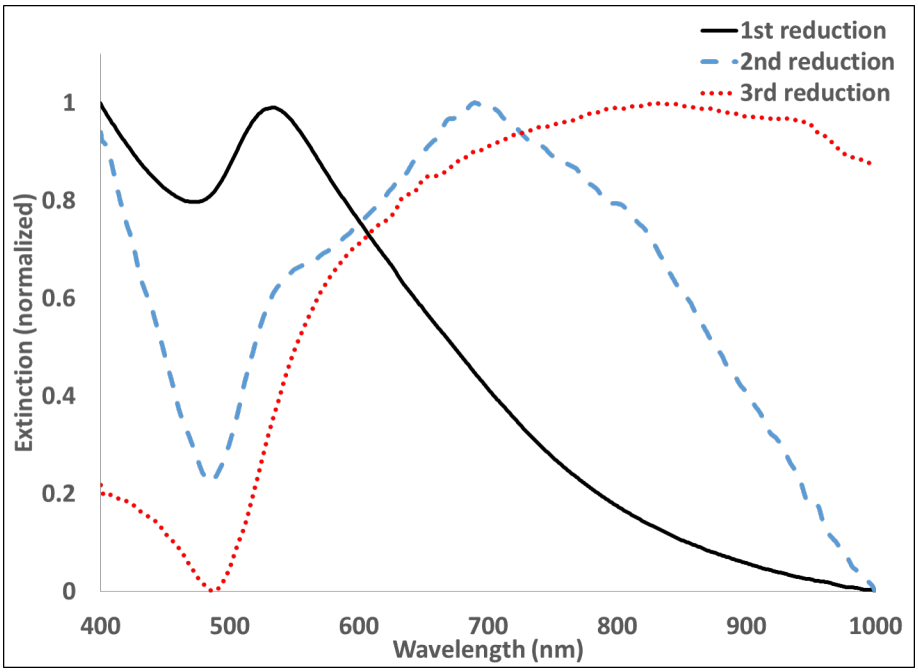


Figure 4.16: UV-visible spectra of LN@Au NPs formed after 1st, 2nd and 3rd reduction with 10 mM $HAuCl_4$ and 0.2 M $NH_2OH.HCl$ beginning with LN@BPEI@AuSeeds1000 NPs.

The UV-visible spectra for the LN@Au NPs produced using the 10 mM $HAuCl_4$ concentration is shown in fig. 4.16. At the first reduction, the spectrum is similar to that obtained at the same step for the 3 mM and 30 mM: single band, with a peak centered within the 530-550 nm range. Then

at the second reduction step, a red-shifted band appeared at 690 nm, with a visible shoulder at 550 nm. We can qualitatively describe it as in between the UV-visible spectra obtained at the same step for the 3 mM and 30 mM $HAuCl_4$ concentrations. Finally, at the third reduction step, we observed a wide single band, ranging from 550-1000 nm. We must point out that our spectral acquisition ended at 1000 nm as it is the upper wavelength limit of our spectrometer. In figure 4.17, we present the UV-visible spectra of the LN@Au after the third reduction step for all three $HAuCl_4$ concentrations tested. What we can safely conclude is that the 30 mM $HAuCl_4$ concentration exhibits a narrower plasmon response centered around 800 nm in comparison to the other two concentrations.

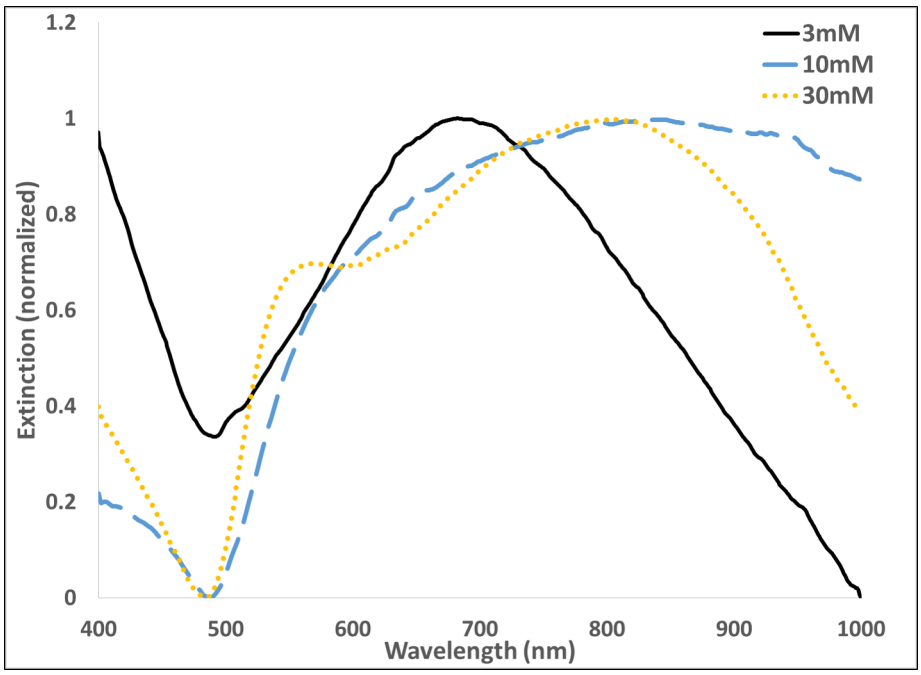


Figure 4.17: UV-visible extinction spectra of LN@Au nanoparticles after the third $HAuCl_4$ reduction steps using 3 mM, 10 mM and 30 mM $HAuCl_4$, and 0.2 M $NH_2OH.HCl$, beginning with LN@BPEI@AuSeeds1000 NPs and neutral pH.

In table 4.7, the additional characterization data (zeta potential, Z-avg and PDI values) pertaining to the 10 mM $HAuCl_4$ concentrations is given. The data is not as clear to interpret as was the case for the 3 mM and the 30 mM and so we relied on the TEM images of these nanoparticles to provide greater clarity. The TEM images are provided in fig. 4.18. Upon analysis, we identified two gold shell morphologies present on the LN cores: the elongated, incomplete gold shell similar to what was observed at the 3 mM $HAuCl_4$ concentration (see fig. 4.18 (a)), and a contiguous shell, with edges and points (see fig. 4.18 (b)), a morphology not before observed in our synthesis. We confirmed by EDS analysis that these particles were in fact comprised of both Au and Nb elements. We have not yet elucidated why the 10 mM concentration produced mixed gold shell nanoparticles, but it coupled with the low zeta potential and high PDI values measured, were sufficient deterrents

for us to halt our study of the 10 mM $HAuCl_4$ concentration.

| | Zeta Potential | Z-Avg(nm) | PDI |
|---|---|---|---|
| $1^{st}$ reduction | +7.95 ± 0.36 | 173.1 | 0.195 |
| $2^{nd}$ reduction | -9.55 ± 0.58 | 275.0 | 0.258 |
| $3^{rd}$ | +20.8 ± 0.27 | 159.3 | 0.225 |

Table 4.7: Zeta potential, Z-avg and PDI values of the LN@Au NPs after the $1^{st}$, $2^{nd}$ and $3^{rd}$ reduction steps using 10 mM $HAuCl_4$, 0.2 M $NH_2OH.HCl$ and starting from LN@BPEI@AuSeeds1000 NPs.

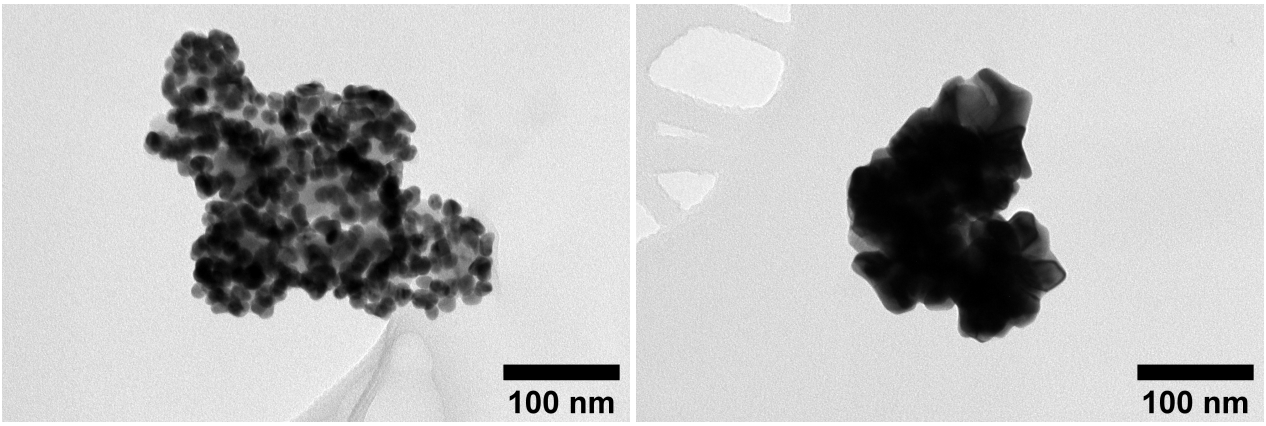


(a) (b)

Figure 4.18: TEM images of LN@Au NPs after $3^{rd}$ reduction with 10 mM $HAuCl_4$, starting with LN@BPEI@AuSeeds1000, and reducing with 0.2 M $NH_2OH.HCl$

| | 3 mM | 10 mM | 30 mM |
|---|---|---|---|
| $\lambda$ extinction peak ($3^{rd}$ reduction (nm) | 693 | broad band (500-1000) | 803 |
| Z-avg (nm) | 198.1 | 159.3 | 163.3 |
| PDI | 0.260 | 0.225 | 0.118 |
| Zeta potential (mV) | +26.1 | +20.8 | +30.2 |
| Shell morphology | elongated Au islands | elongated Au islands and contiguous with edges | overlapping spherical AuNPs |

Table 4.8: Summary of final nanoparticle dispersions produced using 3, 10 and 30 mM $HAuCl_4$ at each reduction step. The initial nanoparticles were LN@BPEI@AuSeeds1000 and 0.2 M $NH_2OH.HCl$ reducer was used.

In table 4.8, a summary of the differentiating characteristics of the nanoparticles produced using 3, 10 and 30 mM $HAuCl_4$ is provided. In conclusion, the 3 mM $HAuCl_4$ concentration, allowed the reaction rate to be sufficiently slow to obtain a flatter, elongated gold deposition on the LN core, however as our desired application is to use them as NIR photothermal conversion probes, having the plasmon response in the NIR region is more attractive than a smoother gold shell. It is possible that continued reduction steps with this concentration may indeed lead to LN@Au NPs with a characteristic plasmonic response around 800 nm, but this balanced against the experimental time and the increasing PDI value was not considered to be the optimal parameters for the gold shell growth. The 10 mM, produced a mixed gold shell morphology that we could not control and so this was not considered the optimal concentration. The final LN@Au NPs produced with the 30 mM $HAuCl_4$ concentration had a plasmon response centered on 800 nm, with a PDI value of 0.11, and was stably dispersed in its aqueous media making it an acceptable nanoparticle dispersion.

We ultimately concluded that when taking into consideration the intended application of these core-shell nanoparticles, the parameters in this LbL synthesis that produced the most suitable LN@Au NPs were: LN@BPEI@AuSeeds1000, neutral (unaltered) pH, 30 mM $HAuCl_4$ concentration reduced with 0.2 M $NH_2OH.HCl$, with a total of three gold reduction steps.

### 4.2.3 Physical and chemical characterization to analyze the Au shell growth on LN NPs

#### 4.2.3.1 Calculation of gold shell thickness using ICP-AES analysis

ICP-AES analysis was used to determine the concentration of each element present in the LN@Au NPs dispersion, corresponding to the optimized synthesis parameters, i.e, starting with LN@BPEI@-AuSeeds1000 NPs, performing three $HAuCl_4$ reductions with 0.2 M $NH_2OH.HCl$ under neutral pH conditions. From the analysis, the Au concentration was determined to be 0.017 mg/mL. Using the density of Au (19.3 $g/cm^3$), we were able to calculate the volume of Au present in 1 mL of the LN@Au sample ($8.808 \times 10^{14}$ $nm^3$). Then using the ICP-AES determined concentration of Nb (0.016 mg/mL), we calculated the mass of $LiNbO_3$ in 1 mL to be 0.025 mg/mL which we converted to $1.126 \times 10^{11}$ NPs/mL using the mass of LN NP ($2.22 \times 10^{-13}$ mg). Then using the formula for surface area of a sphere, we calculated the total surface area of LN. Assuming homogenous deposition of Au on each LN, we took the total volume of Au in 1 mL and divided it by the total surface area of LN in 1 mL, to give us a gold shell width of 1.2 nm.

#### 4.2.3.2 Surface characterizations by XPS and TOF-SIMS

XPS and TOF-SIMS characterization were used in a complementary fashion to provide further analysis on the surface of the nanoparticles at different key steps in the synthesis. The samples analyzed were LN, LN@BPEI@AuSeeds1000, LN@BPEI@AuSeeds3000, LN@BPEI@AuSeeds1000-@BPEI, LN@BPEI@AuSeeds3000@BPEI, LN@Au ($3^{rd}$ reduction from LN@BPEI@AuSeeds1000) and LN@Au ($3^{rd}$ reduction from LN@BPEI@AuSeeds3000).

| Positive Loadings PC1 | |
|---|---|
| Fragments | Peak area |
| Nb_3O_8- | 1.00E+00 |
| Nb_5O_13- | 3.95E-01 |
| Nb_2O_6H- | 1.24E-01 |
| Nb_2O_5- | 1.04E-01 |
| LiNb_2O_6- | 5.19E-02 |
| NbO_3H- | 3.86E-02 |
| Nb_2O_6- | 3.58E-02 |
| LiNb_4O_11- | 3.17E-02 |
| NbO_2- | 1.73E-02 |
| NbO_4H_2- | 1.68E-02 |
| Li_2Nb_3O- | 1.32E-02 |
| NbO_2H- | 9.06E-03 |
| NbO_4H- | 7.65E-03 |
| NbO_4- | 2.39E-03 |
| CsNb_5O_8H_ | 1.94E-03 |
| Nb_2O_5H- | 1.84E-03 |
| NbO_3H_2- | 1.72E-03 |
| CsO_2- | 1.23E-03 |
| CsOH- | 8.88E-04 |
| Nb_7O_9H_3- | 7.92E-04 |

| Negative Loadings PC1 | |
|---|---|
| Fragments | Peak area |
| C_2H_2N- | -2.58E-01 |
| C_2H_3N- | -9.91E-02 |
| CH_2NO- | -9.08E-02 |
| C_2HN- | -3.89E-02 |
| 64.00 u | -3.67E-02 |
| C_2H_4N- | -3.24E-02 |
| Au- | -2.46E-02 |
| C_3HNLi- | -2.36E-02 |
| NN_2O_2H_2 | -2.25E-02 |
| C_3H_4NO- | -2.10E-02 |
| C_3H_3N_2O | -1.17E-02 |
| CHO_2- | -9.20E-03 |
| C_2N- | -7.88E-03 |
| C_2H_3NO_3 | -7.75E-03 |
| C_3H_2N- | -7.52E-03 |
| C_6HN- | -5.91E-03 |
| C_5N- | -5.31E-03 |
| C_3H_2NO_2 | -5.17E-03 |
| C_3H_3O- | -4.95E-03 |
| CH_2N- | -4.48E-03 |

| Positive Loadings PC2 | |
|---|---|
| Fragments | Peak area |
| Au- | 3.44E-01 |
| Au_3- | 5.22E-02 |
| Nb_2O_5H- | 3.03E-02 |
| NbO_2H_2- | 2.42E-02 |
| Au_2- | 1.86E-02 |
| CH_3O- | 1.22E-02 |
| C_5N- | 9.37E-03 |
| Cs- | 8.61E-03 |
| Li- | 7.48E-03 |
| CsO_2- | 6.61E-03 |
| C_8H_11O_4- | 3.63E-03 |
| Au_4- | 3.54E-03 |
| LiOH- | 1.41E-03 |
| AuH- | 1.21E-03 |
| LiH- | 1.12E-03 |
| AuO- | 8.08E-04 |
| Au_4H- | 5.14E-04 |
| CsOH- | 4.51E-04 |
| ^6Li- | 2.07E-04 |
| LiO- | 1.30E-04 |

| Negative Loadings PC2 | |
|---|---|
| Fragments | Peak area |
| C_2H_2N- | -1.00E+00 |
| Nb_3O_8- | -5.76E-01 |
| CH_2NO- | -3.88E-01 |
| C_2H_3N- | -2.90E-01 |
| Nb_5O_13- | -2.19E-01 |
| 64.00 u | -1.42E-01 |
| C_2H_4N- | -1.40E-01 |
| C_2HN- | -1.40E-01 |
| C_3H_4NO- | -9.31E-02 |
| C_3HNLi- | -8.36E-02 |
| NN_2O_2H_2- | -7.23E-02 |
| Nb_2O_5- | -5.73E-02 |
| C_3H_3N_2O- | -4.23E-02 |
| Nb_2O_6H- | -3.47E-02 |
| LiNb_2O_6- | -3.16E-02 |
| CHO_2- | -2.97E-02 |
| C_3H_2N- | -2.60E-02 |
| Nb_2O_6- | -2.19E-02 |
| C_2N- | -1.92E-02 |
| NbO_3H- | -1.90E-02 |

Figure 4.19: TOF-SIMS characteristic peaks areas for PC1 and PC2

TOF-SIMS data mining was performed using principle component analysis (PCA). Typical PCA outputs are Principal Components (PCs), loadings and scores. The scores describe the relationship between each PC and the samples, and the loadings show a group of variables (peak areas), which define each PC. Figure 4.19 shows the peak areas of the most characteristic peaks for PC1 and PC2 loadings shown in fig. 4.20. Loadings are made of positive and negative loadings. All the fragments comprising positive or negative loadings are correlated whereas fragments in positive are anti-correlated to fragments in negative loadings and vice versa. Positive PC1 loadings (PC1+) show correlated peaks corresponding mainly to Li an Nb fragments whereas negative PC1 loadings (PC1-) show correlated peaks corresponding mainly to fragments containing C, H, N and O. This suggests that PC1+ relates to the bare $LiNbO_3$ particles and PC1- relates to the BPEI. PC2+ shows gold fragments as the most intense peak areas, which suggests that this PC could represent mainly samples containing gold. Finally, the PC2- shows a C, H, N, O and Nb fragments as the most intense peak areas, representing both, the $LiNbO_3$ particles and BPEI.

XPS analysis was performed on the same samples used for TOF-SIMS analysis. The results obtained from XPS was in agreement with what was observed by TOF-SIMS. In fig. 4.21 the wide XPS spec-

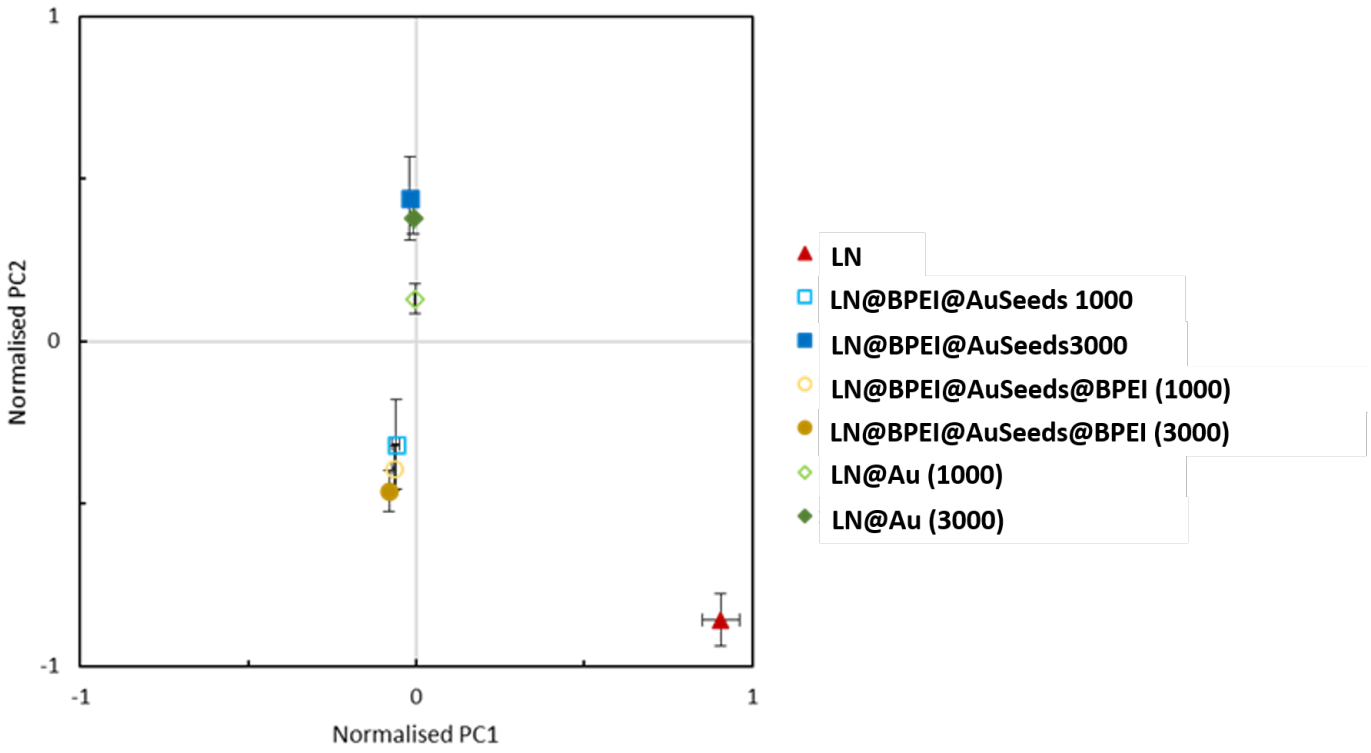


Figure 4.20: TOF-SIMS PC1 and PC2 loadings for LN, LN@BPEI@AuSeeds1000, LN@BPEI@AuSeeds3000, LN@BPEI@AuSeeds1000@BPEI, LN@BPEI@AuSeeds3000@BPEI, LN@Au ($3^{rd}$ reduction from LN@BPEI@AuSeeds1000) and LN@Au ($3^{rd}$ reduction from LN@BPEI@AuSeeds3000)

trum for LN NPs is given while fig. 4.22 displays the XPS survey spectra of the LN@Au NPs at different steps of their synthesis for starting with LN@BPEI@AuSeeds1000 and LN@BPEI@AuSeeds3000 NPs. In the table 4.9 the calculated XPS atomic percentages (at%) are given.

From the LN NPs XPS spectra, the following photoelectrons were observed: O1s (531 eV), Nb 3s (472 eV), Nb 3p (3p3/2 365 eV; 3p1/ 381 eV), C 1s (285 eV), Nb 3d (207 eV), Nb 4s (60 eV), Nb 4p (1/2 and 3/2 at 35 eV) and Nb 5p/O 2s(21. eV). The Nb 3d doublet shows a spin-orbit splitting of 2.73 eV in agreement with published work.[64,227] The photoelectron Li 1s is observed with a low intensity at 55 eV due to its low cross section of photo-ionization. Additional photoelectrons assigned to Si 2s and Si 2p (150 and 100 eV, respectively) were also observed and corresponded to the substrate on which the nanoparticles were casted. A contribution related to hydrocarbon is also observed at 285 eV.

The Nb at% to Li at% is close to the expected value of 1 (1.3). Deviation from the theoretical value can be to some part attributed to the low signal of Li1s and its low RSF (0.057) leading to high

variation in the calculation of Li at %. The O at% over the one of Nb is 2.7 (theoretical= 3). The contribution of silicon oxide to the O1s is very low as the atomic percentage of Si is 2-3%.

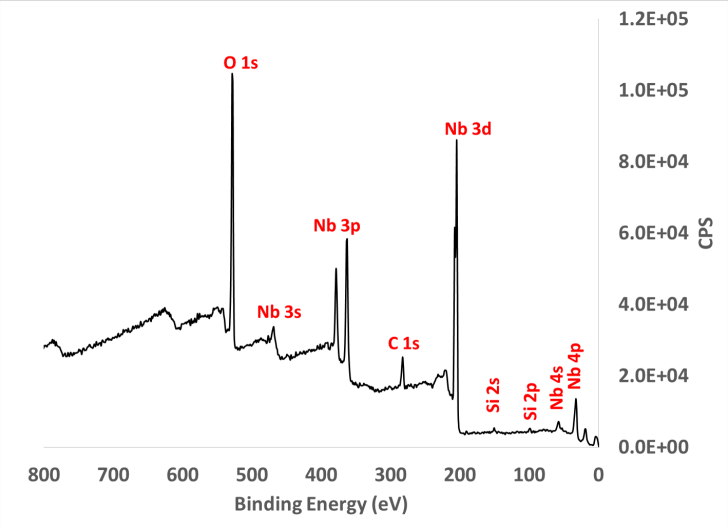


Figure 4.21: Wide XPS spectrum of LN NPs.

Upon BPEI coating followed by gold-seeding of LN leading to LN@BPEI@AuSeeds1000 (fig. 4.22 (a)), additional lines are observed which are characteristic of gold (Au4p 547 eV, Au4d 335 eV, Au4f 84 eV) and nitrogen (N1s 400 eV). As expected the coverage of LN particles by BPEI and gold seeds leads to the decrease of Nb and O atomic percentages as displayed in table 4.9. The Nb at% is reduced by almost a factor of two whereas the atomic % of oxygen is reduced by a factor of 1.2. This discrepancy may be attributed to a higher contribution of the silicon substrate ($SiO_2$). The atomic percentage of carbon and nitrogen are increased due to the BPEI coating from 16.3% to 36% and from 1.5% to 3.9%, respectively. Similar trends are observed for LN@BPEI@AuSeeds3000. The atomic percentages of gold are 8.5% in the case of LN@BPEI@AuSeeds1000 and 11.05% in the case of LN@BPEI@AuSeeds3000. The ratio Au/Nb atomic percentage would suggest that the surface coverage is increased when the AuSeeds to LN@BPEI ratio is increased from 1000 to 3000 contrary to the ICP-AES result (Chapter 3, fig. 3.15, page 105). However, this coverage is not a linear function of the AuSeeds to LN@BPEI ratio as suggested by TEM. For sample LN@BPEI@AuSeeds1000, TOF-SIMS PCA principle component 1 (PC1) scored negatively while its score was nearly 0 for LN@BPEI@AuSeeds3000. It suggest that organic compounds containing nitrogen contribution are higher for LN@BPEI@AuSeeds1000. The discrepancy with XPS results (atomic percentage of C 36.6 and 39%) may arise from the sampling depth of the two techniques: 1-3 nm for TOF-SIMS and 10 nm for XPS. LN@BPEI@AuSeeds1000 scores negatively for PC2 while LN@BPEI@AuSeeds3000 scores positively. Gold related ions contribute positively to PC2 and organic compound negatively. Therefore, TOF-SIMS results suggested that the amount of gold used for the synthesis of

LN@BPEI@AuSeeds3000 was sufficient to reduce the signal coming from the BPEI.

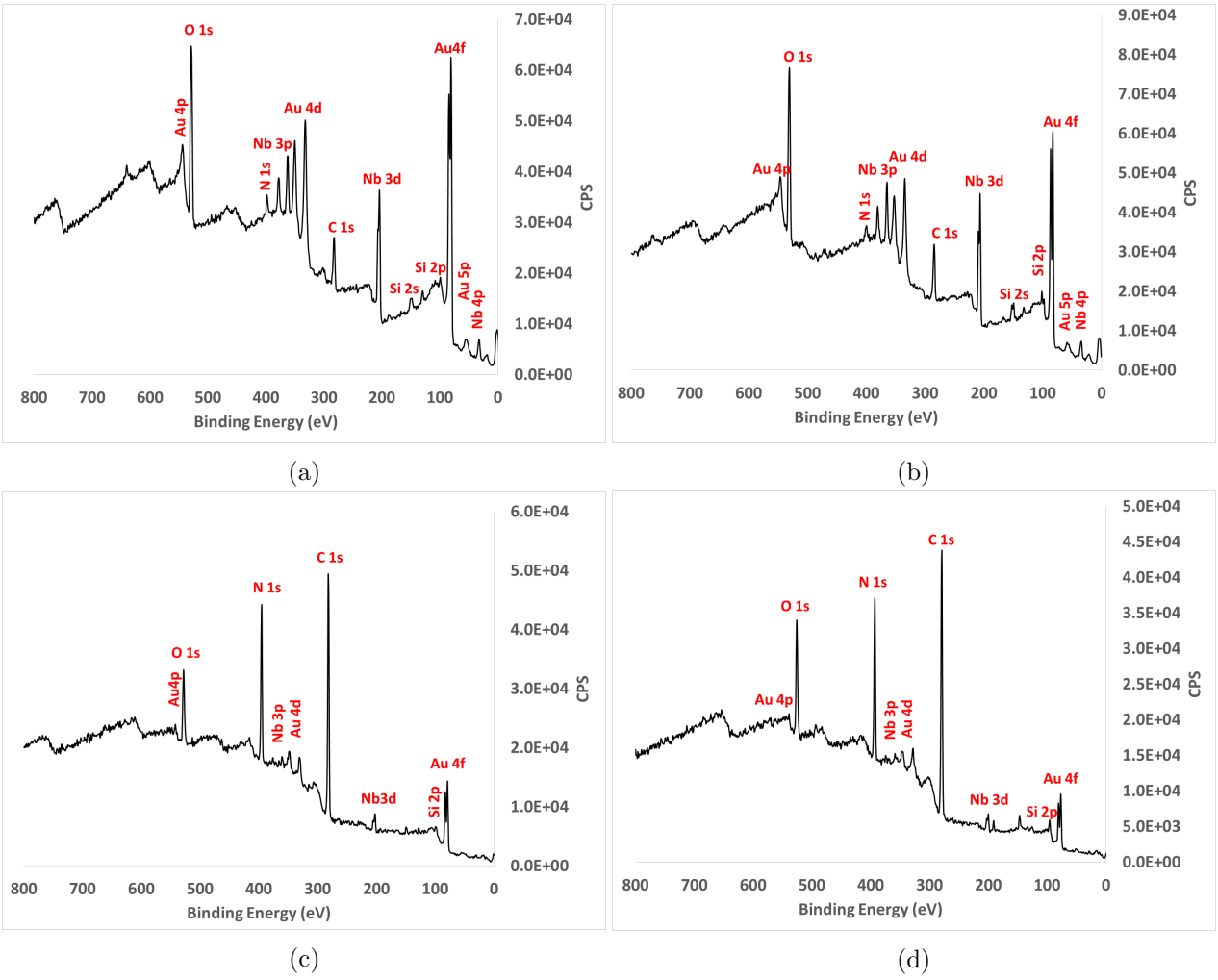


Figure 4.22: XPS spectra of LN, LN@BPEI@AuSeeds, LN@BPEI@AuSeeds@BPEI and LN@Au. (a) LN@BPEI@AuSeeds1000, (b) LN@BPEI@AuSeeds3000, (c) LN@BPEI@AuSeeds1000@BPEI, (d) LN@BPEI@AuSeeds3000@BPEI, (e) LN@Au (starting from LN@BPEI@AuSeeds1000@BPEI) and (f) LN@Au (starting from LN@BPEI@AuSeeds3000@BPEI)

Coating of LN@BPEI@AuSeeds1000 and LN@BPEI@AuSeeds3000, with BPEI, lead to a clear increase of the C1s and N1s contributions while those of Au (Au 4f, Au4d) and Nb (Nb3d, Nb3p) were drastically reduced in the XPS wide scans. The N atomic percentage is increase to 21 % and the C at% to 67%. The C at%/N at% ratio is just above 3. The theoretical ratio for BPEI is 2 suggesting some organic contamination. However, on the C1s core spectrum (provided in the appendix), only a very low intensity contribution at 285 eV was observed suggesting a low hydrocarbon contamination. The N1s core spectra for both LN@BPEI@AuSeeds1000 and LN@BPEI@AuSeeds3000 (given in the appendix), show two contributions at 399 and 400 eV suggesting that the amine function is

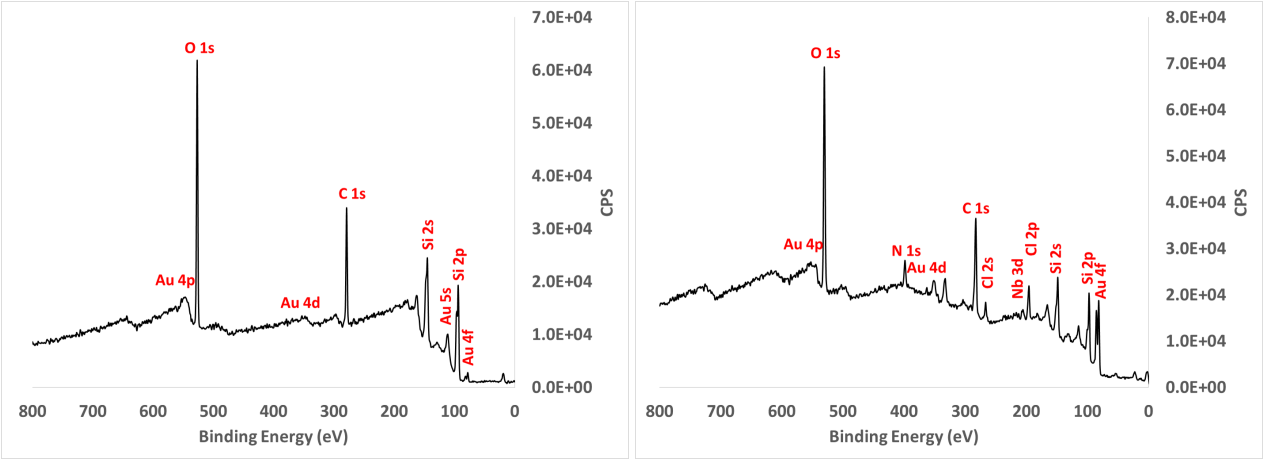


(e) (f)

Figure 4.22: XPS spectra of LN@BPEI@AuSeeds, LN@BPEI@AuSeeds@BPEI and LN@Au. (a) LN@BPEI@AuSeeds1000, (b) LN@BPEI@AuSeeds3000, (c) LN@BPEI@AuSeeds1000@BPEI, (d) LN@BPEI@AuSeeds3000@BPEI, (e) LN@Au (starting from LN@BPEI@AuSeeds1000@BPEI) and (f) LN@Au (starting from LN@BPEI@AuSeeds3000@BPEI).

partially protonated (1/3). Furthermore, the PC1 and PC2 TOF-SIMS scores are both negative suggesting a high contribution of organic compounds containing nitrogen ions.

Finally the LN@Au samples were analysed. Though, XPS at% results for LN@Au issued from the 3rd reduction were not reliable due to the high contribution of the silicon substrate (see fig. 4.22 (e) and (f)) due to deposition problem for these samples, we still performed the determination of the atomic percentages of the elements. As such, the values stated in table 4.9 must be regarded with a degree of uncertainty. The gold reduction steps, resulting in a more complete gold coating on the nanoparticles are clearly observed by the gold photoelectrons while the height of the C1s and N1s peaks are reduced. It must be noted that in the LN samples, XPS detected a N signal. If we are however to attribute the entire N signal to presence of BPEI, the fact that nitrogen is still observed suggests that either the gold layer is thin enough to allow the N1s photoelectrons to escape or that the final gold layer is incomplete. The PC1 TOF-SIMS for this sample is close to zero which means that it is not rich in compounds containing Li, Nb and organic species containing N. This is however to be expected as the gold species from this gold surface layer will predominate the peak areas identified in TOF-SIMS. This is further confirmed by the positive score of PC2 which means that these samples are rich in gold. The inelastic mean free path of a nitrogen photoelectron (kinetic energy of approximately 1050 eV for an Al K$\alpha$ source) traveling through a gold layer is approximately 1.2 nm. Therefore, the XPS probing depth would be between 3-4 nm. The probing depth of TOF-SIMS is 1-2 nm. Consequently, if the layer was to be continuous, its thickness would rank between 1- 4 nm. This was in agreement with the gold shell thickness derived from calculations

using ICP-AES analysis determined to be 1.2 nm. From the TEM images however, we measured AuNPs that comprised the gold shell with diameters of greater than 20 nm. A possible argument for this inconsistency between what was observed by TEM and calculated from XPS and ICP-AES is that the TEM images do not permit us to determine the depth of these AuNPs. Ionic abrasion experiments were considered to slice the particles, and then permit imaging of a cross-section, to determine the width of the layer of gold.

Table 4.9: Atomic percentages as determined from XPS. Standard deviations are shown in brackets. *1* signifies LN@Au formed using LN@BPEI@AuSeeds1000, *2* signifies LN@Au formed using LN@BPEI@AuSeeds3000.

| Sample | Concentrations (at%) | | | | | | |
|---|---|---|---|---|---|---|---|
| | Nb | O | C | N | Li | Au | Au/Nb |
| LN | 18.28 (0.97) | 49.66 (1.52) | 16.30 (0.54) | 1.54 (0.29) | 14.20 (0.36) | – | |
| LN@BPEI@AuSeeds1000 | 9.37 (0.58) | 42.09 (0.78) | 36.66 (2.64) | 3.87 (0.55) | ND | 8.55 (1.07) | 0.91 |
| LN@BPEI@AuSeeds3000 | 8.58 (0.22) | 36.65 (2.5) | 39.00 (2.0) | 4.7 (0.05) | ND | 11.05 (0.22) | 1.28 |
| LN@BPEI@AuSeeds1000@BPEI | 0.37 (0.04) | 9.72 (0.55) | 67.77 (0.87) | 21.40 (0.35) | ND | 0.71 (0.10) | 1.92 |
| LN@BPEI@AuSeeds@3000@BPEI | 0.42 (0.23) | 9.49 (0.60) | 67.85 (1.46) | 21.42 (0.55) | ND | 0.82 (0.08) | 1.95 |
| [1]LN@Au | 10.88 (1.24) | 28.85 (2.65) | 35.54 (3.10) | 3.18 (0.68) | ND | 21.54 (2.12) | 1.97 |
| [2]LN@Au | 0.85 (0.23) | 36.79 (4.70) | 55.16 (4.93) | 3.06 (1.48) | ND | 4.13 (0.65) | 4.86 |
| Nb foil | 20.78 (1.9) | 54.93 (2.1) | 20.69 (2.0) | | | | |
| Au film& | 5.54 | 29.54 (0.55) | (2.9) | | 64.92 | (3.6) | |

#### 4.2.3.3 Analysing the effect of aging on LN@Au nanoparticle dispersions

The characterization of the optimized LN@Au NPs, i.e, LN@Au formed after 3 reduction steps with 30 mM $HAuCl_4$ and 0.2 M $NH_2OH.HCl$ at neutral (unaltered pH), and using LN@BPEI@-AuSeeds1000 as the starting nanoparticles was performed over a period of 33 days. This data was

deemed necessary to understand the longevity of the nanoparticle dispersions. The fig 4.23 shows the evolution of the UV-visible extinction profiles, the Z-avg values, the PDI values and the zeta potential values for these nanoparticles over a 33 day period. The NPs were stored at 4°C. Before taking measurements, the dispersion was sonicated for 10 minutes, and then an aliquot of the sample was removed for analysis.

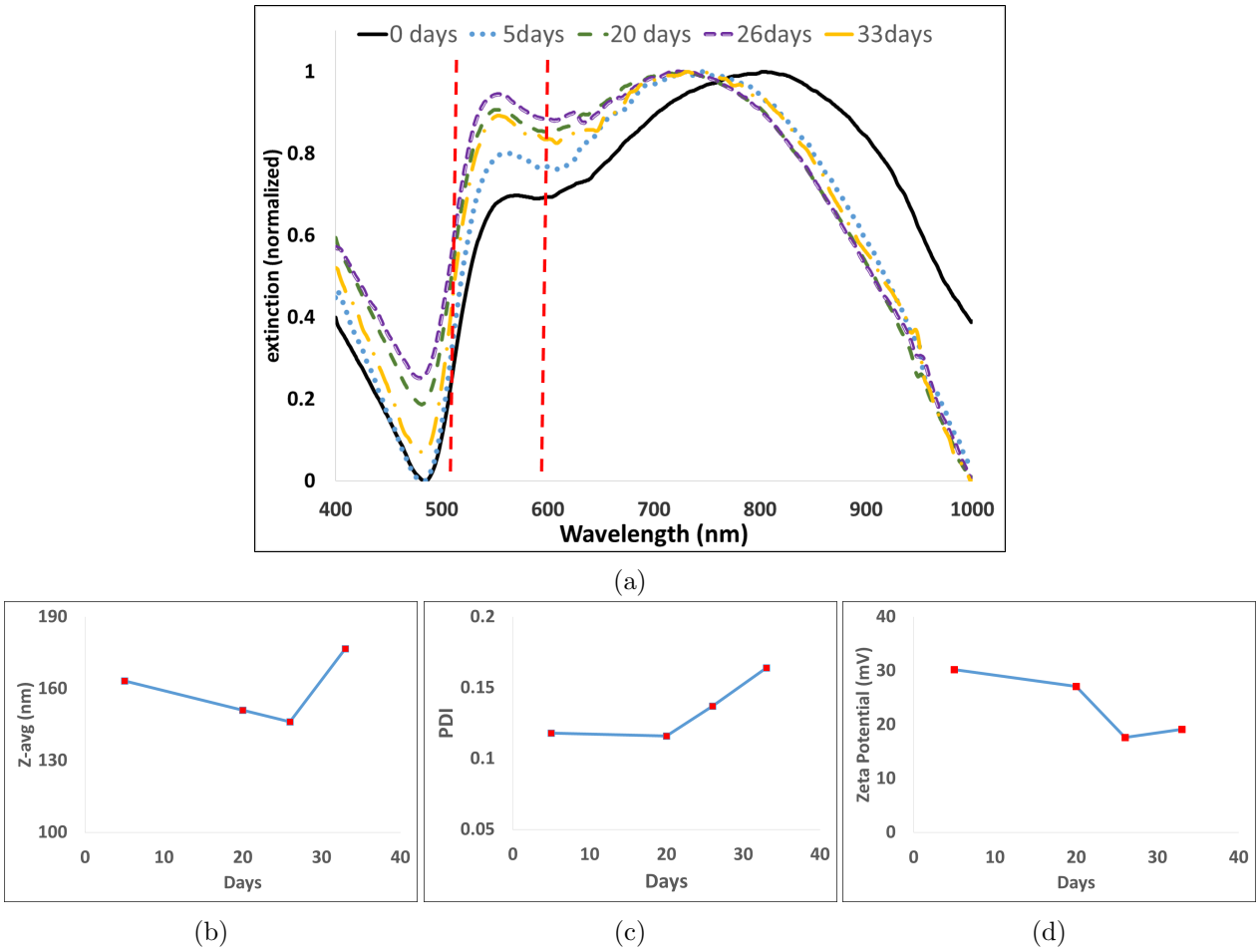


(a)

(b) (c) (d)

Figure 4.23: Evolution of UV-visible extinction profiles, Z-avg, PDI and zeta potential of LN@Au nanoparticles upon ageing.

From the UV-visible spectra, it was observed that the first band, centered on 550 nm, was unchanged from the day of synthesis to day 33 post-synthesis, and the second band in the NIR region underwent a blue-shifting at day 5 of the synthesis, but remained unchanged after day 5. As we have already attributed this double band to the spherical morphology of the AuNPs on the LN NPs and the plasmon coupling of these spherical NPs, we can conclude that this spherical AuNP morphology is maintained upon ageing. It is seen in the literature, that non-isotropic gold nanoparticles such as nanostars and nanoflowers, tend to undergo rearrangement of the Au over time to

give a more isotropic, spherical morphology.[228,229] However, as our LN@Au NPs are made up of spherical AuNPs, we believe that this is a thermodynamically stable configuration, and as such we remain with the as synthesized morphology, confirmed by TEM imaging post synthesis. Atomic rearrangements however could explain the blue-shifting of the second band observed however, this is one hypothesis and has not been shown for our samples.

The data depicted by the zeta potential, Z-avg and PDI values, are an indicator of the colloidal stability of the nanoparticle dispersions in water. We observed a trend of decreasing stability of the nanoparticles dispersed in water after 20 days (fig. 4.23 (b-d)). Additionally, the Z-avg of the NPs was decreasing until day 20, then the Z-avg began to rapidly increase between days 20 to 30. Finally, the PDI value was stable until day 20, at which point the value was seen to significantly increase. The de-stabilization of the nanoparticles observed from day 20 is believed to be a result of two phenomenon. Firstly, it is suspected that some of the AuNPs on LN@Au are dettaching after time, which was corroborated by TEM imaging that showed a higher population of free AuNPs as compared to the initial imaging. The second phenomenon is aggregation dynamics. Nevertheless, a stability of 20 days is still greater than that reported in literature. In the work of Sangnier *et. al*[230] they report that their core-shell, Fe@Au raspberry shaped nanoparticles were stable up to two days in phosphate buffer solution which is a sufficient test for biological applications. We should also conduct our stability experiments, transferring the NPs to a biological approximate such as phosphate buffer solution. We believe that adding a final polymer coating on the gold shell can help prolong the stability of these nanoparticles in its dispersed media.

#### 4.2.3.4 SHG properties of $LiNbO_3$@Au Core-shell nanoparticles

To evaluate whether the Au shell on LN had any impact on their SHG properties, Hyper Rayleigh Scattering measurements were performed on the LN@Au NPs dispersion. The experimental set-up was designed at SYMME laboratory, Annecy and is shown in fig. 4.24. A typical experiment consisted of a range of excitation wavelengths (800-1300 nm). For each excitation wavelength ($\lambda_0$), the intensity ($I_{SHG}$) of light emitted at the $\lambda_0/2$ was collected. Then a plot of the ratio of the $I_{SHG}$ for LN@Au NPs and LN against $\lambda_0$ allowed us to observe any changes in the SHG signal as a result of the gold shell.

In fig. 4.25(a) we note an enhancement of the SHG signal for LN@Au compared to pure LN with two peaks at 1150 nm and 1250 nm. Indeed we were anticipating enhancements at excitation wavelengths at the plasmon resonance wavelengths of the gold shell, similarly as to what was reported by Pu *et. al*[231] in their $BaTiO_3$@Au nanoparticles. Additionally, in the works of Richter *et. al*,[172] they simulated the SHG enhancement of $KNbO_3$ nanowires as a result of a gold coating. Other

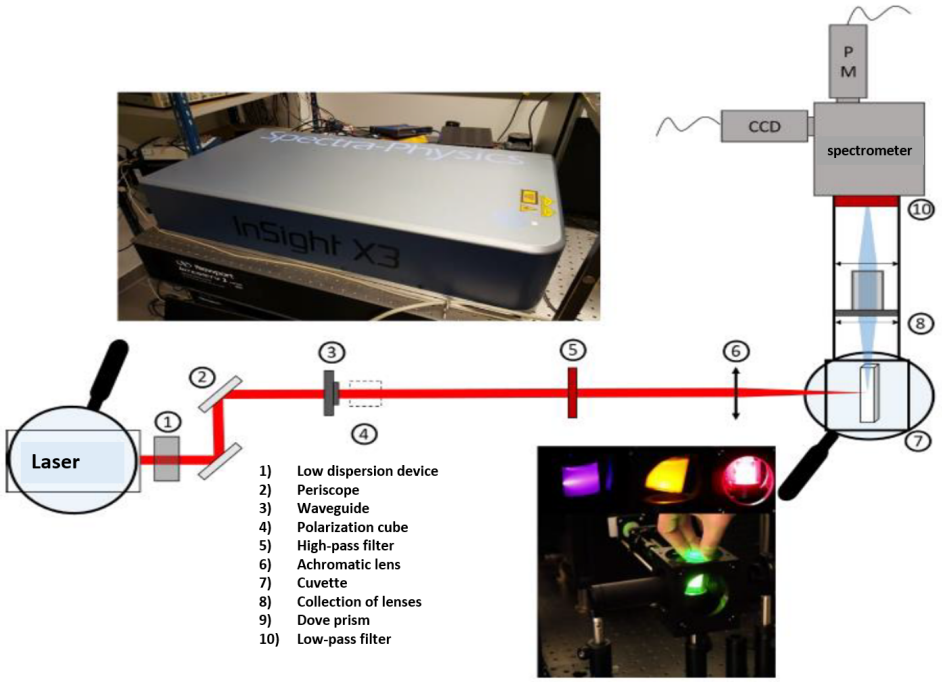


Figure 4.24: Schematic diagram of the second harmonic scattering spectroscopy bench set-up comprising a femtosecond laser tunable in the 680-1300 nm range. Depending on the excitation wavelength, the photos illustrate different second harmonic signals obtained in the visible from a suspended powder of micrometric crystals

research groups have also shown a correlation between the enhancement of NLO response when the NLO object is coupled to a plasmonic entity.[232–234] These results presented are from preliminary analysis and require further investigation. As is seen in fig. 4.25(b), there is an absorbance peak at around 575 nm, corresponding to the $\lambda_0/2$ of the 1150 nm excitation. A hypothesis is that this enhancement observed at that excitation wavelength can possibly be attributed to this absorption band that we postulate has an impact on the near-field response of the hybrid nanoparticles, but further experiments must be completed, complemented by simulations modeling the near-field and far-field response of these nanohybrids similar to what was done by authors Madzharova *et. al*[235] when studying the SHG response of their gold coated barium titanate nanoparticles. It is worth noting that this SHG enhancement is in opposition to the SHG response observed with LN@BPEI@AuSeeds. Reasons for this difference is not fully understood but as the most obvious difference is the size of the gold nanoparticles (and consequently their intraparticle interactions), we suspose that the answer lies in examination of the size dependent optical properties. Though there is not an extensive volume of literature on such core-shell NLO, gold nanoparticles, their work leads us to believe there can be a link between the excitation wavelength and the SHG signal obtained for such NLO-gold composites. Not only this, there is a possibility that the presence of the Au on the NLO nanomaterial can lead to new opportunties for probing of the local environment using Raman

scattering.[235]

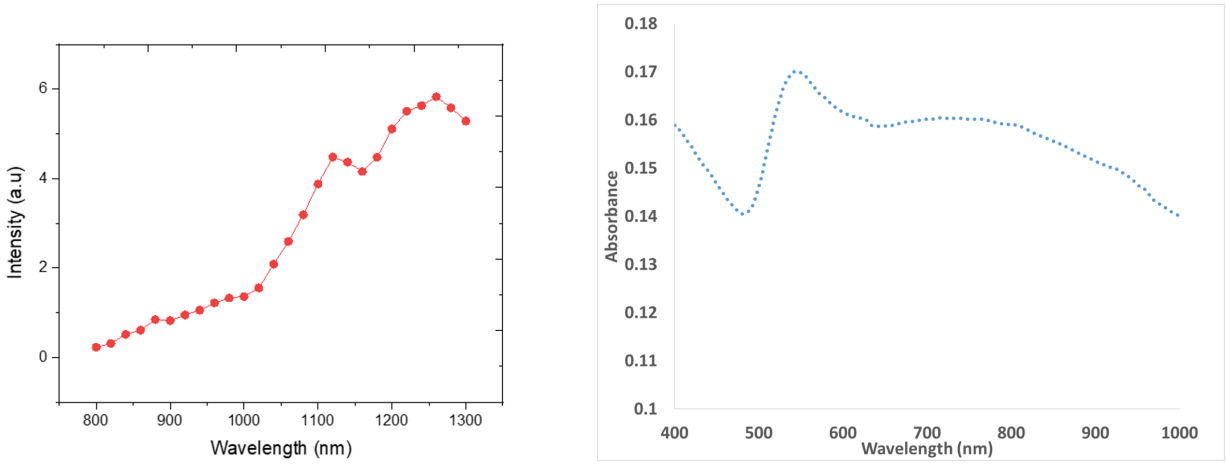


(a) (b)

Figure 4.25: (a) HRS enhancement measurements of LN@Au sample for excitation wavelengths from 800-1300 nm. The values plotted are the ratio of the LN@Au/LN SHG intensities. The intensity was set at 1 at 740 nm. The LN@Au concentration was 0.16 g/L and the LN concentration was 0.17 g/L. (b) The UV-visible extinction profile of LN@Au.

#### 4.2.3.5 Photothermal properties of LN@Au core shell nanoparticles

Our photothermal evaluation of our nanoparticles was done via thermographic imaging, using the set-up described in section 4.1.7. In fig. 4.26 (a), the temperature measured as a function of irradiation time with 808 nm laser is given and in fig. 4.26(b) a typical IR image obtained during the experiment is shown. We used a sample of LN@Au synthesized at natural pH, using $HAuCl_4$ 30 mM concentration after three reduction steps. The mass of Au present in the 200 $\mu$L sample determined based on previous ICP-AES measurements was calculated to be 34 $\times 10^{-4}$ mg. After 34 minutes of irradiation, $\delta$T recorded was 8.6 °C. While the absolute $\delta$T observed for our nanoparticles are much lower than the values reported in literature, there are factors that contribute to this such as the mass of Au in our sample and the volume of water in which these temperature increases are measured.

To compare the LN@Au nanoparticles to PTT agents found in literature, the light-to-heat conversion efficiency ($\eta$), was calculated. The calculations were adapted from Jiang *et. al*[236] and is given in equation 4.1.

$$\eta = \frac{\delta T \times m_s \times C_w \times B}{P_0 - \frac{P_0}{10^A}} \tag{4.1}$$

where $\delta T$= the increase in temperature in °C, $m_s$= mass of the sample (in g), $C_w$= specific heat

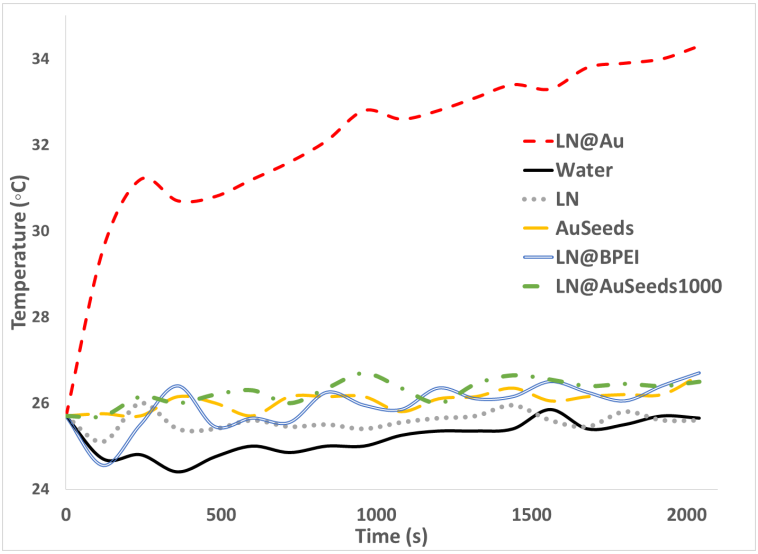


(a)

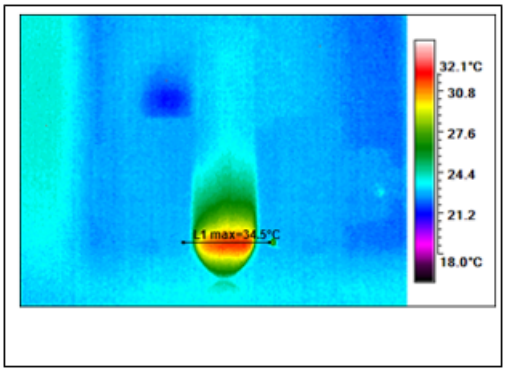


(b)

Figure 4.26: (a) Temperature evolution curves (normalized) upon irradiating the following nanoparticle dispersions with a 808 nm CW laser: LN@Au, LN, LN@AuSeeds1000, LN@BPEI and AuSeeds. The temperature evolution of water alone was taken to normalize the curves. (b) IR Thermographic image of LN@Au nanoparticle dispersion when heated by 808 nm laser.

capacity of water, $P_0$= incident laser power, $A$= absorbance of sample at 808 nm and $B$= the constant rate of heat dissipation from the solution to the environment and is calculated using equation 4.2.

$$e^{-Bt} = \frac{T_t - T_0}{T_m - T_0} \tag{4.2}$$

where $T_t$= temperature at some time t, $T_0$= initial temperature before turning laser on, and $T_m$= maximum temperature.

Using the above equations, the $\eta$ of LN@Au nanoparticles was determined to be 40%. Using the same method for determining $\eta$, Sangnier *et. al*[230] reported a photothermal efficiency of 65% for their gold nanoraspberries, i.e, AuNPs with a raspberry morphology. They also presented the $\eta$

reported in the literature for different gold nanostructures which we present in table 4.10. We see that $\eta$ for our LN@Au NPs is 25% lower than that of AuNRs, but 5% higher than that reported for the AuNSs synthesised by authors Cole *et. al*[237] and gold nanostars reported by authors Espinosa *et. al*.[238] We can therefore conclude that our AuNSs are comparable to that in the literature.

| AuNP shape | nanoraspberries | nanorods | nanostars | nanoshells |
|---|---|---|---|---|
| $\eta$ | 65[230] | 65[237] | 35[238] | 35[237] |

Table 4.10: Photothermal conversion efficiencies for various gold nanostructures.

What has not been studied is the separate absorption and scattering cross-sections of our LN@Au NPs. When we perform the UV-visible spectroscopy, what in fact we obtain is the extinction spectra which is a summation of both absorption and scattering phenomenon. It would be of interest to us to model the absorption contribution and the scattering contributions. This has been done for silver metallic nanoparticles in the shape of spheres and cubes, reported by authors Grand *et. al*, however it requires the use of multiple electromagnetic modeling tools.[239] Nevertheless, if we were to find that at 808 nm, the scattering contribution is high, this would be impacting the proportion of light that is being absorbed and then consequently converted to heat. In chapter 1, section 1.4.4, page 47, we noted that in the work of authors Bi *et. al*,[111] a record high photothermal conversion of 78.8% for their gold nanostars is reported which they attributed to optimizing the size of the core and the number of spikes to minimize the scattering contributions at their chosen excitation wavelength of 980 nm. Further optimization of our LN@Au NPs could be a future avenue to improve $\eta$.

It was mentioned in chapter 1 section 1.4.4 page 47 that in traditional photothermal therapies, the temperature is usually increased within the 41 to 45 °C temperature range.[?,101] However, when we are considering PPTT by nanoparticles, the heat is dissipated locally and studies have shown that the local temperature increase can rise by tens or hundreds of degrees.[240] We intend to incorporate nanothermometry functionality in our nanoparticles by embedding $Er^{3+}$ in the $LiNbO_3$ lattice structure. $Er^{3+}$ has a temperature dependent luminescence[241] and it is possible to utilize the fluorescence intensity ratio (FIR) to elucidate the local temperature.

## 4.3 Conclusion

In this chapter, we discussed two seeded growth synthesis methods for the preparation of LN@Au NPs. The layer-by-layer was proven to be suited to our nanoparticles. An optimization of the experimental conditions was conducted. We determined that starting with LN@BPEI@AuSeeds1000

NPs, and performing the gold reduction using 30 mM $HAuCl_4$ and 0.2 M $NH_2OH.HCl$ in neutral (unaltered) pH, we obtained the optimal LN@Au NP dispersions. We performed surface characterization by TOF-SIMS and XPS analysis, which determined the changing chemical environment of the nanoparticle surface at different steps in the synthesis process. XPS was used to determine that the gold shell thickness was 1-4 nm. This was corroborated by the gold shell thickness determined using the data obtained from ICP-AES analysis, giving a shell thickness of 1.2 nm. The final LN@Au nanoparticle dispersions were shown to maintain their properties (zeta potential, Z-avg, and PDI values) in aqueous media safely up until 20 days post synthesis, and we believe that a protective coating of the nanoparticles with a suitable polymer could prolong this. Our first SHG experiments on these LN@Au nanoparticles showed an enhancement of the SHG signal at excitation wavelengths 1150 nm and 1250 nm however future experiments must be performed to understand the origination of this enhancement. Finally, the photothermal ability of the LN@Au NPs was demonstrated and we determined it to have light-to-heat conversion efficiency of 40%.

# General Conclusions and Perspectives

Strategies that combine imaging and therapeutic functionalities into a single theranostic platform at the nanoscale is an attractive approach in cancer research, however, it requires an investment in fundamental research experiments. This thesis work detailed the fundamental studies in material science, in designing potential cancer theranostic multi-material, core-shell nanohybrids, and serves as the primary step before moving towards biological investigations.

Optical bio-imaging techniques allow us to achieve imaging at the cellular level, which can help us to identify cellular abnormalities before large tumor growth has occurred. More specifically, non-linear optical bio-imaging based on the second order non-linear susceptibility, such as SHG imaging, does not rely on electronic transitions of the imaging probe, and as such, we can achieve wavelength tuneable imaging. This among the other advantages such as high spatial resolution, lack of blinking or photodegradation as is observed in their fluorescent counterparts, as well as the cytotoxic studies performed on NLO nanomaterials such as $LiNbO_3$ nanoparticles are strong arguments for continued research on NLO bio-imaging. Plasmonic photothermal therapy as a cancer treatment has been flagged as a method of destroying cancer cells that is non-lethal to healthy cells. Based on the existing literature, the goal was to combine NLO imaging and plasmonic photothermal therapy into a singular nanoparticle platform.

The characterization of nanoparticle dispersions were performed using an array of techniques that probed both the physical and chemical nature of the nanoparticles as well as different surface depths. A deeper comparative study of these techniques outlining their advantages and their limitations allowed for a robust assessment of the various nanoparticles used throughout this work. It was concluded that to fully characterize nanoparticles, the size, shape and morphological characterizations are essential, and when handling nanoparticles dispersed in aqueous media, their hydrodynamic diameter and zeta potential values are strong indicators of the dispersion stability.

From this work we concluded that the LN nanoparticles synthesized by the solvothermal process (performed at SYMME laboratory) produced pseudo-spherical nanoparticles, with a sphericity of

0.8, and a diameter of 45 nm (as determined by XRD analysis). These LN nanoparticles have a natural zeta potential of -43.2 ± 3.6 mV when dispersed in aqueous media confirming their negative surface charge. Surface modifications of these LN NPs with BPEI polymer successfully reversed the negative charge to +36.05 ± 2.9 mV. From XPS analysis and corroborated by fluorescence based analysis, the BPEI coating was determined to consist of 1259 polymer chains per LN particle, which corresponds to 24% wt of polymer to LN nanoparticle.

Spherical gold nanoparticles (AuSeeds), 2.5 nm in diameter with a zeta potential of -25.3 ± 8.0 mV were attached to the BPEI coated LN NPs, primarily through electrostatic interactions. We demonstrated the variability in the density of the AuSeeds coverage on the LN@BPEI NPs by both TEM and ICP-AES analysis. The maximum percentage of the LN@BPEI surface covered was determined to be 21.1% and 31.5% by TEM and ICP-AES respectively. Additionally, TEM analysis showed a linear correlation with the amount of AuSeeds mixed with the LN@BPEI NPs to the percentage of surface covered, whereas ICP-AES showed a asymptotic correlation. Using the ICP-AES results, the maximum AuSeeds that could be attached to LN corresponded to a 29% wt of Au per LN.

The effect of the attachment of AuSeeds to LN@BPEI NPs on the LN core's non-linear optical (NLO) properties was evaluated by the hyperpolarisability values, obtained by performing HRS experiments. It was finally observed that the hyperpolarisability of these LN@BPEI@AuSeeds nanoparticles (hyperpolarisability values ranging from 0.129 to 0.535 $\times 10^{-24}$) was diminished with respect to the bare LN NPs (hyperpolarisability value of 0.768 $\times 10^{-24}$). Depolarization evaluation of the LN and LN@BPEI@AuSeeds NPs however did not reveal any significant differences between the samples. Further studies on the impact of the density of AuSeeds on the hyperpolarisability of $LiNbO_3$ is still to be performed. This will also include further polarization studies, as well as modeling to better understand the observed result of decreased NLO function of our LN@BPEI@AuSeeds nanoparticles. Although our focus was on biological applications, the literature points to the use of hybrid NLO and plasmonic nanomaterials as nanoantennas for confining incoming radiation, and enhancing the local fields to then be used for non-linear processes such as SHG enhancement.[242] We believe that our LN@BPEI@AuSeeds structures should be further studied for the application to confining light.

In this work, we also presented two seeded-growth protocols for gold shell synthesis starting from LN@BPEI@AuSeeds. We reported that using varied ratios of $HAuCl_4$. to $Na_3Cit$ did not promote a homogenous growth of gold around the core nanoparticles. A layer-by-layer (LbL) approach was demonstrated to be more successful in coating the core particles. We performed synthesis, varying the experimental parameters pH, initial AuSeed density and $HAuCl_4$ concentration. We showed that generally, the LbL method produced nanoparticle dispersions with a plasmon resonance band in the

NIR region after three gold ion reduction steps. It was also demonstrated that the optimal synthesis conditions for gold shell on LN@BPEI@AuSeeds was to start with LN@BPEI@AuSeeds1000 NPs (30% surface coverage), to perform the gold reduction at around pH 7, and to use 30 mM $HAuCl_4$ at each reduction step. These conditions produced LN@Au nanoparticles with a plasmon band peak at 803 nm. Additionally, the zeta potential (+30.2 mV), Z-avg (163.3 nm) and PDI (0.118) values determined the final nanoparticle dispersion to be sufficiently dispersed, not prone to aggregation forces. The nanoparticles were analyzed by UV-visible spectroscopy, DLS, zetametry, TEM, EDX, ICP-AES, XPS and TOF-SIMS analysis. The final morphology of the shell of these nanohybrids has been determined to be raspberry shaped. It is envisioned to prepare similar core-shell NLO-plasmonic structures applying this same synthesis protocol but changing the NLO core. In our laboratory, we have already begun working on bismuth ferrite (BFO).

In preliminary investigations of the SHG response of these LN@Au nanoparticles, we observed an enhancement of the SHG response as opposed to the bare $LiNbO_3$ nanoparticles at the wavelengths 1150 and 1250 nm. Conversely, a decrease in the SHG response was observed for LN@BPEI@AuSeeds nanoparticles. More experiments are to be completed to better explain these preliminary results. An initial hypothesis is that there is a link between the plasmon extinction peaks of the nanoparticle dispersion and the SHG enhancement. This early observation is nevertheless an encouraging observation as it can potentially help us to improve upon the volume scaled SHG response observed for NLO nanoparticles. It is also possible that this raspberry shell structure, can present other interesting functionalities such as Raman and hyper Raman scattering that can be used for sensing.[235] In our reported optimization process, we leave the final nanoparticle with a gold surface (as was evidenced by TOF-SIMS analysis). This is useful for future biological applications as the gold chemistry can be used to then perform further surface functionalization of the nanoparticles to include bio-molecules that can enhance bio-compatibility and/or provide active bio-targeting.

Finally, we demonstrated that our LN@Au NPs have a photothermal energy conversion efficiency of 40%. This was found to be 5% more than that reported in the literature for core-shell nanoparticles.[237] AuNRs, the benchmark nanoparticle for photothermal activity can have photothermal conversion efficiencies of 65% which have been used for destroying cancer cells. Future works will include performing photothermal experiments varying the concentration of Au (i.e the concentration of LN@Au NPs), to determine at what concentration we can achieve an overall heating of 40°C, which has been shown to be sufficient to kill cancer cells. It is also envisioned as future work, the cytotoxic evaluation of the nanoparticles. Once completed, it is envisioned to also perform photothermal experiments with the nanoparticles incubated with cancer cells, and further in animal studies.

Although the rough raspberry structure is hypothesized based on the literature to have strong local field enhancements, we are also interested in the light-to-heat conversion of smooth gold shell surface. It has been demonstrated in literature, heat treatment to gold nanoparticles to cause intra-particle ripening processes to produce smoother surfaces.[143] This is a possible approach to change the final LN@Au structure.

The results presented in this work on controlling the density of gold seeding on LN@BPEI NPs, is now serving as the starting point for a new PhD thesis in our laboratory, that began in November of 2019, in collaboration with RMIT university Australia. These LN@BPEI@AuSeeds nanoparticles will be used for catalytic studies. It has been observed that LN@BPEI@AuSeeds NPs have peroxidase activity, and that their catalytic properties are enhanced compared to dispersions of LN and AuSeeds, as well as mixed dispersions of unlinked LN and AuSeeds. When used for such enzymatic activity, these nanoparticles are termed nanozymes.[243] Further studies on these nanoparticles and their catalytic function is being conducted within our laboratory.

# Appendix A

# Supplementary Data

| | Nanoparticle | |
|---|---|---|
| | $LiNbO_3$ | Au |
| Nanoparticle Diameter (nm) | 45 | 2.5 |
| Density ($g/cm^3$) | 4.65 | 19.3 |
| Molar mass (g/mol) | 147.85 | 196.97 |
| Volume of 1 NP ($nm^3$) | $4.77 \times 10^4$ | 8.18 |
| Mass of 1 NP (g) | $2.22 \times 10^{-16}$ | $1.58 \times 10^{-19}$ |

Table A.1: Table containing the physical properties of $LiNbO_3$ and Au NPs.

| Sample | # AuSeeds per LN (TEM) | % LN surface covered (TEM) | #AuSeeds per LN (ICP-AES) | % LN surface covered (ICP-AES) |
|---|---|---|---|---|
| LN@BPEI@AuSeeds100 | 36 | 2.8 | 12 | 9.31 |
| LN@BPEI@AuSeeds300 | 52 | 4.0 | 241 | 18.63 |
| LN@BPEI@AuSeeds700 | 74 | 5.7 | 373 | 28.79 |
| LN@BPEI@AuSeeds1000 | 94 | 7.3 | 399 | 30.82 |
| LN@BPEI@AuSeeds2000 | 151 | 11.7 | 404 | 31.20 |
| LN@BPEI@AuSeeds3000 | 273 | 21.1 | 408 | 31.46 |

Table A.2: Number of AuSeeds per LN nanoparticle and % LN surface covered by AuSeeds, as determined by TEM and ICP-AES analysis.

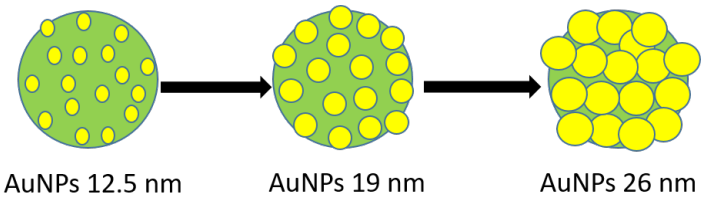


Figure A.1: Scheme of NPs to be modeled. Discrete dipole approximation (DDA) method to be used to determine their UV-visible extinction profiles.

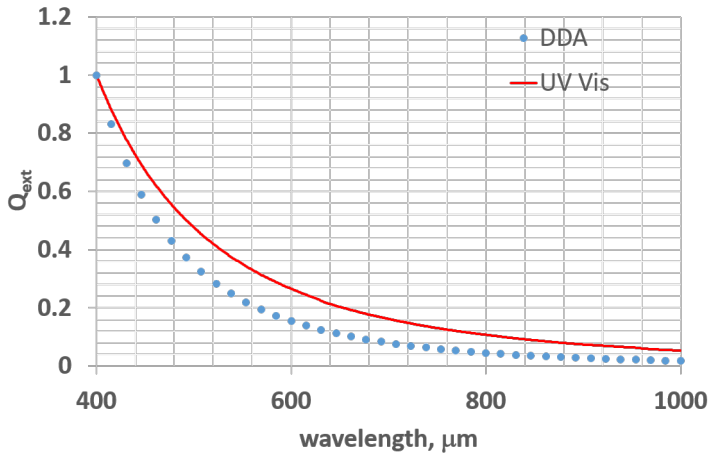


Figure A.2: Discrete dipole approximation of the UV-visible extinction profile of 45 nm $LiNbO_3$ NPs and corresponding experimental extinction profile. Modeling performed by Jaona Randrianalisoa, Institut de Thermique, Mécanique, Matériaux (ITheMM), Université de Reims Champagne-Ardenne.

| Sample | Li/Nb Ratio | PE (eV) |
|---|---|---|
| LN | 0.74 (0.008) | 80 |
| | 0.79 (0.005) | 40 |
| | 0.72 (0.008) | 20 |
| | 0.79 (0.005) | 160 |

Table A.3: XPS determined Li/Nb ratio as a function of the pass energy analysis parameter (PE) for the bare LN nanoparticles.

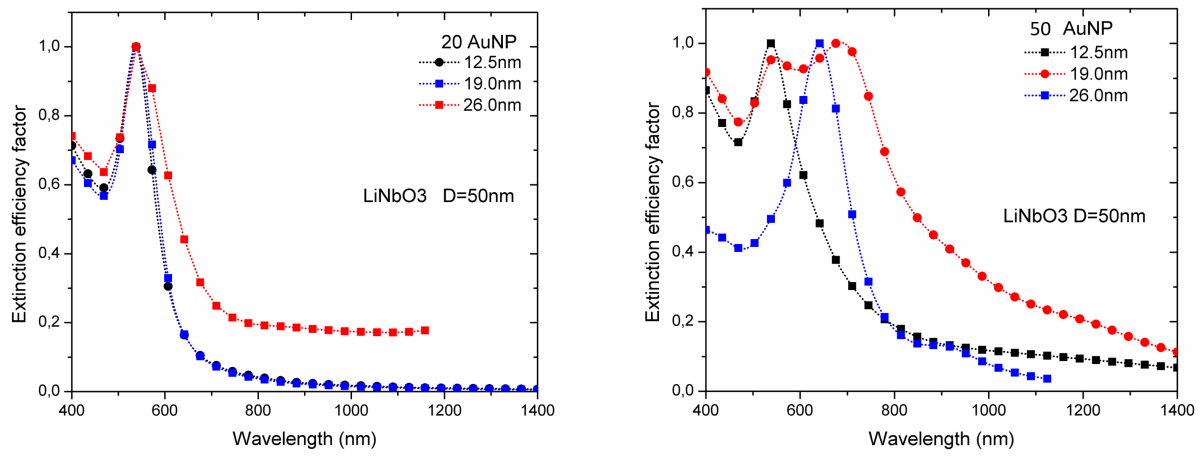


(a) (b)

Figure A.3: Modelization of the extinction spectra of LN@Au varying the number of AuNPs attached to LN and the size of AuNPs. (a) Initial number of AuSeeds attached to LN is 20, and the spectra corresponds to the enlargening of diameter of the AuSeeds (12.5 nm, 19 nm and 26nm). (b) Initial number of AuSeeds attached to LN is 50, and the spectra corresponds to the enlarging diameter of the AuSeeds (12.5 nm, 19 nm and 26nm). Modeling performed by Jaona Randrianalisoa, Institut de Thermique, Mécanique, Matériaux (ITheMM), Université de Reims Champagne-Ardenne.

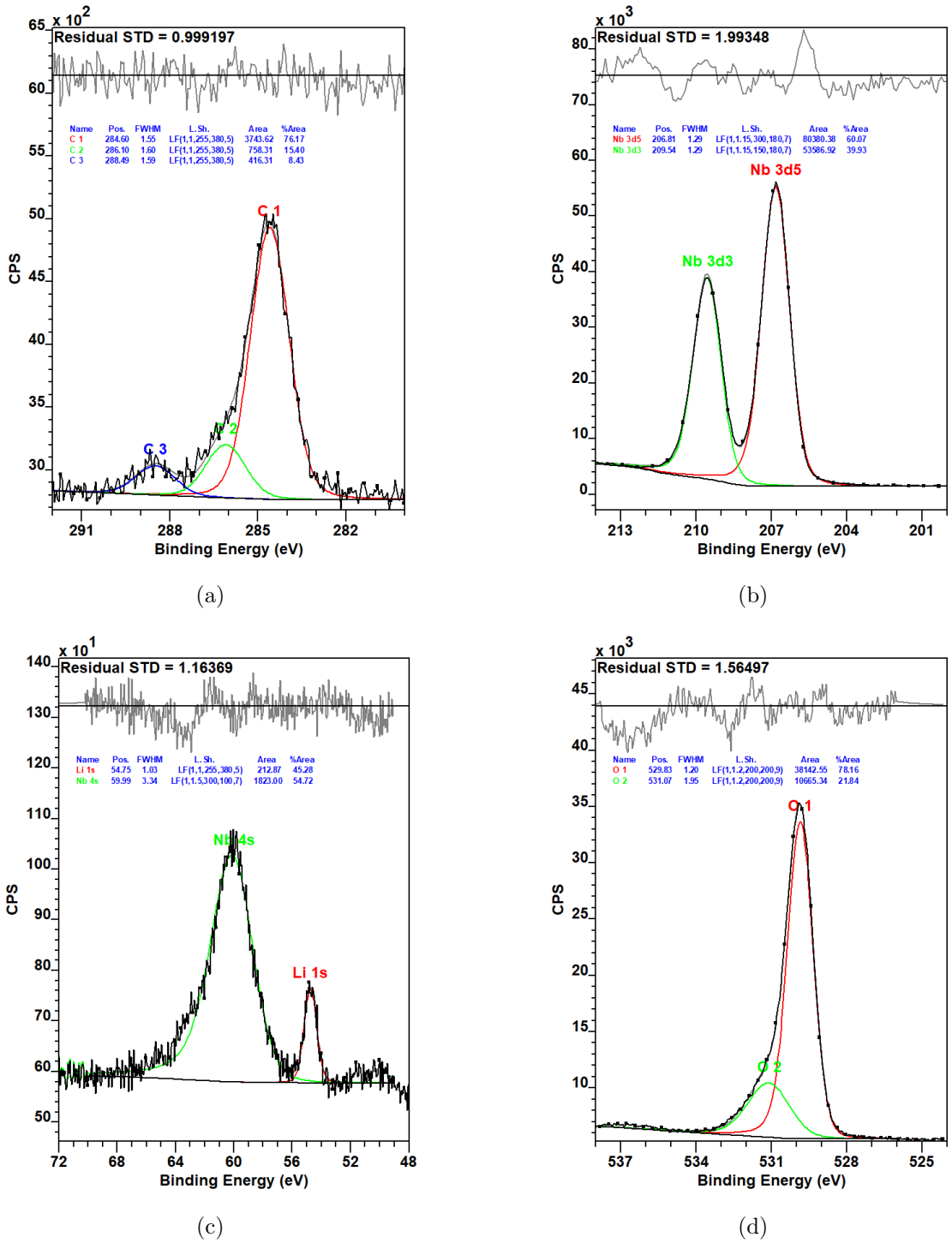


Figure A.4: XPS fine spectra for (a) C1s, (b) Nb3d, (c) Nb4s/Li1s and (d) O1s peaks identified from LN nanoparticle sample.

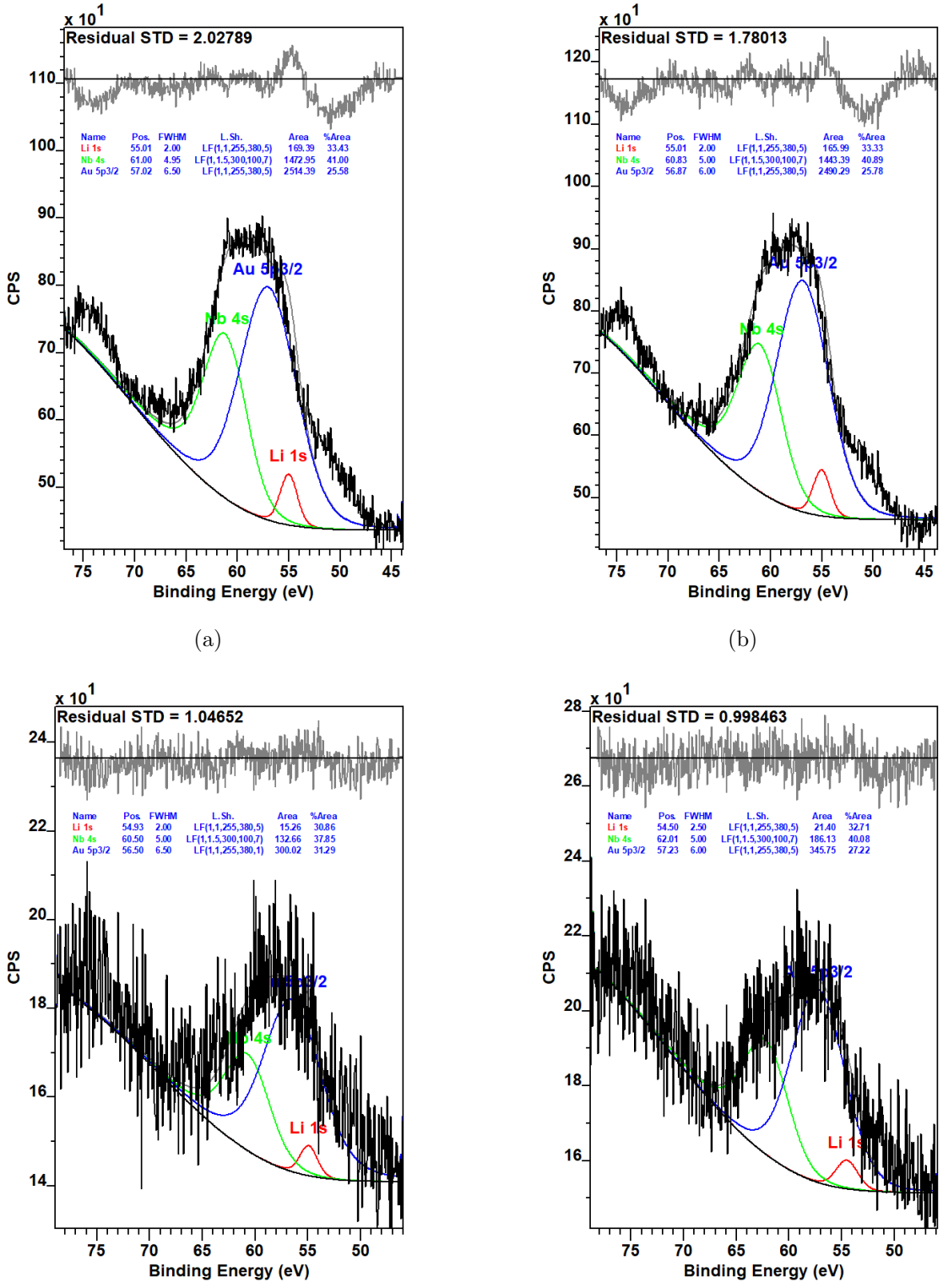


Figure A.5: XPS fine spectra (core level, between 45 and 70 eV) at 40 eV pass energy recorded on (a) LN@BPEI@AuSeeds1000, (b) LN@BPEI@AuSeeds3000, (c) LN@BPEI@AuSeeds1000@BPEI, (d) LN@BPEI@AuSeeds3000@BPEI, (e) LN@Au (from LN@AuSeeds1000) and (f) LN@Au (from LN@AuSeeds3000) samples.

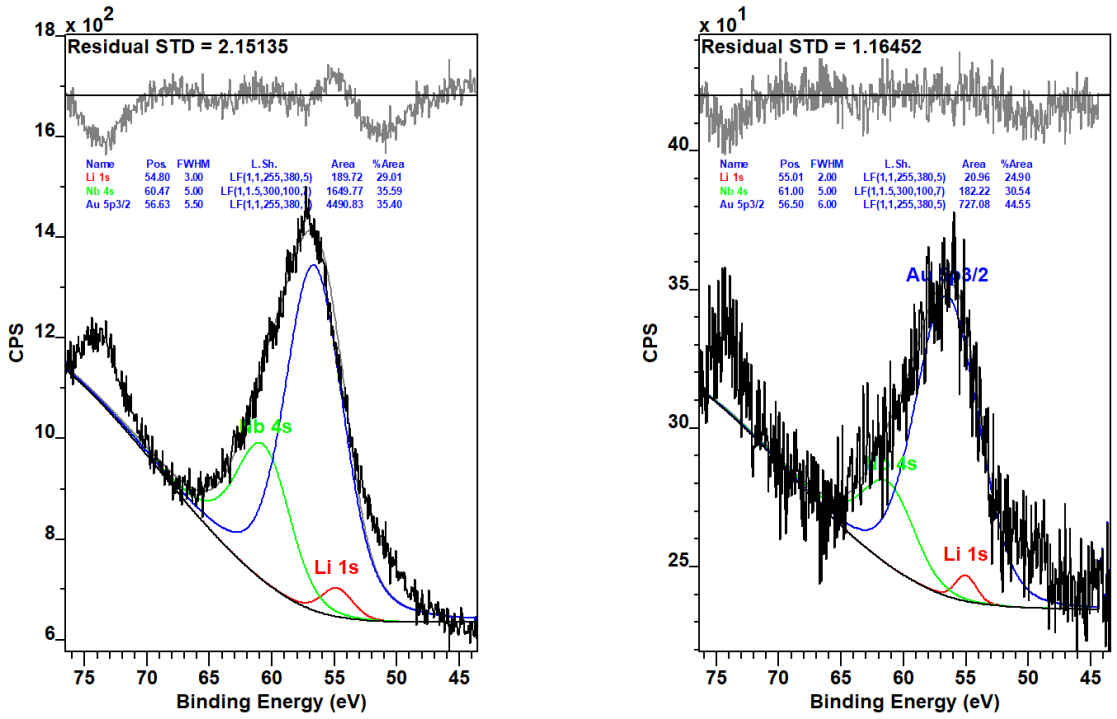


(e) (f)

Figure A.5: XPS fine spectra (core level, between 45 and 70 eV) at 40 eV pass energy recorded on (a) LN@BPEI@AuSeeds1000, (b) LN@BPEI@AuSeeds3000, (c) LN@BPEI@AuSeeds1000@BPEI, (d) LN@BPEI@AuSeeds3000@BPEI, (e) LN@Au (from LN@AuSeeds1000) and (f) LN@Au (from LN@AuSeeds3000) samples.

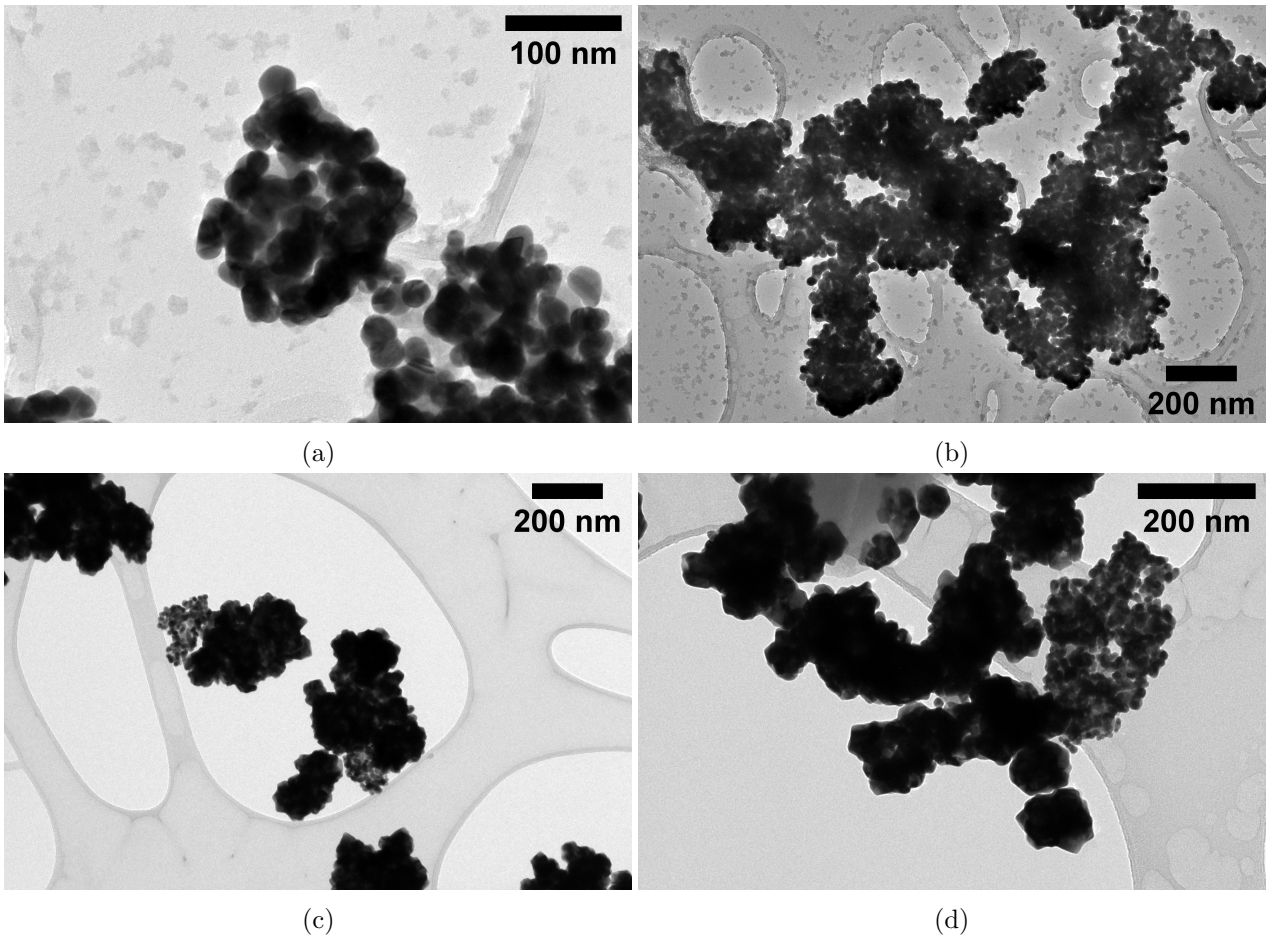


Figure A.6: TEM images of aged LN@Au NPs. (a-b) LN@Au NPs synthesized using LN@BPEI@AuSeeds3000, neutral pH, 30 mM $HAuCl_4$ and 0.2 M $NH_2OH.HCl$. (c-d) LN@Au NPs synthesized using LN@BPEI@AuSeeds1000, neutral pH, 10 mM $HAuCl_4$ and 0.2 M $NH_2OH.HCl$.

# Bibliography


[1] Joseph A. Webb and Rizia Bardhan. Emerging advances in nanomedicine with engineered gold nanostructures. *Nanoscale*, 6:2502–2530, 2014.

[2] Jun Zhao, Michael Wallace, and Marites P Melancon. Cancer theranostics with gold nanoshells. *Nanomedicine*, 9:2041–2057, 2014.

[3] Huafei Li, Hai Jin, Wei Wan, Cong Wu, and Lixin Wei. Cancer nanomedicine: mechanisms, obstacles and strategies. *Nanomedicine*, 13:1639–1656, 2018.

[4] Gizem Bor, Intan Diana Mat Azmi, and Anan Yaghmur. Nanomedicines for cancer therapy: current status, challenges and future prospects. *Therapeutic Delivery*, 10:113–132, 2019.

[5] Freddie Bray, Jacques Ferlay, Isabelle Soerjomataram, Rebecca L. Siegel, Lindsey A. Torre, and Ahmedin Jemal. Global cancer statistics 2018: GLOBOCAN estimates of incidence and mortality worldwide for 36 cancers in 185 countries. *CA: A Cancer Journal for Clinicians*, 68:394–424, 2018.

[6] Yang Shi, Roy van der Meel, Xiaoyuan Chen, and Twan Lammers. The EPR effect and beyond: Strategies to improve tumor targeting and cancer nanomedicine treatment efficacy. *Theranostics*, 10:7921–7924, 2020.

[7] Rakesh K Jain. Molecular regulation of vessel maturation. *Nature Medicine*, 9:685–693, 2003.

[8] Anca Onaciu, Ancuta Jurj, Cristian Moldovan, and Ioana Berindan-Neagoe. Theranostic Nanoparticles and Their Spectrum in Cancer. *Engineered Nanomaterials - Health and Safety*, October 2019.

[9] Thandapani Gomathi, K. Rajeshwari, V. Kanchana, P. N. Sudha, and K. Parthasarathy. Impact of Nanoparticle Shape, Size, and Properties of the Sustainable Nanocomposites. In *Sustainable Polymer Composites and Nanocomposites*, pages 313–336. Springer International Publishing, Cham, 2019.

[10] Daniel Marie-Christine and Astruc Didier. Gold Nanoparticles: Assembly, Supramolecular Chemistry, Quantum-Size-Related Properties, and Applications Toward Biology, Catalysis, and Nanotechnology. *Chemical Reviews*, 104(1):293–346, 2004.

[11] Xiaochun Zhou, Weilin Xu, Guokun Liu, Debashis Panda, and Peng Chen. Size-Dependent Catalytic Activity and Dynamics of Gold Nanoparticles at the Single-Molecule Level. *Journal of the American Chemical Society*, 132:138–146, 2010.

[12] Kenneth J. Klabunde, Jane Stark, Olga Koper, Cathy Mohs, Dong G. Park, Shawn Decker, Yan Jiang, Isabelle Lagadic, and Dajie Zhang. Nanocrystals as Stoichiometric Reagents with Unique Surface Chemistry. *Journal of Physical Chemistry*, 100:12142–12153, 1996.

[13] Xiaohua Huang and Mostafa A. El-Sayed. Gold nanoparticles: Optical properties and implementations in cancer diagnosis and photothermal therapy. *Journal of Advanced Research*, 1:13–28, 2010.

[14] Christopher Loo, Alex Lin, Leon Hirsch, Min-Ho Lee, Jennifer Barton, Naomi Halas, Jennifer West, and Rebekah Drezek. Nanoshell-enabled photonics-based imaging and therapy of cancer. *Technology in cancer research & treatment*, 3:33–40, 2004.

[15] Xiao-Li Liu, Jia-Hong Wang, Shan Liang, Da-Jie Yang, Fan Nan, Si-Jing Ding, Li Zhou, Zhong-Hua Hao, and Qu-Quan Wang. Tuning Plasmon Resonance of Gold Nanostars for Enhancements of Nonlinear Optical Response and Raman Scattering. *The Journal of Physical Chemistry C*, 118:9659–9664, 2014.

[16] Jie Zeng, Qiang Zhang, Jingyi Chen, and Younan Xia. A Comparison Study of the Catalytic Properties of Au-Based Nanocages, Nanoboxes, and Nanoparticles. *Nano Letters*, 10:30–35, 2010.

[17] You Jeong Lee, Eun-Young Ahn, and Youmie Park. Shape-dependent cytotoxicity and cellular uptake of gold nanoparticles synthesized using green tea extract. *Nanoscale Research Letters*, 14:129, 2019.

[18] Xiaogang Han, James Goebl, Zhenda Lu, and Yadong Yin. Role of Salt in the Spontaneous Assembly of Charged Gold Nanoparticles in Ethanol. *Langmuir*, 27:5282–5289, 2011.

[19] Jesús Mosquera, Isabel García, and Luis M. Liz-Marzán. Cellular Uptake of Nanoparticles versus Small Molecules: A Matter of Size. *Accounts of Chemical Research*, 51:2305–2313, 2018.

[20] Sarita Kango, Susheel Kalia, Annamaria Celli, James Njuguna, Youssef Habibi, and Rajesh Kumar. Surface modification of inorganic nanoparticles for development of organic–inorganic nanocomposites—A review. *Progress in Polymer Science*, 38:1232–1261, 2013.

[21] Ajay Kumar Gupta and Mona Gupta. Synthesis and surface engineering of iron oxide nanoparticles for biomedical applications. *Biomaterials*, 26:3995–4021, 2005.

[22] Barbara Blasiak, Frank C. J. M. van Veggel, and Boguslaw Tomanek. Applications of Nanoparticles for MRI Cancer Diagnosis and Therapy. *Journal of Nanomaterials*, 2013:1–12, 2013.

[23] Christophe Alric, Jacqueline Taleb, Géraldine Le Duc, Céline Mandon, Claire Billotey, Alice Le Meur-Herland, Thierry Brochard, Francis Vocanson, Marc Janier, Pascal Perriat, Stéphane Roux, and Olivier Tillement. Gadolinium Chelate Coated Gold Nanoparticles As Contrast Agents for Both X-ray Computed Tomography and Magnetic Resonance Imaging. *Journal American Chemical Society*, 130:5908–5915, 2008.

[24] Xiangjun Han, Ke Xu, Olena Taratula, and Khashayar Farsad. Applications of nanoparticles in biomedical imaging. *Nanoscale*, 11:799–819, 2019.

[25] Hyon Bin Na, In Chan Song, and Taeghwan Hyeon. Inorganic Nanoparticles for MRI Contrast Agents. *Advanced Materials*, 21:2133–2148, 2009.

[26] Xiao Li, Zhongguo Sui, Xin Li, Wen Xu, Qie Guo, Jialin Sun, and Fanbo Jing. Perfluorooctylbromide nanoparticles for ultrasound imaging and drug delivery. *International Journal of Nanomedicine*, 13:3053–3067, 2018.

[27] Qiaofeng Jin, Chih-Yu Lin, Shih-Tsung Kang, Yuan-Chih Chang, Hairong Zheng, Chia-Min Yang, and Chih-Kuang Yeh. Superhydrophobic silica nanoparticles as ultrasound contrast agents. *Ultrasonics Sonochemistry*, 36:262–269, 2017.

[28] Sang Bong Lee, Hye Lan Kim, Hwan-Jeong Jeong, Seok Tae Lim, Myung-Hee Sohn, and Dong Wook Kim. Mesoporous Silica Nanoparticle Pretargeting for PET Imaging Based on a Rapid Bioorthogonal Reaction in a Living Body. *Angewandte Chemie International Edition*, 52:10549–10552, 2013.

[29] Marie-Caline Z. Abadjian, Jaeyeon Choi, and Carolyn J. Anderson. Nanoparticles for PET Imaging of Tumors and Cancer Metastasis. In Jeff W.M. Bulte and Michel M.J. Modo, editors, *Design and Applications of Nanoparticles in Biomedical Imaging*, pages 229–255. Springer International Publishing, Cham, 2017.

[30] Yongfeng Zhao, Bo Pang, Hannah Luehmann, Lisa Detering, Xuan Yang, Deborah Sultan, Scott Harpstrite, Vijay Sharma, Cathy S. Cutler, Younan Xia, and Yongjian Liu. Gold Nanoparticles Doped with $^{199}$ Au Atoms and Their Use for Targeted Cancer Imaging by SPECT. *Advanced Healthcare Materials*, 5:928–935, 2016.

[31] Tamar Dreifuss, Eran Barnoy, Menachem Motiei, and Rachela Popovtzer. Theranostic Gold Nanoparticles for CT Imaging. In *Design and Applications of Nanoparticles in Biomedical Imaging*, pages 403–427. Springer International Publishing, Cham, 2017.

[32] Neil Sim and David Parker. Critical design issues in the targeted molecular imaging of cell surface receptors. *Chemical Society Reviews*, 44:2122–2134, 2015.

[33] Ke Wang, Nicholas G. Horton, Kriti Charan, and Chris Xu. Advanced Fiber Soliton Sources for Nonlinear Deep Tissue Imaging in Biophotonics. *IEEE Journal of Selected Topics in Quantum Electronics*, 20:50–60, 2014.

[34] Selvi Radhakrishna, S. Agarwal, Purvish M. Parikh, K. Kaur, Shikha Panwar, Shelly Sharma, Ashish Dey, K. K. Saxena, Madhavi Chandra, and Seema Sud. Role of magnetic resonance imaging in breast cancer management. *South Asian Journal of Cancer*, 7:69–71, 2018.

[35] Ritse M. Mann, Christiane K. Kuhl, and Linda Moy. Contrast-enhanced MRI for breast cancer screening: Breast MRI for Screening. *Journal of Magnetic Resonance Imaging*, 50:377–390, 2019.

[36] John V. Frangioni. New Technologies for Human Cancer Imaging. *Journal of Clinical Oncology*, 26:4012–4021, 2008.

[37] Or Perlman and Haim Azhari. MRI and Ultrasound Imaging of Nanoparticles for Medical Diagnosis. In *Nanotechnology Characterization Tools for Biosensing and Medical Diagnosis*, pages 333–365. Springer Berlin Heidelberg, Berlin, Heidelberg, 2018.

[38] Katheryne E. Wilson, Keerthi S. Valluru, and Jürgen K. Willmann. Nanoparticles for Photoacoustic Imaging of Cancer. In *Design and Applications of Nanoparticles in Biomedical Imaging*, pages 315–335. Springer International Publishing, Cham, 2017.

[39] Rubel Chakravarty, Shreya Goel, Ashutosh Dash, and Weibo Cai. Radiolabeled inorganic nanoparticles for positron emission tomography imaging of cancer: an overview. *The Quarterly Journal of Nuclear Medicine and Molecular Imaging*, 61:181–204, 2017.

[40] Tang Tang, Joel Garcia, and Angelique Y. Louie. PET/SPECT/MRI Multimodal Nanoparticles. In *Design and Applications of Nanoparticles in Biomedical Imaging*, pages 205–228. Springer International Publishing, Cham, 2017.

[41] Peter T. C. So, Chen Y. Dong, Barry R. Masters, and Keith M. Berland. Two-Photon Excitation Fluorescence Microscopy. *Annual Review of Biomedical Engineering*, 2:399–429, 2000.

[42] Jarmo T. Alander, Ilkka Kaartinen, Aki Laakso, Tommi Pätilä, Thomas Spillmann, Valery V. Tuchin, Maarit Venermo, and Petri Välisuo. A Review of Indocyanine Green Fluorescent Imaging in Surgery. *International Journal of Biomedical Imaging*, 2012:1–26, 2012.

[43] D. Thomas and G. Duguid. Optical coherence tomography—a review of the principles and contemporary uses in retinal investigation. *Eye*, 18:561–570, 2004.

[44] Patrizia Agostinis, Kristian Berg, Keith A. Cengel, Thomas H. Foster, Albert W. Girotti, Sandra O. Gollnick, Stephen M. Hahn, Michael R. Hamblin, Asta Juzeniene, David Kessel, Mladen Korbelik, Johan Moan, Pawel Mroz, Dominika Nowis, Jacques Piette, Brian C. Wilson, and Jakub Golab. Photodynamic therapy of cancer: An update. *CA: A Cancer Journal for Clinicians*, 61:250–281, 2011.

[45] Guosong Hong, Alexander L. Antaris, and Hongjie Dai. Near-infrared fluorophores for biomedical imaging. *Nature Biomedical Engineering*, 1:0010, 2017.

[46] Susan L. Troyan, Vida Kianzad, Summer L. Gibbs-Strauss, Sylvain Gioux, Aya Matsui, Rafiou Oketokoun, Long Ngo, Ali Khamene, Fred Azar, and John V. Frangioni. The FLARE™ Intraoperative Near-Infrared Fluorescence Imaging System: A First-in-Human Clinical Trial in Breast Cancer Sentinel Lymph Node Mapping. *Annals of Surgical Oncology*, 16:2943–2952, 2009.

[47] Joost R. van der Vorst, Boudewijn E. Schaafsma, Merlijn Hutteman, Floris P. R. Verbeek, Gerrit-Jan Liefers, Henk H. Hartgrink, Vincent T. H. B. M. Smit, Clemens W. G. M. Löwik, Cornelis J. H. van de Velde, John V. Frangioni, and Alexander L. Vahrmeijer. Near-infrared fluorescence-guided resection of colorectal liver metastases: Fluorescence Imaging of Liver Cancer. *Cancer*, 119:3411–3418, 2013.

[48] Quirijn R. J.G. Tummers, Floris P. R. Verbeek, Hendrica A. J.M. Prevoo, Andries E. Braat, Coen I. M. Baeten, John V. Frangioni, Cornelis J. H. van de Velde, and Alexander L. Vahrmeijer. First Experience on Laparoscopic Near-Infrared Fluorescence Imaging of Hepatic Uveal Melanoma Metastases Using Indocyanine Green. *Surgical Innovation*, 22:20–25, 2015.

[49] Patricia E. Burrows, Manuel L. Gonzalez-Garay, John C. Rasmussen, Melissa B. Aldrich, Renie Guilliod, Erik A. Maus, Caroline E. Fife, Sunkuk Kwon, Philip E. Lapinski, Philip D. King, and Eva M. Sevick-Muraca. Lymphatic abnormalities are associated with RASA1 gene mutations in mouse and man. *Proceedings of the National Academy of Sciences*, 110:8621–8626, 2013.

[50] Isabella Tavernaro, Christian Cavelius, Henrike Peuschel, and Annette Kraegeloh. Bright fluorescent silica-nanoparticle probes for high-resolution STED and confocal microscopy. *Beilstein Journal of Nanotechnolgy*, 8:1283–1296, 2017.

[51] Ute Resch-Genger, Markus Grabolle, Sara Cavaliere-Jaricot, Roland Nitschke, and Thomas Nann. Quantum dots versus organic dyes as fluorescent labels. *Nature Methods*, 5:763–775, 2008.

[52] Geoffrey New. *Introduction to Nonlinear Optics*. Cambridge Univ. Press, 2011.

[53] YVGS Murti and C vijayan. *Essentials of Nonlinear Optics*. Wiley, 2014.

[54] Cid B de Araújo, Anderson S L Gomes, and Georges Boudebs. Techniques for nonlinear optical characterization of materials: a review. *Reports on Progress in Physics*, 79:036401, 2016.

[55] Luigi Bonacina. Nonlinear Nanomedecine: Harmonic Nanoparticles toward Targeted Diagnosis and Therapy. *Molecular Pharmaceutics*, 10:783–792, 2013.

[56] Andrii Rogov. *Bismuth ferrite and silicon carbide harmonic nanoparticles: from characterization to tissue imaging*. PhD thesis, 2015.

[57] University Berkeley. Two-Photon fluorescence microscopy. http://microscopy.berkeley.edu/courses/tlm/2P/index.html. Accessed: 2020-10-20.

[58] I. Freund, M. Deutsch, and A. Sprecher. Connective tissue polarity. Optical second-harmonic microscopy, crossed-beam summation, and small-angle scattering in rat-tail tendon. *Biophysical Journal*, 50:693–712, 1986.

[59] Lei Guo and Man Shing Wong. Multiphoton Excited Fluorescent Materials for Frequency Upconversion Emission and Fluorescent Probes. *Advanced Materials*, 26:5400–5428, 2014.

[60] Guang S. He, Loon-Seng Tan, Qingdong Zheng, and Paras N. Prasad. Multiphoton Absorbing Materials: Molecular Designs, Characterizations, and Applications. *Chemical Reviews*, 108:1245–1330, 2008.

[61] Hwan Myun Kim, Mun Sik Seo, Seung-Joon Jeon, and Bong Rae Cho. Two-photon absorption properties of hexa-substituted benzene derivatives. Comparison between dipolar and octupolar molecules. *Chem. Commun.*, pages 7422–7424, 2009.

[62] Paul J. Campagnola, Heather A. Clark, Wwilliam A. Mohler, Aaron Lewis, and Leslie M. Loew. Second-harmonic imaging microscopy of living cells. *Journal of Biomedical Optics*, 6:277–286, 2001.

[63] Yuri Nakayama, Peter J. Pauzauskie, Aleksandra Radenovic, Robert M. Onorato, Richard J. Saykally, Jan Liphardt, and Peidong Yang. Tunable nanowire nonlinear optical probe. *Nature*, 447:1098–1101, 2007.

[64] Maëlenn Aufray, Stéphane Menuel, Yves Fort, Julien Eschbach, Didier Rouxel, and Brice Vincent. New synthesis of nanosized niobium oxides and lithium niobate particles and their characterization by XPS analysis. *Journal of Nanoscience and Nanotechnology*, 9:4780–4785, 2009.

[65] Periklis Pantazis, James Maloney, David Wu, and Scott E. Fraser. Second harmonic generating (SHG) nanoprobes for in vivo imaging. *Proceedings of the National Academy of Sciences*, 107(33):14535–14540, 2010.

[66] Chia-Lung Hsieh, Rachel Grange, Ye Pu, and Demetri Psaltis. Three-dimensional harmonic holographic microcopy using nanoparticles as probes for cell imaging. *Optics Express*, 17:2880–2891, 2009.

[67] Rachel Grange, Thomas Lanvin, Chia-Lung Hsieh, Ye Pu, and Demetri Psaltis. Imaging with second-harmonic radiation probes in living tissue. *Biomedical Optics Express*, 2:2532–2539, 2011.

[68] Ronja Bäumner, Luigi Bonacina, Jörg Enderlein, Jèrôme Extermann, Thomas Fricke-Begemann, Gerd Marowsky, and Jean-Pierre Wolf. Evanescent-Field-Induced Second Harmonic Generation by Noncentrosymmetric Nanoparticles. *Optics Express*, 18:23218–25, 2010.

[69] N. Sandeau, L. Le Xuan, D. Chauvat, C. Zhou, J.-F. Roch, and S. Brasselet. Defocused imaging of second harmonic generation from a single nanocrystal. *Optics Express*, 15:16051–16060, 2007.

[70] Aliaksandr V. Kachynski, Andrey N. Kuzmin, Marcin Nyk, Indrajit Roy, and Paras N. Prasad. Zinc Oxide Nanocrystals for Nonresonant Nonlinear Optical Microscopy in Biology and Medicine. *Journal of Physical Chemistry C*, 112:10721–10724, 2008.

[71] Justin C. Johnson, Haoquan Yan, Richard D. Schaller, Poul B. Petersen, Peidong Yang, and Richard J. Saykally. Near-Field Imaging of Nonlinear Optical Mixing in Single Zinc Oxide Nanowires. *Nano Letters*, 2:279–283, 2002.

[72] Davide Staedler, Thibaud Magouroux, Rachid Hadji, Cécile Joulaud, Jérôme Extermann, Sebastian Schwung, Solène Passemard, Christelle Kasparian, Gareth Clarke, Mathias Gerrmann, Ronan Le Dantec, Yannick Mugnier, Daniel Rytz, Daniel Ciepielewski, Christine Galez, Sandrine Gerber-Lemaire, Lucienne Juillerat-Jeanneret, Luigi Bonacina, and Jean-Pierre Wolf. Harmonic Nanocrystals for Biolabeling: A Survey of Optical Properties and Biocompatibility. *ACS Nano*, 6:2542–2549, 2012.

[73] Jung Soo Suk, Qingguo Xu, Namho Kim, Justin Hanes, and Laura M. Ensign. PEGylation as a strategy for improving nanoparticle-based drug and gene delivery. *Advanced Drug Delivery Reviews*, 99:28–51, 2016.

[74] Delphine Boudard, Valérie Forest, Jérémie Pourchez, Najih Boumahdi, Maura Tomatis, Bice Fubini, Bernard Guilhot, Michèle Cottier, and Philippe Grosseau. In vitro cellular responses to silicon carbide particles manufactured through the Acheson process: Impact of physico-chemical features on pro-inflammatory and pro-oxidative effects. *Toxicology in Vitro*, 28:856–865, 2014.

[75] Joice Sophia Ponraj, Sathish Chander Dhanabalan, Giovanni Attolini, and Giancarlo Salviati. SiC Nanostructures Toward Biomedical Applications and Its Future Challenges. *Critical Reviews in Solid State and Materials Sciences*, 41:430–446, 2016.

[76] S. Barillet, M.-L. Jugan, M. Laye, Y. Leconte, N. Herlin-Boime, C. Reynaud, and M. Carrière. In vitro evaluation of SiC nanoparticles impact on A549 pulmonary cells: Cyto-, genotoxicity and oxidative stress. *Toxicology Letters*, 198:324–330, 2010.

[77] M. Boksebeld, V. Kilin, A. Géloën, G. Ceccone, A. Jaffal, C. Schmidt, S. Alekseev, V. Lysenko, J. P. Wolf, L. Bonacina, E. Souteyrand, Y. Chevolot, and V. Monnier. Folate-modified silicon carbide nanoparticles as multiphoton imaging nanoprobes for cancer-cell-specific labeling. *RSC Advances*, 7(44):27361–27369, 2017.

[78] Chia-Lung Hsieh, Rachel Grange, Ye Pu, and Demetri Psaltis. Bioconjugation of barium titanate nanocrystals with immunoglobulin G antibody for second harmonic radiation imaging probes. *Biomaterials*, 31:2272–2277, 2010.

[79] Bobo Gu, Artem Pliss, Andrey N. Kuzmin, Alexander Baev, Tymish Y. Ohulchanskyy, Jossana A. Damasco, Ken-Tye Yong, Shuangchun Wen, and Paras N. Prasad. In-situ second harmonic generation by cancer cell targeting ZnO nanocrystals to effect photodynamic action in subcellular space. *Biomaterials*, 104:78–86, 2016.

[80] Shaowei Wang, Xinyuan Zhao, Jun Qian, and Sailing He. Polyelectrolyte coated $BaTiO_3$ nanoparticles for second harmonic generation imaging-guided photodynamic therapy with improved stability and enhanced cellular uptake. *RSC Advances*, 6:40615–40625, 2016.

[81] V. Kilin, G. Campargue, I. Fureraj, S. Sakong, T. Sabri, F. Riporto, A. Vieren, Y. Mugnier, C. Mas, D. Staedler, J.M. Collins, L. Bonacina, A. Vogel, J.A. Capobianco, and J.-P. Wolf. Wavelength-Selective Nonlinear Imaging and Photo-Induced Cell Damage by Dielectric Harmonic Nanoparticles. *ACS nano*, 14:4087–4095, 2020.

[82] Devika B. Chithrani, Salomeh Jelveh, Farid Jalali, Monique van Prooijen, Christine Allen, Robert G. Bristow, Richard P. Hill, and David A. Jaffray. Gold nanoparticles as radiation sensitizers in cancer therapy. *Radiation Research*, 173:719–728, 2010.

[83] Shashi K Murthy. Nanoparticles in modern medicine: State of the art and future challenges. *International Journal of Nanomedicine*, 2:129–141, 2007.

[84] Lu Wang, Meng Wang, Benqing Zhou, Feifan Zhou, Cynthia Murray, Rheal A. Towner, Nataliya Smith, Debra Saunders, Gang Xie, and Wei R. Chen. PEGylated reduced-graphene oxide hybridized with Fe3O4 nanoparticles for cancer photothermal-immunotherapy. *Journal of Materials Chemistry B*, 7:7406–7414, 2019.

[85] Eun Ji Hong, Dae Gun Choi, and Min Suk Shim. Targeted and effective photodynamic therapy for cancer using functionalized nanomaterials. *Acta Pharmaceutica Sinica B*, 6:297–307, 2016.

[86] Heejung Kim, Kyungwha Chung, Seungjin Lee, Dong Ha Kim, and Hyukjin Lee. Near-infrared light-responsive nanomaterials for cancer theranostics: NIR light-responsive nanomaterials for cancer theranostics. *Wiley Interdisciplinary Reviews: Nanomedicine and Nanobiotechnology*, 8:23–45, 2016.

[87] Raviraj Vankayala, Yu-Kuan Huang, Poliraju Kalluru, Chi-Shiun Chiang, and Kuo Chu Hwang. First Demonstration of Gold Nanorods-Mediated Photodynamic Therapeutic Destruction of Tumors via Near Infra-Red Light Activation. *Small*, 10(8):1612–1622, 2014.

[88] Wen-Xiu Qiu, Li-Han Liu, Shi-Ying Li, Qi Lei, Guo-Feng Luo, and Xian-Zheng Zhang. ACPI Conjugated Gold Nanorods as Nanoplatform for Dual Image Guided Activatable Photodynamic and Photothermal Combined Therapy In Vivo. *Small*, 13:1603956, 2017.

[89] Yinghui Wang, Hengguo Wang, Dapeng Liu, Shuyan Song, Xiao Wang, and Hongjie Zhang. Graphene oxide covalently grafted upconversion nanoparticles for combined NIR mediated imaging and photothermal/photodynamic cancer therapy. *Biomaterials*, 34:7715–7724, 2013.

[90] Barbara Krammer and Thomas Verwanger. Molecular Biological Mechanisms in Photodynamic Therapy. In *Photodynamic Therapy*, pages 59–66. Springer Berlin Heidelberg, Berlin, Heidelberg, 2014.

[91] Thomas J Dougherty, Charles J Gomer, Barbara W Henderson, Giulio Jori, David Kessel, Mladen Korbelik, Johan Moan, and Qian Peng. Photodynamic Therapy. *Journal of the National Cancer Institute*, 90:889–905, 1998.

[92] Ulrich E. Steiner. Fundamentals of Photophysics, Photochemistry, and Photobiology. In *Photodynamic Therapy*, pages 25–58. Springer Berlin Heidelberg, Berlin, Heidelberg, 2014.

[93] M. D. Daniell and J. S. Hill. A History Of Photodynamic Therapy. *Australian and New Zealand Journal of Surgery*, 61:340–348, 1991.

[94] Mahmoud H. Abdel-Kader. History of Photodynamic Therapy. In *Photodynamic Therapy*, pages 3–22. Springer Berlin Heidelberg, Berlin, Heidelberg, 2014.

[95] American Cancer Society. Getting Photodynamic Therapy. https://www.cancer.org/treatment/treatments-and-side-effects/treatment-types/radiation/photodynamic-therapy.html. accessed: 2020-06-07.

[96] Raviraj Vankayala, Arunachalam Sagadevan, Priya Vijayaraghavan, Chien-Lin Kuo, and Kuo Chu Hwang. Metal Nanoparticles Sensitize the Formation of Singlet Oxygen. *Angewandte Chemie International Edition*, 50:10640–10644, 2011.

[97] George Pasparakis. Light-Induced Generation of Singlet Oxygen by Naked Gold Nanoparticles and its Implications to Cancer Cell Phototherapy. *Small*, 9:4130–4134, 2013.

[98] Raviraj Vankayala, Chien-Lin Kuo, Arunachalam Sagadevan, Po-Hung Chen, Chi-Shiun Chiang, and Kuo Chu Hwang. Morphology dependent photosensitization and formation of singlet oxygen ($1\delta g$) by gold and silver nanoparticles and its application in cancer treatment. *Journal of Materials Chemistry B*, 1:4379–4387, 2013.

[99] Gerald L. DeNardo and Sally J. DeNardo. Update: Turning the Heat on Cancer. *Cancer Biotherapy and Radiopharmaceuticals*, 23:671–679, 2008.

[100] Olav Dahl and Jens Overgaard. A Century With Hyperthermic Oncology In Scandinavia. *Acta Oncologica*, 34:1075–1083, 1995.

[101] D. Jaque, L. Martínez Maestro, B. del Rosal, P. Haro-Gonzalez, A. Benayas, J. L. Plaza, E. Martín Rodríguez, and J. García Solé. Nanoparticles for photothermal therapies. *Nanoscale*, 6:9494–9530, 2014.

[102] Liang Cheng, Chao Wang, Liangzhu Feng, Kai Yang, and Zhuang Liu. Functional Nanomaterials for Phototherapies of Cancer. *Chemical Reviews*, 114:10869–10939, 2014.

[103] Vladimir P. Zharov, Valentin Galitovsky, and Mark Viegas. Photothermal detection of local thermal effects during selective nanophotothermolysis. *Applied Physics Letters*, 83:4897–4899, 2003.

[104] Vladimir P. Zharov, Jin-Woo Kim, David T. Curiel, and Maaike Everts. Self-assembling nanoclusters in living systems: application for integrated photothermal nanodiagnostics and nanotherapy. *Nanomedicine: Nanotechnology, Biology and Medicine*, 1:326–345, 2005.

[105] Vladimir P. Zharov, Elena N. Galitovskaya, Carl Johnson, and Thomas Kelly. Synergistic enhancement of selective nanophotothermolysis with gold nanoclusters: Potential for cancer therapy. *Lasers in Surgery and Medicine*, 37:219–226, 2005.

[106] Georgy S. Terentyuk, Galina N. Maslyakova, Leyla V. Suleymanova, Nikolai G. Khlebtsov, Boris N. Khlebtsov, Garif G. Akchurin, Irina L. Maksimova, and Valery V. Tuchin. Laser-induced tissue hyperthermia mediated by gold nanoparticles: toward cancer phototherapy. *Journal Biomedical Optics*, 14:021016, 2009.

[107] Ekaterina Y Hleb, Jason H Hafner, Jeffrey N Myers, Ehab Y Hanna, Betty C Rostro, Sergey A Zhdanok, and Dmitri O Lapotko. LANTCET: elimination of solid tumor cells with photothermal bubbles generated around clusters of gold nanoparticles. *Nanomedicine*, 3:647–667, 2008.

[108] I Elsayed, X Huang, and M Elsayed. Selective laser photo-thermal therapy of epithelial carcinoma using anti-EGFR antibody conjugated gold nanoparticles. *Cancer Letters*, 239:129–135, 2006.

[109] Jing-Liang Li, Lei Wang, Xiang-Yang Liu, Zhi-Ping Zhang, Hong-Chen Guo, Wei-Min Liu, and Sing-Hai Tang. In vitro cancer cell imaging and therapy using transferrin-conjugated gold nanoparticles. *Cancer Letters*, 274:319–326, 2009.

[110] Boris Khlebtsov, Vladimir Zharov, Andrei Melnikov, Valery Tuchin, and Nikolai Khlebtsov. Optical amplification of photothermal therapy with gold nanoparticles and nanoclusters. *Nanotechnology*, 17(20):5167–5179, 2006.

[111] Cuixia Bi, Jin Chen, Ying Chen, Yahui Song, Anran Li, Shuzhou Li, Zhengwei Mao, Changyou Gao, Dayang Wang, Helmuth Möhwald, and Haibing Xia. Realizing a Record Photothermal Conversion Efficiency of Spiky Gold Nanoparticles in the Second Near-Infrared Window by Structure-Based Rational Design. *Chemistry of Materials*, 30:2709–2718, 2018.

[112] Xiao-Ming Zhu, Hong-Ye Wan, Henglei Jia, Liang Liu, and Jianfang Wang. Porous Pt Nanoparticles with High Near-Infrared Photothermal Conversion Efficiencies for Photothermal Therapy. *Advanced Healthcare Materials*, 5:3165–3172, 2016.

[113] Lile Dong, Guanming Ji, Yu Liu, Xia Xu, Pengpeng Lei, Kaimin Du, Shuyan Song, Jing Feng, and Hongjie Zhang. Multifunctional Cu–Ag2S nanoparticles with high photothermal conversion efficiency for photoacoustic imaging-guided photothermal therapy in vivo. *Nanoscale*, 10:825–831, 2018.

[114] Jinfeng Zhang, Caixia Yang, Rui Zhang, Rui Chen, Zhenyu Zhang, Wenjun Zhang, Shih-Hao Peng, Xiaoyuan Chen, Gang Liu, Chain-Shu Hsu, and Chun-Sing Lee. Biocompatible D-A Semiconducting Polymer Nanoparticle with Light-Harvesting Unit for Highly Effec-

tive Photoacoustic Imaging Guided Photothermal Therapy. *Advanced Functional Materials*, 27:1605094, 2017.

[115] R. B. M. Schasfoort and Anna J. Tudos, editors. *Handbook of surface plasmon resonance*. RSC Pub, Cambridge, UK, 2008.

[116] Katherine A. Willets and Richard P. Van Duyne. Localized Surface Plasmon Resonance Spectroscopy and Sensing. *Annual Review of Physical Chemistry*, 58:267–297, 2007.

[117] Stefan A. Maier. *Plasmonics: fundamentals and applications*. Springer, New York, 2007.

[118] Guillaume Baffou and Romain Quidant. Thermo-plasmonics: using metallic nanostructures as nano-sources of heat: Thermoplasmonics. *Laser & Photonics Reviews*, 7:171–187, 2013.

[119] Guillaume Baffou, Julien Polleux, Hervé Rigneault, and Serge Monneret. Super-Heating and Micro-Bubble Generation around Plasmonic Nanoparticles under cw Illumination. *Journal Physical Chemistry C*, 118:4890–4898, 2014.

[120] Dmitri Lapotko. Plasmonic nanoparticle-generated photothermal bubbles and their biomedical applications. *Nanomedicine (London)*, 4:813–845, 2009.

[121] Ardeshir R. Rastinehad, Harry Anastos, Ethan Wajswol, Jared S. Winoker, John P. Sfakianos, Sai K. Doppalapudi, Michael R. Carrick, Cynthia J. Knauer, Bachir Taouli, Sara C. Lewis, Ashutosh K. Tewari, Jon A. Schwartz, Steven E. Canfield, Arvin K. George, Jennifer L. West, and Naomi J. Halas. Gold nanoshell-localized photothermal ablation of prostate tumors in a clinical pilot device study. *Proceedings of the National Academy of Sciences*, 116:18590–18596, 2019.

[122] Santiago Sánchez-Cabezas, Roberto Montes-Robles, Juan Gallo, Félix Sancenón, and Ramón Martínez-Máñez. Combining magnetic hyperthermia and dual T1/T2 MR imaging using highly versatile iron oxide nanoparticles. *Dalton Transactions*, 48:3883–3892, 2019.

[123] Harikrishna Devalapally, Dinesh Shenoy, Steven Little, Robert Langer, and Mansoor Amiji. Poly(ethylene oxide)-modified poly(beta-amino ester) nanoparticles as a pH-sensitive system for tumor-targeted delivery of hydrophobic drugs: part 3. Therapeutic efficacy and safety studies in ovarian cancer xenograft model. *Cancer Chemotherapy and Pharmacology*, 59:477–484, 2007.

[124] Costas G. Hadjipanayis, Revaz Machaidze, Milota Kaluzova, Liya Wang, Albert J. Schuette, Hongwei Chen, Xinying Wu, and Hui Mao. EGFRvIII Antibody–Conjugated Iron Oxide Nanoparticles for Magnetic Resonance Imaging–Guided Convection-Enhanced Delivery and Targeted Therapy of Glioblastoma. *Cancer Research*, 70:6303–6312, 2010.

[125] Geoffrey von Maltzahn, Ji-Ho Park, Amit Agrawal, Nanda Kishor Bandaru, Sarit K. Das, Michael J. Sailor, and Sangeeta N. Bhatia. Computationally Guided Photothermal Tumor Therapy Using Long-Circulating Gold Nanorod Antennas. *Cancer Research*, 69:3892–3900, 2009.

[126] Priyanka Singh, Santosh Pandit, V. R. S. S. Mokkapati, Abhroop Garg, Vaishnavi Ravikumar, and Ivan Mijakovic. Gold Nanoparticles in Diagnostics and Therapeutics for Human Cancer. *International Journal of Molecular Sciences*, 19:1979, 2018.

[127] Victor K. LaMer and Robert H. Dinegar. Theory, Production and Mechanism of Formation of Monodispersed Hydrosols. *Journal of the American Chemical Society*, 72:4847–4854, 1950.

[128] Hilmar Koerner, Robert I. MacCuspie, Kyoungweon Park, and Richard A. Vaia. In Situ UV/Vis, SAXS, and TEM Study of Single-Phase Gold Nanoparticle Growth. *Chemistry of Materials*, 24:981–995, 2012.

[129] Yugang Sun. Controlled synthesis of colloidal silver nanoparticles in organic solutions: empirical rules for nucleation engineering. *Chemical Society Reviews*, 42:2497–2511, 2013.

[130] John Turkevich, Peter Cooper Stevenson, and James Hillier. A study of the nucleation and growth processes in the synthesis of colloidal gold. *Discussions of the Faraday Society*, 11:55, 1951.

[131] Mathias Brust, Merryl Walker, Donald Bethell, David J. Schiffrin, and Robin Whyman. Synthesis of thiol-derivatised gold nanoparticles in a two-phase Liquid–Liquid system. *Journal of the Chemical Society, Chemical Communications*, pages 801–802, 1994.

[132] Christophe Deraedt, Lionel Salmon, Sylvain Gatard, Roberto Ciganda, Ricardo Hernandez, Jaime Ruiz, and Didier Astruc. Sodium borohydride stabilizes very active gold nanoparticle catalysts. *Chemical Communications*, 50:14194–14196, 2014.

[133] P. C. Pandey, Shubhangi Shukla, and Yashashwa Pandey. 3-Aminopropyltrimethoxysilane and graphene oxide/reduced graphene oxide-induced generation of gold nanoparticles and their nanocomposites: electrocatalytic and kinetic activity. *RSC Advances*, 6:80549–80556, 2016.

[134] Kenneth R. Brown and Michael J. Natan. Hydroxylamine Seeding of Colloidal Au Nanoparticles in Solution and on Surfaces. *Langmuir*, 14:726–728, 1998.

[135] Rui Wang, Xiaohui Ji, Zhenzhen Huang, Yurui Xue, Dayang Wang, and Wensheng Yang. Citrate-Regulated Surface Morphology of $SiO_2$@Au Particles To Control the Surface Plasmonic Properties. *Journal of Physical Chemistry C*, 120:377–385, 2016.

[136] Matthew N. Martin, James I. Basham, Paul Chando, and Sang-Kee Eah. Charged gold nanoparticles in non-polar solvents: 10-min synthesis and 2D self-assembly. *Langmuir*, 26:7410–7417, 2010.

[137] Masafumi Harada and Syoko Kizaki. Formation Mechanism of Gold Nanoparticles Synthesized by Photoreduction in Aqueous Ethanol Solutions of Polymers Using In Situ Quick Scanning X-ray Absorption Fine Structure and Small-Angle X-ray Scattering. *Crystal Growth & Design*, 16:1200–1212, 2016.

[138] Wissanu Patungwasa and José H. Hodak. pH tunable morphology of the gold nanoparticles produced by citrate reduction. *Materials Chemistry and Physics*, 108:45–54, 2008.

[139] P. Alexandridis. Gold Nanoparticle Synthesis, Morphology Control, and Stabilization Facilitated by Functional Polymers. *Chemical Engineering & Technology*, 34:15–28, 2011.

[140] Nikhil R. Jana, Latha Gearheart, and Catherine J. Murphy. Seeding Growth for Size Control of 5-40nm Diameter Gold Nanoparticles. *Langmuir*, 17:6782–6786, 2001.

[141] Daniel Andreescu, Tapan Kumar Sau, and Dan V. Goia. Stabilizer-free nanosized gold sols. *Journal of Colloid and Interface Science*, 298:742–751, 2006.

[142] Grigoris Mountrichas, Stergios Pispas, and Efstratios I. Kamitsos. Effect of Temperature on the Direct Synthesis of Gold Nanoparticles Mediated by Poly(dimethylaminoethyl methacrylate) Homopolymer. *Journal of Physical Chemistry C*, 118:22754–22759, 2014.

[143] Christoph Ziegler and Alexander Eychmuller. Seeded Growth Synthesis of Uniform Gold Nanoparticles with Diameters of 15-300 nm. *Journal of Physical Chemistry C*, 115:4502–4506, 2011.

[144] Jessica Rodríguez-Fernández, Jorge Pérez-Juste, F. Javier García de Abajo, and Luis M. Liz-Marzán. Seeded Growth of Submicron Au Colloids with Quadrupole Plasmon Resonance Modes. *Langmuir*, 22:7007–7010, 2006.

[145] Jill E. Millstone, Wei Wei, Matthew R. Jones, Hyojong Yoo, and Chad A. Mirkin. Iodide ions control seed-mediated growth of anisotropic gold nanoparticles. *Nano Letters*, 8:2526–2529, 2008.

[146] Nikhil R. Jana. Gram-Scale Synthesis of Soluble, Near-Monodisperse Gold Nanorods and Other Anisotropic Nanoparticles. *Small*, 1:875–882, 2005.

[147] Catherine J. Murphy, Tapan K. Sau, Anand M. Gole, Christopher J. Orendorff, Jinxin Gao, Linfeng Gou, Simona E. Hunyadi, and Tan Li. Anisotropic metal nanoparticles: Synthesis, assembly, and optical applications. *Journal of Physical Chemistry B*, 109:13857–13870, 2005.

[148] Tapan K. Sau and Catherine J. Murphy. Room Temperature, High-Yield Synthesis of Multiple Shapes of Gold Nanoparticles in Aqueous Solution. *Journal of the American Chemical Society*, 126:8648–8649, 2004.

[149] Linyou Cao, Tao Zhu, and Zhongfan Liu. Formation mechanism of nonspherical gold nanoparticles during seeding growth: Roles of anion adsorption and reduction rate. *Journal of Colloid and Interface Science*, 293:69–76, 2006.

[150] N. R. Jana, L. Gearheart, and C. J. Murphy. Seed-Mediated Growth Approach for Shape-Controlled Synthesis of Spheroidal and Rod-like Gold Nanoparticles Using a Surfactant Template. *Advanced Materials*, 13:1389–1393, 2001.

[151] Hao Ming Chen, Ru-Shi Liu, and Din Ping Tsai. A Versatile Route to the Controlled Synthesis of Gold Nanostructures. *Crystal Growth & Design*, 9:2079–2087, 2009.

[152] Marek Grzelczak, Jorge Pérez-Juste, Paul Mulvaney, and Luis M. Liz-Marzán. Shape control in gold nanoparticle synthesis. *Chemical Society Reviews*, 37:1783–1791, 2008.

[153] R. D. Averitt, D. Sarkar, and N. J. Halas. Plasmon resonance shifts of Au-coated Au 2 S nanoshells: insight into multicomponent nanoparticle growth. *Physical Review Letters*, 78:4217, 1997.

[154] Susie Eustis and Mostafa A. El-Sayed. Why gold nanoparticles are more precious than pretty gold: Noble metal surface plasmon resonance and its enhancement of the radiative and nonradiative properties of nanocrystals of different shapes. *Chemical Society Reviews*, 35:209–217, 2006.

[155] S.J Oldenburg, R.D Averitt, S.L Westcott, and N.J Halas. Nanoengineering of optical resonances. *Chemical Physics Letters*, 288:243–247, 1998.

[156] Tan Pham, Joseph B. Jackson, Naomi J. Halas, and T. Randall Lee. Preparation and Characterization of Gold Nanoshells Coated with Self-Assembled Monolayers. *Langmuir*, 18:4915–4920, 2002.

[157] Werner Stöber, Arthur Fink, and Ernst Bohn. Controlled growth of monodisperse silica spheres in the micron size range. *Journal of Colloid and Interface Science*, 26:62–69, 1968.

[158] Yandong Han, Ziyang Lu, Zhaogang Teng, Jinglun Liang, Zilong Guo, Dayang Wang, Ming-Yong Han, and Wensheng Yang. Unraveling the Growth Mechanism of Silica Particles in the Stöber Method: In Situ Seeded Growth Model. *Langmuir*, 33:5879–5890, 2017.

[159] Steven J. Oldenburg, Sarah L. Westcott, Richard D. Averitt, and Naomi J. Halas. Surface enhanced Raman scattering in the near infrared using metal nanoshell substrates. *The Journal of Chemical Physics*, 111:4729–4735, 1999.

[160] Sandra Jean Rosenthal and David W. Wright, editors. *Nanobiotechnology protocols*. Methods in molecular biology. Humana Press, Totowa, N. J, 2005.

[161] Shunying Liu, Zhongshi Liang, Feng Gao, Jiahui Yu, Shufang Luo, Jesus N. Calata, and Guoquan Lu. A Facile Approach to the Synthesis of Gold Nanoshells with Near Infrared Responsive Properties. *Chinese Journal of Chemistry*, 27:1079–1085, 2009.

[162] Jun-Hyun Kim, William W. Bryan, and T. Randall Lee. Preparation, Characterization, and Optical Properties of Gold, Silver, and Gold-Silver Alloy Nanoshells Having Silica Cores. *Langmuir*, 24:11147–11152, 2008.

[163] Sangeun Park, Minyim Park, Pokeun Han, and Sangwha Lee. Relative Contributions of Experimental Parameters to NIR-Absorption Spectra of Gold Nanoshells. *Journal of Industrial and Engineering Chemistry*, 13:65–70, 2007.

[164] Daniel G. Duff, Alfons Baiker, and Peter P. Edwards. A new hydrosol of gold clusters. 1. Formation and particle size variation. *Langmuir*, 9:2301–2309, 1993.

[165] Mariano J. García-Soto and Omar González-Ortega. Synthesis of silica-core gold nanoshells and some modifications/variations. *Gold Bulletin*, 49:111–131, 2016.

[166] S. J. Oldenburg. *Light Scattering from Gold Nanoshells*. PhD thesis, Rice University, 1999.

[167] Bruce E. Brinson, J. Britt Lassiter, Carly S. Levin, Rizia Bardhan, Nikolay Mirin, and Naomi J. Halas. Nanoshells Made Easy: Improving Au Layer Growth on Nanoparticle Surfaces. *Langmuir*, 24:14166–14171, 2008.

[168] Thomas C. Preston and Ruth Signorell. Growth and optical properties of gold nanoshells prior to the formation of a continuous metallic layer. *ACS Nano*, 3:3696–3706, 2009.

[169] Yong Taik Lim, O. Ok Park, and Hee-Tae Jung. Gold nanolayer-encapsulated silica particles synthesized by surface seeding and shell growing method: near infrared responsive materials. *Journal of Colloid & Interface Science*, 263:449–453, 2003.

[170] James C. Y. Kah, Nopphawan Phonthammachai, Rachel C. Y. Wan, Jing Song, Timothy White, Subodh Mhaisalkar, Iman Ahmadb, Colin Sheppardа, and Malini Olivoc. Synthesis of gold nanoshells based on the depositionprecipitation process. *Gold Bulletin*, 41:23–36, 2008.

[171] Nopphawan Phonthammachai, James C. Y. Kah, Guo Jun, Colin J. R. Sheppard, Malini C. Olivo, Subodh G. Mhaisalkar, and Timothy J. White. Synthesis of Contiguous Silica-Gold Core-Shell Structures: Critical Parameters and Processes. *Langmuir*, 24:5109–5112, 2008.

[172] J. Richter, A. Steinbrück, T. Pertsch, A. Tünnermann, and R. Grange. Plasmonic Core–Shell Nanowires for Enhanced Second-Harmonic Generation. *Plasmonics*, 8:115–120, 2013.

[173] Dong Kyu Lee, Younseong Song, Van Tan Tran, Jeonghyo Kim, Enoch Y. Park, and Jaebeom Lee. Preparation of concave magnetoplasmonic core-shell supraparticles of gold-coated iron oxide via ion-reducible layer-by-layer method for surface enhanced Raman scattering. *Journal of Colloid and Interface Science*, 499:54–61, 2017.

[174] Zhichuan Xu, Yanglong Hou, and Shouheng Sun. Magnetic Core/Shell Fe $_3$ O $_4$ /Au and Fe $_3$ O $_4$ /Au/Ag Nanoparticles with Tunable Plasmonic Properties. *Journal of the American Chemical Society*, 129:8698–8699, 2007.

[175] Yuping Bao and Kannan M. Krishnan. Preparation of functionalized and gold-coated cobalt nanocrystals for biomedical applications. *Journal of Magnetism and Magnetic Materials*, 293:15–19, 2005.

[176] Marcos Pita, José María Abad, Cristina Vaz-Dominguez, Carlos Briones, Eva Mateo-Martí, José Angel Martín-Gago, Maria del Puerto Morales, and Víctor M. Fernández. Synthesis of cobalt ferrite core/metallic shell nanoparticles for the development of a specific PNA/DNA biosensor. *Journal of Colloid and Interface Science*, 321:484–492, 2008.

[177] Derrick Mott, JaeDong Lee, Nguyen Thi Bich Thuy, Yoshiya Aoki, Prerna Singh, and Shinya Maenosono. A Study on the Plasmonic Properties of Silver Core Gold Shell Nanoparticles: Optical Assessment of the Particle Structure. *Japanese Journal of Applied Physics*, 50:065004, 2011.

[178] Weili Shi, Y. Sahoo, Mark T. Swihart, and P. N. Prasad. Gold Nanoshells on Polystyrene Cores for Control of Surface Plasmon Resonance. *Langmuir*, 21:1610–1617, 2005.

[179] Rizia Bardhan, Nathaniel K. Grady, Tamer Ali, and Naomi J. Halas. Metallic Nanoshells with Semiconductor Cores: Optical Characteristics Modified by Core Medium Properties. *ACS Nano*, 4:6169–6179, 2010.

[180] Maxime Boksebeld, Vasyl Kilin, Rachael Taitt, Luigi Bonacina, Alain Géloën, Vladimir Lysenko, Yann Chevolot, and Virginie Monnier. Nonlinear plasmonic nanohybrids as probes for multimodal cell imaging and potential phototherapeutic agents. *Biomedical Physics and Engineering Express*, 5:025039, 2019.

[181] Helmut Goesmann and Claus Feldmann. Nanoparticulate Functional Materials. *Angewandte Chemie International Edition*, 49:1362–1395, 2010.

[182] K. Lance Kelly, Eduardo Coronado, Lin Lin Zhao, and George C. Schatz. The Optical Properties of Metal Nanoparticles: The Influence of Size, Shape, and Dielectric Environment. *The Journal of Physical Chemistry B*, 107:668–677, 2003.

[183] An-Hui Lu, E. L. Salabas, and Ferdi Schüth. Magnetic Nanoparticles: Synthesis, Protection, Functionalization, and Application. *Angewandte Chemie International Edition*, 46:1222–1244, 2007.

[184] Dan Guo, Guoxin Xie, and Jianbin Luo. Mechanical properties of nanoparticles: basics and applications. *Journal of Physics D: Applied Physics*, 47:013001, 2014.

[185] Jayanta Kumar Patra, Gitishree Das, Leonardo Fernandes Fraceto, Estefania Vangelie Ramos Campos, Maria del Pilar Rodriguez-Torres, Laura Susana Acosta-Torres, Luis Armando Diaz-Torres, Renato Grillo, Mallappa Kumara Swamy, Shivesh Sharma, Solomon Habtemariam, and Han-Seung Shin. Nano based drug delivery systems: recent developments and future prospects. *Journal of Nanobiotechnology*, 16:71, 2018.

[186] S. Moein Moghimi, A. Christy Hunter, and J. Clifford Murray. Nanomedicine: current status and future prospects. *The FASEB Journal*, 19:311–330, 2005.

[187] Megan A. Hahn, Amit K. Singh, Parvesh Sharma, Scott C. Brown, and Brij M. Moudgil. Nanoparticles as contrast agents for in-vivo bioimaging: current status and future perspectives. *Analytical and Bioanalytical Chemistry*, 399:3–27, 2011.

[188] Yongdong Jin. Multifunctional Compact Hybrid Au Nanoshells: A New Generation of Nanoplasmonic Probes for Biosensing, Imaging, and Controlled Release. *Accounts of Chemical Research*, 47:138–148, 2014.

[189] Wenwan Zhong. Nanomaterials in fluorescence-based biosensing. *Analytical and Bioanalytical Chemistry*, 394:47–59, 2009.

[190] Chunbai He, Jianqin Lu, and Wenbin Lin. Hybrid nanoparticles for combination therapy of cancer. *Journal of Controlled Release*, 219:224–236, 2015.

[191] Peter Ercius, Osama Alaidi, Matthew J. Rames, and Gang Ren. Electron Tomography: A Three-Dimensional Analytic Tool for Hard and Soft Materials Research. *Advanced Materials*, 27:5638–5663, 2015.

[192] David B. Williams and C. Barry Carter. *Transmission electron microscopy: a textbook for materials science*. Springer, New York, 2nd edition, 2008.

[193] Benjamin Michen, Christoph Geers, Dimitri Vanhecke, Carola Endes, Barbara Rothen-Rutishauser, Sandor Balog, and Alke Petri-Fink. Avoiding drying-artifacts in transmission electron microscopy: Characterizing the size and colloidal state of nanoparticles. *Scientific Reports*, 5, 2015.

[194] Seifollah Nasrazadani and Shokrollah Hassani. Modern analytical techniques in failure analysis of aerospace, chemical, and oil and gas industries. In *Handbook of Materials Failure Analysis with Case Studies from the Oil and Gas Industry*, pages 39–54. Elsevier, 2016.

[195] Emilia Tomaszewska, Katarzyna Soliwoda, Kinga Kadziola, Beata Tkacz-Szczesna, Grzegorz Celichowski, Michal Cichomski, Witold Szmaja, and Jaroslaw Grobelny. Detection Limits of DLS and UV-Vis Spectroscopy in Characterization of Polydisperse Nanoparticles Colloids. *Journal of Nanomaterials*, 2013:1–10, 2013.

[196] Vincent A. Hackley. Measuring the Size of Nanoparticles in Aqueous Media Using Batch-Mode Dynamic Light Scattering. Technical report, National Institute of Standards and Technology, 2015.

[197] Sourav Bhattacharjee. DLS and zeta potential – What they are and what they are not? *Journal of Controlled Release*, 235:337–351, 2016.

[198] Patrick Bertrand and Lu-Tao Weng. Time-of-Flight Secondary Ion Mass Spectrometry (ToF-SIMS) in: Benoit D., Bresse JF., Van't dack l., Werner H., Wernisch J. (eds) Microbeam and Nanobeam Analysis. *Mikrochimica Acta Supplement*, 13:167–182, 1996.

[199] NIST. Time-of-Flight Secondary Ion Mass Spectrometry. https://www.nist.gov/programs-projects/time-flight-secondary-ion-mass-spectrometry, 2017. Accessed: 2019-11-15.

[200] N. Iyi, K. Kitamura, F. Izumi, J. K. Yamamoto, T. Hayashi, H. Asano, and S. Kimura. Comparative study of defect structures in lithium niobate with different compositions. *Journal of Solid State Chemistry*, 101:340–352, 1992.

[201] Sarah L. Westcott, Steven J. Oldenburg, T. Randall Lee, and Naomi J. Halas. Formation and Adsorption of Clusters of Gold Nanoparticles onto Functionalized Silica Nanoparticle Surfaces. *Langmuir*, 14:5396–5401, 1998.

[202] Patrick Neuberg and Antoine Kichler. Chapter Nine - Recent Developments in Nucleic Acid Delivery with Polyethylenimines. In *Advances in Genetics*, volume 88 of *Nonviral Vectors for Gene Therapy*, pages 263–288. Academic Press, 2014.

[203] Makiya Nishikawa, Shigeru Kawakami, Fumiyoshi Yamashita, and Mitsuru Hashida. Glycosylated Cationic Liposomes for Carbohydrate Receptor–Mediated Gene Transfer. In *Methods in Enzymology*, volume 373 of *Liposomes, Part C*, pages 384–399. Academic Press, 2003.

[204] Surendra Nimesh. 10 - Polyethylenimine nanoparticles. In *Gene Therapy*, Woodhead Publishing Series in Biomedicine, pages 197–223. Woodhead Publishing, 2013.

[205] Tian Xia, Michael Kovochich, Monty Liong, Huan Meng, Sanaz Kabehie, Saji George, Jeffrey I. Zink, and Andre E. Nel. Polyethyleneimine Coating Enhances the Cellular Uptake of Mesoporous Silica Nanoparticles and Allows Safe Delivery of siRNA and DNA Constructs. *ACS Nano*, 3:3273–3286, 2009.

[206] Polyethylenimine, branched 408727. https://www.sigmaaldrich.com/catalog/product/aldrich/408727. Accessed: 2020-10-27.

[207] Wei Lu, Min Ling, Min Jia, Ping Huang, Chengkui Li, and Biao Yan. Facile synthesis and characterization of polyethylenimine-coated Fe3O4 superparamagnetic nanoparticles for cancer cell separation. *Molecular Medicine Reports*, 9:1080–1084, 2014.

[208] Ian Y. Goon, Leo M. H. Lai, May Lim, Paul Munroe, J. Justin Gooding, and Rose Amal. Fabrication and Dispersion of Gold-Shell-Protected Magnetite Nanoparticles: Systematic Control Using Polyethyleneimine. *Chemistry of Materials*, 21:673–681, 2009.

[209] Kimberly A. Curtis, Danielle Miller, Paul Millard, Saswati Basu, Ferenc Horkay, and Preethi L Chandran. Unusual Salt and pH Induced Changes in Polyethylenimine Solutions. *PLOS ONE*, 11:158147, 2016.

[210] Firdos Khan, Sultan Akhtar, Sarah Almofty, Dana Almohazey, and Munthar Alomari. FMSP-Nanoparticles Induced Cell Death on Human Breast Adenocarcinoma Cell Line (MCF-7 Cells): Morphometric Analysis. *Biomolecules*, 8:32, 2018.

[211] Jessica M. Rosenholm, Annika Meinander, Emilia Peuhu, Rasmus Niemi, John E. Eriksson, Cecilia Sahlgren, and Mika Lindén. Targeting of Porous Hybrid Silica Nanoparticles to Cancer Cells. *ACS Nano*, 3:197–206, 2009.

[212] Shu Wang, Kun Qian, XingZhen Bi, and Weixin Huang. Influence of Speciation of Aqueous HAuCl $_4$ on the Synthesis, Structure, and Property of Au Colloids. *Journal of Physical Chemistry C*, 113:6505–6510, 2009.

[213] Lihua Pei, Koichi Mori, and Motonari Adachi. Formation process of two-dimensional networked gold nanowires by citrate reduction of AuCl4- and the shape stabilization. *Langmuir*, 20:7837–7843, 2004.

[214] Qiguang Li, Jiwen Zheng, and Zhongfan Liu. Site-Selective Assemblies of Gold Nanoparticles on an AFM Tip-Defined Silicon Template. *Langmuir*, 19:166–171, 2003.

[215] Ashavani Kumar, Saikat Mandal, P. R. Selvakannan, Renu Pasricha, A. B. Mandale, and Murali Sastry. Investigation into the Interaction between Surface-Bound Alkylamines and Gold Nanoparticles. *Langmuir*, 19:6277–6282, 2003.

[216] Agampodi S. De Silva Indrasekara, Stephen J. Norton, Nicholas K. Geitner, Bridget M. Crawford, Mark R. Wiesner, and Tuan Vo-Dinh. Tailoring the Core–Satellite Nanoassembly Architectures by Tuning Internanoparticle Electrostatic Interactions. *Langmuir*, 34:14617–14623, 2018.

[217] Cécile Joulaud, Yannick Mugnier, Gnon Djanta, Marc Dubled, Jean-Christophe Marty, Christine Galez, Jean-Pierre Wolf, Luigi Bonacina, and Ronan Le Dantec. Characterization of the nonlinear optical properties of nanocrystals by Hyper Rayleigh Scattering. *Journal of Nanobiotechnology*, 11(Suppl 1):S8, 2013.

[218] Robert Boyd. *Nonlinear Optics*. Academic Press, 3rd edition, 2008.

[219] Bordwell pKa Table, https://organicchemistrydata.org/hansreich/resources/pka/. https://organicchemistrydata.org/hansreich/resources/pka/. Accessed: 2020-10-09.

[220] Kathryn A. Whitaker and Eric M. Furst. Layer-by-Layer Synthesis of Mechanically Robust Solvent-Permeable Silica Nanoshells. *Langmuir*, 30:584–591, 2014.

[221] Kwadwo E. Tettey, Jeanne W. C. Ho, and Daeyeon Lee. Modulating Layer-by-Layer Assembly of Oppositely Charged Nanoparticles Using a Short Amphiphilic Molecule. *The Journal of Physical Chemistry C*, 115:6297–6304, 2011.

[222] Nguyen T. K. Thanh, N. Maclean, and S. Mahiddine. Mechanisms of Nucleation and Growth of Nanoparticles in Solution. *Chemical Reviews*, 114:7610–7630, 2014.

[223] Sujit Kumar Ghosh and Tarasankar Pal. Interparticle Coupling Effect on the Surface Plasmon Resonance of Gold Nanoparticles: From Theory to Applications. *Chemical Reviews*, 107:4797–4862, 2007.

[224] Pengxiang Zhao, Na Li, and Didier Astruc. State of the art in gold nanoparticle synthesis. *Coordination Chemistry Reviews*, 257:638–665, 2013.

[225] Neus G. Bastús, Joan Comenge, and Víctor Puntes. Kinetically Controlled Seeded Growth Synthesis of Citrate-Stabilized Gold Nanoparticles of up to 200 nm: Size Focusing versus Ostwald Ripening. *Langmuir*, 27:11098–11105, 2011.

[226] Lili Zhao, Xiaohui Ji, Xuejiao Sun, Jun Li, Wensheng Yang, and Xiaogang Peng. Formation and Stability of Gold Nanoflowers by the Seeding Approach: The Effect of Intraparticle Ripening. *The Journal of Physical Chemistry C*, 113:16645–16651, 2009.

[227] L. J. Hu, Y. H. Chang, F. S. Yen, S. P. Lin, I-Nan Lin, and W. Y. Lin. Crystal growth and characterization of heavily MgO-doped LiNbO3. *Journal of Applied Physics*, 69:7635–7639, 1991.

[228] Hsiang-Yang Wu, Michael Liu, and Michael H. Huang. Direct synthesis of branched gold nanocrystals and their transformation into spherical nanoparticles. *The Journal of Physical Chemistry. B*, 110:19291–19294, 2006.

[229] Chun-Hong Kuo and Michael H. Huang. Synthesis of branched gold nanocrystals by a seeding growth approach. *Langmuir*, 21:2012–2016, 2005.

[230] Anouchka Plan Sangnier, Romain Aufaure, Soshan Cheong, Laurence Motte, Bruno Palpant, Richard D. Tilley, Erwann Guenin, Claire Wilhelm, and Yoann Lalatonne. Raspberry-like small multicore gold nanostructures for efficient photothermal conversion in the first and second near-infrared windows. *Chemical Communications*, 55:4055–4058, 2019.

[231] Ye Pu, Rachel Grange, Chia-Lung Hsieh, and Demetri Psaltis. Nonlinear Optical Properties of Core-Shell Nanocavities for Enhanced Second-Harmonic Generation. *Physical Review Letters*, 104:207402, 2010.

[232] Emre Gürdal, Anke Horneber, Nadim Shaqqura, Alfred J. Meixner, Dieter P. Kern, Dai Zhang, and Monika Fleischer. Enhancement of the second harmonic signal of nonlinear crystals by self-assembled gold nanoparticles. *The Journal of Chemical Physics*, 152:104711, 2020.

[233] Nadia M. Jassim, Kai Wang, Xiaobo Han, Hua Long, Bing Wang, and Peixiang Lu. Plasmon assisted enhanced second-harmonic generation in single hybrid Au/ZnS nanowires. *Optical Materials*, 64:257–261, 2017.

[234] Heiko Linnenbank, Yevgen Grynko, Jens Förstner, and Stefan Linden. Second harmonic generation spectroscopy on hybrid plasmonic/dielectric nanoantennas. *Light: Science & Applications*, 5:e16013–e16013, 2016.

[235] Fani Madzharova, Álvaro Nodar, Vesna Živanović, Michael R. S. Huang, Christoph T. Koch, Rubén Esteban, Javier Aizpurua, and Janina Kneipp. Gold- and Silver-Coated Barium Titanate Nanocomposites as Probes for Two-Photon Multimodal Microspectroscopy. *Advanced Functional Materials*, 29:1904289, 2019.

[236] Ke Jiang, David A. Smith, and Anatoliy Pinchuk. Size-Dependent Photothermal Conversion Efficiencies of Plasmonically Heated Gold Nanoparticles. *The Journal of Physical Chemistry C*, 117:27073–27080, 2013.

[237] Joseph R. Cole, Nikolay A. Mirin, Mark W. Knight, Glenn P. Goodrich, and Naomi J. Halas. Photothermal Efficiencies of Nanoshells and Nanorods for Clinical Therapeutic Applications. *The Journal of Physical Chemistry C*, 113:12090–12094, 2009.

[238] Ana Espinosa, Jelena Kolosnjaj-Tabi, Ali Abou-Hassan, Anouchka Plan Sangnier, Alberto Curcio, Amanda K. A. Silva, Riccardo Di Corato, Sophie Neveu, Teresa Pellegrino, Luis M. Liz-Marzán, and Claire Wilhelm. Magnetic (Hyper)Thermia or Photothermia? Progressive Comparison of Iron Oxide and Gold Nanoparticles Heating in Water, in Cells, and In Vivo. *Advanced Functional Materials*, 28:1803660, 2018.

[239] Johan Grand, Baptiste Auguié, and Eric C. Le Ru. Combined Extinction and Absorption UV-Visible Spectroscopy as a Method for Revealing Shape Imperfections of Metallic Nanoparticles. *Analytical Chemistry*, 91:14639–14648, 2019.

[240] Nardine S. Abadeer and Catherine J. Murphy. Recent Progress in Cancer Thermal Therapy Using Gold Nanoparticles. *The Journal of Physical Chemistry C*, 120:4691–4716, 2016.

[241] Oleksandr A. Savchuk, Joan J. Carvajal, C. Cascales, M. Aguiló, and F. Díaz. Benefits of Silica Core–Shell Structures on the Temperature Sensing Properties of Er,Yb:GdVO $_4$ Up-Conversion Nanoparticles. *ACS Applied Materials & Interfaces*, 8:7266–7273, 2016.

[242] Mario Hentschel, Bernd Metzger, Bastian Knabe, Karsten Buse, and Harald Giessen. Linear and nonlinear optical properties of hybrid metallic–dielectric plasmonic nanoantennas. *Beilstein Journal of Nanotechnology*, 7:111–120, January 2016.

[243] Dawei Jiang, Dalong Ni, Zachary T. Rosenkrans, Peng Huang, Xiyun Yan, and Weibo Cai. Nanozyme: new horizons for responsive biomedical applications. *Chemical Society Reviews*, 48:3683–3704, 2019.

# Résumé de la thèse en français

# Nanoparticules cœur-coquille actives en optique non linéaire pour l'imagerie et la photothérapie du cancer

## Introduction

Depuis ces vingt dernières années, l'utilisation des nanomatériaux dans le domaine médical s'est considérablement accrue. En particulier, les nanoparticules ont été utilisées en tant qu'agent de contraste dans le diagnostic du cancer. De plus, leur accumulation préférentielle dans les tumeurs leur permet de véhiculer des agents thérapeutiques. Les nanoparticules qui ont été intégrées dans des dispositifs médicaux sont généralement produites par des méthodes de chimie en solution. Il y a cependant encore beaucoup de paramètres à optimiser, comme leur tendance à s'agréger, la formation d'une couronne de protéines lorsqu'elles sont injectées *in vivo*, ainsi que le manque de données sur leur toxicité à long terme. Malgré tout, elles sont envisagées comme alternative thérapeutique aux traitements actuels du cancer car elles devraient permettre de réduire les effets secondaires entraînés par la chimio et la radiothérapie.

Les nanoparticules utilisées en nanomédecine peuvent être classées en fonction des matériaux les constituant qu'ils soient organiques (polymères, liposomes) ou inorganiques (semi-conducteurs, métaux, oxydes). Concernant les nanoparticules inorganiques élaborées par chimie en solution, les méthodes de synthèse permettent un bon contrôle de la taille, de la forme et des propriétés de surface selon les conditions expérimentales utilisées. Un moindre changement de ces conditions modifie totalement le type de

nanoparticule obtenue. Par conséquent, le protocole de synthèse doit être clairement établi et les nanoparticules caractérisées de façon approfondie.

Les nanoparticules permettant de fournir simultanément des fonctions diagnostique et thérapeutique sont appelées nanoparticules théranostiques. Une des approches pour les élaborer est de combiner au moins deux matériaux différents conservant de façon indépendante leurs propriétés initiales. On appelle ce type de nanoparticules des nanohybrides.

Dans ce manuscrit, nous nous intéressons à la synthèse de nanohybrides cœur-coquille pouvant être potentiellement utilisés en tant que nanoparticules théranostiques, avec une fonctionnalité pour l'imagerie médicale provenant des propriétés optiques non linéaires du cœur en niobate de lithium ($LiNbO_3$), et une fonctionnalité thérapeutique due aux propriétés plasmoniques photothermique de la coquille en or. Ce manuscrit contient quatre chapitres :

Le **Chapitre 1** introduit l'état de l'art bibliographique de ce sujet et les objectifs détaillés du projet et de la thèse.

Le **Chapitre 2** décrit les techniques de caractérisation utilisées et propose une comparaison et une discussion sur leurs performances pour l'analyse de nanoparticules cœur-coquille.

Le **Chapitre 3** concerne la fonctionnalisation des nanoparticules de $LiNbO_3$ par des germes d'or nanométriques, le contrôle de la densité de germes à l'aide de plusieurs techniques de caractérisation, ainsi que les propriétés optiques non linéaires de ces nanoparticules hybrides.

Enfin, le **Chapitre 4** s'intéresse à la formation de la coquille d'or à partir des germes immobilisés ainsi que sa caractérisation détaillée. L'influence de plusieurs paramètres

expérimentaux (pH, concentration de précurseur d'or, densité de germes) sur la morphologie et les propriétés finales des nanoparticules cœur-coquille est évaluée. Enfin, les propriétés optiques non linéaires et photothermiques sont étudiées.

# Chapitre 1 : Etat de l'art

## 1.1. Du matériau massif au nano

De nombreux exemples montrent que la diminution de taille à l'échelle nanométrique (1-100 nm) permet d'apporter aux matériaux de nouvelles propriétés qui sont applicables soit dans le domaine du textile (tissus auto-nettoyants, anti-bactériens, résistants à l'inflammation), de l'agro-alimentaire (encapsulation de nutriments, arômes artificiels) ou dans l'industrie chimique (nano-capteurs et nano-catalyseurs). Dans le domaine médical, la littérature scientifique associée aux mots-clés « nanoparticules pour le cancer » présente une croissance exponentielle sur ces quatre dernières décennies.

Cet intérêt pour les nanoparticules provient des propriétés physico-chimiques spécifiques obtenues à l'échelle nanométrique, notamment dues à la forte proportion d'atomes situés en surface (supérieure à 50% pour des nanoparticules dont le diamètre est inférieur à 5 nm). En plus de la taille, la forme des nanoparticules influe sur les propriétés obtenues, notamment pour les nanoparticules d'or. Ainsi en modifiant le rapport d'aspect de nanobâtonnets d'or ou l'épaisseur de la coquille d'or pour des nanoparticules cœur de silice/coquille d'or ($SiO_2$@Au), le spectre d'extinction de ces nanoparticules peut être déplacé du domaine visible au proche infrarouge [Huang 2010]. La charge de surface des nanoparticules a aussi une grande importance car elle affecte leur stabilité en solution et leur agrégation. De plus ces propriétés influent sur leurs utilisations en nanomédecine. Par exemple, l'internalisation des nanoparticules dans les cellules est directement contrôlée par leur taille, leur forme et leur charge. De plus, la possibilité d'immobiliser des

biomolécules sur leur surface leur permet un ciblage actif et une délivrance contrôlée de principes actifs.

### 1.2. Nanoparticules pour l'imagerie du cancer

Des outils de diagnostic performants sont nécessaires pour identifier rapidement et précisément les cancers, ce qui permet de démarrer au plus tôt un protocole thérapeutique. Les techniques d'imagerie médicale actuelles permettant un diagnostic *in vivo* sont nombreuses : imagerie par résonance magnétique (IRM), tomographie par les rayons X (CT), tomographie par émission de positrons (PET), etc. La résolution minimale obtenue est de 0,25 mm. Cependant, étant donné que le développement d'un cancer démarre à l'échelle cellulaire, des techniques d'imagerie optique telles que la microscopie confocale de fluorescence permettant une résolution de 0,1 µm sont employées *ex vivo* sur des biopsies.

Pour ces différentes techniques, les nanoparticules sont utilisées en tant qu'agent de contraste pour améliorer la précision des images : nanoparticules d'oxyde de fer pour l'IRM, nanoparticules d'or pour la CT ou pour la PET par exemple. En plus d'une sensibilité améliorée, ces nanoparticules permettent également une plus grande profondeur d'analyse.

Concernant l'imagerie optique, les molécules fluorescentes généralement utilisées en tant qu'agent de contraste sont cependant sensibles au photoblanchiment, et l'auto-fluorescence des tissus biologiques rend difficile leur détection. C'est pourquoi l'amélioration des techniques d'imagerie optique passe par un décalage de la plage de détection vers les fenêtres de transparence biologique entre 700 et 900 nm et entre 1000 et 1700 nm, dans laquelle l'absorption et la diffusion des tissus sont minimales. Ces fenêtres sont notamment atteignables en utilisant des processus optiques non linéaires.

### 1.3. Imagerie optique non linéaire pour le diagnostic du cancer

Lorsqu'un milieu répond de façon non linéaire à l'excitation par une onde électromagnétique, il acquiert une polarisation $P$ s'écrivant :

$$P = \varepsilon_0(\chi^{(1)}E + \chi^{(2)}E^2 + \chi^{(3)}E^3 + \cdots)$$

avec $\varepsilon_0$ la permittivité diélectrique du vide, $\chi^{(n)}$ la susceptibilité électrique d'ordre n et $E$ le champ électrique. Cette réponse non linéaire n'est en revanche obtenue que pour une excitation intense avec un champ électrique se situant typiquement entre $10^4$ V/m et $10^8$ V/m. De plus, les susceptibilités électriques d'ordre supérieur ou égal à 2 dépendent de la symétrie du milieu. Par exemple, la génération de seconde harmonique (SHG) résulte de la susceptibilité électrique d'ordre 2 et est observée uniquement pour les milieux non centrosymétriques. La SHG est un processus dans lequel deux photons de même énergie produisent un seul photon d'énergie double (Figure 1b). Il faut noter que ce processus ne fait intervenir qu'un niveau d'énergie virtuel.

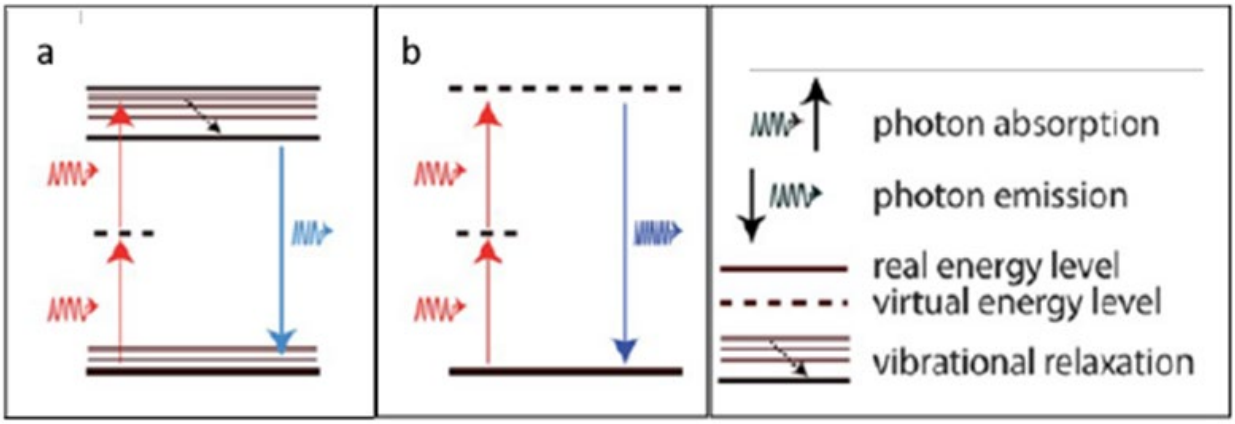

**Figure 1.** Illustration des processus d'absorption et d'émission pour (a) la fluorescence excitée à deux photons (TPEF) et (b) la génération de seconde harmonique (SHG) [Bonacina 2012].

La fluorescence excitée à deux photons (TPEF) résulte de la susceptibilité électrique d'ordre 3. C'est aussi un processus à deux photons mais ceux-ci sont absorbés par le milieu permettant l'excitation vers un niveau d'énergie réel, suivi d'une désexcitation entraînant l'émission d'un photon d'énergie inférieure à la somme des énergies des deux photons absorbés (Figure 1a).

La caractérisation des propriétés optiques non linéaires est possible grâce à l'utilisation de lasers pulsés, générant un signal très intense. Actuellement c'est la Diffusion Hyper Rayleigh (HRS) qui permet de mesurer l'hyperpolarisabilité $\beta$ du milieu, l'équivalent de la susceptibilité électrique à l'échelle microscopique. Cette technique permet également d'accéder au rapport de dépolarisation en faisant varier la polarisation incidente, ce qui permet d'avoir des informations sur la symétrie du milieu.

Les techniques de microscopies basées sur la SHG et sur la TPEF sont très attractives pour l'imagerie médicale parce qu'elles permettent une excitation dans le proche infrarouge donc dans les fenêtres de transparence biologique. Un autre avantage est que l'excitation à deux photons est limitée spatialement car le signal est proportionnel au carré de l'intensité d'excitation. Ceci permet une imagerie 3D en sectionnant virtuellement les plans focaux comme il est possible de le faire en microscopie confocale. Enfin, la détection dans le visible, loin de l'excitation dans le proche infrarouge permet de bien discriminer les deux signaux et de maximiser le rapport signal sur bruit.

Bien qu'il existe des sondes biologiques endogènes présentant une activité optique non linéaire, il est la plupart du temps nécessaire, afin d'amplifier le signal détecté, d'utiliser

des sondes exogènes pour les microscopies SHG et TPEF. Ces sondes se divisent en deux grandes familles : les sondes organiques et les sondes inorganiques. Les sondes organiques sont des molécules présentant une forte absorption à deux photons, donc actives en TPEF, du fait de la présence de groupements donneurs et accepteurs d'électrons π. Les sondes inorganiques et plus particulièrement les nanoparticules dites « harmoniques » sont utilisées pour leur activité SHG. Elles sont composées de matériaux à structure cristalline non centrosymétrique comme par exemple $KNbO_3$, $BaTiO_3$, SiC ou ZnO. Elles présentent l'avantage de ne pas être soumises au photoblanchiment. De plus, ces nanoparticules présentent une charge surfacique élevée à pH neutre, ce qui rend les dispersions colloïdales stables en milieu physiologique. Cette stabilité peut être améliorée en ajoutant à leur surface des polyéthylènes glycols. Enfin, leur cytotoxicité, qui a été étudiée sur plusieurs lignées cellulaires, est faible [Staedler 2012]. A notre connaissance, il existe seulement quelques travaux publiés montrant l'utilisation de ces nanoparticules pour l'imagerie médicale et la thérapie du cancer.

### 1.4. Nanoparticules pour la thérapie du cancer

Les nanoparticules à visée thérapeutique sont développées dans le but de minimiser voire éliminer les effets secondaires des thérapies du cancer traditionnelles. Les thérapies envisagées à l'aide des nanoparticules sont les suivantes. Tout d'abord, l'utilisation de nanoparticules d'or en tant qu'agent radio-sensibilisant devrait permettre d'améliorer la précision de la radiothérapie en évitant aux rayons X d'atteindre les tissus sains environnant la tumeur. Par ailleurs, les nanoparticules telles que les liposomes ou les micelles peuvent être utilisées en tant que capsules pour transporter vers la tumeur un traitement ou une hormone. La photothérapie dynamique (PDT) consiste à utiliser des agents photo-sensibilisants, comme par exemple des nanoparticules d'or, de façon à produire des radicaux oxygène et azote dans l'environnement local de la tumeur. Enfin, la

photothérapie thermique (PTT) qui nous intéresse ici, consiste à générer une élévation de température sous excitation lumineuse. Il a été montré que les cellules cancéreuses, contrairement aux cellules saines, sont détruites au-delà de 45°C. Ceci nécessite l'utilisation d'agents de conversion photothermique absorbant la lumière et dégageant de la chaleur lors de leur processus de relaxation. Parmi les candidats intéressants, on peut citer les agents à base de carbone (nanotubes mono ou multi-parois), les nanoparticules à base de semi-conducteurs organiques polymériques ou les nanoparticules d'or. Ce sont ces dernières qui présentent les meilleures efficacités de conversion photothermique (jusqu'à 80 %).

### 1.5. Thérapie plasmonique photothermique

Pour bien comprendre le fonctionnement des nanoparticules d'or en tant qu'agent de conversion photothermique, il faut d'abord rappeler quelques notions de nanoplasmonique. A l'interface entre un métal et un milieu diélectrique soumis à une onde électromagnétique incidente, il existe une onde électromagnétique qui se propage le long de l'interface, appelée plasmon de surface. Si au lieu d'une surface métallique plane on s'intéresse à des nanoparticules métalliques, la longueur d'onde d'excitation dans le visible devient grande devant le rayon des nanoparticules. Ceci entraîne la formation d'un dipôle électrique dans les nanoparticules, avec des électrons oscillant à l'intérieur du métal. Quand la fréquence de l'onde incidente coïncide avec la fréquence d'oscillation des électrons, on observe une extinction de l'onde incidente par les nanoparticules. Cette fréquence particulière, appelée résonance plasmonique localisée, dépend de la taille et de la forme des nanoparticules, ainsi que de la nature du métal les composant. Dans le cas particulier des métaux or et argent, cette fréquence de résonance se situe dans le visible ou dans l'infrarouge.

Ces nanoparticules sont donc capables d'absorber une énergie radiative et de faire par conséquent passer les électrons sur un niveau d'énergie excité. La désexcitation peut suivre une voie radiative ou une voie non radiative. Lors d'une désexcitation non radiative, les collisions entre électrons entraînent une augmentation de la température à la surface du métal. Le retour à la température d'équilibre se fait par des échanges d'énergie entre électrons et phonons, et entre phonons. Lors de ce processus qui dégage de la chaleur, on peut également observer la formation de microbulles qui peuvent, en plus de l'effet thermique, avoir une action destructrice sur les cellules cancéreuses en imposant une force sur les membranes cellulaires.

### 1.6. Conclusion sur les nanoparticules pour la thérapie du cancer

Les nanoparticules sont maintenant inclues dans l'ensemble des techniques thérapeutiques du cancer, que ce soit en tant qu'agents radio- ou photo-sensibilisants, ou pour la délivrance de principes actifs. La possibilité de les modifier en surface permet d'améliorer leur capacité de ciblage. En particulier, la thérapie photothermique est attractive car les nanoparticules d'or présentent de bonnes efficacités de conversion photon-chaleur.

### 1.7. Nanohybrides avec une coquille d'or pour le théranostique

La conception de nanoparticules théranostiques repose sur la combinaison d'une fonction d'imagerie et d'une fonction thérapeutique au sein du même nano-objet. Cette combinaison ne doit pas interférer sur leur fonctionnement individuel, ni entraîner une toxicité. Il y actuellement quelques exemples de nanohybrides à visée thérapeutique au stade d'essai clinique : liposomes encapsulant un médicament et sensibles au pH pour le diagnostic, nanoparticules d'oxyde de fer utilisables en IRM et permettant la thérapie hormonale, nanobâtonnets d'or réalisant des fonctions de PTT et de CT pour l'imagerie et

enfin nanoparticules de silice recouvertes d'or. C'est plus précisément à ce dernier type de nanoparticules que nous allons nous intéresser, qui est le plus proche des nanohybrides étudiés dans cette thèse.

La synthèse de nanoparticules d'or monodisperses par les méthodes type « bottom-up » (de l'atome à la nanoparticule) peut être expliquée en première approximation par la théorie de LaMer [LaMer 1950]. La concentration en espèces atomiques dans le milieu doit atteindre rapidement une valeur élevée pour franchir le palier de nucléation, ce qui entraîne la formation de nombreux germes homogènes. Puis dans un deuxième temps la croissance démarre par ajout d'atomes additionnels sur les germes formés. Plusieurs méthodes de synthèse de nanoparticules d'or sphériques ont été développées depuis la méthode originale de Turkevich [Turkevich 1951] faisant intervenir le citrate de sodium en tant que réducteur du sel d'or. Ces différentes méthodes font varier le réducteur choisi, le milieu réactionnel, le pH, les agents stabilisants, la concentration en or et la température de réaction.

La synthèse de nanoparticules d'or de géométrie plus complexe est en général basée sur des processus multi-étapes dans lesquels la réduction de l'or doit être réalisée sur des germes formés lors d'une étape initiale.

Dans le cas de la synthèse de nanocoquilles d'or sur des cœurs de silice, la méthode consiste à modifier chimiquement la surface des nanoparticules de silice par des amines (typiquement par un aminosilane) pour promouvoir l'adsorption de germes d'or sur la surface [Oldenburg 1998]. Ces germes d'or sont préparés séparément en utilisant le THPC comme réducteur de $HAuCl_4$ en milieu basique et nécessitent un vieillissement de quelques jours à quelques semaines pour être mieux adsorbés par les fonctions amines, ceci étant attribué à une oxydation en Au(I) qui a une meilleure affinité pour les amines. Enfin, la

croissance de la coquille d'or se fait par ajout d'une solution de $HAuCl_4$ contenant du carbonate de potassium. Depuis cette méthode originale, de nombreuses autres ont été publiées qui tentent de proposer des pistes pour réduire le nombre d'étapes de synthèse.

Alors que la synthèse de coquilles d'or sur des cœurs de silice est bien décrite, il y a beaucoup moins de travaux concernant l'utilisation d'autres matériaux pour le cœur. En effet, le procédé utilisé pour la silice est plus difficilement transférable pour des cœurs ne présentant pas une géométrie sphérique. Quelques exemples ont cependant été publiés avec des cœurs de $BaTiO_3$ [Wang 2016a] ou des cœurs d'oxyde de fer [Lee 2017].

En ce qui concerne la combinaison de nanomatériaux actifs en optique non linéaire et plasmoniques pour des applications théranostiques, une première tentative a été réalisée dans le cadre d'une thèse précédente en couplant des nanobâtonnets d'or avec des nanoparticules de SiC à l'aide du surfactant cationique CTAB. Même si les fonctions initiales (SHG et PTT) sont maintenues dans les nanohybrides, les résultats obtenus sont mitigés puisque les nanohybrides sont toxiques pour les cellules cancéreuses même en absence d'excitation lumineuse, ce qui est probablement dû à la présence de CTAB et/ou au détachement des nanobâtonnets d'or de la surface [Boksebeld 2019].

### 1.8. Objectifs de cette thèse

Dans ce contexte, l'objectif de ce travail est de synthétiser des nanohybrides cœur-coquille combinant un matériau actif en optique non linéaire en tant que coeur ($LiNbO_3$) et une coquille plasmonique d'or avec une action plasmonique photothermique. Ces nanohybrides seront synthétisés par une méthode en plusieurs étapes assistée par la formation de germes d'or nanométriques. Les paramètres pouvant influencer le processus de croissance de la coquille seront étudiés. La morphologie, les propriétés plasmoniques, optiques non linéaires et photothermiques de ces nanohybrides seront examinées à l'aide

de plusieurs techniques de caractérisation complémentaires que nous présenterons dans le prochain chapitre.

## Chapitre 2 : Méthodes de caractérisation

L'utilisation des nanoparticules dans le domaine biomédical nécessite une bonne compréhension des interactions entre nanoparticules et milieu biologique qui dépendent de la taille et de la chimie de surface des nano-objets. Il n'existe aucune technique analytique permettant de caractériser de façon complète les nanoparticules, d'autant plus dans le cas des nanohybrides, donc plusieurs techniques complémentaires sont nécessaires. Les caractéristiques extraites de ces différentes techniques sont présentées dans la Table 1.

| | **Caractéristique des nanoparticules** | | | | |
|---|---|---|---|---|---|
| **Technique** | Taille | Composition élémentaire | Concentration | Stabilité colloïdale | Propriétés de surface |
| DLS | ☑ | ☒ | ☒ | ☑ | ☒ |
| EDS | ☒ | ☑ | ☒ | ☒ | ☒ |
| ICP-AES | ☒ | ☑ | ☑ | ☒ | ☒ |
| LDV/Electrophorèse | ☒ | ☒ | ☒ | ☑ | ☑ |
| TEM | ☑ | ☒ | ☒ | ☒ | ☑ |
| TOF-SIMS | ☒ | ☑ | ☒ | ☒ | ☑ |
| UV-Vis | ☒ | ☒ | ☑ | ☒ | ☑ |
| XPS | ☒ | ☑ | ☒ | ☒ | ☑ |

**Table 1.** Données de caractérisation obtenues par diverses techniques analytiques, spécifiques aux dispersions de nanoparticules de ce travail.

### 2.1. Aspect théorique des techniques analytiques utilisées

*Microscopie Electronique en Transmission (TEM).* Cette technique est basée sur l'interaction entre des électrons émis par une source portée à une haute tension (> 100 kV) et la matière. Elle fournit des images de l'échantillon avec une précision inférieure au nanomètre. Elle nécessite cependant quelques précautions. En effet, elle fournit une image bi-dimensionnelle d'un échantillon tri-dimensionnel, donc elle ne permet pas d'obtenir d'informations sur la profondeur de l'échantillon. De plus, les électrons peuvent causer une dégradation des échantillons en particulier s'ils contiennent de la matière organique. Enfin, les échantillons doivent être suffisamment fins (quelques centaines de nm d'épaisseur) pour être transparents aux électrons. Dans notre cas, nous avons dû mettre au point une méthode permettant d'éviter l'agrégation des nanoparticules lors du dépôt sur la grille et du séchage. Les nanoparticules étant déposées en solution aqueuse, la grille a été préalablement traitée à l'UV-ozone pour la rendre hydrophile, ce qui permet d'augmenter la mouillabilité de la dispersion de nanoparticules lors du dépôt. Dans ce travail, le microscope utilisé est un JEOL-2100HT muni d'une source $LaB_6$ portée à 200 kV. Les images TEM ont été analysées à l'aide du logiciel ImageJ.

*Spectroscopie de photoélectrons X (XPS).* Cette technique est basée sur l'interaction entre un faisceau de rayons X et la surface de l'échantillon. Lors de la photo-excitation, des photoélectrons provenant des différents niveaux d'énergie des éléments chimiques contenus dans l'échantillon sont émis. Il est possible de mesurer leur énergie cinétique et d'en déduire leur énergie de liaison. Les photoélectrons ont un libre parcours moyen (IMFP) entre 4 et 30 Å, ce qui limite la profondeur d'analyse en XPS à environ 10 nm. Dans ce travail, deux appareils ont été utilisés fonctionnant avec une source de rayons X

AlKα à 1486,6 eV. Le premier est un appareil VSW localisé à l'INL. Le second est un appareil Axis Ultra-DLD de chez Kratos situé au laboratoire JRC Nanobiotechnology à Ispra en Italie. Les données ont été analysées avec le logiciel CasaXPS.

*Spectroscopie de rayons X à dispersion d'énergie (EDX/EDS).* Cette technique permet une caractérisation des éléments chimiques d'un échantillon en analysant la fluorescence X émise par ces éléments sous excitation électronique ou par un rayonnement X. Contrairement à la spectroscopie XPS, la spectroscopie EDX n'est pas limitée à la surface de l'échantillon. Elle n'est cependant pas adaptée aux éléments légers et ne permet pas l'analyse de traces. Dans ce travail, la spectroscopie EDX a été réalisée pendant les mesures TEM avec un détecteur EDX XMAX en silicium en focalisant le faisceau d'électrons sur différentes régions de l'échantillon. Des cartographies chimiques ont également été obtenues avec un microscope TITAN ETEM FEI. Le logiciel Aztec (Oxford Instruments) a été utilisé pour l'analyse des spectres.

*Diffusion dynamique de la lumière (DLS).* Cette technique utilise les fluctuations de l'intensité lumineuse diffusée par des particules en solution soumises au mouvement Brownien. Ces fluctuations permettent de déterminer le coefficient de diffusion des particules qui est lié au à leur rayon hydrodynamique. La conversion de la distribution des intensités mesurées en distribution en nombre ou en volume de particules est basée sur la théorie de Mie qui suppose que les particules sont sphériques, homogènes et que leurs propriétés optiques sont connues. Dans ce travail, un appareil Malvern Nanoseries Zetasizer ZS a été utilisé. Les mesures ont été réalisées à un angle de rétrodiffusion de 173°.

*Vélocimétrie laser et électrophorèse.* Autour d'une particule dispersée en milieu liquide se forme une double couche électrique composée de la couche de Stern, constituée de charges

opposées à la charge de surface de la particule, suivie de la couche diffuse dans laquelle les espèces chargées sont moins liées à la particule. Le potentiel zeta est le potentiel électrique mesuré au niveau d'un plan appelé plan de cisaillement situé dans la couche diffuse qui sépare la région du liquide mobile et la région du liquide qui reste attachée à la particule. La vélocimétrie laser combinée à l'électrophorèse permet d'extraire le potentiel zeta, en déterminant la vitesse de migration des particules soumise à un champ électrique. Dans ce travail, un appareil Malvern Nanoseries Zetasizer ZS a été utilisé avec des cuves capillaires munies d'électrodes en or pour appliquer le champ électrique.

*Spectroscopie d'absorption UV-Visible.* Cette technique de caractérisation optique permet d'étudier les transitions entre les niveaux d'énergie électronique de molécules en solution sous excitation lumineuse. L'absorbance mesurée est reliée à la concentration par la loi de Beer-Lambert. Dans le cas des nanoparticules, il faut également tenir compte de la diffusion de la lumière. Le spectre mesuré correspond donc au spectre d'extinction, qui tient compte de l'absorption et de la diffusion. L'appareil utilisé dans ce travail est un spectromètre SAFAS-UV mc2. Les échantillons sont placés dans une cuve en quartz de 1 cm d'épaisseur.

*Spectrométrie à plasma à couplage inductif (ICP-AES).* Cette technique de quantification élémentaire est basée sur la digestion acide de l'échantillon et l'injection de la solution résiduelle dans un plasma. L'interaction des atomes de l'échantillon avec les particules chargées du plasma provoque des pertes d'électrons et des recombinaisons entraînant l'émission d'un rayonnement caractéristique des éléments présents. Les concentrations détectables sont de l'ordre du µg/L. Les appareils utilisés sont ceux du laboratoire CREALINS de Lyon, ICP-AES ICAP 6300 et ICAP 6500 de Thermofisher Scientific. Le milieu de digestion acide utilisé est composé de 4% de $H_2SO_4$, 4% de $HNO_3$ et 4% de HCl.

*Spectrométrie de masse des ions secondaires (TOF-SIMS)*. Cette technique d'analyse de surface consiste à bombarder l'échantillon par un faisceau ionique de quelques keV. Les collisions des ions avec les noyaux des atomes de l'échantillon entraînent des cascades de collisions qui permettent aux atomes de quitter l'échantillon sous forme d'ions secondaires qui peuvent être différenciés par leur rapport masse/charge. Dans ce travail, les analyses TOF-SIMS ont été réalisées au laboratoire JRC Nanobiotechnology à Ispra en Italie sur un appareil TOFSIMS IV de IONTOF GmbH équipé d'une source d'ions primaires $Bi_3^{++}$. Le logiciel SurfaceLab V6 a été utilisé pour le traitement des données et le logiciel simsMVA pour l'Analyse en Composantes Principales.

### 2.2. Discussion sur les techniques analytiques utilisées pour la caractérisation des nanohybrides

*Techniques utilisées pour caractériser la taille des nanoparticules*. La microscopie TEM et la DLS ont été utilisées, ainsi que la diffraction des rayons X, mais uniquement pour le LN, comme nous le verrons dans le Chapitre 3. L'utilisation du TEM nécessite plusieurs précautions. Premièrement, le contour des nanoparticules observées sur les images n'est pas facilement identifiable lorsqu'elles se superposent les unes sur les autres. Pour limiter cela, un traitement UV/ozone des grilles TEM a été mis au point pour que la goutte de nanoparticules s'étale mieux lors du dépôt. Deuxièmement, de nombreuses images ont été acquises pour chaque échantillon pour obtenir une valeur moyenne du diamètre des nanoparticules avec une statistique correcte sur un minimum de 100 nanoparticules. Il faut noter également que les nanoparticules de LN présentant une géométrie quasi-sphérique, le diamètre pris en compte au TEM correspond à la plus grande dimension mesurée. En DLS, nous avons négligé cette géométrie quasi-sphérique. Il faut également considérer que dans ce cas, le diamètre mesuré est le diamètre hydrodynamique des nanoparticules prenant

en compte le diamètre de la nanoparticule, la couche de Stern et une partie de la couche diffuse qui se déplace avec la nanoparticule.

*Techniques utilisées pour déterminer les propriétés de surface des nanoparticules.* D'après la Table 1, cinq techniques permettent d'obtenir des informations sur la surface des nanoparticules. Tout d'abord la spectroscopie d'absorption UV-Visible permet de suivre l'évolution de la bande plasmon de la couche d'or présente à la surface du LN (Figure 2). Cette mesure spectroscopique est bien entendu complétée par des images TEM.

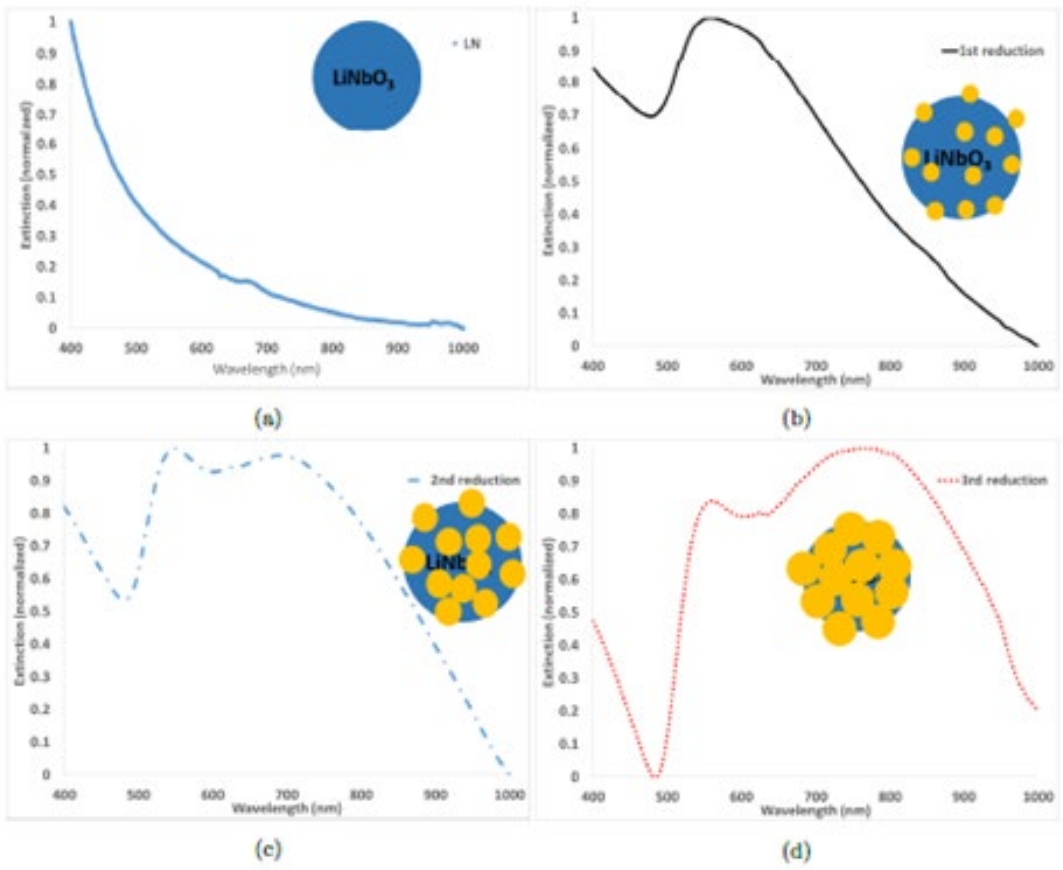


**Figure 2.** Spectres d'absorption UV-Visible de dispersions de LN et LN@Au. Les schémas donnent une représentation possible de la répartition de l'or sur le niobate de lithium dans les différents cas. (a) LN, (b) LN@Au formé après une réduction de $HAuCl_4$,

(c) LN@Au formé après deux réductions de $HAuCl_4$ et (d) LN@Au formé après trois réductions de $HAuCl_4$.

Ensuite l'évolution de la chimie de surface des nanoparticules peut être suivie par la mesure du potentiel zeta, de façon qualitative. Pour obtenir des informations plus précises et quantitatives, nous avons également utilisé la spectroscopie XPS et l'analyse TOF-SIMS.

*Techniques utilisées pour déterminer la concentration de LN et de nanohybrides*. La poudre de LN utilisée est dispersée dans l'eau a une concentration précise. Une courbe de calibration a été réalisée par spectroscopie UV-Visible en mesurant l'absorbance à 350 nm. Cependant, le spectre d'absorption étant très différent pour les nanohybrides, d'autres méthodes ont été mises au point. La première utilisée a été la microscopie TEM qui nous a permis de compter le nombre de germes d'or par nanoparticule LN en supposant l'observation d'un hémisphère complet sur les images TEM et en multipliant les germes comptés par 2 pour obtenir le nombre total de germes d'or par nanoparticule LN. L'ICP-AES a ensuite permis d'obtenir des valeurs plus précises en déterminant le nombre de germes d'or par nanoparticule LN à partir des concentrations absolues de Au et Nb dans les échantillons de nanohybrides.

## Chapitre 3 : Immobilisation de germes d'or sur les nanoparticules de $LiNbO_3$

Dans ce chapitre, nous détaillons le protocole (Figure 3) permettant d'immobiliser des germes d'or sur les nanoparticules de LN, première étape en vue de la synthèse d'une coquille d'or, ainsi que la caractérisation structurale et optique de ces nanoparticules.

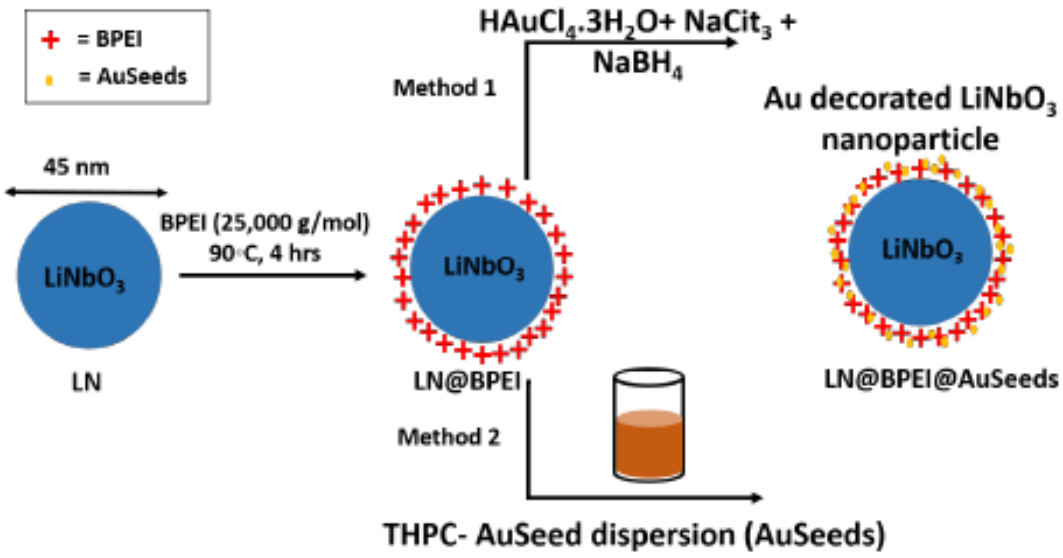


**Figure 3.** Schéma de préparation des nanoparticules de $LiNbO_3$ décorées par des germes d'or (LN@BPEI@AuSeeds).

### 3.1. Matériel et méthodes

Les nanoparticules de LN ont été synthétisées au laboratoire SYMME d'Annecy par un procédé solvothermal en faisant réagir l'éthoxyde de lithium niobium en présence de butane-1,4-diol. Les nanoparticules de LN obtenues ont été dispersées dans l'eau à une concentration de 1 mg/mL. Ensuite la polyethyleneimine ramifiée (BPEI) à 25 kDa a été déposée à la surface des nanoparticules à 90°C pendant 4 h puis l'excès de BPEI a été

éliminé par 6 étapes de centrifugation/lavage dans l'eau à 10°C et 9103g. Puis les nanoparticules résultantes (LN@BPEI) ont été dispersées dans l'eau à 0,35 mg/mL. Deux méthodes différentes ont été testées pour former des germes d'or à la surface des nanoparticules LN@BPEI. La première consiste en une réduction directe *in situ* de $HAuCl_4$ sur LN@BPEI en présence de citrate de sodium et borohydrure de sodium. La seconde méthode est un procédé en deux étapes consistant d'abord en la synthèse ex situ de germes d'or en faisant réagir $HAuCl_4$ avec le THPC en milieu basique [Duff 1993] puis l'interaction électrostatique de ces germes avec LN@BPEI. Plusieurs quantités différentes de germes par rapport à la quantité de LN ont été testées (Table 2).

| **Nom de l'échantillon** | **Volume de la dispersion de AuSeeds (mL)** | **Volume d'$H_2O$ (mL)** | **Concentration finale en AuSeeds (NPs/mL)** | **Rapport théorique AuSeeds:LN** |
|---|---|---|---|---|
| LN@BPEI@AuSeeds100 | 0,349 | 10,239 | $6{,}98 \times 10^{12}$ | 100 |
| LN@BPEI@AuSeeds300 | 1,046 | 9,542 | $2{,}09 \times 10^{13}$ | 300 |
| LN@BPEI@AuSeeds700 | 2,441 | 8,147 | $4{,}88 \times 10^{13}$ | 700 |
| LN@BPEI@AuSeeds1000 | 3,486 | 7,102 | $6{,}97 \times 10^{13}$ | 1000 |
| LN@BPEI@AuSeeds2000 | 6,973 | 3,615 | $1{,}39 \times 10^{14}$ | 2000 |
| LN@BPEI@AuSeeds3000 | 10,459 | 0,129 | $2{,}09 \times 10^{14}$ | 3000 |

**Table 2.** Volumes et concentrations finales des dispersions de AuSeeds utilisées pour faire varier la densité de germes d'or à la surface des nanoparticules LN@BPEI. La dispersion

de AuSeeds utilisée a une concentration de $2{,}32 \times 10^{14}$ NPs/mL. Pour chaque échantillon, 1 mL de LN@BPEI à $1{,}58 \times 10^{12}$ NPs/mL a été utilisé.

La quantité de BPEI présente dans les surnageants lors du lavage a été déterminée par spectroscopie de fluorescence en utilisant l'interaction entre les groupements amines du BPEI et la fluorescamine émettant de la fluorescence à une longueur d'onde de 472 nm. Les propriétés de SHG des nanoparticules LN et LN@BPEI@AuSeeds ont été caractérisées à l'Institut Lumière Matière de l'Université de Lyon en utilisant un montage de HRS contenant un laser pulsé femtoseconde à 800 nm avec un taux de répétition de 80 MHz et des impulsions de 140 fs.

## 3.2. Résultats et discussion

### 3.2.1. Synthèse et caractérisation des nanoparticules de LN

Les nanoparticules de LN ont été définies par cinq caractéristiques : leur phase cristalline, leur diamètre moyen, leur distribution en taille, leur morphologie et leur niveau d'agglomération. Avec les conditions de synthèse décrites dans le paragraphe précédent, la structure cristalline du LN obtenu est trigonale et les nanoparticules sont monocristallines. La formule de Scherrer permet de calculer la taille des cristallites à partir de largeur à mi-hauteur des pics de diffraction. Selon la direction cristallographique [110], une valeur maximale de 45 nm pour le diamètre de Scherrer des nanoparticules a été calculée. La microscopie TEM a également été utilisée pour déterminer un diamètre moyen des nanoparticules de $34 \pm 12$ nm (Figure 4).

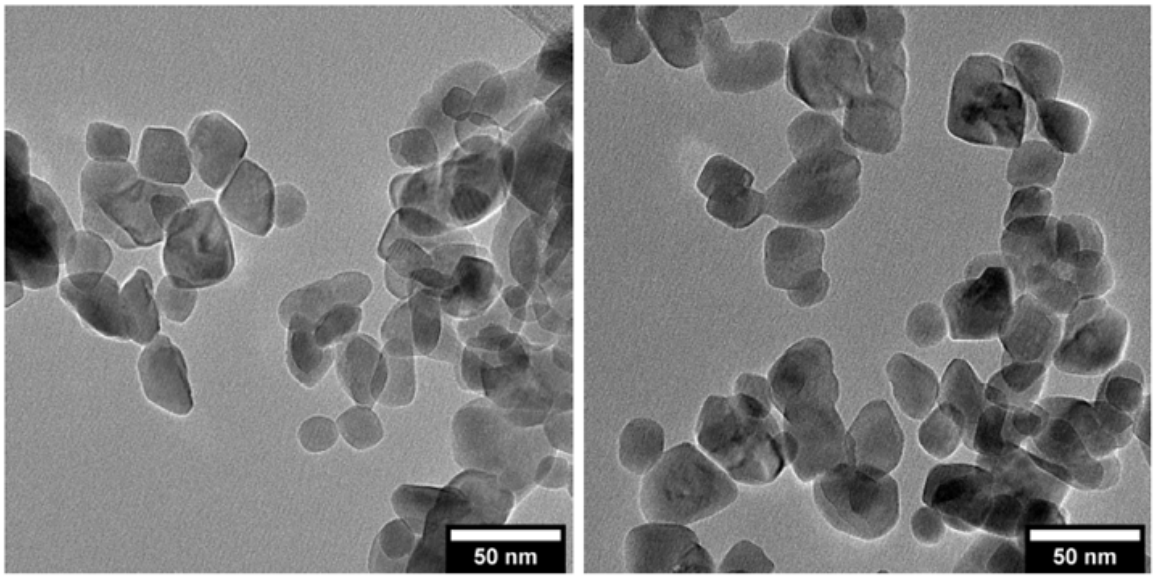


**Figure 4.** Images TEM des nanoparticules de LN utilisées dans ce travail montrant la morphologie pseudo-sphérique du LN.

Ces nanoparticules ont une morphologie pseudo-sphérique avec un degré de sphéricité moyen (rapport du petit diamètre sur le grand diamètre) de 0,8. Lors de la mesure TEM, l'orientation des nanoparticules sur la grille est aléatoire, le diamètre mesuré se situe donc le long de n'importe quelle direction cristallographique. Il n'est donc pas étonnant de trouver un diamètre TEM inférieur au diamètre de Scherrer. Le diamètre hydrodynamique déterminé par DLS est de 135 $\pm$ 15,7 nm. Il est nettement supérieur aux diamètres déterminés par les techniques précédentes car il prend en compte la couche de solvatation complète autour des nanoparticules alors que par les autres techniques on ne considère que les limites des cristaux de nanoparticules. Les nanoparticules ne sont cependant pas agrégées avec un diamètre hydrodynamique inférieur à 300 nm. Le potentiel zeta est quant à lui de -43,2 $\pm$ 3,6 mV, ce qui offre une grande stabilité aux nanoparticules lors qu'elles sont dispersées en milieu aqueux, la valeur négative du potentiel zeta étant attribuée aux groupements de surface Li-O.

### 3.2.2. Modification de la surface du LN par le polymère BPEI

En vue d'immobiliser les germes d'or, les nanoparticules de LN doivent subir des modifications de surface. Une revue de la littérature montre qu'il est possible d'utiliser différents silanes sur des nanoparticules de silice sphériques. Les silanes terminés par des amines et des thiols présentent la meilleure efficacité pour l'immobilisation des germes d'or. Différentes molécules, dont les aminosilanes, ont été testées sur les nanoparticules de LN, des polyélectrolytes comme la poly-L-lysine et le BPEI ou l'adsorption de $Sn^{2+}$ pour favoriser la réduction de l'or à la surface du LN. Le BPEI permet d'inverser facilement la charge de surface des nanoparticules de LN. De plus, il présente d'autres avantages qui lui permettent d'être un polymère largement utilisé dans les applications biologiques. Sa forte charge cationique lui permet de se lier facilement à un grand nombre de biomolécules. Sa faible toxicité (qui dépend de son poids moléculaire) rend biocompatible les nanoparticules sur lesquelles il est déposé. Le BPEI a déjà été utilisé pour modifier chimiquement des nanoparticules d'oxydes métalliques. Ici c'est un poids moléculaire de 25 kDa qui a été sélectionné car il a été montré qu'il permettait d'assurer une bonne stabilité colloïdale à des nanoparticules de diamètre 50 nm environ. Le degré de protonation du BPEI à pH 7,5 est d'environ 44%, ce qui permet d'immobiliser un grand nombre de germes d'or et d'utiliser les nanoparticules LN@BPEI en conditions physiologiques. Elles présentent un potentiel zeta de $+36{,}05 \pm 2{,}9$ mV et un diamètre hydrodynamique de $159{,}6 \pm 34{,}1$ nm.

Afin de s'assurer de l'absence de BPEI libre dans la dispersion de nanoparticules après les étapes de lavage, une analyse de la quantité d'amines a été réalisée par fluorescence à l'aide de la fluorescamine en adaptant un protocole précédemment publié [Khan 2018]. La fluorescamine est une molécule non fluorescente qui devient fluorescente par réaction avec les amines primaires. Le complexe fluorescamine-BPEI émet à 472 nm sous excitation à 388 nm. Une courbe de calibration a été acquise permettant de montrer une relation linéaire

entre la concentration de BPEI et la fluorescence mesurée jusqu'à une concentration de BPEI de 1 mg/mL. L'analyse de la fluorescence des surnageants après les différentes étapes de centrifugation/lavage suivant l'élaboration des nanoparticules LN@BPEI montre une suppression totale de la bande d'émission à 472 nm après la troisième étape de lavage. Ceci permet d'affirmer qu'après 6 étapes de lavage, il ne reste plus de BPEI libre dans la dispersion de nanoparticules. La mesure de la quantité de BPEI éliminée lors des lavages permet également de remonter à la quantité de BPEI immobilisée à la surface des nanoparticules de LN. Par cette méthode un nombre de chaînes polyméres de BPEI compris entre 1000 et 1600 par nanoparticule de LN a été calculé.

L'analyse XPS permet également une quantification des molécules de BPEI à la surface du LN. La mesure des pourcentages atomiques donne un rapport Nb sur N égal à 1:0,6. En considérant que la profondeur d'analyse maximale en XPS est de 10 nm et que les nanoparticules de LN ont une géométrie sphérique avec un diamètre de 45 nm, un volume de $6{,}36 \times 10^{-4}$ $nm^3$ analysé pour chaque nanoparticule de LN a été calculé. Ensuite, à partir de la densité du $LiNbO_3$, la masse des atomes de Nb par nanoparticule de LN peut être déterminée. Connaissant la formule développée du BPEI, le nombre d'atomes d'azote par chaîne polymère est calculé. Enfin avec le rapport atomique Nb:N obtenu par XPS, on peut en déduire qu'il y a 1259 chaînes polymères de BPEI par nanoparticule de LN, ce qui correspond à un pourcentage massique de 24% de polymère par nanoparticule de LN. Ce résultat est du même ordre de grandeur que celui de Rosenholm *et al* [Rosenholm 2009] pour lequel un pourcentage massique de PEI de 18% a été déterminé sur des nanoparticules de silice par thermogravimétrie.

### 3.2.3. Immobilisation des germes d'or sur LN@BPEI

La première méthode utilisée pour préparer les nanoparticules LN@BPEI@AuSeeds est adaptée du travail de Wang *et al* [Wang 2016b]. Le protocole est basé sur la réduction des ions or par $NaBH_4$. L'article rapporte une réduction rapide de $HAuCl_4$ menant à des germes d'or de 4 nm de diamètre environ uniformément répartis sur des nanoparticules de silice aminées. Cependant, cette méthode appliquée aux nanoparticules LN@BPEI n'a pas fonctionné car elle conduit à une répartition inhomogène de nanoparticules d'or d'environ 18 nm de diamètre sur la surface du LN avec un potentiel zeta de -15,5 $\pm$ 0,6 mV, un diamètre hydrodynamique de 159,6 $\pm$ 5,8 nm et un indice de polydispersité de 0,37. Ces résultats montrent une forte agrégation des nanoparticules.

La seconde méthode se déroule en deux étapes, avec tout d'abord la synthèse des germes d'or puis leur ajout dans la dispersion de LN@BPEI. La synthèse des germes d'or est réalisée selon le protocole de Duff *et al* [Duff 1993]. La réaction se déroule à pH 11,1, les ions $OH^-$ transformant le THPC en THP et formaldéhyde. A ce pH, l'espèce d'or prédominante est $Au(OH)_4^-$. L'Au(III) est réduit pour former des complexes THP-Au(I) et le formaldéhyde réduit Au(I) en Au(0) pour former les germes d'or. L'incorporation de groupements phosphines pourrait laisser supposer la formation de germes chargés positivement. Cependant un potentiel zeta de -25,3 $\pm$ 8,0 mV est obtenu, ce qui est attribué à la présence d'ions $AuCl_4^-$. Ces germes d'or sont sphériques, de diamètre moyen 2,5 $\pm$ 0,5 nm et ne présentent pas de bande d'absorption caractéristique. A partir du diamètre, on peut calculer une concentration théorique de AuSeeds de 0,037 mg/mL ou $2{,}32 \times 10^{14}$ NPs/mL, ce qui est en accord avec les valeurs reportées dans la littérature [Garcia-Soto 2016]. L'ICP-AES nous a permis de déterminer que la concentration réelle des AuSeeds

était de 0,028 mg/mL soit $1,77 \times 10^{14}$ NPs/mL. Les valeurs théorique et expérimentale sont donc du même ordre de grandeur.

L'immobilisation des AuSeeds sur les nanoparticules LN@BPEI est réalisée par interaction électrostatique entre les LN@BPEI chargées positivement (+36,05 $\pm$ 2,9 mV) et les AuSeeds chargés négativement (-25,3 $\pm$ 8,0 mV). En plus de ces interactions électrostatiques, il est aussi possible qu'il y ait des réactions de complexation entre les ions or trouvés à la surface des AuSeeds et les amines. Avec l'estimation de 1259 chaînes BPEI par LN déterminée par XPS, on peut calculer qu'il y a au maximum 267989 sites $NH_2$ disponibles pour l'immobilisation de AuSeeds sur chaque nanoparticule de LN.

Nous avons cherché à déterminer le pourcentage maximum de couverture des AuSeeds sur les LN@BPEI en faisant varier la quantité de AuSeeds présents dans la dispersion (Table 2). Les images TEM montrent une distribution aléatoire des AuSeeds sur les nanoparticules de LN. Ces résultats sont comparables à ceux obtenus dans la littérature pour des nanoparticules d'or modifiées citrate immobilisées sur des nanoparticules de silice à pH neutre [De Silva Indrasekara 2018]. L'imagerie TEM et l'ICP-AES ont été employés conjointement pour quantifier le nombre de AuSeeds immobilisés sur chaque LN et pour en déduire le pourcentage de couverture. Pour la quantification par TEM, une population de 50 nanoparticules de LN a été utilisée et le nombre moyen de AuSeeds par nanoparticule sur le cœur LN@BPEI a été calculé. Pour la quantification par ICP-AES, la concentration totale en Nb et Au dans l'échantillon a permis de déterminer la concentration en LN@BPEI et en AuSeeds, et en assumant que la concentration d'Au mesurée provenait uniquement des AuSeeds, de calculer le nombre moyen de AuSeeds par nanoparticule. La Figure 5 présente l'évolution du pourcentage de surface de LN@BPEI recouvert par les AuSeeds en fonction du rapport théorique AuSeeds:LN, déterminé par TEM et par ICP-AES.

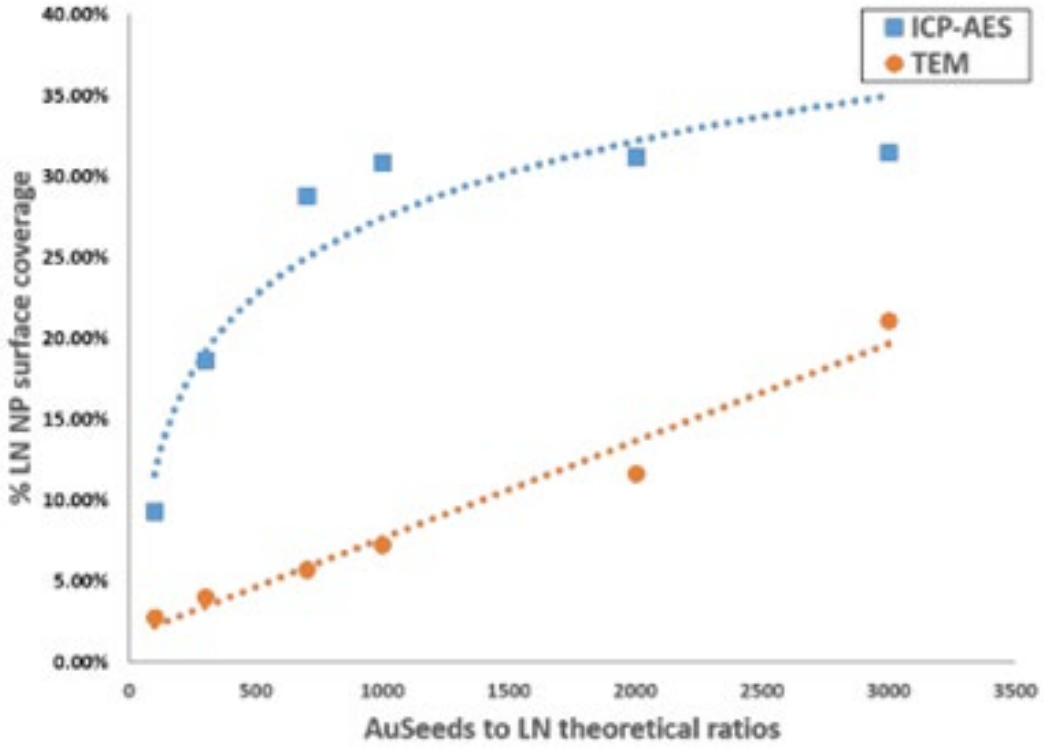


**Figure 5.** Pourcentage de surface de LN@BPEI recouvert par les AuSeeds pour chaque échantillon LN@BPEI@AuSeeds avec différents rapports AuSeeds:LN déterminé par TEM et ICP-AES.

A partir de l'analyse TEM, une évolution linéaire est observée. Cette tendance linéaire laisse supposer une possibilité d'augmenter encore le pourcentage de surface en augmentant la concentration de AuSeeds. Il est cependant obligatoire qu'il y ait un maximum à cause de la répulsion électrostatique entre particules, des forces attractives de Van der Waals, des forces hydrophobes et stériques dues au polymère et de la couche de solvatation. Enfin, la conformation du BPEI sur les cœurs de LN impacte aussi le positionnement des amines de surface. La sous-estimation du pourcentage de surface par l'analyse TEM était attendue, d'une part parce qu'elle est limitée statistiquement, d'autre part parce que nous avons supposé que nous observions un hémisphère complet de chaque

nanoparticule, et extrapolé le nombre total de AuSeeds en multipliant leur nombre mesuré par deux.

L'analyse ICP-AES révèle une tendance asymptotique avec un pourcentage de surface maximum de 31,5% pour un pourcentage massique de Au de 29%. Dans la littérature, un pourcentage massique de 47,7% de Au a été obtenu pour des nanoparticules cubiques d'oxyde de fer de 50 nm, ce qui correspond à un pourcentage de surface de 74% [Goon 2009]. Le pourcentage plus faible obtenu dans notre cas peut être expliqué par la forme cubique des nanoparticules de Fe ans la publication de Goon qui offre une plus grande surface spécifique que la forme pseudo-sphérique de nos nanoparticules de LN. De plus, la forme cubique modifie la conformation du BPEI, rendant peut-être plus accessible les fonctions amines pour l'interaction avec les AuSeeds. Dans notre cas, le maximum atteint à partir de LN@BPEI@AuSeeds1000 a également été observé à l'œil nu lors de la centrifugation, le surnageant ayant la couleur des AuSeeds dans ce cas, alors qu'il était incolore pour LN@BPEI@AuSeeds100 et LN@BPEI@AuSeeds700.

Les valeurs de potentiel zeta attestent qualitativement de la modification de surface des nanoparticules (Figure 6) : à chaque modification, la charge de surface est inversée.

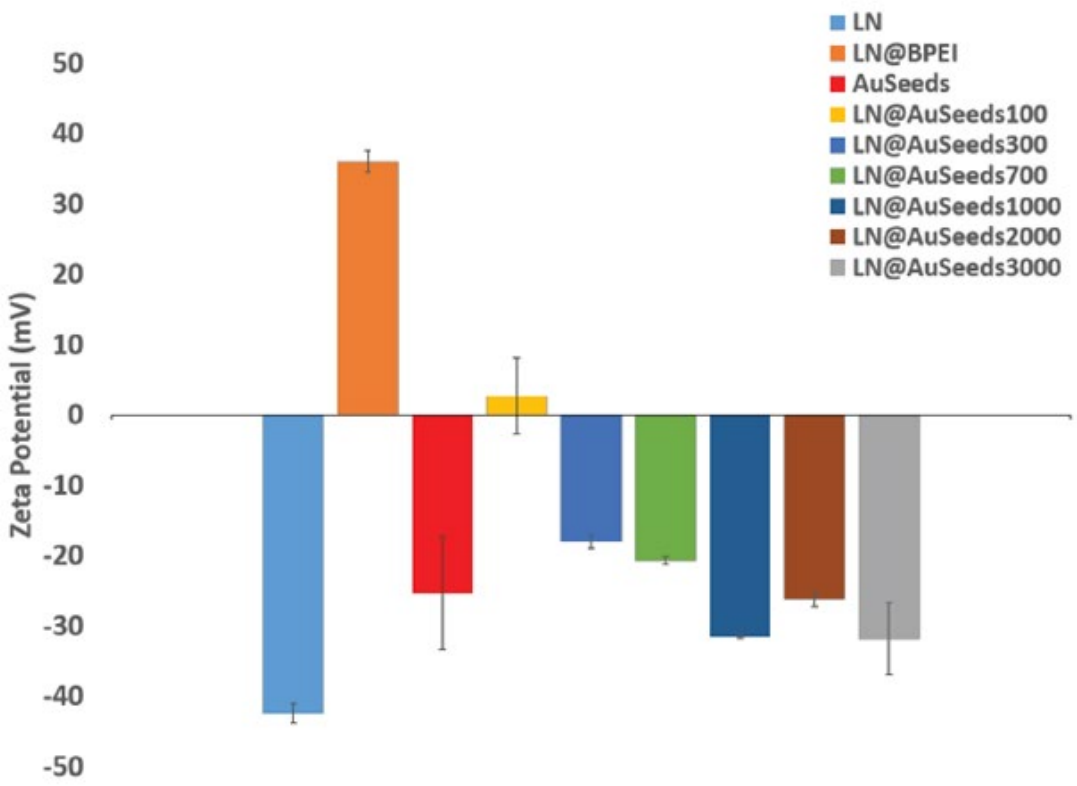


**Figure 6.** Potentiel zeta de LN, LN@BPEI et LN@BPEI@AuSeeds montrant l'alternance de valeurs négatives et positives en modifiant la surface des nanoparticules.

Les nanoparticules LN@BPEI@AuSeeds100 et LN@BPEI@AuSeeds700 sédimentent au bout de quelques minutes tandis que les nanoparticules LN@BPEI@AuSeeds1000 et LN@BPEI@AuSeeds3000 demeurent bien dispersées comme l'indiquent les valeurs de potentiel zeta.

### 3.2.4. Spectroscopie HRS

Comme précisé dans le Chapitre 1, le paramètre microscopique permettant de quantifier la réponse SHG des nanoparticules est $\beta$. Les intensités HRS mesurées pour une dispersion de nanoparticules peuvent être exprimées avec l'équation 1.

$$I_{HRS} = G(N_s F_s \langle \beta_s^2 \rangle + N_{np} T_{np} \langle \beta_{np}^2 \rangle) I_\omega^2 \quad \text{Equation 1}$$

où $G$ est une constante de proportionnalité expérimentale, $N_s$ est la concentration du solvant, $F_s$ est un facteur de champ proche dépendant de l'indice de réfraction du solvant, $\beta_s$ est l'hyperpolarisabilité du solvant, $N_{np}$ est la concentration des nanoparticules, $T_{np}$ est un facteur de champ interne, $\beta_{np}$ est l'hyperpolarisabilité moyenne des nanoparticules et $I_\omega$ est l'intensité du rayonnement incident. En variant la concentration en nanoparticules et en mesurant l'intensité HRS correspondante, puis en utilisant la référence externe, les valeurs d'hyperpolarisabilité de la dispersion de nanoparticules peuvent être déduites de la pente (Figure 7) à partir de l'équation 2.

| | |
|---|---|
| $I_{HRS} = 1 + \frac{\langle \beta_{LN}^2 \rangle}{N_W \langle \beta_W^2 \rangle} N_{LN}$ | Equation 2 |

L'hyperpolarisabilité ($\beta$) peut être extraite de la pente en utilisant la méthode de la référence interne. L'intensité HRS du solvant (ici W signifie que le solvant est de l'eau) est $N_W$= 55.56 mol/L avec une valeur $\sqrt{\langle \beta_W^2 \rangle}$ de $0.087\times10^{-30}$ esu. $N_{LN}$ est la concentration des nanoparticules de LN. L'intensité HRS a aussi été mesurée pour les échantillons LN@BPEI@AuSeeds300, LN@BPEI@AuSeeds1000 et LN@BPEI@AuSeeds3000, ainsi que pour la dispersion de AuSeeds.

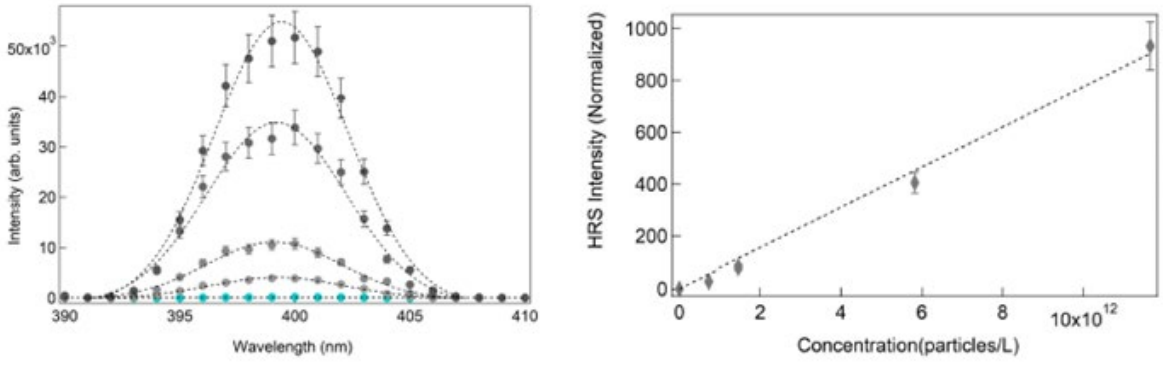


(a) (b)

**Figure 7.** Intensités HRS des dispersions de LN obtenues en utilisant une longueur d'onde incidente de 800 nm, verticalement polarisée, et en variant la concentration de LN (a). Intensités maximales corrigées en fonction de la concentration de LN (b).

Les valeurs de $\beta$ obtenues sont présentées dans la Table 3, ainsi que les valeurs des coefficients de seconde harmonique moyens $< d >$ qui prennent en compte l'effet du volume des nanoparticules selon l'équation 3.

| $\langle \beta_{np} \rangle = \langle d \rangle V_{np}$ | Equation 3 |
|---|---|

où $V_{np}$est le volume moyen d'une nanoparticule. Dans l'équation 3, on admet qu'il n'y a pas de contribution surfacique et que la première hyperpolarisabilité dépend uniquement du volume, ce qui est une hypothèse correcte pour les matériaux diélectriques non centro-symétriques. Cette équation néglige également l'orientation du rayonnement incident par rapport aux axes cristallographiques.

| **Nom de l'échantillon** | $\sqrt{\langle \beta^2 \rangle}$ **(esu)** | $\langle d \rangle$ **(pm/V)** |
|---|---|---|
| AuSeeds | $3.42\times10^{-28}$ | 17.5 |
| LN@BPEI@AuSeeds300 | $0.535\times10^{-24}$ | 4.7 |
| LN@BPEI@AuSeeds1000 | $0.129\times10^{-24}$ | 1.1 |
| LN@BPEI@AuSeeds3000 | $0.140\times10^{-24}$ | 1.2 |
| LN | $0.768\times10^{-24}$ | 6.7 |
| Référence LN | $16.3\times10^{-24}$ | 6.7 |

**Table 3.** Hyperpolarisabilités déterminées à partir de la pente des graphes donnant l'intensité HRS en fonction de la concentration en nanoparticules pour les AuSeeds, LN@BPEI@AuSeeds300, LN@BPEI@AuSeeds1000, LN@BPEI@AuSeeds3000, LN utilisé dans ce travail (diamètre 45 nm) et le LN de référence (diamètre 125 nm) issu de la

littérature [Joulaud 2013]. Dans la deuxième colonne sont donnés les coefficients de seconde harmonique moyens $< d >$ correspondants.

On constate que les valeurs de $< d >$ obtenues pour le LN de notre travail et le LN issu de la littérature sont en accord. Ensuite, il apparaît que la présence de AuSeeds à la surface des LN diminue les coefficients de seconde harmonique, que ce soit $\beta$ ou $< d >$. Une explication est que les contributions surfaciques de l'intensité HRS du LN sont significatives. Pour justifier cette hypothèse, nous avons mené des expériences résolues en polarisation, dans lesquelles l'angle de la polarisation incidente varie et le faisceau de sortie est polarisé verticalement. Le rapport de dépolarisation $D$ peut alors être calculé selon l'équation 4.

| | |
|---|---|
| $D = \frac{I_{HRS}^{H}}{I_{HRS}^{V}}$ | Equation 4 |

où $I_{HRS}^{V}$et $I_{HRS}^{H}$ sont les intensités obtenues pour une polarisation incidente verticale et horizontale, respectivement. Les valeurs de $D$ obtenues pour nos échantillons sont présentées dans la Table 4.

| **Nom de l'échantillon** | ***D*** |
|---|---|
| LN | 0.16 |
| LN@BPEI@AuSeeds100 | 0.2 |
| LN@BPEI@AuSeeds300 | 0.17 |
| LN@BPEI@AuSeeds1000 | 0.18 |
| LN@BPEI@AuSeeds3000 | 0.18 |
| AuSeeds | 0.43 |

**Table 4.** Valeurs de rapport de dépolarisation $D$ obtenues pour LN, AuSeeds et LN@BPEI@AuSeeds.

Théoriquement, le rapport de dépolarisation pour un tenseur unique d'une molécule dipolaire non linéaire vaut 0,2. Inversement, les molécules symétriques planes du groupe ponctuel $D_{3h}$ ont un rapport de dépolarisation de 2/3. Le niobate de lithium, qui appartient au groupe ponctuel $C_{3v}$ présente une forte non linéarité selon un certain axe, ce qui est cohérent avec la valeur proche de 0,2 observée pour LN et LN@BPEI@AuSeeds. Les AuSeeds ont en revanche une valeur de rapport de dépolarisation plus proche du système $D_{3h}$, ce qui est probablement dû à leur géométrie sphérique. Les tracés polaires confirment ces résultats. On constate que l'ajout de AuSeeds sur LN fait peu varier le rapport $D$ par rapport au LN. Il nous reste donc encore à comprendre pourquoi l'ajout de AuSeeds sur LN fait diminuer $\beta$. Des simulations sont en cours pour expliquer la variation des propriétés optiques des nanoparticules.

# Chapitre 4 : Synthèse de la coquille d'or sur les nanoparticules de $LiNbO_3$

Dans ce dernier chapitre, nous présentons la synthèse d'une coquille d'or autour du cœur de $LiNbO_3$ pour former des nanoparticules cœur-coquille LN@Au. Plusieurs protocoles de synthèse ont été testés, basés sur une méthode de croissance par ensemencement de germes (Figure 8). Les paramètres expérimentaux qui ont été variés sont le pH, la densité de AuSeeds déposés sur LN et la concentration en sel d'or. La surface des nanoparticules a été caractérisée à chaque étape de la synthèse. L'impact du vieillissement sur les propriétés des dispersions de nanoparticules a été étudié. Enfin, la réponse optique non linéaire et les propriétés photothermales des LN@Au sont présentées.

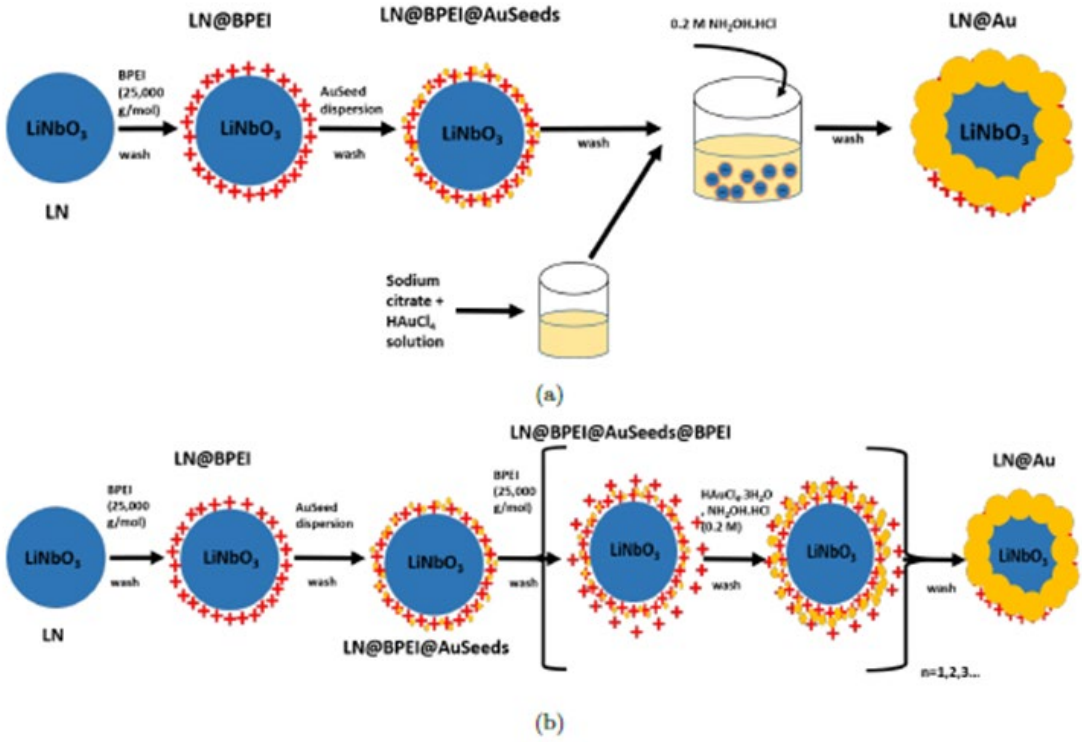


**Figure 8.** Schéma des deux protocoles utilisés pour la synthèse de LN@Au. (a) Synthèse de LN@Au en utilisant le citrate de sodium dans la solution de croissance de $HAuCl_4$. (b) Synthèse de LN@Au en utilisant une approche « couche par couche ».

### 4.1. Matériel et méthodes

La première étape de la synthèse des LN@Au consiste en l'immobilisation de AuSeeds sur les nanoparticules LN en présence de BPEI comme présenté dans le Chapitre 3. L'étape suivante (formation de la coquille de Au) a été testée avec les deux protocoles suivants.

*Synthèse des LN@Au en utilisant une solution de citrate de sodium pour la croissance.* Des solutions de croissance composées de $Na_3Cit$:$HAuCl_4$ avec des rapports molaires de 1:1, 8:1 et 40:1 ont été préparées. A chaque solution de croissance a été ajouté 1 mL de LN@BPEI@AuSeeds3000 suivi de 10,7 µL de $NH_2OH$, HCl à 0,2 M. Après réaction pendant 10 min, les mélanges ont été centrifugés pendant 10 min à 20°C et 9103g et redispersés dans 1 mL d'eau après élimination du surnageant.

*Synthèse « couche par couche » des LN@Au.* Les nanoparticules LN@BPEI@AuSeeds (1 mL à 0,35 mg/mL) sont mélangées à 4 mg de BPEI dissous dans 5 mL d'eau à 60°C pendant 2 h. Après refroidissement, le mélange est centrifugé 2 fois pendant 10 min à 10°C et 9103g et redispersé dans 1 mL d'eau. Selon l'expérience, le pH de l'eau a été gardé tel quel (environ 7,7) ou ajusté à 11,5 en utilisant NaOH à 0,1 M. Puis sous agitation, 1 mL de dispersion de nanoparticules a été ajoutée à 18 mL d'eau suivi de 50 µL de $HAuCl_4$ et 75 µL de $NH_2OH$, HCl à 0,2 M. Après 10 min d'agitation, le mélange est centrifugé 2 fois pendant 10 min à 10°C et 9103g et redispersé dans 1 mL d'eau. La Table 5 présente les différentes conditions expérimentales qui ont été testées avec ce protocole.

| **Variable expérimentale** | **Conditions expérimentales** |
|---|---|
| pH | 1) LN@BPEI@AuSeeds3000, pH 11,5, $HAuCl_4$ = 30 mM<br>2) LN@BPEI@AuSeeds3000, pH 7,7, $HAuCl_4$ = 30 mM |

| | |
|---|---|
| LN@BPEI@AuSeeds | 1) LN@BPEI@AuSeeds3000, pH 7,7, $HAuCl_4$ = 30 mM<br>2) LN@BPEI@AuSeeds1000, pH 7,7, $HAuCl_4$ = 30 mM |
| Concentration en $HAuCl_4$ | 1) LN@BPEI@AuSeeds1000, pH 7,7, $HAuCl_4$ = 3 mM<br>2) LN@BPEI@AuSeeds1000, pH 7,7, $HAuCl_4$ = 10 mM<br>3) LN@BPEI@AuSeeds1000, pH 7,7, $HAuCl_4$ = 30 mM<br>4) LN@BPEI@AuSeeds1000, pH 7,7, $HAuCl_4$ = 100 mM |

**Table 5.** Conditions expérimentales pour la croissance de la coquille « couche par couche ».

Les mesures photothermiques ont été réalisées à l'aide d'un montage composé de la façon suivante. Un porte-échantillon contenant 200 µL de dispersion de nanoparticules dans un tube eppendorf de 2 mL a été fixé dans une boîte noire. Un laser continu à 808 nm muni d'une fibre optique de 200 µm est utilisé pour produire un faisceau avec une puissance de sortie de 47 $mW/cm^2$. Une caméra thermique est positionnée à 90°C du faisceau incident, à une distance de 10 cm de l'échantillon.

### 4.2. Résultats et discussion

#### 4.2.1. Synthèse de LN@Au en utilisant le citrate de sodium

Dans le but de contrôler le dépôt d'or sur les LN@BPEI, un protocole utilisant le citrate de sodium, mis au point sur des nanoparticules de silice aminées de 120 nm de diamètre, a été testé [Wang 2016b]. Dans ce protocole, le rapport molaire $Na_3Cit$:$HAuCl_4$ permet de faire varier la densité de l'or sur la surface de silice en allant d'îlots pour de faibles rapports à une couche dense pour de forts rapports. La première étape de ce protocole consiste en la réduction *in situ* de l'or par $NaBH_4$. Cependant, comme nous l'avons démontré au

chapitre précédent, cette méthode n'a pas fonctionné sur les LN@BPEI. Par conséquent, ce sont les nanoparticules LN@BPEI@AuSeeds qui ont été utilisées ici, plus particulièrement les LN@BPEI@AuSeeds3000 qui sont stables dans l'eau avec un potentiel zeta de -31,8 $\pm$ 20,3 mV et un indice de polydispersité de 0,2.

Trois rapports molaires $Na_3Cit$:$HAuCl_4$ ont été testés: 1:1, 8:1 et 40:1. Pour les deux premiers rapports, dès l'ajout du réducteur $NH_2OH$, HCl, le milieu change de couleur allant du rouge-brun (correspondant aux AuSeeds) au violet. On observe l'apparition d'une bande d'extinction unique à 535 nm et 526 nm pour les rapports 1:1 et 8:1, respectivement. Les valeurs de potentiel zeta et de diamètre hydrodynamique mesurées semblent montrer qu'il s'agit de dispersions composées d'une seule population de nanoparticules avec plutôt des îlots d'or sur la surface de LN, suffisamment éloignés les uns des autres pour qu'il n'y ait aucun effet de couplage entre eux. Pour le rapport molaire 40:1, une bande d'extinction à 597 nm est obtenue, ce qui correspond à un décalage en longueur d'onde de 60 nm environ comparé aux rapports molaires précédents, mais qui reste bien inférieur aux 200 nm de décalage obtenus par Wang *et al* [Wang 2016b]. Les images TEM montrent la présence d'îlots d'or comme nous l'avions supposé pour les rapports molaires 1:1 et 8:1. Nos résultats peuvent être expliqués par les valeurs différentes de pKa entre les groupements amines accrochés à la surface de silice (9 environ) et ceux du BPEI (7 environ). Ici le citrate de sodium a une fonction régulatrice sur le pH à cause de ses 3 groupements carboxylates, ce qui diminue le degré de protonation des fonctions amines du BPEI. Nous avons ainsi conclu que ce protocole n'était pas adapté à la formation d'une coquille d'or sur les LN@BPEI@AuSeeds.

4.2.2. Croissance d'une coquille d'or « couche par couche »

Pour ce protocole, nous nous sommes inspirés des travaux de Lee *et al* [Lee 2017] qui ont utilisé une méthode de dépôt couche par couche pour la croissance d'une coquille d'or sur des nanoparticules sphériques d'oxyde de fer. Ce protocole a nécessité de nombreuses optimisations pour être adapté à nos nanoparticules de LN. Plusieurs paramètres expérimentaux (pH, densité de AuSeeds déposés sur LN et concentration en sel d'or) ont ainsi été variés.

4.2.2.1. Rôle du pH

Dans l'article de Lee *et al* [Lee 2017], la réduction de $Au^{3+}$ est réalisée en conditions basiques (pH = 11,5). Même si le pH permet de contrôler la morophologie de la coquille d'or obtenue, il faut aussi tenir compte du fait que la charge électrique du BPEI diminue fortement lorsque le pH augmente. C'est pourquoi nous avons testé à la fois des conditions de pH neutre et basique pour la synthèse de la coquille d'or. Les bandes plasmons obtenues dans les 2 cas pour les 3 réductions successives de l'or sont présentées sur la Figure 9.

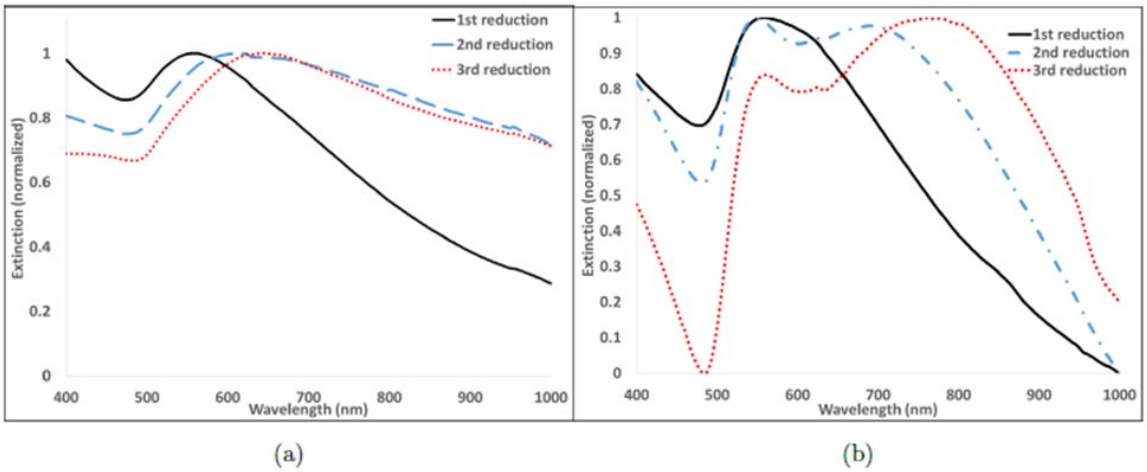


**Figure 9.** Spectres UV-Visible des dispersions de nanoparticules après la 1ère, 2ème et 3ème étape de réduction de l'or à pH = 11,5 (a) et sans ajuster le pH du milieu réactionnel (b).

Pour les deux conditions de pH, un décalage progressif vers le rouge de la bande plasmon est obtenu au fil des étapes de réduction, ce qui est associé à une diminution de la distance inter-particules d'or à la surface du LN. En conditions basiques, la 3$^{ème}$ réduction conduit à une bande plasmon autour de 625 nm. L'observation TEM et les spectres EDS montrent des nanoparticules LN@Au probablement constituées de plusieurs cœurs LN encapsulés dans une même coquille Au. En conditions neutres, la 3$^{ème}$ réduction conduit à une bande plasmon autour de 776 nm, ce qui est beaucoup plus proche des objectifs recherchés. Les images TEM révèlent une morphologie type « framboise » pour ces nanoparticules LN@Au avec la présence de nanoparticules d'or sphériques individuelles. Cette morphologie contraste avec la morphologie rugueuse et « à pointes » obtenue par Lee *et al*. Nous supposons que l'utilisation d'un pH neutre conduit à un dépôt d'or plus homogène car il permet de passer par une étape préliminaire de dépôt de nanocristaux $AuCl(OH)_3^-$ suivi de la réduction en $Au^0$. L'analyse TEM permet d'identifier la présence de deux populations de LN@Au avec des diamètres autour de 80-120 nm et 200 nm, ce qui nous laisse supposer que les LN@Au sont à la fois composées de cœur de LN unique et multiples. Une cartographie EDS permet de montrer la co-localisation des 3 éléments Nb, O et Au dans une nanoparticule LN@Au unique (Figure 10).

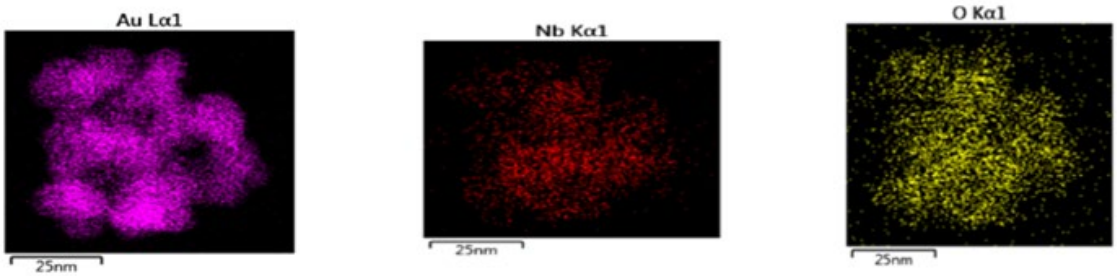


**Figure 10.** Cartographie chimique des éléments Au, Nb et O sur LN@Au obtenue après 3 étapes de réduction. Les conditions de synthèse sont les suivantes : LN@BPEI@AuSeeds3000, pH neutre, $[HAuCl_4]$ = 30 mM.

4.2.2.2. Rôle de la densité de AuSeeds

Après avoir conclu que les conditions de pH neutres étaient plus favorables pour la synthèse de la coquille d'or, nous avons donc étudié l'influence de la densité de AuSeeds sur la surface de LN dans ces conditions de pH. Il a été montré en effet que le rapport entre les germes d'or et les précurseurs d'or influençait le mode de croissance (homogène ou inhomogène) des nanoparticules d'or [Bastus 2011]. Les deux échantillons de LN@BPEI@AuSeeds sélectionnés pour cette étude sont LN@BPEI@AuSeeds1000 et LN@BPEI@AuSeeds3000 car ils forment des dispersions stables et présentent une différence de 13,8% en pourcentage de surface recouvert comme nous l'avons vu au Chapitre 3. Les bandes plasmons obtenues dans les 2 cas pour les 3 réductions successives de l'or sont présentées sur la Figure 11.

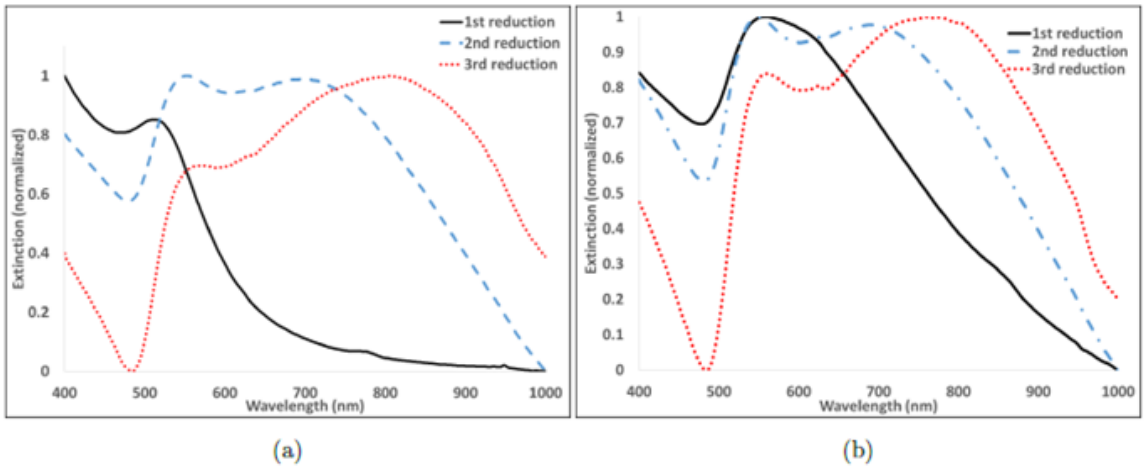


**Figure 11.** Spectres UV-Visible des dispersions de nanoparticules après la 1ère, 2ème et 3ème étape de réduction de l'or pour LN@BPEI@AuSeeds1000 (a) et LN@BPEI@AuSeeds3000 (b).

On constate la présence de deux pics pour tous les spectres à chaque étape de réduction avec un décalage progressif du deuxième pic vers le rouge au fil des étapes de réduction comme observé précédemment. Les LN@Au ainsi formées présentent une bande plasmon

large entre 700 et 900 nm, ce qui correspond aux objectifs souhaités. Les mesures de potentiel zeta et de diamètre hydrodynamique montrent cependant des différences notables entre les deux échantillons. Alors que les LN@Au formées à partir des LN@BPEI@AuSeeds3000 ont un potentiel zeta toujours inférieur à 20 mV en valeur absolue quelle que soit l'étape de réduction, les LN@Au formées à partir des LN@BPEI@AuSeeds1000 ont un potentiel zeta positif qui augmente progressivement au cours des étapes de réductions jusqu'à +30,2 mV. Ceci est également associé à des valeurs de diamètre hydrodynamique et d'indice de polydispersité plus faibles pour LN@BPEI@AuSeeds1000 que pour LN@BPEI@AuSeeds3000, montrant une moindre agrégation. Les images TEM montrent aussi que les LN@Au préparées à partir de LN@BPEI@AuSeeds1000 ne présentent aucune nanoparticule d'or libre (Figure 12). Ceci est corroboré par un faible indice de polydispersité (0,118) pour les LN@Au finales. Ces résultats très différents obtenus avec les LN@BPEI@AuSeeds1000 et les LN@BPEI@AuSeeds3000 peuvent être expliqués par le fait que dans le cas des LN@BPEI@AuSeeds3000, l'excès de AuSeeds reste dans la dispersion même après centrifugation, possiblement attaché au BPEI dans la sphère de solvatation des nanoparticules.

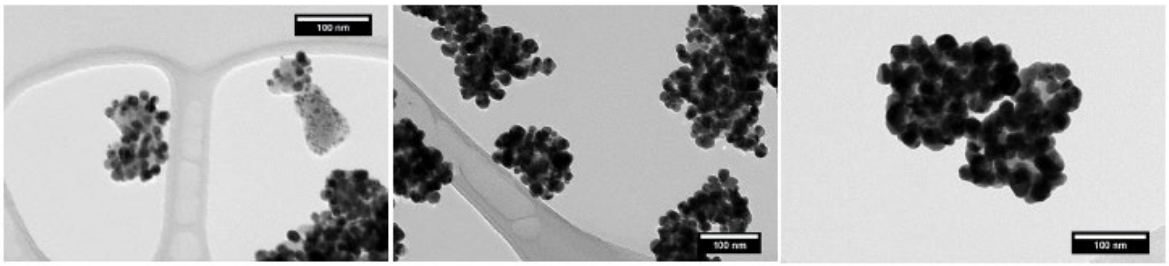


(a) (b) (c)

**Figure 12.** Images TEM des LN@Au après la 1ère (a), 2ème (b) et 3ème (c) étape de réduction formées à partir des LN@BPEI@AuSeeds1000. Les autres conditions de synthèse sont : pH neutre, [$HAuCl_4$] = 30 mM.

Une morphologie type « framboise » est obtenue dans les deux cas. On constate une évolution du diamètre moyen des nanoparticules d'or au cours des étapes de réduction : 12,5 ± 2,5 nm, 19,0 ± 4,1 nm et 26,0 ± 5,6 nm après la 1ère, 2ème et 3ème étape de réduction, respectivement.

#### 4.2.2.3. Rôle de la concentration en sel d'or

Il a été montré dans des travaux précédents que changer la concentration de réducteur permet d'influencer la cinétique de la réduction de l'or, ce qui a pour conséquence de modifier la morphologie de la coquille en allant de sphères « lisses » à des « nanofleurs » [Zhao 2009]. Dans notre cas, comme le réducteur $NH_2OH$, HCl a toujours été utilisé en excès, c'est $HAuCl_4$ qui est le réactif limitant, nous avons donc décidé de faire varier sa concentration à 3 mM, 10 mM, 30 mM et 100 mM en gardant fixes les autres paramètres expérimentaux (LN@BPEI@AuSeeds1000, pH neutre) pour former la coquille. A la concentration 100 mM, une rapide agrégation des nanoparticules est observée. Notre étude s'est donc focalisée sur les 3 concentrations les plus basses.

Les nanoparticules LN@Au produites avec une concentration de 3 mM en $HAuCl_4$ présentent une bande plasmon unique après la 3ème réduction contrairement à celles produites avec une concentration de 30 mM. La bande est centrée à 693 nm, décalée vers le bleu de 110 nm par rapport à celle obtenue avec une concentration de 30 mM (Figure 13). Les images TEM montrent une couverture incomplète de la surface de LN avec des nanoparticules d'or de morphologie allongée et aplaties sur la surface, ce qui explique peut-

être la présence d'une seule bande plasmon. Nous supposons que dans la synthèse réalisée avec une concentration de 30 mM $HAuCl_4$, nous avons des espèces $AuCl(OH)_3^-$ sur la surface du LN et dans le milieu de dispersion, qui après ajout du réducteur, forment rapidement des $Au^0$, qui s'agglomèrent dans la forme thermodynamique la plus stable, c'est-à-dire sous forme de sphère. Dans la synthèse à 3 mM, à cause de la faible quantité de $AuCl(OH)_3^-$, les $Au^0$ se réarrangent par eux-mêmes sur la surface de LN.

Concernant la synthèse à 10 mM, la 3ème réduction conduit à l'observation d'une large bande plasmon entre 550 et 1000 nm, plus large que celle obtenue à 30 mM (Figure 13). Après imagerie TEM, deux morphologies sont identifiées : des nanoparticules d'or allongées, identiques à celles obtenues pour la synthèse à 3 mM et des coquilles d'or continues. L'analyse EDS confirme que ces nanoparticules contiennent toutes à la fois des éléments Nb et Au.

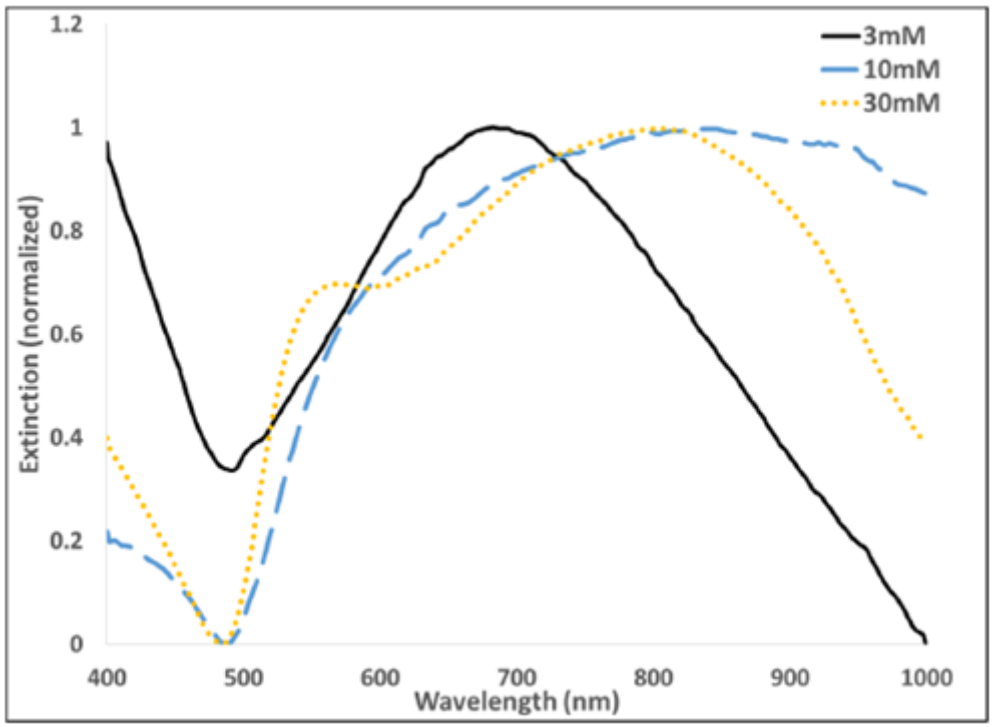

**Figure 13.** Spectres d'extinction UV-Visible des LN@Au après la 3ème étape de réduction en utilisant des concentrations en $HAuCl_4$ de 3, 10 et 30 mM à partir des LN@BPEI@AuSeeds1000. Les autres conditions de synthèse sont : pH neutre, [$HAuCl_4$] = 30 mM.

La Table 6 fournit un récapitulatif des caractéristiques des LN@Au obtenues en faisant varier la concentration en sel d'or.

| $HAuCl_4$ concentration | 3 mM | 10 mM | 30 mM |
|---|---|---|---|
| $\lambda$ du pic d'extinction (3ème réduction) en nm | 693 | Large bande (500-1000) | 803 |
| Diamètre hydrodynamique (nm) | 198,1 | 159,3 | 163,3 |
| Indice de polydispersité | 0,260 | 0,225 | 0,118 |
| Potentiel zeta (mV) | +26,1 | +20,8 | +30,2 |
| Morphologie de la coquille | Ilots d'or allongés | Ilots d'or allongés et coquilles d'or continues | Sphères d'or se superposant |

**Table 6.** Résumé des caractéristiques des dispersions finales de nanoparticules LN@Au obtenues en utilisant des concentrations en $HAuCl_4$ de 3, 10 et 30 mM à chaque étape de réduction. Les nanoparticules initiales sont LN@BPEI@AuSeeds1000 et une concentration de 0,2 M en $NH_2OH$, HCl a été utilisée.

En conclusion, les nanoparticules optimales LN@Au obtenues par la méthode « couche par couche » sont celles préparées à partir de LN@BPEI@AuSeeds1000, à pH neutre, avec $[HAuCl_4]$ = 30 mM.

4.2.3. Caractérisation physico-chimique du suivi de la croissance de la coquille d'or sur les nanoparticules de LN

L'analyse ICP-AES nous permet de déterminer la concentration de Nb et de Au, ce qui conduit, en supposant un dépôt homogène de Au sur LN, à une épaisseur de la coquille d'or de 1,2 nm.

Les spectroscopies XPS et TOF-SIMS ont été utilisées pour caractériser les nanoparticules aux différentes étapes de la synthèse. Les échantillons analysés sont les suivants : LN, LN@BPEI@AuSeeds1000, LN@BPEI@AuSeeds3000, LN@BPEI@AuSeeds1000@BPEI, LN@BPEI@AuSeeds3000@BPEI, LN@Au (obtenu après la 3$^{ème}$ réduction de LN@BPEI@AuSeeds1000) et LN@Au (obtenu après la 3$^{ème}$ réduction de LN@BPEI@AuSeeds3000).

L'étude des données TOF-SIMS a été réalisée après analyse par composantes principales. Deux composantes PC1 et PC2 sont extraites. Les PC1 de charge positive (PC1+) correspondent aux fragments Li et Nb tandis que les PC1- sont associés aux fragments contenant C, H, N et O, ce qui laisse penser que PC1+ est lié au $LiNbO_3$ tandis que PC1- est lié au BPEI. PC2+ montre principalement des fragments Au et PC2- des fragments contenant C, H, N, O et Nb représentant $LiNbO_3$ et BPEI. La répartition des échantillons

analysés en fonction de ces composantes est cohérente avec les compositions chimiques attendues (Figure 14).

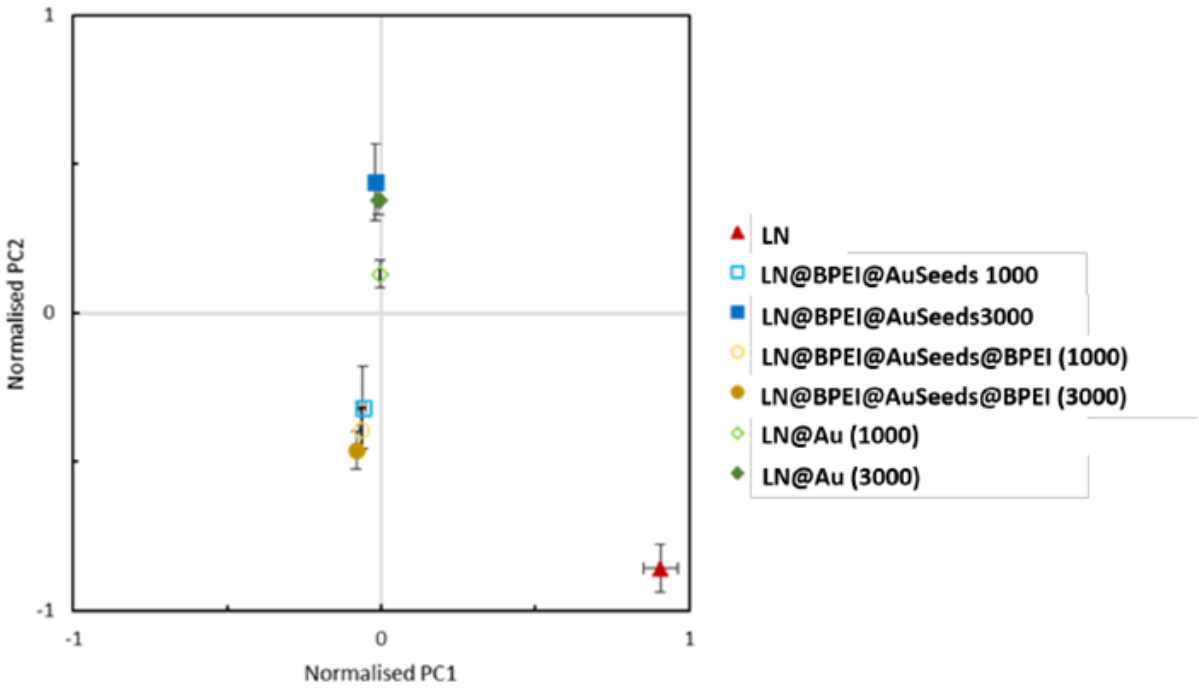


**Figure 14.** Répartition des échantillons analysés en fonction des composantes principales PC1 et PC2.

L'analyse des spectres larges XPS permet de constater également l'apparition des pics d'or (Au4p, Au4d, Au4f) et de l'azote (N1s) pour les nanoparticules LN@BPEI@AuSeeds par rapport aux nanoparticules initiales de LN. La spectroscopie XPS donne également accès aux pourcentages atomiques des espèces contenues dans ces différents échantillons (Table 7). Les pourcentages atomiques en C et en N passent respectivement de 16,3% à 36% et de 1,5% à 3,9% pour LN@BPEI@AuSeeds1000 par rapport à LN. La même tendance est observée pour LN@BPEI@AuSeeds3000. On observe également une augmentation du pourcentage atomique de Au entre LN@BPEI@AuSeeds1000 (8,5%) et LN@BPEI@AuSeeds3000 (11,05%). L'analyse TOF-SIMS donne un PC2- pour LN@BPEI@AuSeeds1000 et un PC2+ pour LN@BPEI@AuSeeds3000, laissant supposer

que la quantité d'or utilisée dans le cas de LN@BPEI@AuSeeds3000 est suffisante pour recouvrir complétement le BPEI.

| Echantillon | Concentration (at%) | | | | | |
|---|---|---|---|---|---|---|
| | Nb | O | C | N | Li | Au |
| LN | 18,28 (0,97) | 49,66 (1,52) | 16,30 (0,54) | 1,54 (0,29) | 14,20 (0,36) | - |
| LN@BPEI@AuSeeds1000 | 9,37 (0,58) | 42,09 (0,78) | 36,66 (2,64) | 3,87 (0,55) | ND | 8,55 (1,07) |
| LN@BPEI@AuSeeds3000 | 8,58 (0,22) | 36,65 (2,5) | 39,00 (2,0) | 4,7 (0,05) | ND | 11,05 (0,22) |
| LN@BPEI@AuSeeds1000@BPEI | 0,37 (0,04) | 9,72 (0,55) | 67,77 (0,87) | 21,40 (0,35) | ND | 0,71 (0,10) |
| LN@BPEI@AuSeeds3000@BPEI | 0,42 (0,23) | 9,49 (0,60) | 67,85 (1,46) | 21,42 (0,55) | ND | 0,82 (0,08) |
| LN@Au[1] | 10,88 (1,24) | 28,85 (2,65) | 35,54 (3,10) | 3,18 (0,68) | ND | 21,54 (2,12) |
| LN@Au[2] | 0,85 (0,23) | 36,79 (4,70) | 55,16 (4,93) | 3,06 (1,48) | ND | 4,13 (0,65) |
| Feuillets de Nb* | 20,78 (1,9) | 54,93 (2,1) | 20,69 (2,0) | | | |
| Couche de Au* | | 5,54 (0,55) | 29,54 (2,9) | | | 64,92 (3,6) |

**Table 7.** Pourcentages atomiques déterminés par XPS.

Après ajout de la deuxième couche de BPEI sur LN@BPEI@AuSeeds1000 et LN@BPEI@AuSeeds3000, on observe une augmentation nette des contributions de C et N tandis que celles de Au et Nb diminuent fortement. Le spectre fin autour de N1s pour les deux échantillons montre deux contributions à 399 et 400 eV, suggérant que les amines du BPEI sont partiellement protonées. Les composantes TOF-SIMS correspondantes sont PC1- et PC2- montrant une forte proportion de composés organiques contenant des ions azotes.

Enfin, l'analyse XPS des LN@Au finales révèle une augmentation de l'intensité des pics de Au et une diminution des pics de C et N. La quantification est ici peu fiable à cause d'une forte contribution du substrat de silicium. Ceci est confirmé en TOF-SIMS par une composante PC1 proche de 0 (peu d'espèces Li, Nb et N) et une composante PC2+ non nulle (échantillons riches en Au). Compte tenu des profondeurs sondées en XPS et en TOF-SIMS, si la couche d'or est continue, son épaisseur devrait se situer entre 1 et 4 nm, ce qui est cohérent avec l'épaisseur d'or de 1,2 nm déterminée par ICP-AES. Le diamètre des nanoparticules d'or mesuré au TEM (supérieur à 20 nm) provient peut-être du fait que l'imagerie TEM ne permet pas de déterminer l'épaisseur de ces nanoparticules.

Les nanoparticules LN@Au ont été caractérisées sur une période de 33 jours pour étudier la stabilité des dispersions. Les spectres d'extinction UV-Visible, les diamètres hydrodynamiques, les indices de polydispersité et les potentiels zeta de ces dispersions ont été obtenus (Figure 15).

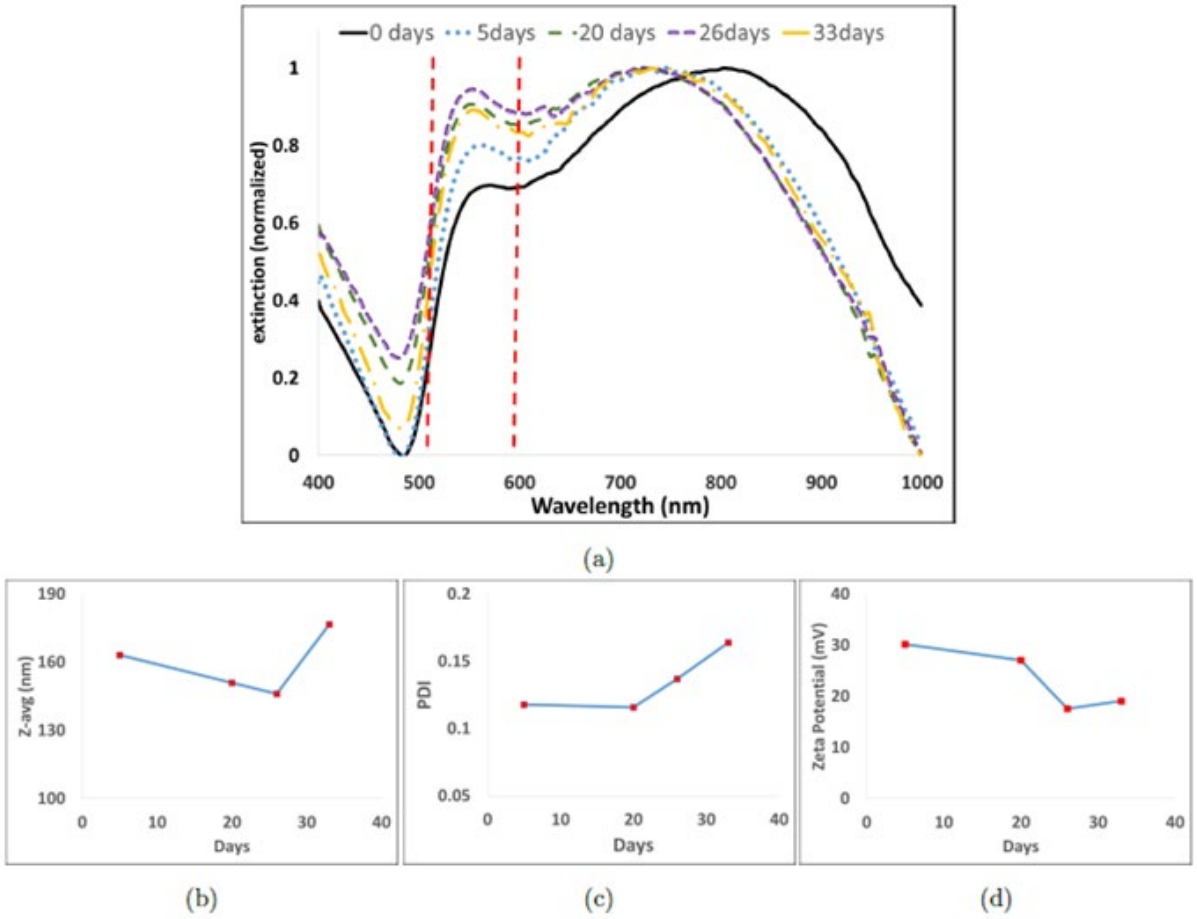


**Figure 15.** Evolution des spectres UV-Visible, diamètres hydrodynamiques, indices de polydispersité et potentiels zeta des LN@Au au cours de leur vieillissement.

On constate qu'après 5 jours de stockage, le spectre d'extinction a subi un décalage vers le bleu mais reste ensuite inchangée. Ceci est cohérent avec une réorganisation de l'or au cours du temps vers des morphologies plus isotropes. L'évolution du diamètre hydrodynamique, indice de polydispersité et potentiel zeta montre une stabilité qui diminue après 20 jours de stockage. Cette stabilité semble plus longue que celle de 2 jours indiquée pour des nanoparticules « framboise » Fe@Au [Plan Sangnier 2019]. Cependant, l'ajout final d'une coquille de polymère sur la coquille d'or pourrait aider à prolonger la stabilité des nanoparticules.

Des mesures préliminaires HRS ont été réalisées sur les nanoparticules cœur-coquille LN@Au (Figure 16). Pour chaque longueur d'onde d'excitation $\lambda_0$ entre 800 et 1300 nm, l'intensité SHG à $\lambda_0/2$ est mesurée.

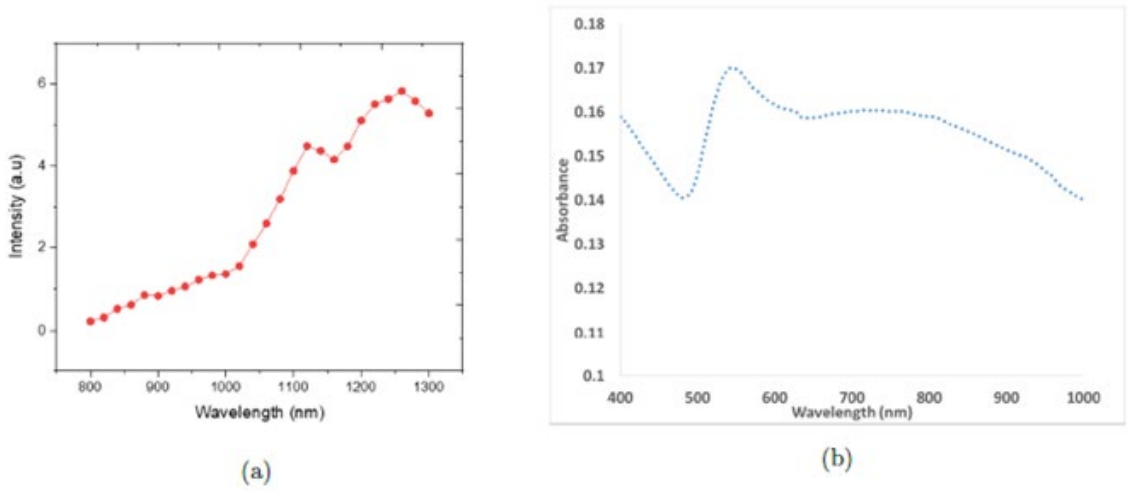


**Figure 16.** (a) Mesure HRS de LN@Au pour des longueurs d'onde d'excitation comprises entre 800 et 1300 nm. Les valeurs de l'ordonnée correspondent au rapport des intensités SHG mesurées pour LN@Au par rapport à celles mesurées pour LN. L'intensité est normalisée à 1 pour λ = 740 nm. Les concentrations de LN@Au et LN sont 0,16 g/L et 0,17 g/L, respectivement. (b) Spectres d'extinction des LN@Au.

On observe une exaltation du signal SHG de LN@Au comparé au LN pur avec 2 pics à 1150 et 1250 nm. Ceci est cohérent avec la présence de la coquille d'or comme l'ont démontré des travaux précédents [Richter 2013, Gürdal 2020]. L'exaltation obtenue à 1150 nm pourrait être attribuée au pic d'absorption des nanoparticules à 575 nm ($\lambda_0/2$). Des simulations sont nécessaires pour mieux interpréter le lien entre les propriétés SHG et la structure des nanoparticules cœur-coquille.

Enfin, les propriétés photothermiques des nanoparticules LN@Au ont été étudiées par thermographie infrarouge en utilisant le dispositif décrit précédemment. Les températures

mesurées en fonction de la durée d'irradiation avec le laser 808 nm et une image thermique typique sont présentées sur la Figure 17.

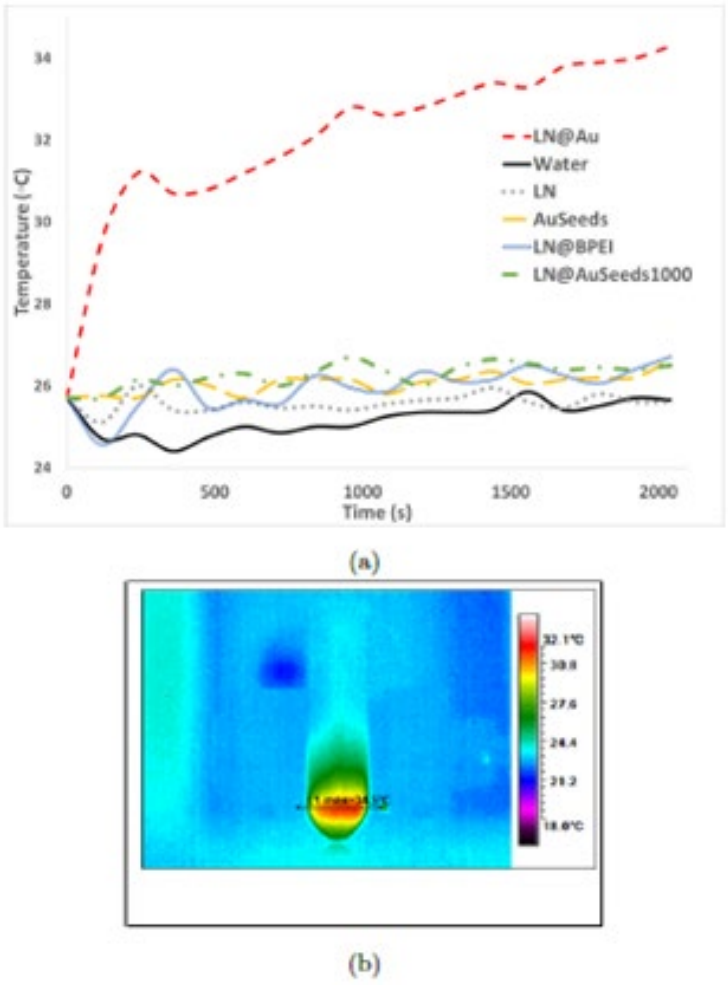


**Figure 17.** Evolution de la température sous irradiation à 808 nm des dispersions LN@Au, LN, LN@AuSeeds1000, LN@BPEI et AuSeeds (a). Image thermique des LN@Au (b).

Pour comparer nos nanoparticules aux autres agents photothermiques trouvés dans la littérature, l'efficacité de conversion lumière-chaleur ($\eta$) a été calculée à partir des travaux de Jiang *et al* [Jiang 2013], selon l'équation 5.

| | |
|---|---|
| $$\eta = \frac{\delta T \times m_s \times C_w \times B}{P_0 - \frac{P_0}{10^A}}$$ | Equation 5 |

où $\delta T$ est l'augmentation de la température en °C, $m_s$ la masse de l'échantillon en g, $C_w$ la chaleur spécifique de l'eau, $P_0$ la puissance du laser incident, $A$ l'absorbance de l'échantillon à 808 nm et $B$ le taux de dissipation de chaleur de la solution à l'environnement qui est calculé selon l'équation 6.

| | |
|---|---|
| $$e^{-Bt} = \frac{T_t - T_0}{T_m - T_0}$$ | Equation 6 |

où $T_t$ est la température mesurée au temps $t$, $T_0$ est la température initiale mesurée avant la mise en route du laser et $T_m$ est la température maximale mesurée.

En utilisant les équations précédentes, une efficacité de 40% est calculée pour les LN@Au. Une efficacité de 65% est reportée dans la littérature pour des nanoparticules « framboises » Fe@Au [Plan Sangnier 2019]. Comparé aux autres morphologies, nos nanoparticules présentent une meilleure efficacité que les nanoétoiles et les nanocoquilles mais moins bonne que les nanobâtonnets d'or. Il resterait cependant à étudier la contribution de l'absorption et de la diffusion à cette efficacité, ce qui permettrait d'optimiser les propriétés photothermiques des nanoparticules.

# Conclusion

Ce travail de thèse a concerné la mise au point de nanoparticules cœur-coquille avec des applications théranostiques potentielles. L'imagerie optique non linéaire est utilisée pour la fonction diagnostique, plus particulièrement la SHG, qui permet de faire varier la longueur d'onde d'excitation et de détection, d'obtenir une bonne résolution spatiale, d'éviter la photodégradation (contrairement aux sondes fluorescentes) et de minimiser la cytotoxicité, en particulier en utilisant des nanoparticules de $LiNbO_3$. La fonction thérapeutique est assurée par l'effet plasmonique photothermique d'une coquille en or.

La caractérisation des nanoparticules a été réalisée à l'aide de techniques physico-chimiques multiples et complémentaires. Une étude comparative a permis de souligner leurs avantages et inconvénients pour caractériser de façon la plus complète possible la taille, la forme, la morphologie et la stabilité des nanoparticules.

Les nanoparticules de LN synthétisées sont pseudo-sphériques avec un diamètre moyen de 45 nm et une charge de surface négative qui peut être renversée après ajout du polymère BPEI à leur surface. Une analyse XPS corroborée par une analyse par fluorescence ont permis de montrer qu'il y avait environ 1259 chaînes polymères par LN, ce qui correspond à 24% en pourcentage massique.

Des nanosphères d'or (AuSeeds) de 2,5 nm de diamètre avec une charge de surface négative ont été attachées par des interactions électrostatiques aux LN@BPEI. Nous avons démontré qu'il était possible de faire varier la densité de AuSeeds à la surface du LN par TEM et ICP-AES, le TEM montrant une corrélation linéaire entre le taux de couverture et la quantité de AuSeeds ajoutée tandis que l'ICP-AES montre une corrélation logarithmique.

L'effet sur les propriétés optiques non linéaires de l'ajout de AuSeeds sur LN a été évalué en mesurant l'hyperpolarisabilité par HRS. Nous avons constaté que cette hyperpolarisabilité diminuait sur LN@BPEI@AuSeeds par rapport au LN. Par contre, l'ajout de AuSeeds sur LN ne semble pas avoir d'effet sur le rapport de dépolarisation. Une modélisation de la structure des nanoparticules devrait permettre de mieux comprendre les propriétés observées.

Nous avons ensuite présenté deux méthodes de croissance de coquille d'or par ensemencement de germes en partant des LN@BPEI@AuSeeds. La méthode utilisant le citrate de sodium s'est avérée inadaptée pour nos nanoparticules. Par contre, la méthode « couche par couche » a montré plus de succès. Les paramètres expérimentaux tels que le pH, la densité d'AuSeeds et la concentration en $HAuCl_4$ ont été ajustés. Cette méthode permet d'obtenir une bande plasmon dans le proche infrarouge, ce qui était l'objectif recherché. En particulier, l'utilisation de LN@BPEI@AuSeeds1000, à pH neutre et avec une concentration en $HAuCl_4$ de 30 mM conduit à une bande plasmon autour de 803 nm, avec des nanoparticules bien dispersées ayant une structure type « framboise ». Les nanoparticules ont été caractérisées de façon détaillée, notamment par XPS et TOF-SIMS. L'étude préliminaire de la réponse SHG des LN@Au montre une exaltation comparée au LN même si des expériences complémentaires sont nécessaires. Enfin, nos nanoparticules présentent une efficacité de conversion lumière-chaleur de 40%, ce qui est du même ordre de grandeur que pour les autres structures décrites dans la littérature.

Les perspectives de ce travail sont nombreuses. Tout d'abord, il faudra tester les nanoparticules cœur-coquille en présence de cellules cancéreuses et sous irradiation pour voir si elles induisent un effet photothérapeutique. Ensuite, ces nanoparticules pourraient également être envisagées pour d'autres fonctionnalités comme par exemple pour leur activité en diffusion Raman, qui est supposée être forte pour des structures « framboise ».

Enfin, avec les nanoparticules LN@BPEI@AuSeeds, une thèse est en cours pour les utiliser en tant que catalyseur biologique mimant l'activité de la peroxidase.

## Bibliographie


[Bastus 2011] N. G. Bastus, J. Comenge, V. Puntes. Kinetically controlled seeded growth synthesis of citrate-stabilized gold nanoparticles of up to 200 nm: size focusing versus Ostwald ripening. *Langmuir*, 27(17):11098-11105, 2011.

[Boksebeld 2019] M. Boksebeld, V. Kilin, R. Taitt, L. Bonacina, A. Géloën, V. Lysenko, Y. Chevolot, V. Monnier, Nonlinear plasmonic nanohybrids as probes for multimodal cell imaging and potential phototherapeutic agents. *Biomed. Phys. Eng. Express*, 5(2):025039, 2019.

[Bonacina 2012] L. Bonacina, Nonlinear Nanomedicine: Harmonic nanoparticles toward targeted diagnosis and therapy. *Molecular Pharmaceutics*, 10(3):783-792, 2013.

[De Silva Indrasekara 2018] A. S. De Silva Indrasekara, S. J. Norton, N. K. Geitner, B. M. Crawford, M. R. Wiesner, T. Vo-Dinh. Tailoring the core-satellite nanoassembly architectures by tuning internanoparticle electrostatic interactions. *Langmuir*, 34(48):14617-14623, 2018.

[Duff 1993] D. G. Duff, A. Baiker, P. P. Edwards, A new hydrosol of gold clusters. 1. Formation and particle size variation. *Langmuir*, 9(9):2301-2309, 1993.

[Garcia-Soto 2016] M. J. Garcia-Soto, O. Gonzalez-Ortega. Synthesis of silica-core gold nanoshells and some modifications/variations. *Gold Bulletin*, 49(3):111-131, 2016.

[Goon 2009] I. Y. Goon, L. M. H. Lai, M. Lim, P. Munroe, J. J. Gooding, R. Amal. Fabrication and dispersion of gold-shell-protected magnetite nanoparticles: systematic control using polyethyleneimine. *Chemistry of Materials*, 21(4):673-681, 2009.

[Gürdal 2020] E. Gürdal, A. Horneber, N. Shaqqura, A. J. Meixner, D. P. Kern, D. Zhang, M. Fleischer. Enhancement of the second harmonic signal of nonlinear crystals by self-assembled gold nanoparticles. *The Journal of Chemical Physics*. 152(10):104711, 2020.

[Huang 2010] X. Huang, M. El-Sayed, Gold nanoparticles: Optical properties and implementations in cancer diagnosis and photothermal therapy, *Journal of Advanced Research*, 1(1):13-28, 2010.

[Jiang 2013] K. Jiang, D. A. Smith, A. Pinchuk. Size-dependent photothermal conversion efficiencies of plasmonically heated gold nanoparticles. *J. Phys. Chem. C*, 117(51):27073-27080, 2013.

[Joulaud 2013] C. Joulaud, Y. Mugnier, G. Djanta, M. Dubled, J. C. Marty, C. Galez, J. P. Wolf, L. Bonacina, R. Le Dantec. Characterization of the nonlinear optical properties of nanocrystals by Hyper Rayleigh Scattering. *J. Nanobiotechnol.,* 11(Suppl 1):S8, 2013.

[Khan 2018] F. Khan, S. Akhtar, S. Almofty, D. Almohazey, M. Alomari. FMSP-nanoparticles induced cell death on human breast adenocarcinoma cell line (MCF-7 cells): Morphometric analysis. *Biomolecules*, 8(2):32, 2018.

[LaMer 1950] V. K. LaMer, R. H. Dinegar, Theory, production and mechanism of formation of monodispersed hydrosols. *J. Am. Chem. Soc.,* 72(11):4847-4854, 1950.

[Lee 2017] D. K. Lee, Y. Song, V. T. Tran, J. Kim, E. Y. Park, J. Lee. Preparation of concave magnetoplasmonic core-shell supraparticles of gold-coated iron oxide via ion-reducible layer-by-layer method for surface enhanced Raman scattering. *J. Coll. Interf. Sci.,* 499:54-61, 2017.

[Oldenburg 1998] S. J. Oldenburg, R. D. Averitt, S. L. Westcott, N. J. Halas, Nanoengineering of optical resonances. *Chem. Phys. Lett.,* 288(2-4):243-247, 1998.

[Plan Sangnier 2019] A. Plan Sangnier, R. Aufaure, S. Cheong, L. Motte, B. Palpant, R. D. Tilley, E. Guenin, C. Wilhelm, Y. Lalatonne. Raspberry-like small multicore gold nanostructures for efficient photothermal conversion in the first and second


# RACHAEL TAITT

**11 RUE LANTERNE, 69001, LYON, FRANCE**
**rachaeltaitt@gmail.com**


## EXPERIENCE

10/2020- 03/2021 **Ingénieur d'étude, CNRS**

- Research on core-shell nanoparticles with photothermal and non-linear optical properties.

10/2017- 03/2021 **PhD student researcher at Institute of Nanotechnologies Lyon (INL), France**

- Research based on the synthesis and characterization of theranostics hybrid nanoparticles for cancer imaging and treatment. (optimized a synthesis protocol, designed photothermal laser experiment, performed data analysis, gave oral presentations, wrote scientific articles)

01/2018- 08/2020 **Chemistry laboratory practicals teacher, Ecole Centrale de Lyon, France (132 hrs total)**

- Guiding the students in practical work and grading reports. Year 1 and year 2 Ecole engineer students. Experiments based on gas phase chromatography and oxidation-reduction reactions.

01/2017- 07/2017 **Master 2 Chemistry Intern, Laboratoire Photophysique et Photochimie de Supramoleculaires et Macromoleculaires (PPSM, ENS Cachan), France**

- Thesis based on an interdisciplinary project aimed at making fluorescent surfaces for bacteria detection using the bottom-up nanoscale assembly technique of layer-by-layer.

02/2014- 06/2014 **Undergraduate Student Researcher, University of Gothenburg, Sweden**

- Conducted research on air quality (analysis of NOx and PM10 concentration in the air). Supervisor: Prof. Johan Boman

## COMMUNICATION

10/2019 **Caribbean Science and Innovation Meeting (Le Gossier, Guadeloupe)- Conference presentation**
R. Taitt, *et. al,* Synthesis of core-shell $LiNbO_3$@Au nanoparticles as multifunctional bio-imaging and photothermal therapy probes for cancer

11/2018 **Metallic Nano-Objects (MNO) 2018, (Lyon, France)- Workshop poster presentation**
R. Taitt, *et. al,* Core-shell $LiNbO_3$@Au nanoparticles for bioimaging and photothermal therapy: synthesis to application

07/2018 **Gold 2018 (Paris, France)- International Conference presentation**
R. Taitt**,** *et. al,* Gold-coated harmonic nanoparticles for multi-modal targeted imaging and treatment of cancer

06/2018 **Photothermal Effects in Plasmonics (Porquerolles, France)- Poster presentation**
R. Taitt, *et. al,* Gold-coated harmonic nanoparticles for multi-modal targeted treatment of cancer

## PUBLICATIONS

2021 R. Taitt et. al, Gold-seeded lithium niobate nanoparticles: influence of gold surface coverage on second harmonic properties. (Accepted for publication. Journal: Nanomaterials)

2021 R. Taitt et. al, Gold shell growth on $LiNbO_3$ nanoparticle core: Shell growth optimization for photothermal application. (A working title, to be submitted for publication in 2021)

2019 Maxime Bokesbeld *et al*, Nonlinear plasmonic nanohybrids as probes for multimodal cell imaging and potential phototherapeutic agents, Biomedical Physics & Engineering Express, **5**, 025029. DOI: 10.1088/2057-1976/ab0232

## EDUCATION

| | |
|---|---|
| 10/2017- 03/2021 | **PhD in Chemistry** *(defended 22nd March 2021)*<br>Ecole Centrale de Lyon, France<br>Specialty: Engineering for biology. |
| 09/2015- 07/2017 | **Msc Chemistry** *( Multiple diploma International Masters Rank: 6/17)*<br>University Paris-Saclay, France & University of Porto, Portugal<br>Erasmus Mundus Excellence Master Programme SERP-Chem, University Paris-Sud Orsay, France<br>Acceptance based on selection by a panel. |
| 11th-22nd July 2016 | **School on Science Management for Scientists and Engineers** (Genoa, Italy) |
| 09/2010- 07/2014 | **Bsc Chemistry & Management** *(graduated with Upper second-class Honors)*<br>The University of the West Indies Mona, Jamaica W.I |

## GRANTS & AWARDS

| | |
|---|---|
| 2019 | **INL PhD Days Prize Winner (Lyon, France)**<br>*(Awarded to the best scientific talk by PhD student)* |
| 2014 | **Linnaeus Palme Grant (Gothenburg, Sweden)**<br>*(Undergraduate chemistry exchange research grant)* |

## SKILLS & COMPETENCIES

| | |
|---|---|
| Spectroscopies | Transient Absorption, Time resolved Fluorescence, Steady state fluorescence and absorbance, EDX, XPS |
| Microscopies | TEM, SEM, Epi-fluorescence |
| Specializations | Synthesis and characterization of inorganic nanoparticles (working knowledge of XRD and HRS) |
| Softwares | LaTex, CasasXPS, Origin Data Analysis and Graphing, ImageJ, Microsoft Office |

## ACTIVITIES

| | |
|---|---|
| 09/2020- present | Singer in country-rock band ***Jascal Billy*** |
| 01/2020- present | Committee Member of the International Advancement Committee (IAC) of the Caribbean Cancer Research Initiative (CCRI) *(Non-profit Organization)* |
| 07/2018- 09/2020 | PhD representative for the department STMS, Ecole Centrale de Lyon, France |

## SOFT SKILLS

Excellent oral and written communication in english, networking, adaptability, creativity, teamwork

## LANGUAGES

English (native speaker) and French (B1)

**Core-shell nanoparticles active in non-linear optics for the imagery and phototherapy of cancer**


## Abstract

This thesis details the synthesis of core-shell nanohybrids designed for cancer theranostics application. The nanohybrid core is comprised of a non-linear optically active nanoparticle ($LiNbO_3$) that is intended to provide multiphoton bio-imaging. A gold shell is grown on the core whose purpose is to provide localized heating by way of plasmonic photothermal therapy. This work is focused on the growth of the gold shell using seeded-growth methods to provide a template for shell growth for the subsequent gold atoms produced by the reduction of gold salt. Included in this work is the evaluation of the surface preparation of the core nanoparticles with silanes and polyelectrolytes to permit gold seed attachment. Then the optimization of the gold shell growth experimental parameters pH, gold seed density on the core, and the concentration of the gold salt to be reduced is discussed. The characterizations of the nanoparticles and nanohybrids in this work were performed by XRD, TEM, UV-visible and ICP-AES. Additionally, the surface chemistry of the nanoparticles was evaluated by the techniques TOF-SIMS and XPS. On the other hand, the non-linear optical properties of the nanohybrids were investigated by way of Hyper Rayleigh Scattering. Lastly, the photothermal ability of the nanohybrid dispersion was determined using infra-red thermographic imaging.



Keywords: nanohybrids, non-linear optics, plasmonic, light-to-heat conversion, gold, lithium niobate


---

**Nanoparticules cœur-coquille actives en optique non linéaire pour l'imagerie et la photothérapie du cancer**


## Résumé

Cette thèse concerne la synthèse de nanohybrides à structure cœur-coquille en vue d'applications théranostiques du cancer. Le cœur du nanohybride est composé d'une nanoparticule active en optique non linéaire ($LiNbO_3$) pour l'imagerie biomédicale multiphotonique. La croissance d'une coquille d'or sur le cœur permet de produire un chauffage localisé par thérapie plasmonique photothermique. Ce travail est focalisé sur la croissance de la coquille d'or en utilisant des méthodes par ensemencement de germes permettant de construire un support pour l'ajout d'atomes d'or obtenus par la réduction de sels d'or. La préparation de la surface du cœur par des silanes et des polyélectrolytes pour réaliser l'accrochage des germes d'or est évaluée. Ensuite, la croissance de la coquille d'or est optimisée en faisant varier les paramètres suivants : pH, densité de germes d'or sur le cœur et concentration de sels d'or à réduire. La caractérisation des nanoparticules et nanohybrides est réalisée par XRD, TEM, spectroscopie UV-Visible et ICP-AES. De plus, la chimie de surface des nanoparticules est évaluée par TOF-SIMS et XPS. Les propriétés optiques non linéaires des nanohybrides sont caractérisées par Diffusion Hyper Rayleigh. Enfin, l'efficacité photothermique de la dispersion de nanohybride est déterminée par imagerie thermique infrarouge.



Mots-clés : nanohybrides, optique non linéaire, plasmonique, conversion lumière-chaleur, or, niobate de lithium.

*dernière page de la thèse*

# AUTORISATION DE SOUTENANCE

Vu les dispositions de l'arrêté du 25 mai 2016,

Vu la demande du directeur de thèse

Madame V. MONNIER et Monsieur Y.CHEVOLOT

et les rapports de

M. C. CHARNAY
Maître de Conférences HDR - Equipe IMNO - Place Eugène Bataillon - ICGM-IMNO
Bâtiment 17-CC1701 - 34095 Montpellier cedex 5

et de

Mme R. GRANGE
Professeure - ETH Zürich - HPT H2 - Institut für Quantenelektronik - Auguste-Piccard-Hof 1
8093 Zürich - Suisse

## Madame TAITT Rachael

est autorisée à soutenir une thèse pour l'obtention du grade de **DOCTEUR**

**Ecole doctorale** ELECTRONIQUE, ELECTROTECHNIQUE, AUTOMATIQUE

Fait à Ecully, le 12 mars 2021

P/Le directeur de l'E.C.L.
Le directeur des Etudes

Grégory VIAL